

Dissertation  
submitted to the  
Combined Faculties for the Natural Sciences and for Mathematics  
of the Ruperto-Carola University of Heidelberg, Germany  
for the degree of  
Doctor of Natural Sciences

presented by  
Michael Wayne Froese  
born in Winnipeg, Canada

Oral examination: January 20th, 2010



**A cryogenic electrostatic ion trap and  
first experiments on delayed emission of  
aluminum anion clusters and  
self-bunching**

Michael Froese

**Referees: Prof. Dr. Andreas Wolf  
Prof. Dr. Thomas Stöhlker**



**Zusammenfassung:** Zur Überprüfung von Technologien und Konzepten für die Entwicklung des kryogenen Ionenspeicherrings CSR wurde eine elektrostatische kryogene Falle für schnelle Ionenstrahlen (CTF) aufgebaut. Restgasdichten im Bereich von 2000 Teilchen/cm<sup>3</sup> (vergleichbar mit einem Druck von  $8 \cdot 10^{-14}$  mbar bei Raumtemperatur) wurden demonstriert, wobei mittlere Speicherlebensdauern von über 5 Minuten für 7.1 keV N<sub>2</sub><sup>+</sup> Ionen gemessen wurden. Die extrem reduzierte Umgebungsstrahlung in der CTF wurde danach für Untersuchungen der verzögerten Elektronenemission gespeicherter Aluminium-Clusterionen bei verschiedenen Temperaturen genutzt. Dabei wurden temperaturabhängig dramatische Abweichungen vom bekannten 1/t-Verhalten beim Zerfall heißer Clusterionen beobachtet und auch die photoneninduzierte verzögerte Elektronenemission erforscht. Diese Experimente deuten auf eine wesentlich stärkere Verringerung der Clustertemperatur als bisher erreicht hin, werfen aber auch Fragen über die Gültigkeit der gegenwärtig verwendeten Modelle auf. Die geringen Restgasdichten in der CTF haben außerdem Untersuchungen von spontan oder durch RF-Beschleunigung erzeugten Strahlpaketen in elektrostatischen Strahlfallen (EIBT) mit bislang unerreichter Präzision ermöglicht. Außerdem wurde durch ein falleninternes Massentrennungungsverfahren erstmals resonante transversale Strahlanregung in einer EIBT direkt gemessen.

**Abstract:** The Cryogenic electrostatic Trap for Fast ion beams (CTF) has been successfully built, fulfilling the Cryogenic Storage Ring (CSR) project goals of developing and testing the technologies and concepts to build this instrumentally challenging device, and demonstrating rest-gas-densities on the order of 2000 particles/cm<sup>3</sup> (or a room-temperature equivalent pressure of  $8 \cdot 10^{-14}$  mbar) with mean storage lifetimes of over 5 min for 7.1 keV N<sub>2</sub><sup>+</sup> ions. Since this is the first cryogenic electrostatic ion beam trap (EIBT), the resulting environment of greatly reduced blackbody radiation was exploited by investigating the time dependence of delayed electron emission from aluminum cluster anions at different temperatures. Dramatic deviations from the commonly observed 1/t decay of hot clusters were observed, demonstrating this decay's dependence on the temperature of the storage environment. Delayed emission following the excitation of the aluminum clusters with a pulsed laser was also observed. The results indicate a considerable reduction in the cluster temperature than seen so far and raises questions about the validity of the present model. The very low rest gas densities achieved also enabled the exploration of many properties of self-bunching and RF bunching with unprecedented sensitivity. An in-situ mass-selection technique exploiting the resonant transverse excitation of the stored ions was also demonstrated inside an EIBT for the first time.

# Contents

<b>1</b>	<b>Introduction</b>	<b>1</b>
1.1	Physics and astro-chemistry with storage rings . . . . .	1
1.2	The Cryogenic Storage Ring (CSR) . . . . .	3
1.3	The Cryogenic Trap for Fast ion beams (CTF) . . . . .	6
1.4	Outline of this work . . . . .	7
<b>2</b>	<b>Theoretical background</b>	<b>9</b>
2.1	Ion trapping in an EIBT . . . . .	9
2.2	Trapped ion losses . . . . .	12
2.2.1	Electron capture . . . . .	12
2.2.2	Collisional detachment . . . . .	12
2.2.3	Single and multiple scattering . . . . .	13
2.2.4	Intrabeam scattering . . . . .	14
2.2.5	Modeling of trap losses . . . . .	15
2.3	The tune of an EIBT . . . . .	16
2.4	Self-bunching of ions stored in an EIBT . . . . .	17
2.5	Delayed emission and fragmentation of small metal cluster anions . .	19
2.5.1	Temperature induced cluster dissociation . . . . .	19
2.5.2	Photon-induced delayed emission . . . . .	24
2.5.3	Limitation of the above model: Delayed fragmentation . . . .	26

<b>3</b>	<b>Experimental setup</b>	<b>29</b>
3.1	The cryogenic electrostatic ion beam trap . . . . .	31
3.1.1	Heat transport mechanisms . . . . .	31
3.1.2	Cryogenic design . . . . .	33
3.1.3	Temperature measurement . . . . .	40
3.1.4	Vacuum system . . . . .	42
3.1.5	Trap electrodes . . . . .	45
3.1.6	Pickup electrodes . . . . .	47
3.1.7	First bake-able charcoal-based UHV cryopump . . . . .	48
3.2	Surrounding instrumentation . . . . .	50
3.2.1	Ion injection beam line . . . . .	50
3.2.2	Experimental control and data acquisition . . . . .	53
3.2.3	Bake-out system . . . . .	55
3.2.4	Interlock and safety system . . . . .	57
3.3	Laser experiments with the CTF . . . . .	59
3.4	CTF driven CSR design modifications . . . . .	61
3.4.1	Experimental chamber suspension . . . . .	61
3.4.2	Pumping requirements . . . . .	63
3.4.3	Thermal shield design . . . . .	64
3.4.4	Thermal conductivity and temperature sensors . . . . .	65
<b>4</b>	<b>Beam storage in a cryogenic ion trap</b>	<b>67</b>
4.1	First operation of the new ion trap . . . . .	67
4.2	Self-bunched ions and ions oscillating in a cryogenic trap . . . . .	72
4.2.1	Extended self-bunching observation . . . . .	72
4.2.2	Self-bunching decay lifetimes . . . . .	77
4.2.3	RF Bunching . . . . .	80
4.2.4	Bunch length measurements via photo-detachment . . . . .	84
4.2.5	Mass resolution . . . . .	87
4.2.6	Ion bunching conclusions . . . . .	88

4.3	Mass selection inside the electrostatic ion trap . . . . .	89
4.3.1	RF-kick . . . . .	90
4.3.2	RF Knock-out and trap tune measurement . . . . .	92
4.4	Demonstrating $10^{-14}$ mbar RTE . . . . .	94
<b>5</b>	<b>Decay and fragmentation of excited aluminum cluster anions</b>	<b>99</b>
5.1	Long-time decay of negative atomic ions and $\text{Al}_n^-$ clusters . . . . .	99
5.1.1	Neutral fragment decay . . . . .	99
5.1.2	Decay measurements via photo-detachment . . . . .	102
5.2	Fast decays of highly excited $\text{Al}_n^-$ . . . . .	106
5.2.1	$\text{Al}^-/\text{O}^-$ results . . . . .	107
5.2.2	Aluminum molecular and cluster anion measurement conditions	109
5.2.3	Fast decay of initially, highly excited $\text{Al}_2^-$ . . . . .	114
5.2.4	Fast decay of initially, highly excited $\text{Al}_n^-$ clusters . . . . .	117
5.3	Photon-induced delayed electron emission and fragmentation of $\text{Al}_n^-$ .	123
5.3.1	Basic observations . . . . .	124
5.3.2	Analysis and Discussion . . . . .	128
5.3.3	Conclusions on cluster cooling . . . . .	141
<b>6</b>	<b>Summary and Prospects</b>	<b>143</b>
	<b>Bibliography</b>	<b>147</b>

# List of Figures

1.1	A schematic layout of the CSR. . . . .	3
1.2	CSR optical lattice schematic. . . . .	5
1.3	CTF experiment setup schematic. . . . .	7
2.1	Trap electrode position and potentials corresponding to ions with a kinetic energy of 6.0 keV. . . . .	10
2.2	Space charge distribution of the oscillating ion bunch. . . . .	17
3.1	CTF $N_2^+$ experimental setup schematic . . . . .	29
3.2	Photo of the CTF setup used for the first experiments. . . . .	30
3.3	CTF cross-sectional schematic view. . . . .	33
3.4	Schematic of the CTF experimental vacuum chambers. . . . .	34
3.5	CTF cross section showing the cooling unit. . . . .	35
3.6	Cool-finger shortcut between superfluid 1.8K helium and pumped helium gas line used to cool the chambers. . . . .	36
3.7	Labeled CTF cross-sectional photo. . . . .	37
3.8	Photo of the trap chamber suspension before the test chamber is installed. . . . .	38
3.9	A sample 2K thermal anchor for the HV electrode cables plus Cu cooling bands for the chambers. . . . .	38
3.10	Photo of the 80K thermal shields with water cooling lines and multilayer insulation visible. . . . .	39
3.11	Photos of the temperature sensors used in the CTF isolation vacuum. . . . .	41
3.12	Silicon diode sensor and its thermally anchored cables. . . . .	42
3.13	CTF and beamline vacuum schematic. . . . .	43
3.14	Photo of a molecular sieve mounted in the isolation vacuum. . . . .	44

3.15 Photo of trap electrodes. . . . .	45
3.16 Schematic of one of the two mirrored CTF trap electrode stacks. . . . .	46
3.17 Photo of the pickup electrodes. . . . .	48
3.18 Activated charcoal layer of the cryopump. . . . .	49
3.19 Photo of the bake-able, charcoal-based, UHV cryopump. . . . .	50
3.20 Beam cleaner schematic. . . . .	52
3.21 MCP data acquisition schematic. . . . .	54
3.22 MCP timing schematic employed in lifetime measurements. . . . .	55
3.23 Experimental vacuum chamber heating coil schematic. . . . .	56
3.24 CTF interlock schematic. . . . .	58
3.25 CTF setup employing a laser to photo-detach stored anions. . . . .	59
3.26 A photo of the CTF setup used to perform photo-detachment experiments. . . . .	60
3.27 CTF laser setup schematic. . . . .	61
3.28 CSR cryogenic cross-section schematic. . . . .	62
3.29 CSR precision ion optic support stand schematic. . . . .	63
3.30 CSR pumping schematic for one corner of the ring. . . . .	64
4.1 First room-temperature $N_2^+$ CTF lifetime measurement. . . . .	68
4.2 7.1 keV $N_2^+$ 300 s lifetime measurement . . . . .	69
4.3 Sample 7.1 keV $N_2^+$ pre-amplified pulse as seen on the pickup electrodes inside the trap with an oscilloscope. . . . .	70
4.4 Spectrum analyzer sweep and FFT showing the presence of $Al_3^-$ at a trap temperature of 92 K. . . . .	71
4.5 Self-bunching $N_2^+$ frequency amplitude vs (a) injection time and (b) time after bunch decay. . . . .	73
4.6 Spectrum analyzer ion current calibration. . . . .	75
4.7 Number of bunched $N_2^+$ and $Al_2^-$ ions plotted with respect to bunch decay time. . . . .	75
4.8 Sample $N_2^+$ and $Al_2^-$ ion bunch decay curves with an exponential lifetime fit. . . . .	77
4.9 Exponential bunch lifetime vs number of initially stored for (a) $N_2^+$ and (b) $Al_2^-$ ions. . . . .	78
4.10 Fitting results from intrabeam scattering. . . . .	79

4.11	Demonstration of re-bunching using RF after the bunch has dispersed.	80
4.12	Comparison between ion bunches in self-bunching mode to those additionally driven with RF.	81
4.13	Pickup signals as a function of time for three well-defined relative phases between RF and the injected ion pulse.	82
4.14	Amplitude (a) and lifetime (b) of the pickup signal for an RF-bunched beam vs RF bunching phase.	82
4.15	6.0 keV $N_2^+$ ion bunch signal amplitude vs 600s storage time.	83
4.16	Two sample $Al_2^-$ ion bunch length measurements with the laser striking and missing the ion bunch.	85
4.17	$Al_2^-$ bunch length measurement performed by varying the laser time delay.	86
4.18	RF kick mass selection schematic.	90
4.19	Spectrum analyzer spectrum demonstrating kick-out mass selection.	91
4.20	Demonstration of the RF knock-out mass selection technique.	92
4.21	Trap tune measurement using RF Knock-out mass selection.	93
4.22	Temperature, pressure, ion current, and rest-gas-density as a function of time during the warmup which demonstrated $10^{-14}$ mbar RTE pressures.	98
5.1	Lifetime measurements of $O^-$ and $Al^-$ .	100
5.2	Decay measurements of $Al_2^-$ over 1 s and 100 s.	101
5.3	Two sample TOF spectra of neutrals counted after a laser pulse.	102
5.4	$Al^-$ , $Al_2^-$ , and $Al_3^-$ photo-detachment decay curves.	103
5.5	$Al_4^-$ , $Al_5^-$ , $Al_6^-$ , and $Al_7^-$ photo-detachment decay curves.	105
5.6	Decay from a hot $Al^-/O^-$ mixed beam at a trap temperature of 90 K, fit to an exponential decay.	108
5.7	Spectrum analyzer sweeps of different stored ion beams at trap temperatures below 15 K.	111
5.8	Spectrum analyzer sweeps of different stored ion beams at trap temperatures around 90 K.	112
5.9	Laser prompts of different stored beams at trap temperatures below 15 K.	113
5.10	Laser prompts of different stored beams at trap temperatures around 90 K.	114

5.11	Delayed emission of a hot, mass-selected $\text{Al}_2^-$ beam at a trap temperature $<15$ K, fit to two different functions. . . . .	115
5.12	Decay of a hot, mass-selected $\text{Al}_2^-$ beam at a trap temperature $<15$ K, fit to a modified $1/t$ power law for metal anion dimers. . . . .	116
5.13	Delayed emission plots of hot $\text{Al}_n^-$ dominated beams at a trap temperature $<15$ K, fit to a modified $1/t$ power law. . . . .	118
5.14	Delayed emission of a hot $\text{Al}_n^-$ dominated beam at a trap temperature of around 90 K, fit to a modified $1/t$ power law. . . . .	119
5.15	Fast decay of a highly excited $\text{Al}_4^-$ dominated beam at a trap temperature of 95 K, fit to a modified $1/t$ power law. . . . .	120
5.16	Blackbody spectrum at 10, 40, and 90 K. . . . .	121
5.17	An illustration of the photon absorption induced delayed emission used to measure aluminum anion cluster temperatures. . . . .	123
5.18	Sample oscillation frequency scan of the ion beam used in the delayed emission experiment. . . . .	124
5.19	Fragment arrival TOF spectrum demonstrating the various masses inside the trap during a delayed emission experiment. . . . .	125
5.20	Sample aluminum cluster instantaneous decay rate measurement with laser pulses. . . . .	126
5.21	Sample delayed emission spectrum including prompt and background. . . . .	127
5.22	Sample delayed emission spectrum showing mass peak assignment. . . . .	128
5.23	$\text{Al}_4^-$ delayed emission as a function of time after laser excitation for sample probe times at CTF trap temperatures $<15$ in comparison to a previous measurement at room-temperature. . . . .	130
5.24	Fitted $\text{Al}_4^-$ and $\text{Al}_5^-$ internal cluster temperature as a function of time after ion injection. . . . .	131
5.25	Delayed emission counts as a function of time after laser excitation for $\text{Al}_4^-$ , $\text{Al}_5^-$ , $\text{Al}_6^-$ , and $\text{Al}_7^-$ . . . . .	133
5.26	Total delayed emission events for $\text{Al}_4^-$ to $\text{Al}_8^-$ as a function of time after injection. . . . .	134
5.27	Investigation of the ion current dependency of delayed emission. . . . .	135
5.28	The unexpectedly large $\text{Al}_4^-$ delayed emission at $8.7 \mu\text{s}$ . . . . .	136
5.29	The unexpectedly large $\text{Al}_5^-$ delayed emission at $9.7 \mu\text{s}$ . . . . .	137
5.30	Sample laser shot demonstrating the unexpected large number of delayed events at short times in addition to investigating the statistical model's dependencies. . . . .	140

# List of Tables

3.1	CSR/CTF cryogenic refrigeration system specifications . . . . .	34
3.2	CTF temperature sensor ranges . . . . .	40
3.3	Typically employed trap voltages . . . . .	46
3.4	Typical Penning ion source operational parameters. . . . .	51
3.5	Typical operational parameters for the sputter source. . . . .	51
3.6	Experimental vacuum chamber heating channel characteristics . . . . .	57
4.1	Table of employed CTF ion oscillation frequencies and harmonics at 6.0 keV. . . . .	72
5.1	Table of experimental parameters used to select the aluminum cluster anions in the fast decay experiments. . . . .	110
5.2	Table of fitted values using equation 2.42 to describe the delayed emission from various aluminum anion clusters by including the effects of radiative cooling. . . . .	117
5.3	Table of values used in the temperature analysis of the observed $Al_4^-$ and $Al_5^-$ photon-induced delayed emission. . . . .	129



# Chapter 1

## Introduction

### 1.1 Physics and astro-chemistry with storage rings

Interstellar gas and dust constitute the primary material from which the solar system was formed. It has been proposed that the delivery of larger organic molecules through comets to the later cooled planetary bodies and other molecular formation processes were essential in the formation of life [1–5]. A wide variety of simple organic molecules have also been found in high abundance throughout the formation regions of young circumstellar disks [6]. Over 70 different molecules, for example, have already been identified in a single dusty envelope around a carbon star [7]. For this reason, it is important to understand the formation of these molecules in space [8]. With this incentive, the role positive ions play in molecular formation has quickly developed in the short time since they were discovered in space [9]. Positive ions such as  $\text{H}_3\text{O}^+$ , which play a decisive role in the formation of water, were already identified in 1986 [10, 11]. Negative ions, such as  $\text{C}_6\text{H}^-$ , have only been recently (2006) found in space [12], followed by a host of other anionic species and the confirmation of significant abundances [7, 13–16].

Atomic and molecular physics, in addition to astrophysics and astrochemistry, have significantly developed due to the experimental input gained from ion storage devices. Magnetic storage rings, such as the Test Storage Ring (TSR) in Heidelberg, continue to perform recombination rate experiments with phase-space cooled ions at MeV kinetic energies to understand how these molecules are created by studying how molecular ions dissociate into smaller fragments through the capture of an electron (e.g. [17, 18]). Branching ratios, which are used to describe the fragments produced in such reactions as well as their relative amounts, are also measured [19]. The fragmentation geometry can also be explored to determine if the molecule pref-

entially captures an electron incident from a particular direction with respect to the molecular frame of reference [20]. These collisions are studied as a function of collision energy between a molecular ion and an electron. The species stored in these rings are typically produced in hot ion sources where they acquire considerable vibrational excitation. For molecules with a permanent electric dipole moment, this excitation relaxes during storage in a ring (or a trap) by emission of IR radiation, resulting in the rapid vibrational cooling of the stored molecular ions. Such rings are flexible in that they can also be used to study dielectronic recombination of atomic ions [21] and perform mass measurements [22], furthering the understanding of atomic and nuclear physics. Despite their flexibility, such magnetic rings have two limitations. Firstly, the maximum mass that can be stored is limited by the rigidity of the beam and the field of the employed bending magnets. The necessary magnetic field strength  $B$  of these bending elements with radius  $r$  is given by  $Br = \sqrt{2mE}/q$ , where  $m$ ,  $E$ , and  $q$  are the ion mass, energy, and charge, respectively. While higher charge states can be used to store slightly heavier ions, clear limitations are set for the maximum masses achievable with low charge states. Secondly, the 300 K blackbody radiation from the vacuum chambers generally prevents the stored molecular ions from cooling below room-temperature, let alone approach the cryogenic temperatures valuable to atomic and molecular physics and typically found in space. Achieving cold, well defined molecular systems in rovibrational ground states through radiative cooling and electron phase-space cooling is of significant interest for atomic, molecular, and cluster physics. As the number of involved energy states is significantly limited at cryogenic temperatures, very well defined initial states can be prepared. The limited number of precisely defined states greatly simplifies the theory needed to describe collision interactions, thus promoting a more exact understanding of the processes involved (e.g. dissociation) by testing these models at higher sensitivities.

Larger molecular systems and clusters are of particular interest lately, given the rise in the number of electrostatic storage devices that can investigate such large systems as discussed below. Given that clusters represent the transition between small atomic and molecular systems that are generally quantum dynamically understood, and larger macroscopic systems which are described by bulk properties, cluster physics represents a very challenging field, filled with complex physics. Systematic studies on how the properties of matter change as a function of size can be explored via clusters. The geometry, and therefore the properties, of such few body systems dramatically changes, moving from planar clusters to larger clusters with three dimensional geometry [23], requiring higher dimensional models. This entails more interactions between the constituent atoms in the cluster, giving rise to more vibrational degrees of freedom and modes in which to store energy. The

Schroedinger equation, however, cannot be readily applied to such large and complicated systems to determine basic properties such as cluster energy levels, binding energies, geometric states, vibrational modes, and heat capacities. Experiments, therefore, are required to further the understanding of the physics contained within these large systems.

## 1.2 The Cryogenic Storage Ring (CSR)

To overcome both the cooling and mass limitations that apply to room-temperature magnetic storage rings, a new type of storage ring is currently being constructed at the Max Planck Institute for Nuclear Physics in Heidelberg (see Fig. 1.1). Designed as an electrostatic storage ring, the device depends on electrostatic fields to bend the stored ions along a closed orbit. The mass limitation is essentially removed for such storage devices since electrostatic rigidity is proportional to  $E/q$ , where  $E$  and  $q$  are the ion energy and charge, respectively. In contrast with magnetic rings, the ion's mass does not enter into the electrostatic rigidity, permitting the investigation of not just highly charged atomic ions but large polyatomic molecules as well. Other smaller electrostatic rings exist which are based on the race-track-style design, beginning with ELISA in 1998 [24, 25]. The TMU electrostatic ring followed in 2004 with a similar geometry, but with the added ability to cool the electrodes to

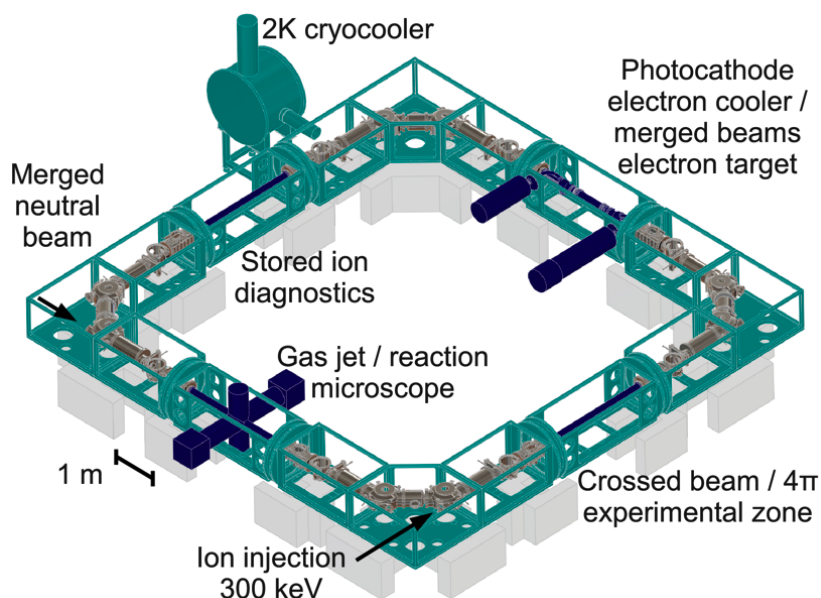


Figure 1.1: A schematic layout of the CSR.

liquid nitrogen temperatures, thereby allowing the cooling of vibrationally excited states of large molecules [26]. The Cryogenic Storage Ring (CSR), however, will be the first electrostatic storage ring where the beam-pipe can be cooled to any given temperature between 10 K and 300 K, allowing complete ro-vibrational cooling by emission of IR radiation to simulate the environment found in space. Due to these cryogenic vacuum chambers, which will also be baked to 350°C, and other cryogenic and conventional pump facilities, rest gas densities on the order of 2000 particles per cm<sup>3</sup> (or a vacuum on the order of several 10<sup>-14</sup> mbar room-temperature equivalent) will be created, surpassing all previously achieved storage ring vacuum by orders of magnitude. Vacuum on this level will greatly reduce the number of collisions between the stored ions and rest gas molecules that lead to beam loss. This will promote long storage lifetimes for beam energies in the 20-300 keV per charge range, which were previously unavailable due to inherently high rest gas collision cross-sections [27]. These reduced beam energies also translate to readily manageable voltages of the electrostatic ion optics. The achievement of these vacuum levels in a large vacuum system was first demonstrated by the CSR prototype device, called the Cryogenic Trap for Fast ion beams (CTF). A detailed description of the CTF will be given within this work. The ability to prepare species in their rotational and vibrational ground states will expand the atomic and molecular physics program currently being pursued using room-temperature storage rings.

With its 35 m circumference, the CSR is also the first electrostatic ring consisting of four straight sections, which will be dedicated to experiments and diagnostics (see Fig. 1.1), while the corners will use two 6° and two 39° deflectors allowing the injection and detection of a wide range of ionic masses and charge states, as shown in the lattice schematic of Fig. 1.2. The CSR cryogenic beam-pipe will be cooled using 1.8 K superfluid helium from the cryocooler, which was already used to cool the CTF [28]. Copper surfaces in direct contact to the superfluid helium will ensure optimal cryo-pumping of hydrogen, as described in more detail in Section 3.4.2. The cryogenic vacuum chambers will be enclosed in two thermal shields (cooled with a second helium gas cooling circuit to 40 K and 80 K) and multi-layer insulation, all of which will be encased in an outer isolation vacuum chamber (see Fig. 3.28). Specially designed low cross-section titanium supports will be used to provide the necessary thermal isolation and to support the weight of the cold vacuum chambers between the inner vacuum chamber and the 40 K shield, and again between the 40 K shield and the outer room-temperature vacuum chamber. Precision alignment of the ion optic elements at any operational temperature will be accomplished by mechanically de-coupling the electrode supports from those used for the inner vacuum chambers (see Fig. 3.29).

## 1.2. The Cryogenic Storage Ring (CSR)

---

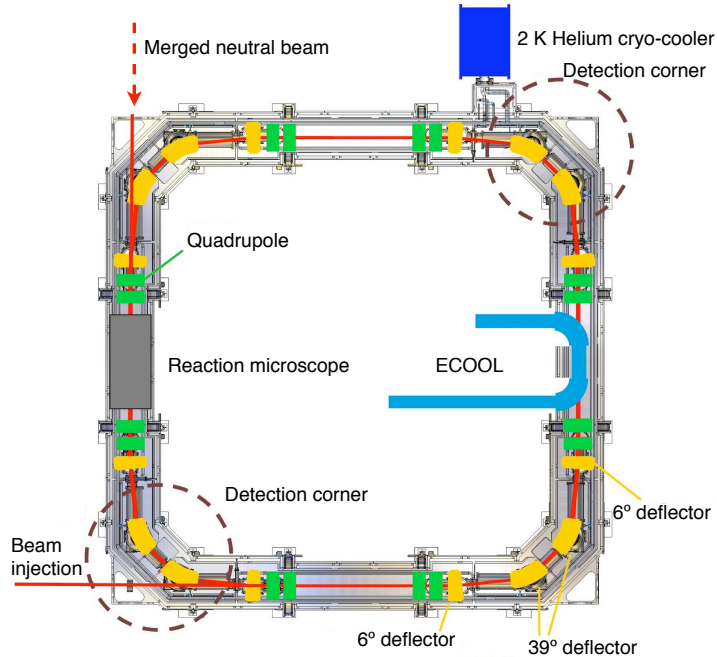


Figure 1.2: CSR optical lattice schematic.

One straight section will include a unique photocathode electron cooler [29–31], where cold, intense electron beams at very low energies (velocity-matched to the stored ions) will phase-space cool the stored molecular ions, or act as targets for the stored ions. Detectors following the electron cooler will be able to detect both neutral and charged fragments resulting from such collisions.

A variety of beam diagnostic detectors will be available, all of which will have to operate in the same extremely demanding cryogenic, yet bake-able, extreme high vacuum (XHV) environment. The diagnostics will also extend the detection range of d.c. ion beams down to nA intensities, to accommodate the low production rates of heavier bio-molecules [32]. Such small currents will be detected with a direct current transformer using a SQUID device, while an array of position sensitive pickups [33] will monitor the position and intensity of pulsed beams. One straight section is reserved exclusively for such beam diagnostic detectors, in addition to a beam profile measurement device [34], though additional diagnostic detectors will be distributed throughout the ring.

The last straight section will be equipped with a reaction microscope [35,36], which employs a supersonically expanded gas jet to produce low temperature atomic beams as a collision target for the stored molecular ions. A reaction microscope consisting

of a series of magnetic coils and electric fields will be used to capture all of the resulting collisional fragments. The entire collision process, including the distribution of kinetic energy amongst the products, can thereby be measured in a kinematically complete scattering experiment.

This technologically demanding storage ring was preceded by the Cryogenic Trap for Fast Ion beams (CTF), which as a prototype, allowed the testing and development of the technology and methods necessary to design and build the CSR. The design modifications to the CSR due to experience, tests, and results from the CTF are also documented within this work in Section 3.4.

### 1.3 The Cryogenic Trap for Fast ion beams (CTF)

While the necessity of building a prototype device to test the technologies for such a challenging project as the CSR is clear, the CTF is a device with many applications and can greatly contribute to physics in its own right. The trapping principle is based upon the 1997 design of the Electrostatic Ion Beam Trap (EIBT) by Zajfman *et al.* [37]. This type of electrostatic trap, where ions with kinetic energies of several keV are trapped in stable orbits between two sets of electrostatic mirrors, can now be found in various laboratories around the world [37–41]. What sets the CTF apart from these traps, is its unique ability to be cooled to any temperature between 10 and 300 K and its extremely high vacuum, resulting in very long storage times (see Section 4.1). Superfluid helium at 1.8 K is used to cool the CTF vacuum chambers and trap electrodes to cryogenic temperatures. The cryogenic beam-pipe containing the stored ions is encased in a series of thermal shield layers to protect this region from room-temperature radiation (see Fig. 1.3). Thermal conduction via air convection is prevented by placing this entire system of layers inside a pumped cryostat vacuum chamber. An ion injection beam line is then used to produce pulsed ion beams, which are let into the trap by switching off the voltages on the entry side electrostatic mirror, then trapped by quickly raising the voltages after the ion pulse has entered the trap. Neutral fragments can then be counted via a particle detector along the beam axis behind the trap. Additional measurement possibilities have been exploited by crossing the stored ion beam with a pulsed laser beam.

Due to the cryogenic design of this trap, residual gas densities on the order of 2000 particles/cm<sup>3</sup> have been achieved, which would correspond to a vacuum of  $8 \cdot 10^{-14}$  mbar in a room-temperature vacuum system. This extreme high vacuum (XHV) suppresses the rest-gas-density dependent ion losses from the trap which limit the lifetime of stored beams in other such traps. This has allowed new aspects of beam dynamics in an EIBT to be studied. The so-called self-bunching mode is of

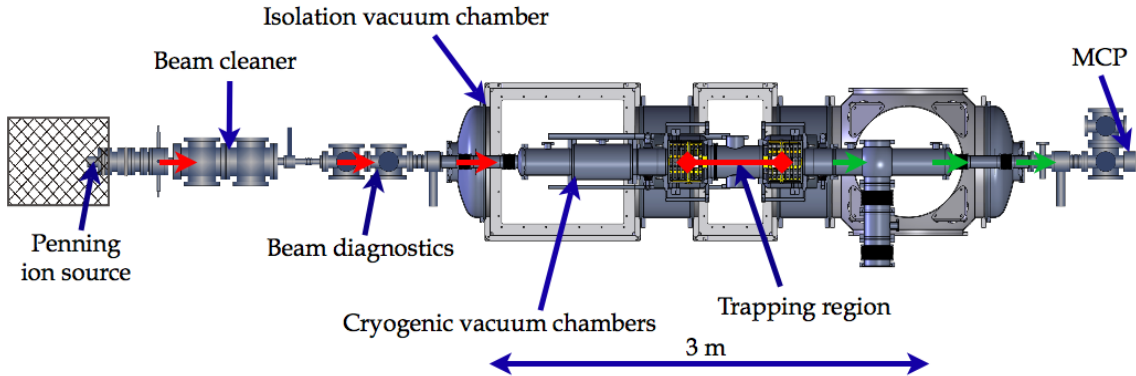


Figure 1.3: A schematic of the CTF setup used for the first experiments.

particular interest here, given the possibilities of performing mass cleaning and mass spectrometry measurements with very high precision [42], which could possibly be competitive with storage rings.

The dramatically reduced blackbody radiation environment also lends itself to radiative cooling studies, which have been frequently performed in both EIBTs and storage rings at room-temperature, but have never been carried out at such low temperatures in an EIBT before. Combining the greatly reduced blackbody radiation environment with the mass independent trapping ability, inherent to electrostatic devices, aluminum clusters were chosen as the first species to be investigated. Other aspects of physics, can also be investigated with the CTF. The long lifetimes achievable in the CTF allow a much clearer investigation of metastable states in comparison to those done by EIBTs at room-temperature [43]. The CTF can also contribute to atmospheric physics, by assisting in the understanding of how aerosols and larger clusters, which are essential to cloud formation, are formed [44] and destroyed through temperature dependent collisional studies.

## 1.4 Outline of this work

The next chapter will provide the theoretical background for the experiments, as well as providing a basic introduction to heat transport mechanisms. This is essential to understand the cryogenic construction of the CTF device. The ion trapping process in an EIBT is then explained, followed by an introduction to the trapping mode known as self-bunching. An ion loss model for the trap is also presented. This is followed by a discussion of a previously unexplored property of the trap, known in

storage ring physics as the tune. This is followed by a brief background on statistical mechanics concerning the delayed emission of cluster anions.

The experimental setup is then described in detail, focusing first on the CTF itself, then the associated instrumentation, and finally the laser setup. A summary of the CSR design modifications due to the experience and tests with the CTF is also included here.

The next two chapters report the multitude of experimental results gained from the CTF. The first chapter on beam storage in a cryogenic trap demonstrates the first room-temperature trapping with this device, followed by a host of exciting, new measurements on ion bunching, which were made possible due to the extremely low rest gas densities of around 2000 particles/cm<sup>3</sup> achieved in the CTF. Two different procedures for mass-selection of ions inside the trap are presented. One of these procedures (the knock-out method) is employed for the first time inside an EIBT. The measurement demonstrating the achieved rest gas densities is then presented, followed by decay measurements of aluminum cluster anions. Some of these decay measurements were performed using a novel laser-induced photo-fragmentation approach.

The second experimental chapter focuses on the decay and fragmentation of excited anionic aluminum clusters. The decay of initially hot clusters is first analyzed, demonstrating the typically observed 1/t decay pattern at temperatures around 90 K, as well as the first demonstration of the temperature dependence of this decay below 15 K. At such low temperatures, the time dependence of the emission deviates strongly from the normally observed behaviour. Refined theoretical models accounting for radiative cooling cannot completely explain these results. The possible implications and origins of this decay are explored. Photon-induced delayed emission of the same clusters is then presented. Laser-induced delayed emission is observed in five different clusters and the radiative cooling of Al<sub>4</sub><sup>-</sup> and Al<sub>5</sub><sup>-</sup> is studied in detail. A theoretical model is applied, which attempts to measure the cluster temperature.

The conclusions summarize the experimental results performed during these first measurements with the CTF and an outlook examining the wide range of possible measurements is presented.

# Chapter 2

## Theoretical background

This chapter will provide the necessary theoretical background to understand the experiments performed within the scope of this work, in addition to introducing concepts useful in understanding the functionality of electrostatic ion beam traps (EIBTs). The process of ion trapping using an EIBT will be outlined, followed by an explanation of the trap losses which occur and how these are modeled. A type of trapping mode known as self-bunching will then be introduced. An additional property of the trap, namely the tune, will also be introduced, as this is necessary to understand one of the mass-selection methods. Finally, the processes of the fast decay of highly excited anions and laser-induced delayed emission of anions will be discussed.

### 2.1 Ion trapping in an EIBT

The CTF employs an electrostatic ion trap of the type described in the initial paper by D. Zajfman *et al.* [37], commonly called an electrostatic ion beam trap (EIBT). Using two stacks of electrodes (see Fig. 2.1) forming two opposing electrostatic mirrors, ions are reflected back and forth inside the trap. The ions are decelerated as they approach the higher potential barrier and are reaccelerated back towards the other side of the trap. Each stack consists of 5 electrodes plus an Einzel lens, all of which act to ensure that the ions travel along stable trajectories inside the trap over many oscillations, even when they have an initial angle or offset from the symmetry axis of the trap. In principle, fewer trap electrodes could be used to create a potential barrier for the ions, but the multiple electrodes provide finer control over the slope of the reflecting potential, which plays an important role for the second possible trapping modes discussed in the following section. Ions are injected into

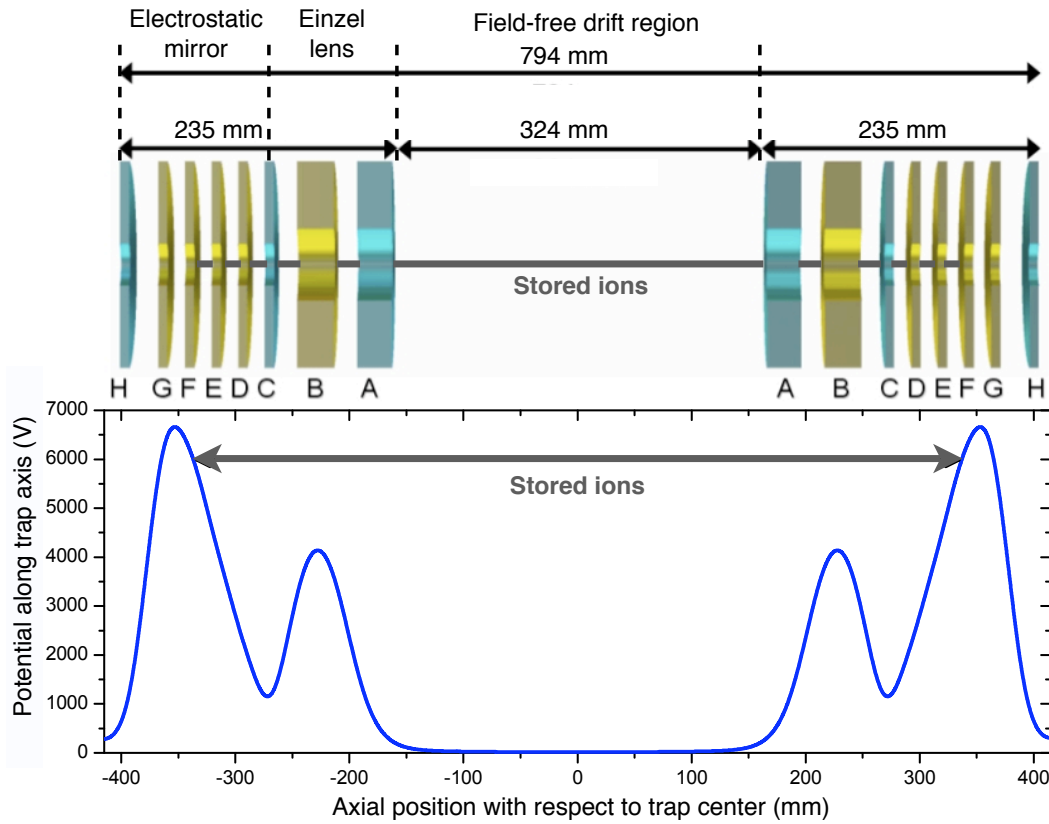


Figure 2.1: Top: Schematic view of the trap electrodes; bottom: Potentials corresponding to ions with a kinetic energy of 6.0 keV. Grounded electrodes (A, C, and H) are marked in cyan, while all electrodes at high voltage are displayed in yellow. Some mechanical trap dimensions are indicated in the trap schematic, while the distance between the turning points is indicated in the graph below.

the trap simply by having the entry side electrodes initially at zero and quickly switching them after the ions have entered the trap.

The oscillation frequency  $f$  of the ions in the trap is described by

$$f = \frac{\bar{v}}{L}, \quad (2.1)$$

where  $\bar{v}$  is the mean velocity and  $L$  is the trap length (distance between the turning points). It follows that the frequency variation  $\Delta f$  can be expressed as

$$\frac{\Delta f}{f} = \frac{\Delta \bar{v}}{\bar{v}} - \frac{\Delta L}{L}. \quad (2.2)$$

## 2.1. Ion trapping in an EIBT

---

At a fixed beam energy, the path length variation  $\Delta L$  is a function of the trap potential at the turn around points. At the mean point of return  $\tilde{x}_0$  for a mean energy  $E_0$ , the potential slope can be linearly approximated as

$$\Delta L = 4 \frac{1}{\frac{\delta\phi(\tilde{x}_0)}{\delta x} q} \Delta E, \quad (2.3)$$

where  $q$  is the ion charge and  $\delta\phi(\tilde{x}_0)/\delta x$  the gradient of the potential at the point  $\tilde{x}_0$ . The slip factor  $\eta_E$ , which is commonly used in storage ring physics, can be introduced to describe the temporal development of an initially well localized cloud of ions (or ion bunch). The  $\eta_E$  parameter is defined as the normalized ratio of the oscillation frequency variation  $\Delta f$  over the energy variation  $\Delta E$ ,  $\eta_E = \Delta f/\Delta E$ . Depending on whether  $\eta_E$  is positive, negative, or zero, the bunch will disperse, converge, or retain its initial shape. Combining  $\eta_E$  with Eq. 2.2 yields

$$\eta_E = \frac{\Delta f/f_0}{\Delta E/E_0} = \frac{\Delta\bar{v}/\bar{v}}{\Delta E/E_0} - \frac{\Delta L/L}{\Delta E/E_0}, \quad (2.4)$$

where the last term is commonly designated as  $\alpha_E$

$$\alpha_E = \frac{\Delta L/L}{\Delta E/E_0} = 4 \frac{1}{\frac{\delta\phi(\tilde{x}_0)}{\delta x} q} \frac{E_0}{L}. \quad (2.5)$$

Note that when  $\eta_E = 0$ , the frequency variation  $\Delta f$  has to vanish as well, meaning that ions with energies at a given kinetic energy  $E_0$ , will have the same oscillation frequency and hence an initially injected bunch will retain its initial shape. By examining Fig. 2.1, it is evident that ions with higher energy must travel a longer path as expressed by the  $\alpha_E$  factor. The average velocity can now be expressed as a function of energy in order to express  $\eta_E$  in terms of the ion kinetic energy in the field-free region as opposed to the frequency for particles with non-constant velocities. A scaling factor  $\kappa$  relates the average velocity to the one in the field-free region

$$\bar{v} = \kappa(E) v_{max}. \quad (2.6)$$

Combining equations 2.6 and 2.4 yields the simplified slip factor  $\eta_E$  for a linear ion trap

$$\eta_E = \frac{1}{2} + \frac{\Delta\kappa/\kappa}{\Delta E/E_0} - \alpha_E. \quad (2.7)$$

Since some theory papers in the following section on the self-bunching trapping mode have defined the slip factor  $\eta_T$  as a function of momentum and oscillation period, despite perhaps the disadvantage in application to this type of trap, it is

useful to note the relationship between these two slip factors. Combining  $f=1/T$  and  $E = p_0^2/2m$  where  $\Delta f/f = -\Delta T/T$  and  $\Delta E/E = 2 \Delta p_0/p_0$ , the slip factor  $\eta_E$  can be expressed with this change of variables as

$$\eta_E = -\frac{\Delta T/T}{2\Delta p_0/p_0} = -\eta_T/2. \quad (2.8)$$

## 2.2 Trapped ion losses

The ions stored inside the electrostatic trap are eventually lost via various competing effects, which depend on the ion species, mass, energy, and charge (eg: positive or negatively charged ions and clusters), as well as on trap characteristics such as the applied trapping potential, rest-gas-density, and the phase space acceptance of the trap. Loss processes such as electron capture, as well as single and multiple scattering will be discussed. Ion trap losses such as spontaneous cluster dissociation, which occurs within the first hundreds of microseconds or photon-induced delayed emission will not be discussed here, but in Section 2.5.

### 2.2.1 Electron capture

Positively charged atomic and molecular ions can be lost from the trap via electron capture. This involves the capture of an electron from the rest gas, thereby neutralizing the trapped particle and allowing it to escape from the trap. Assuming the trapped species was a molecule, upon neutralization it may also dissociate into smaller components. Neutral particles created by electron capture can be observed with a detector behind the trap at a rate that follows an exponential decay law with a mean lifetime  $k_c^{-1}$ ,

$$k_c = n \langle \sigma_c v \rangle, \quad (2.9)$$

where  $n$  is the residual gas density and  $\langle \sigma_c v \rangle$  is the averaged product of the capture cross section and the ion velocity. Note that for later application in this work, the cross section is approximately energy independent over the energies considered, allowing  $\sigma_c$  to be considered a constant which is multiplied by the average ion velocity.

### 2.2.2 Collisional detachment

Collisional detachment refers to the neutralization, with or without additional fragmentation, of anions after a collision with rest gas removes a bound electron. Regardless of whether the anion fragments or is only neutralized, at least one neutral

particle leaves the electrostatic trap. A charged fragment can only remain trapped if a small percentage of the initial anion mass was lost, allowing the charged fragment's energy to still fulfill the stable trapped path conditions in the trap. Akin to electron capture, ion loss through this mechanism is described by an exponentially decaying rate of neutral particles emerging from the trap with a mean lifetime  $k_{cd}^{-1}$ , where

$$k_{cd} = n \langle \sigma_{cd} v \rangle . \quad (2.10)$$

Here,  $\sigma_{cd}$  is the total velocity-dependent cross section for all detachment processes, regardless of how many neutral fragments are created per event.

### 2.2.3 Single and multiple scattering

A trapped species can also be lost due to scattering off rest gas particles. This loss process can be divided into two sub-processes, namely, single and multiple scattering. Both processes are dependent on the trap acceptance  $A$  at the center of the trap given by

$$A = \pi y_{max} y'_{max} , \quad (2.11)$$

where  $y_{max}$  and  $y'_{max}$  are the maximum stable values of the transversal position and angle, respectively.

Single scattering occurs when the stored species scatters off a rest gas particle at a large angle, so that after the collision, the particle is outside the acceptance of the trap. It is, therefore, more likely to occur with light stored species colliding with a heavy rest gas particle.

Multiple scattering refers to the process by which the stored species is slowly dispersed from the middle of the trap phase space via multiple consecutive collisions with rest gas particles, until it is outside the trap acceptance. This loss process also yields an exponential decaying loss rate where the decay rate constant  $k_m$ , is given by

$$k_m = n \alpha_s , \quad (2.12)$$

where  $n$  is the residual gas density and  $\alpha_s$  is the rate coefficient for scattering loss. While particles are lost from the trap via this loss process, they are still charged and hence are not detected by the MCP behind the trap. Due to the complexity of the process and the involvement of various trap parameters, however, no simple description using a single cross-section is possible. While a more exact formula is available for devices such as storage rings, this is due to the fact that the kinetic energy of the ion remains constant. The kinetic energy inside an EIBT approaches zero when the ions change directions inside one of the electrostatic mirrors, which causes

the multiple scattering cross-section to dramatically increase. Stable trajectories at these points, however, must include large angles (i.e. the angular trap acceptance significantly increases), as millions of oscillations have been observed. Real trajectories in the trap also include small transversal velocity components, significantly decreasing the likelihood that the ion's velocity could be reduced exactly to zero. A comparably exact formula for use inside EIBTs is, therefore, not currently available. An empirical determination of multiple scattering, however, is possible given the relative sizes of the nuclei involved in such scattering processes considered here. The Rutherford scattering cross-section (which is dependent on the solid angle  $d\omega$ )  $d\sigma/d\Omega$  is proportional to  $1/E^2$ . The rate coefficient  $\alpha_s$  can then be written as the product of the Rutherford scattering cross-section and the velocity (averaged over one trap oscillation) as

$$\alpha_s = \chi \frac{1}{E^{3/2}}, \quad (2.13)$$

where  $E$  is the beam energy. By performing measurements at different beam energies, the relative rate coefficients for electron capture and multiple scattering were determined in the CTF. The proportionality constant  $\chi$  in the CTF was determined to be  $6 \cdot 10^{-4} \text{cm}^3 \text{s}^{-1} (\text{eV})^{3/2}$  [45], yielding a rate coefficient at least one order of magnitude smaller than that for electron capture at a beam energy of 7.1 keV. For this reason, this process can be ignored in experiments with cations, as electron capture dominates.

## 2.2.4 Intrabeam scattering

Intrabeam scattering refers to the process where ions in the stored beam collide with each other, resulting in the scattering of one or both ions out of the trap. It should be noted that a collision does not guarantee that any participating ion will be scattered out of the trap's acceptance. This process is important for higher ion densities, which could occur in EIBTs when an intense ion beam is injected or near the turning points in the mirrors when the ion velocity is very small and the beam is compressed longitudinally. Simulations were done by Pedersen *et al.* [46] on this loss process with an estimated rate constant put forward. As was stated there, however, the acceptance of the trap  $A$  should also be calculated, which was recently done for the CTF trap geometry in [47]. The rate for this loss process scales with the square of the number of ions, but due to the complex contributions of multiple ion-loss processes at the relevant time scales, this individual loss process has not yet been clearly studied in an EIBT. Assuming this process is present, it would modify the number of ions  $N(t)$  in the trap by the relation

$$\dot{N}(t) = -N(t)k - \alpha (N(t))^2, \quad (2.14)$$

where  $k$  incorporates all other loss processes. Solving this differential equation leads to the following expression for the observed detection rate

$$R(t) = R_0 / [\exp(kt) - c_1 k^{-1} + c_1 k^{-1} \exp(kt)], \quad (2.15)$$

where  $R_0 = \text{Constant } N_0 k_c$ , and  $c_1 = \alpha N_0$ . Recall that  $k_c$  is the loss rate for electron capture (or collisional dissociation for anions) and  $k$  is the combined loss rate as defined in Eq. 2.19. Note that while the  $\alpha$  term is independent of ion density, this term is dependent on the trap acceptance in addition to the mass, velocity, and charge of the stored ions.

### 2.2.5 Modeling of trap losses

Disregarding intrabeam scattering, the population of ions in the trap  $N$  can be expressed as a function of time as

$$N(t) = N_0 \exp(-kt), \quad (2.16)$$

$$\frac{dN}{dt} = -N_0 k \exp(-kt), \quad (2.17)$$

where  $N_0$  is the initial ion quantity,  $k$  is the reaction rate (where  $k^{-1}$  is the mean lifetime due to ion losses), and  $dN/dt$  is the rate of loss. If, however, various loss processes are involved, their respective loss rate constants must be summed

$$\frac{dN}{dt} = \sum_i \left( \frac{dN}{dt} \right)_i = -N_0 \left( \sum_i k_i \right) \exp(-kt) \quad (2.18)$$

$$k = \sum_i k_i, \quad (2.19)$$

For ion loss processes such as electron capture, single/multiple scatter, or collisional detachment, the combined loss rate constant  $k$  (the inverse of the observed beam lifetime) is linearly dependent on the residual gas density  $n$  as given by

$$k \propto n. \quad (2.20)$$

The residual gas density  $n$  can be expressed as a linear function of both the pressure and the temperature by using the ideal gas law as

$$\frac{n}{\text{m}^{-3}} = 7.246 \cdot 10^{24} \frac{p}{\text{T}} \frac{K}{\text{mbar}}. \quad (2.21)$$

The particle loss rate in the trap can be expressed by combining equation 2.19 with the loss processes described above as

$$\frac{dN}{dt} = -(k_c + k_m)N(t) = -(\langle\sigma_c v\rangle + \alpha_s) n N(t). \quad (2.22)$$

While the beam decay constant  $k$  includes all trap loss processes, only particles lost by electron capture (or collisional detachment for anions) leave through the central holes of the electrostatic mirror and are seen on the MCP behind the trap. The total particle detection rate, therefore, on this on-axis MCP is given by

$$R(t) = \frac{1}{2}\epsilon\Omega k_c N_0 \exp(-kt) = R_0 \exp(-kt), \quad (2.23)$$

where  $\epsilon$  is the detector efficiency,  $\Omega$  is the fraction of the produced fragments hitting the detector,  $k$  is the combined rate constant for the relevant loss processes, and the factor of one half arises from half of the particles leaving the trap in the direction away from the detector.

## 2.3 The tune of an EIBT

The ions in a stored ion beam normally exhibit transversal oscillation around the optimal beam axis, which due to historical reasons, are also called betatron oscillations. The ratio of the betatron oscillation frequency to the trap oscillation frequency is called the “tune” of the trap. If this ratio is an integer multiple of the tune, beam deflections via small imperfections in the electromagnetic field of the storage device will coherently add up, quickly resulting in the ion loss. The tune is, therefore, usually set to a non-integer number so that such small deflections will be averaged to zero over many trap oscillations. Additional information on this common property in the context of storage rings can be found in many sources, such as [48]. The frequency of these transversal betatron oscillations in both storage rings and EIBTs, can be written as

$$f_B(n) = f_0 (n \pm q), \quad (2.24)$$

where  $f_0$  is the longitudinal oscillation frequency of a particular ion species (eg: 123.18 kHz for 7.1 keV  $N_2^+$  in the CTF) and  $(n + q)$  is the tune of the device ( $n$

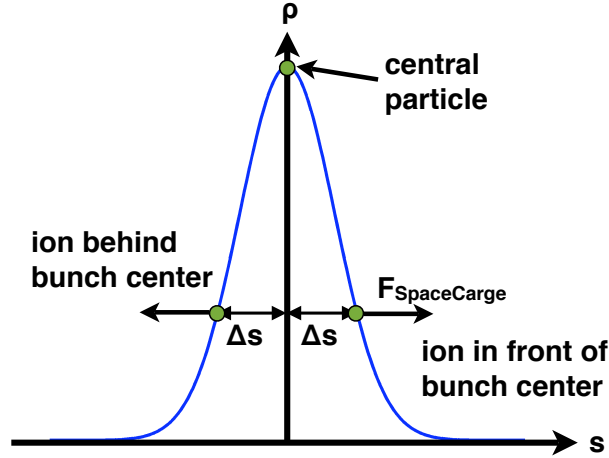


Figure 2.2: Space charge distribution of the oscillating ion bunch. Space charge  $\rho$  is plotted versus distance  $s$  from the center of the bunch.

is an arbitrary integer and  $q$  is the non-integer part of the tune). Exciting the stored ions at a frequency  $f_B$  (via an RF excitation), which corresponds to one of the transversal resonances of the stored ion, results in the ion absorbing energy by increasing its transversal oscillation amplitude with every trap oscillation. Large enough amplitudes will eventually lead to loss from the trap, since the ions leave the stable phase space acceptance of the trap. This property can be exploited to perform the so-called “knock-out” mass selection technique, as first performed in an EIBT using the CTF and reported in Section 4.3.2.

## 2.4 Self-bunching of ions stored in an EIBT

The so-called self-bunching trapping mode in EIBTs has been studied in depth both experimentally [49–52] and theoretically [53–55]. This is a process by which the ions stored inside an electrostatic trap are kept together in a coherent bunch through the Coloumb repulsion force between each individual ion and the space-charge caused by the ion bunch. Such a trapping mode employs a negative  $\eta_E$  value by adjusting the trap potentials.

Consider for example, particles near the front of a stored bunch (see Fig.2.2). These particles will experience an accelerating force due to Coloumb repulsion from the space charge of the bunch. This means that ions with a distance  $\Delta s > 0$ , (i.e. at the front of the bunch) will travel faster ( $\Delta v > 0$ ) than the ideal particle, which is always located at the center of the bunch. Due to the negative  $\eta_E$  defined in

Eq. 2.7, the oscillation period of these accelerated particles will become larger than that of the ideal central particle. This larger period results in the decrease of  $|\Delta s|$  one trap oscillation later, moving these particles back towards the central particle. Conversely, ions lagging behind the central particle are decelerated due to the space charge of the bunch. Again, the negative  $\eta_E$  parameter now yields a shorter oscillation time with respect to the bunch, resulting in a gradual decrease of the distance  $|\Delta s|$  between these slower ions and the central particle over a number of oscillations. Self-bunching, therefore, results in an oscillation of the ions around the center of the bunch (i.e. the ions rotate in phase space around the center), keeping the bunch coherently together.

This self-bunching effect, while relatively new to the ion-trapping field of physics, was first introduced as the negative mass instability by Nielsen, Sessler, and Symon in 1959 for relativistic circular accelerators and storage rings [56]. This effect has also been observed recently in the TSR Storage ring using carbon ions at 50 MeV [57]. A review of the extensive experimental and theoretical treatment of this effect for such larger devices can be found in [58].

The idea that the ion bunch trapped in this self-bunching mode requires a minimum amount of charge to remain stable has been theoretically proposed by two sources. The first one considers a particle located inside a homogeneously charged sphere (the bunch) oscillating in a simple one dimensional potential [53]. Using this model, the minimum density  $\rho$  required for a stable bunch of particles of size  $\approx 2R_0$  is given by

$$\rho > \frac{4 \eta_T \epsilon_0 p_0^2}{m q R_0^2}, \quad (2.25)$$

where  $m$ ,  $q$ , and  $p_0$  are the mass, charge, and momentum of the stored ions respectively,  $\epsilon_0$  is the vacuum permittivity,  $R_0$  is the radius of the spherical bunch, and  $\eta_T$  is the slip factor defined by

$$\eta_T = \frac{|P_0|}{T} \frac{dT}{d|P_0|}, \quad (2.26)$$

where  $P_0$  is the initial center-of-mass momentum and  $T$  is half of an oscillation period.

The second theoretical treatment by [55] is still a one dimensional model, but does not assume that the bunch remains spherical. In this model, the bunch is only spherical in the electrostatic mirrors when the ion bunch is being reflected, but spatially spreads out in the middle of the trap. This model proposes that the

minimum number of particles  $N_{min}$  in a stable bunch is given by

$$N_{min} = \frac{3\sqrt{2\pi} d^{3/2} F^{3/2}}{\mathcal{I}(1) \sqrt{mq}} \Delta T_i, \quad (2.27)$$

where  $d$  is the beam diameter,  $F$  is the field gradient in the electrostatic mirrors,  $\Delta T_i$  is the spatial dispersion of the bunch,  $m$  and  $q$  are the mass and charge of the ion, and  $\mathcal{I}$  is an integral [55], which assumes that the ratio between the beam diameter and bunch length is one.

While both models are one dimensional, the latter one attempts to account for more realistic ion paths, which do not oscillate along the trap axis, but along paths with slight offsets from the axis and a small velocity component perpendicular to the trap axis, by inserting an additional parameter to try and account for these path differences. Both models will be compared to experimental results in Section 4.2.1.

## 2.5 Delayed emission and fragmentation of small metal cluster anions

The well understood macroscopic process of thermionic emission of electrons from hot metals [59] appears to be analogous to the statistical process of the delayed electron emission from microscopic sources such as ionic clusters [60]. Such decays have been observed from initially stored hot clusters [60–65], in addition to photon-induced delayed emission of such species [66,67]. Statistical theories have successfully described these decays by considering that thermal emission occurs when sufficient energy from several degrees of freedom is coincidentally and simultaneously transferred into the electronic degree of freedom [66,68]. Both of these delayed emission processes will be covered here, where the concept of the cluster’s microcanonical temperature will be used to theoretically describe the cluster’s photon-induced delayed emission. Delayed emission of just an electron as opposed to the delayed fragmentation of the stored cluster will also be discussed as well as the ramifications these two processes have on the delayed emission studied here.

### 2.5.1 Temperature induced cluster dissociation

The observation of the decay of ions and clusters created in hot sources, which dissociate during their storage in rings or ion traps, resulting in the thermal emission of electrons, atoms, or small molecules, has been extensively observed (see [60–65] and the references contained within). Hot sources such as sputter sources, typically

produce ions that exhibit a very high rovibrational excitation, which results in thermal emission. While this delayed emission is dominant on very short time scales, at some point radiative cooling of the cluster takes over as the very hot ion cools down during storage and emission becomes less likely. While two particular theoretical approaches will be described below, a cautionary note is necessary. A plethora of slightly different theoretical models exist to reproduce the typically observed  $1/t$  dependence of the decay rate on the storage time  $t$ , which may or may not include terms dependent on additional effects. The general approach for these theories is the same, but the details and mechanisms in these decays are not yet fully understood.

### Statistical description of electron emission

Following the arguments of Andersen *et al.* in [60], the fundamental theory of detailed balance demands that for a cluster in statistical equilibrium undergoing particle emission, the decay rate is related to the reverse process of particle absorption. This relates the rates of transitions in both directions between any two quantum states. Averaging over the initial states and summing these transition rates over final states, one obtains the rate constants  $k$ . Assuming the energetically available states have a level density  $\rho$ , the statistical balance is given by

$$k_{decay} \rho_{parent} = k_{formation} \rho_{products} . \quad (2.28)$$

Consider the rotational, vibrational, and electronic state angular momentum of a cluster. Normally, the majority of angular momentum is stored in collective rotations, so that the moment of inertia is large, which leads to a small spacing of rotational energy levels. The transfer of a significant amount of angular momentum between rotation and internal excitations (vibrational or electronic) is not very likely, since exciting internal states with a large amount of angular momentum would remove a significant amount of energy from the vibrational heat bath, due to the different level spacing. The rotational and internal energy can, therefore, be considered separately conserved for isolated clusters. As electron emission at low kinetic energies only results in small changes of the angular momentum and the moment of inertia in a cluster, rotational energy is not significantly affected by electron emission.

Returning to the level density  $\rho$  in Eq. 2.28, the energy  $\epsilon$  of the captured or emitted electron also contributes to the level density on the right side of the equation. The total level density is given by the level density of the daughter multiplied by the number of states within a small energy interval  $d\epsilon$  for a free electron contained in a volume  $V$  ( $\rho_{products} = \rho_{daughter} \rho_e$ ). The rate of electron attachment is simply defined as the electron velocity multiplied by its spatial density  $1/V$  and the capture cross

section  $\sigma_c(\epsilon)$ . Combining these definitions over a small energy interval  $d\epsilon$ , the rate constant for emission of electrons can be written as [60]

$$k(E, \epsilon)d\epsilon = \frac{2m}{\pi^2\hbar^3}\sigma_c(\epsilon)\epsilon\frac{\rho_{daughter}(E - E_b - \epsilon)}{\rho_{parent}(E)}d\epsilon, \quad (2.29)$$

where  $m$  is the electron mass,  $E_b$  is the electron binding energy, and  $E$  is the internal excitation energy of the parent.

Assuming the electron energy  $\epsilon$  is small in comparison with the total energy,  $\ln\rho_d(E - E_b - \epsilon)$  can be expanded to first order in  $\epsilon$ , while introducing the microcanonical temperature  $T_d$  of the daughter, with an energy of  $E - E_b$ . By definition, a microcanonical ensemble is an ensemble representing a system in statistical equilibrium at a well defined energy. The microcanonical temperature  $T_m$  of a system with an excitation energy  $E$  and a level density  $\rho(E)$  is defined as

$$\frac{1}{k_B T_m} = \frac{d}{dE} \ln \rho(E), \quad (2.30)$$

where  $k_B$  is Boltzmann's constant. The above two formulae can be combined to express the emission rate for electrons as

$$k(E, \epsilon)d\epsilon = \frac{2m}{\pi^2\hbar^3}\sigma_c(\epsilon)\epsilon\frac{\rho_{daughter}(E - E_b)}{\rho_{parent}(E)}e^{-\epsilon/k_B T_d}d\epsilon. \quad (2.31)$$

By integrating over  $\epsilon$ , the total emission rate constant becomes

$$k(E) = \nu \frac{\rho_{daughter}(E - E_b)}{\rho_{parent}(E)}, \quad (2.32)$$

where  $\nu \simeq \frac{2mk_B^2}{\pi^2\hbar^3}\sigma_c T_d^2$  and the capture cross section has been averaged over the thermal energy distribution at the microcanonical daughter temperature  $T_d$ .

Returning to the microcanonical temperature  $T_m$  of the system before emission, this temperature applies when the clusters emerge from an oven with a well defined thermodynamic temperature. A canonical energy distribution is maintained inside of the oven via rapid energy exchange with the rest gas and the walls. Outside the oven, however, the clusters are isolated and their energy can then be considered a conserved quantity. Using Eq. 2.30, the most probable energy of a canonical distribution can be written as a function of the thermodynamic temperature. Due to the slightly skewed canonical distribution, however, there is a small difference between the peak

value  $E$  at temperature  $T_m$  and the average energy  $\bar{E}(T_m)$  given by

$$E \simeq \bar{E}(T_m) - k_B T_m, \quad (2.33)$$

where the equivalent formula relating the microcanonical and the canonical heat capacities can be expressed as  $C_m = C_c - k_B$ . It is the temperature of the daughter, however, that determines the energy distribution of the emitted particles [60]. Via a Taylor expansion, the rate constant given in Eq. 2.32 can be written in Arrhenius form as

$$k(E) = \nu \exp\left(\frac{-E_b}{k_B T_e}\right), \quad (2.34)$$

where  $k_B$  is the Boltzmann factor and the barrier energy is given by  $E_b$ . The effective emission temperature  $T_e$  can be expressed as a function of the temperature of the system before emission via

$$T_e \simeq T_m - \frac{E_b}{2C_m} - \frac{E_b^2}{12C_m^2 T_m}. \quad (2.35)$$

The second term directly after the microcanonical temperature is commonly referred to as the finite-heat-bath correction [69].

### Total emission rate

To obtain an expression for the total emission rate, consider an ensemble with an energy distribution  $g(E, t)$  in combination with the rate constant  $k(E)$  [68]

$$I(t) = \int dE k(E) g(E, t). \quad (2.36)$$

If all interactions with other clusters and the surroundings can be ignored, which entails that the emission and absorption of radiation are not considered, the excitation energy  $E$  is conserved and the clusters decay individually. This leads to a change in the shape of the energy distribution  $g(E, t)$  and the emission rate becomes

$$I(t) = \int dE k(E) g(E, 0) \exp(-k(E) t). \quad (2.37)$$

The rate function  $k$  rapidly increases causing the product  $k(E) \exp(-k(E)t)$  to exhibit a sharp maximum at an energy  $E_m$ , where  $k = 1/t$ . For molecules with a broad energy distribution,  $g(E, 0)$  can be extracted from the integral, leading to the observed  $1/t$  power law decay. A Gaussian approximation of the energy distribution around this maximum also yields a peak width, which varies slowly with time, producing an emission rate that scales approximately as  $1/t$  [60]. Extensive

experimental studies from metal clusters to large bio-molecules have confirmed  $1/t$  type power law decays due to delayed emission [61–63, 65, 68, 69].

### Radiative cooling correction

As introduced by Andersen *et al.* in [62], if the emitted photon energies are so low that their emission acts in such a way as to continuously cool the cluster, which is the case for IR radiation from vibrations, then the radiated power  $P_r$  varies slowly with temperature in comparison to the exponential dissociation rate. Previous experiments have only observed a quenching caused by this cooling over a narrow time range and expressed the cooling to first order in  $t/\tau_c$  as

$$\begin{aligned} T_m(t) &= T_m/(1 + t/\tau_c) \\ 1/\tau_c &= P_r/CT_m. \end{aligned} \quad (2.38)$$

Due to the finite heat bath correction, there is a slight shift in  $\tau_c$ , where  $\tau'_c = \tau_c \frac{T_e}{T(0)}$  [62]. Combining the above formulae allows the total emission to be written as a reduction of the decay rate with time due to radiative cooling, instead of a time variation in the emitted temperature  $T_e$  (i.e. at a fixed energy  $E$  and temperature  $T_e$ ). This correction factor is then multiplied by the Arrhenius exponential factor in Eq. 2.37

$$\begin{aligned} I(t) &\simeq g(E_m)C(E_m) \int dT_e \nu \exp\left(-\frac{E_b(1 + t/\tau')}{k_B T_e}\right) \\ &\quad \times \exp\left(-\nu \int_0^t dt' \exp\left[-\frac{E_b(1 + t'/\tau'_c)}{k_B T_e}\right]\right) \\ &= g(E_m)C(E_m) \int dT_e k(T_e) e^{-Gt/\tau'_c} \exp\left(-k(T_e)G^{-1}\tau'_c(1 - e^{-Gt/\tau'_c})\right). \end{aligned} \quad (2.39)$$

The slowly varying energy distribution and heat capacity (due to the change of variable from  $E$  to  $T_e$ ) was extracted from the integral. Since the Gspann parameter  $G = E_b/k_B T_e$  varies more slowly with temperature than  $k$ , it can also be treated as a constant. An effective decay temperature  $T_{e,m}$  with an energy  $E_m$  (defined earlier when considering the total emission rate where a sharp maximum is observed when  $k = 1/t$ ) can then be defined at the maximum of the integrand, corresponding to

$$k(T_{e,m}) = [G^{-1}\tau'_c(1 - \exp(-Gt/\tau'_c))]^{-1}. \quad (2.40)$$

Using this equation to simplify Eq. 2.39 above yields

$$I(t) \simeq \frac{1}{\tau(\exp(t/\tau) - 1)} g(E_m)C(E_m) \frac{k_B T_{e,m}^2}{E_b}, \quad (2.41)$$

where  $\tau = \tau'_c/G$ . At short times ( $t \ll \tau$ ) when the radiative cooling is not yet important, the equation above yields the expected  $1/t$  power law. At times on the order of  $\tau$ , however, the total emission rate is exponentially reduced by radiative cooling. For fitting experimental data, the equation above can be written by replacing the last three factors with a power law factor  $(t/\tau)^\delta$

$$I(t) = N(t/\tau)^\delta (e^{t/\tau} - 1)^{-1} + K, \quad (2.42)$$

where  $N$  is a normalization constant, the factor  $(t/\tau)^\delta$  corrects the effective power in the  $t^n$  power law at short times ( $t < \tau$ ) to  $n=-1+\delta$ ,  $\tau$  is the quenching time when radiative cooling begins to dominate, and  $K$  accounts for collisions with rest gas.

### Diatomic metal anions

Diatomic metal anions were found to exhibit a thermally induced metastable decay, despite lacking multiple vibrational degrees of freedom as required by the statistical models where the approximately harmonic vibrations of the nuclei in molecules and clusters are the dominant contribution to the heat capacity [65]. This observed diatomic anion decay fit well to a power law with an exponent of -1, signaling the presence of a continuum of decay constants in the observed ensemble of ions. A quantum mechanical tunneling decay of high angular momentum states populated in the source was proposed in [65], where the intensity as a function of time was given by

$$I(t) = \sum_{\nu, L} (2L + 1) k(\nu, L) e^{-k(\nu, L)t} \rho(\nu, L), \quad (2.43)$$

where  $L$  is the rotational quantum number,  $\rho$  is the number of stored molecules,  $k$  is the tunneling decay rate constant, and  $\nu$  is an attempt frequency with which the internuclear separation hits the barrier (expected to be around  $10^{12}$  Hz for the species considered here). Fedor *et al.* [65] demonstrated that the intensity decay of these metal anion dimers can be very well approximated using a modified  $1/t$  decay law

$$I(t) \propto \frac{1}{t} (1 - e^{-\nu t}) \approx 1/t. \quad (2.44)$$

## 2.5.2 Photon-induced delayed emission

Photon-induced delayed emission is a process in which clusters are irradiated by a short (ns) laser pulse and emit electrons in a time window extending to several hundreds of microseconds after the incident laser (see Fig. 5.17). This process has been extensively studied in large molecules, metal clusters, fullerenes and biomolecules [62]. Additional information and references concerning this process can be found in a review by Campbell and Levine [70].

In photon-induced delayed emission, the clusters are illuminated by a short laser pulse with a photon energy that is, in principle, sufficient to detach the excess electron. For a portion of the ions, the absorbed energy leads to the immediate emission of an electron. The strong coupling between the electronic and vibrational degrees of freedom can also lead to the energy being transferred to the vibrational motion of the cluster. In this case, the electron can only be detached if enough energy is coincidentally transferred back into the electronic degree of freedom from different vibrational modes, which depends on the total internal energy of the cluster. Due to the statistical nature of this process, the concentration of energy in this one degree of freedom is not very likely so that electron emission can only occur after a comparatively long delay of several hundred microseconds. The absorbed photon energy is hence stored in the cluster's vibrational degrees of freedom. Using statistical analysis with the precisely defined photon energy, the observed time dependence of the delayed electron detachment rate after the laser shot is related to the energy stored in the cluster *before* the absorption of the photon. Describing the subsequent emission of an electron via a statistical process similar to thermionic emission from a bulk material was verified by comparing the decay of clusters excited in an oven and by laser absorption [68]. Colder clusters, therefore, will emit electrons at later times than hot clusters. This model proposes that the resulting delayed emission curves from many equivalent ensembles (i.e. the stored ions) can be used to determine the temperature of the clusters as they cool in the ion trap.

Now consider the case, again beginning with Eq. 2.36, where instead of ignoring all interactions with the surroundings as treated above, the clusters are in contact with a heat reservoir at a temperature  $T$ . The rate of delayed emission  $k$  as given in Eq. 2.34 can still be used, where the Arrhenius factor has been renamed from  $\nu$  to  $A$  to avoid confusion

$$k(E) = A \exp\left(\frac{-E_b}{k_b T_e(E)}\right). \quad (2.45)$$

As before,  $E_b$  is the barrier energy for electron emission from the cluster,  $k_b$  is the Boltzmann's constant, and  $T_e$  is the effective temperature for electron emission given by equation 2.35 or stated again for clarity

$$T_e(E) \simeq T_m(E) - \frac{E_b}{2C_m} - \frac{E_b^2}{12C_m^2 T_m(E)}, \quad (2.46)$$

where  $C_m$  is the microcanonical heat capacity of the cluster and  $T_m$  is the microcanonical temperature, which is related to the energy  $E$  by  $dE/dT_m = C_m$ . One can ensure the time scale of this process is observable and much shorter than the com-

peting radiative cooling process by selecting a suitable photon energy  $h\nu$ . Following the procedure outlined in [66] and [67] to analyze the shape of the delayed emission in bio-molecules and aluminum clusters, respectively, the probability of having a cluster with an internal energy  $E_i$  can be described by a canonical ensemble with a temperature  $T_i$ . This distribution can be approximated by a Gaussian resulting in

$$g(E, E_i) = \rho(E) \exp\left(\frac{-E}{k_b T_i}\right) \simeq \frac{1}{\sqrt{2\pi\sigma^2}} \exp\left(\frac{-(E - E_i)^2}{2\sigma^2}\right), \quad (2.47)$$

where  $\sigma = \sqrt{k_b C_m T_i}$ ,  $\rho(E)$  is the density of states, and  $E_i$  is the energy for which  $T_m(E_i) = T_i$ . The intensity of the delayed emission can then be written as a function of time  $\tau$  after the application of a short laser pulse

$$I_i(\tau) = \int dE N(t_i) P_{ph} g(E, E_i + h\nu) k(E) \exp(-k(E)\tau), \quad (2.48)$$

where  $N(t_i)$  is the number of clusters in the trap at time  $t_i$  and  $P_{ph}$  is the probability of absorbing a photon of energy  $h\nu$ . Note that the absorption of the photon shifts the energy distribution by the photon energy, hence the change in the probability function above. To fit the delayed emission data, Eq. 2.48 must now be integrated over the relevant energy range to account for the contributions from the entire cluster energy distribution.

It is instructive to consider how the observed distribution changes as a function of temperature (see Fig. 5.30(c) for an example). Colder temperatures result in a narrower energy distribution leading to very few energy states contributing to the produced delayed electron emission spectrum. This ultimately leads to a spectrum produced by a single exponential function. At warmer temperatures, however, higher energy states are populated that lead to more decays at earlier times due to the steeper decay slopes and a delayed emission spectrum consisting of multiple exponential functions. As there are necessarily fewer ions in the ensemble occupying colder states at warmer temperatures, there is less emission at longer times after photon absorption.

### 2.5.3 Limitation of the above model: Delayed fragmentation

What the above model fails to address, however, is the role that charged fragments play in the observed decay rates. This is of particular importance to devices such as EIBTs, where charged fragments cannot be detected with the on-axis detector behind the trap, but the neutral smaller fragments are detectable with a given detector efficiency, which is dependent on the beam energy. A competition between

electron emission and fragmentation following single photon absorption has already been observed in metal anion clusters [71, 72]. This process similarly applies to hot cluster anions in storage devices, where these two competing decay paths de-excite the stored ions. Furthermore, the branching ratio between the production of neutral fragments and charged fragments changes as a function of the absorbed photon energy [73]. Observations from this work suggest that the branching ratio may also be temperature dependent. As a result, the observed intensity rate for laser-induced delayed emission may not be fully explained by the discussed statistical model.

Instead of the decay rate  $k$  being given above by Eq. 2.45, the photon-induced delayed emission rate may be better characterized by

$$k(E) = A_1 \exp\left(\frac{-E_{b1}}{k_b T_e(E)}\right) + A_2 \exp\left(\frac{-E_{b2}}{k_b T_e(E)}\right), \quad (2.49)$$

where a second decay rate term, generally accounting for a different Arrhenius constant and barrier energy of the delayed fragmentation, should be considered. A third term may even be applicable in the case where multiple isomers of the cluster anion exist, each of which could have a different Arrhenius constant. The addition of so many terms with so many free parameters, however, while reproducing the experimental data, renders this model at the present time ineffective in determining the actual cluster temperature.



# Chapter 3

## Experimental setup

The Cryogenic Trap for Fast Ion Beams (CTF) and its auxiliary components will be described in detail, including the laser setup used during the second CTF experimental phase. This will also include a special section on the design modifications to the original Cryogenic Storage Ring (CSR) plans due to the experience and results gained through the CTF.

While the CTF experimental setup has changed significantly throughout its operation, its principle layout and major components have remained the same. As schematically shown in Fig. 3.1 and pictured in Fig. 3.2, the CTF consists of a 0.8 m long electrostatic trap [37] mounted inside a 3 m long cryogenic beam-pipe, which is cooled by 1.8 K superfluid helium evaporation. These vacuum chambers are cooled to temperatures around 10 K and enclosed in thermal shields at 40 K and 80 K. Multi-layer insulation is wrapped around the thermal shields and this entire as-

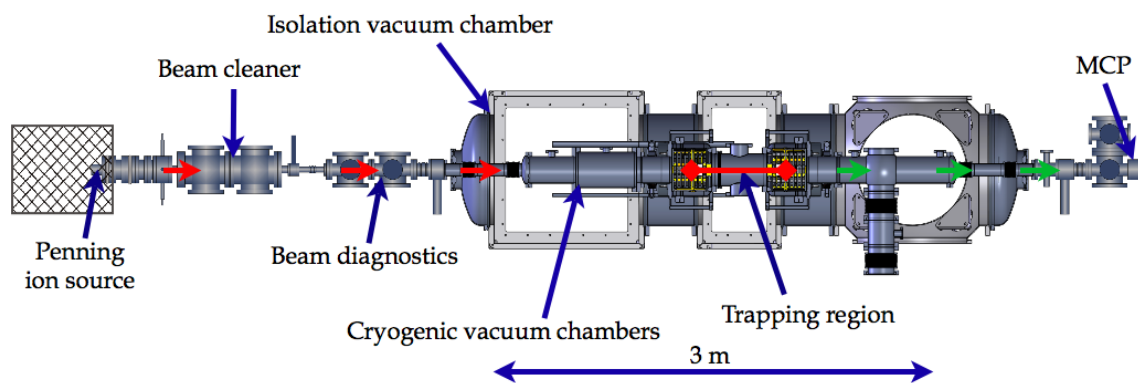


Figure 3.1: A schematic of the complete CTF setup used for the first experiments.

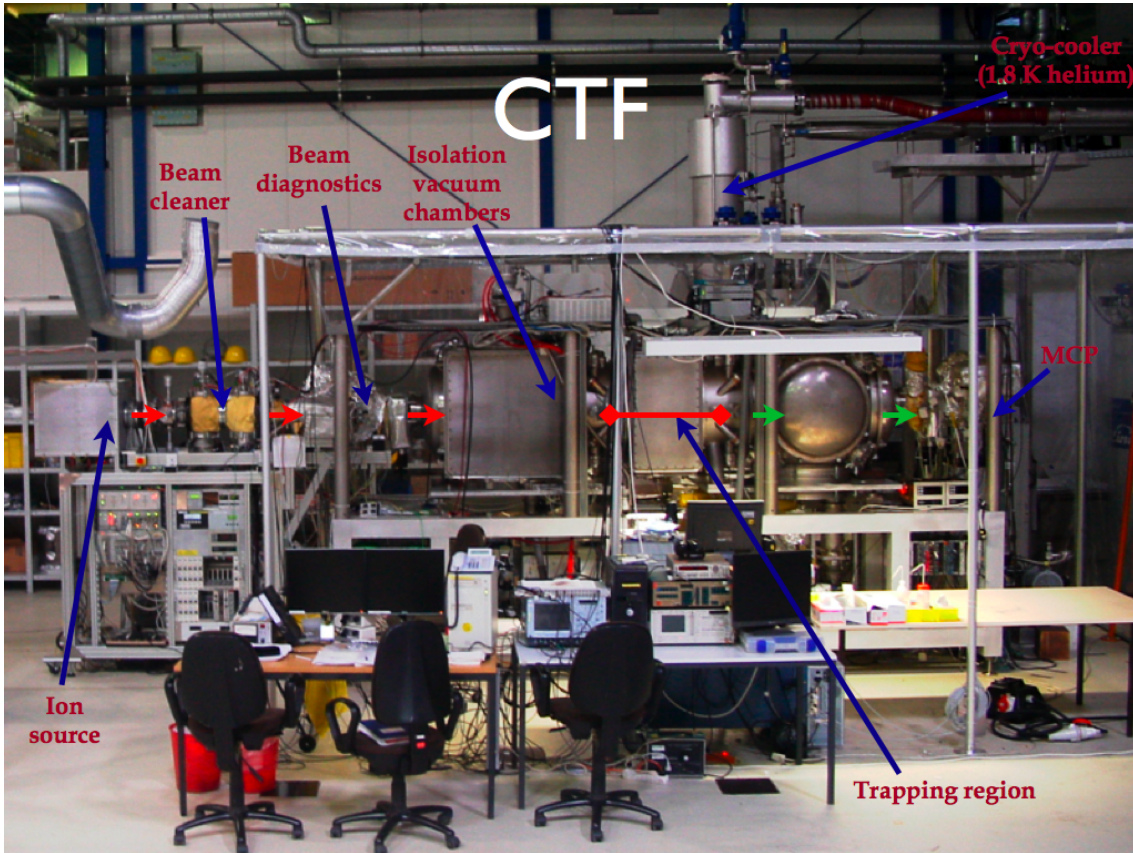


Figure 3.2: A photo of the CTF setup used for the first experiments.

sembly is encased in a cryostat vacuum chamber which is pumped to an isolation vacuum between  $10^{-6}$  and  $10^{-8}$  mbar, depending on whether the CTF is at room-temperature or at cryogenic temperatures. The cryogenic beam-pipe (also called the experimental vacuum chambers) is pumped to pressures on the order of  $10^{-9}$  mbar (before baking) /  $10^{-10}$  mbar (after baking) at room-temperature and  $10^{-13}$  mbar (room-temperature equivalent) during cryogenic operation. Ions produced in either a Penning Ion Source or a Cesium Sputter Source were injected into the trap using an injection beam line featuring all-electrostatic optics: two Einzel lenses, a beam cleaner, a faraday cup, two sets of steerer electrodes, as well as two beam viewers [74]. The beam cleaner consists of four pairs of electrostatic plates, which vertically displace the beam while it passes through a differential pumping tube, blocking most neutral particles coming from the source region before guiding the beam back along the initial beam axis. The first plate can be switched, allowing the beam cleaner to act as a chopper, thereby creating a beam pulse of a given length. This unit was built by our collaborators at the Weizmann Institute in Rehovot, Israel. Behind the

CTF, the second beam viewer as well as a chevron micro-channel plate (MCP) particle detector were installed in a baked room-temperature extension of the cryogenic beam-pipe to observe the neutral fragments that escape the electrostatic trap.

## 3.1 The cryogenic electrostatic ion beam trap

As already mentioned in the introduction, numerous experimental setups around the world employ an electrostatic ion beam trap [37–40]. What sets the CTF apart from other traps of this type, is its ability to be cooled to cryogenic temperatures. The CTF's complex design will be detailed in this section in addition to the heat transport mechanisms, which needed to be carefully considered. Particular attention will be paid to the mechanical assembly of the device as it was built during the scope of this research.

### 3.1.1 Heat transport mechanisms

Given that the CTF is cryogenically cooled and that minimizing the black body radiation environment and thereby creating an excellent vacuum environment are the primary technological challenges of the CSR/CTF project, it is extremely important to understand the mechanisms of heat transfer between two bodies. While describing this process in detail is outside the scope of this thesis, more information can be found in many other sources such as [75].

It is useful to consider the general equation for the heat flow  $Q$  through a solid in one dimension  $x$  and in the steady-state with temperatures  $T_1$  and  $T_2$  at the ends of the solid at  $x_1$  and  $x_2$ , respectively:

$$Q = -K(T) \frac{A(x)}{dx} dT, \quad (3.1)$$

where  $K(T)$  is the thermal conductivity and  $A(x)$  is the cross-sectional area. The minus sign refers to the definition of heating flowing opposite to the temperature gradient. Assuming that  $K(T)$  and  $A(x)$  are both constant and solving for the temperature  $T$  yields:

$$T(x) = -\frac{Qx}{KA} + T_0, \quad (3.2)$$

This formula applies differently to the two different regions of the CTF. For the inner vacuum chambers of the cryogenic beam-pipe, the heat conductance between the chambers needs to be maximized to ensure a low thermal gradient under the residual heat input from other components and thus optimally cooled chambers. In

this case, maximizing the cross section and the thermal conductivity of the material will both reduce the thermal resistance to facilitate the maximum amount of heat transport per time.

In order to maintain the lowest possible inner chamber temperatures, the heat transfer to these chambers needs to be minimized. Minimizing both the cross section and thermal conductivity of the materials used in all connections between the cryogenic beam-pipe and warmer components (e.g. structural supports to room-temperature mounting points) needs to be considered. As is often the case in many cryogenic cooling devices, the coolant can dissipate significant additional power, albeit at higher temperatures during its return from the coldest parts to a compressor unit. It, therefore, makes sense to establish intermediate heat sinks along the connections between room-temperature and the cryogenic base temperature. While this does not reduce the total amount of power to be dissipated, the highly nonlinear efficiency of these machines with respect to temperature ensures that this can greatly reduce the primary power needed at the base temperature and hence the cost of operation.

Considering heat transfer via radiation, it is useful to examine the Stefan-Boltzmann law for thermal emission where the power radiated per unit area  $A$  is given by:

$$P = e \sigma T^4, \quad (3.3)$$

where  $e$  is the emissivity of the object (which is unity for an ideal blackbody),  $\sigma$  is the Stefan-Boltzmann constant ( $5.6703 \cdot 10^{-8} \text{ Wm}^{-2}\text{K}^{-4}$ ), and  $T$  is the temperature of the object.

This can be extended to the case of radiative exchange between two bodies at different temperatures. For two long, concentric cylinders of identical surface area  $A$  and a temperature independent emissivity  $e$ , the net radiation power absorbed by the cooler body at temperature  $T_c$  (eg: the cryogenic beam-pipe in comparison to the warmer 40 K thermal shields) can be approximately given by:

$$P = e \sigma A (T^4 - T_c^4). \quad (3.4)$$

Clearly minimizing the temperature difference between two radiating surfaces strongly reduces the amount of power absorbed by the cooler surface, in addition to minimizing the surface area and choosing surfaces with lower emissivity.

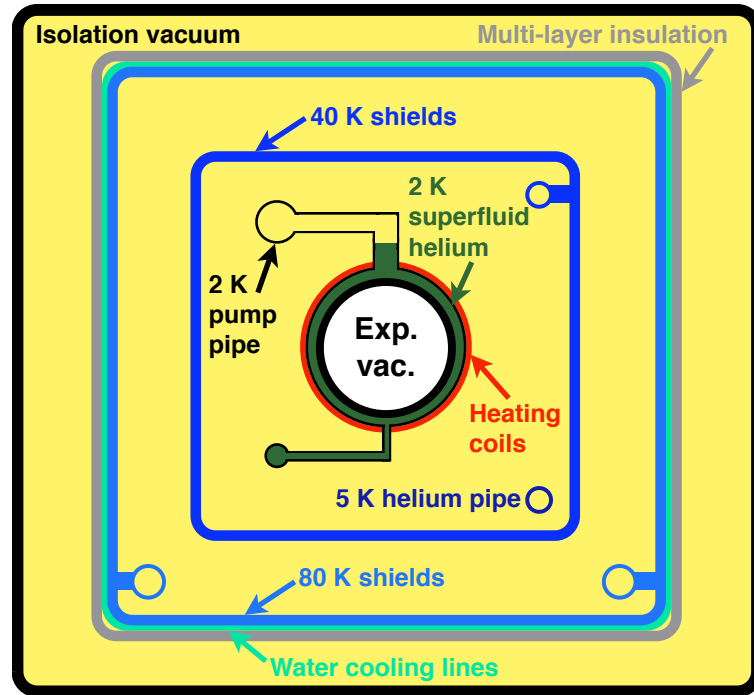


Figure 3.3: CTF cross-sectional schematic view.

### 3.1.2 Cryogenic design

Minimizing the black body radiation environment and creating an excellent vacuum environment were the main goals of the CTF project. It is, therefore, extremely important to not only reduce the temperature of the vacuum chambers below 10 to 15 K in all regions visible to the beam, but to also obtain wall temperatures below 2 K in some locations to effectively pump all rest gas species, including hydrogen. Two topics will, therefore, be discussed: the cooling of the experimental vacuum chambers, as well as the minimization of heat transfer to these chambers, which is described in Section 3.1.1. It should be noted that unique and very demanding restrictions were placed on the cryogenic design, as the cryogenic beam-pipe is also bake-able up to temperatures of 600 K (see Section 3.2.3), prohibiting the use of standard cryogenic technology and methods.

#### Cooling the beam-pipe

An onion-like layering of the thermal shields between room-temperature and the cryogenic beam-pipe was used as illustrated in Fig. 3.3 and with a photographed cross-section in Fig. 3.7. The experimental chambers are cooled via 1.8 K superfluid helium (He II) from a commercial closed-cycle refrigeration system (see Table 3.1 for

Table 3.1: CSR/CTF cryogenic refrigeration system specifications

Helium temperature	Available cooling power
1.8 K	20 W
2 K	27 W
5 K	600 W

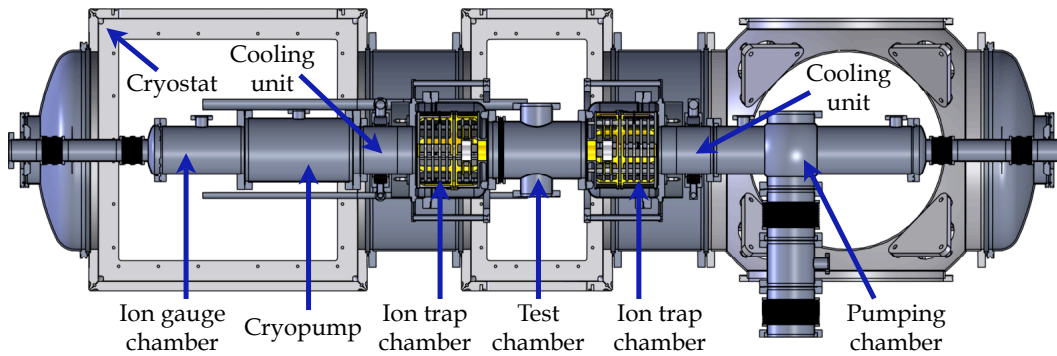


Figure 3.4: Schematic of the CTF experimental vacuum chambers.

specifications [28, 76]), which is brought into the isolation vacuum through stainless steel pipes. This refrigeration system is designed for use with the CSR, so the heat load represented by the CTF is much less ( $\approx 1$  W at 2 K and  $\approx 60$  W at 5 K for the shields) than what is required for the ring. Additional details and commissioning results of the refrigeration system are reported in [28, 76]. The extensive safety tests necessary to ensure proper operation and installation of the helium pipes (welding techniques, pressure tests, x-ray inspection, etc) will not be discussed here. The liquid helium is brought in direct contact with the experimental vacuum chambers in the two cooling units on either side of the test chamber (see Fig. 3.4). These cooling units (see Fig. 3.5) are filled with He II to a certain height that is actively regulated by a superconducting level sensor incorporated into the helium pipes. The helium exhaust pipe is pumped to 16 mbar (the vapour pressure of helium at 1.8 K) to aid the evaporation and hence the heat transport.

While this cooling power is also used to cool the neighbouring vacuum chambers, it must flow through the relatively thin stainless steel chamber walls, offering a small cross-section with relatively poor thermal conduction. High purity (99.997%) copper bands are used to ensure optimal heat transfer at temperature below 80 K, where the thermal conductivity of copper varies by 1.5 orders of magnitude according to its purity (see Equation 3.1.1). To avoid the poor thermal conductivity of stainless steel, these copper bands are directly connected to the copper heat-sinks installed

### 3.1. The cryogenic electrostatic ion beam trap

---

in the cooling units. These heat-sinks have a large surface area, which is immersed in the superfluid helium for optimum thermal transfer. This high purity copper conducts heat 4.5 orders of magnitude better than stainless steel, thereby acting as the main cooling conduit, allowing the cooling of the experimental vacuum chambers. The cooling cross-section is, however, limited by the resulting rigidity of the copper bands during the installation process (see the photo in Fig. 3.9).

A copper cool-finger (see Fig. 3.6), acting as a short-cut between the liquid helium supply line and the pumping line is also installed near the middle of the trap. High purity copper bands are compressed against the cool-finger, connecting it to the middle chamber and the sides of the ion trap chambers. This ensures that these essential parts of the CTF (where the ions are stored) are cooled as effectively as possible.

The temperature distribution of the cryogenically cooled inner chambers results in an average inner chamber temperature of 17 K as described in detail in [47]. Given that the coldest measured temperature (via a silicon diode) on the copper cool-finger is 3.1 K, which has direct contact to liquid helium, and considering that the liquid helium supply and return lines in the refrigeration system are both at 1.8 K,

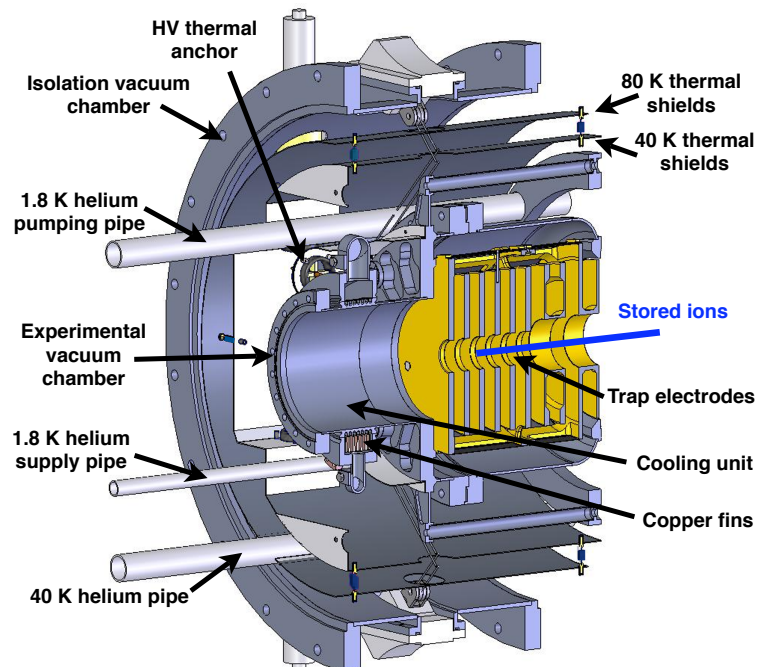
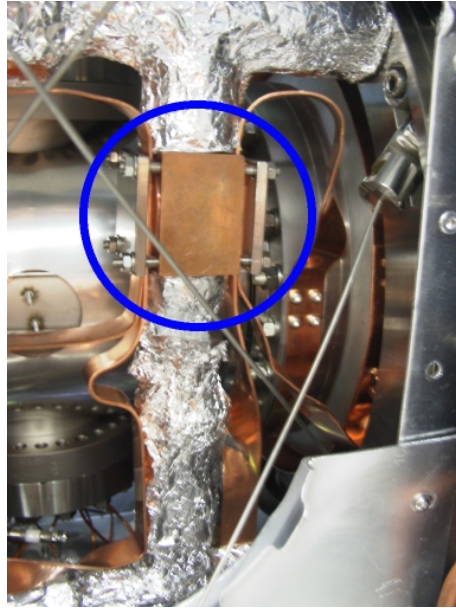


Figure 3.5: CTF cross section showing the cooling unit. The copper fins which are immersed in 1.8 K superfluid helium are used to transfer the cooling power to the surrounding chambers.

Figure 3.6: Cool-finger shortcut (circled in blue) between superfluid 1.8K helium and the pumped helium gas line used to cool the chambers. The test chamber can be seen on the left in addition to the Cu bands used to cool this chamber leading from the cool finger. One of the trap suspension wires in addition to the 40 K shields is also visible on the right.



it seems reasonable to assume that the sensors and the associated wires are the limiting factor. The reported temperature distribution, should therefore, be treated as an upper limit as opposed to the actual values of the experimental chambers. As demonstrated in Section 3.1.2, the achieved experimental chamber temperatures are more than sufficient to produce pressures on the order of  $10^{-13}$  mbar.

### Minimizing heat transfer

Moving from the cooling of the cryogenic beam-pipe to minimizing the heat transfer to this region, three processes need to be minimized: conduction, convection, and radiation.

Minimization of heat transfer via convection is achieved by housing the experimental chambers inside an isolation vacuum chamber (also called a cryostat). Provided that the isolation vacuum is better than  $10^{-4}$  mbar, the density of the rest gas is low enough to ensure that both convection heat transfer and electrical breakdowns from high voltage are minimized.

Heat transfer due to conduction includes: the vacuum chambers connecting to room-temperature, the chamber support wires, the electrical cables for the trap electrodes, the heating coils, the temperature sensors, the multilayer insulation, and any other physical connections between room-temperature and colder regions.

Minimizing the cross section of these connections in combination with maximizing the length between the room-temperature region and the cryogenic region is considered in the CTF design. For this reason, the beam line entry and exit to the cryogenic region is constricted to a diameter of 63 mm and lengthened with the use

### 3.1. The cryogenic electrostatic ion beam trap

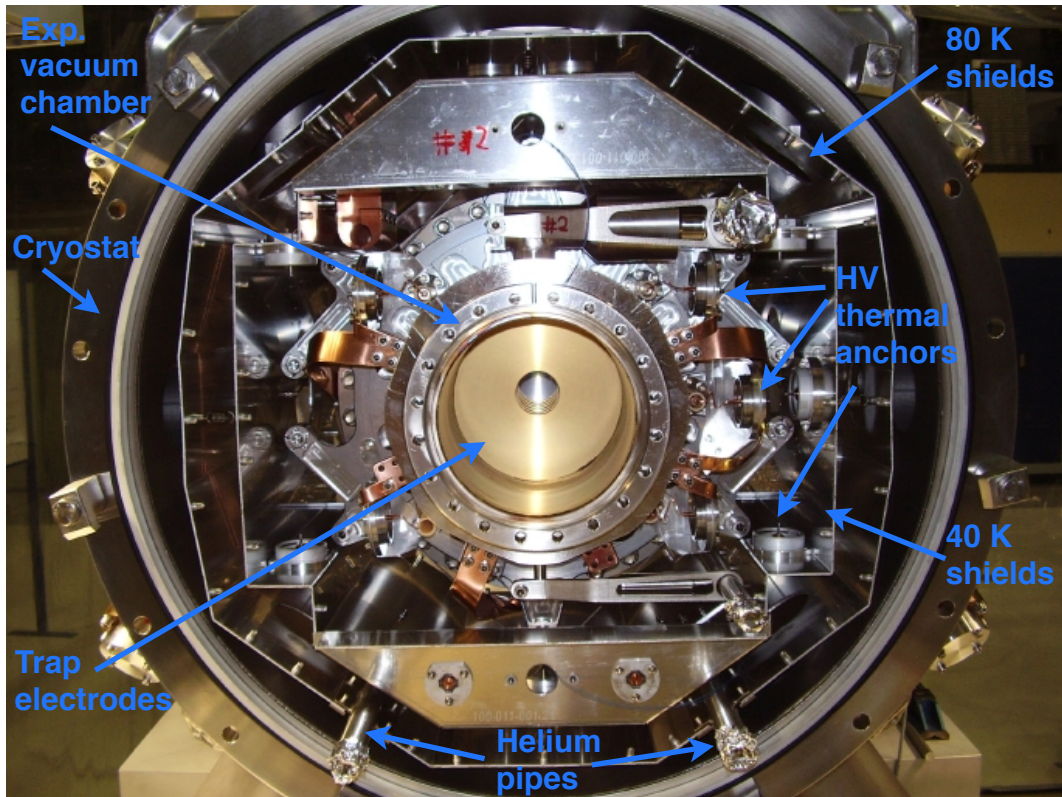


Figure 3.7: CTF labeled cross-sectional view. Note that the multi-layer insulation between the 80 K thermal shields and the cryostat vacuum chamber is not yet installed in this photo.

of two bellows (with the intermediate piece of beam-pipe cooled to around 40 K), which provide a smaller cross-section over a longer path to minimize heat transfer.

Such a reduction of the cross section as used for the beam entry region is not possible for the pumping station below the CTF, as the cross-sectional area also defines the maximum pumping speed. The pump connection is also designed with two bellows and a thermally anchored 40 K region between them.

The suspension wires which support the experimental chambers from the room-temperature cryostat also contribute a large amount of heat to these chambers. The wires have to be strong enough to support the stainless steel chambers, but as thin as possible to minimize heat conduction. For these reasons, inconel stainless steel wires (which are also non-magnetic) are used, as they have a particularly high tensile strength in comparison to other stainless steel alloys. The two chambers housing the electrostatic mirrors, for example, are each suspended with twelve wires (see Fig. 3.8).

Figure 3.8: Photo of the trap chamber suspension before the test chamber is installed. The gold-coloured electrodes can be seen mounted in the ion trap vacuum chamber, which is surrounded by two thermal shields, multilayer insulation, and mounted inside the cryostat. Some of the 24 suspension wires required for both sides of the trap can be seen.

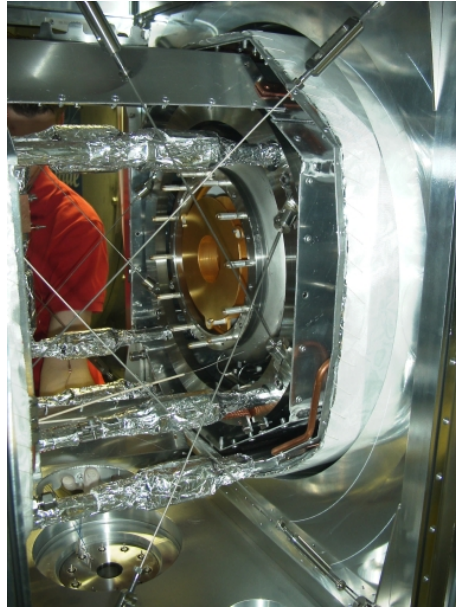


Figure 3.9: A sample 2 K thermal anchor (circled in blue) for the HV electrode cables plus Cu cooling bands between the Cu cooling unit on the right and a neighbouring vacuum chamber in the bottom left corner.



The only large heat source remaining comes from the trap electrode high voltage wires and the heating wires. Due to necessity, both of these must have larger cross sections to prevent field emission and sparking in the case of the HV wires, and to accommodate the high heating currents required. In both of these cases, special thermal anchors are installed which provide good thermal contact to the cooled surrounding region while providing electrical isolation (see the HV thermal anchors pictured in Fig. 3.9). This is achieved primarily through the use of sapphire which meets both of these criteria. To ensure the trap electrodes are not exposed to an additional heat load from the HV wires themselves, the wires are thermally anchored at both 40 K and 2 K.

The remaining electrical wires for the temperature sensors are generally thin with small cross sections, though these too are thermally anchored where possible, to

### 3.1. The cryogenic electrostatic ion beam trap

---



Figure 3.10: Photo of the 80 K thermal shields with water cooling lines (contact points with the shield are marked with arrows) and multilayer insulation (on the left) visible. A braided copper wire used to thermally anchor one of the chamber suspension wires is visible in the upper right corner. Two access ports to the enclosed 40 K shields and vacuum chambers can also be seen.

minimize heat conduction and to facilitate more accurate temperature measurements. This refers to measuring the actual temperature of the surface in question, as opposed to the temperature of the cable itself due to heat transfer.

Radiation of heat is the last remaining process which needs to be minimized. Similarly to heat conduction, the heat transfer via radiation can be vastly decreased by reducing the temperature change between two neighbouring surfaces as shown in Equation 3.1.1. For this reason, the experimental chambers are encased in a 40 K thermal shield to ensure that the blackbody radiation striking the chamber will be as cool as possible, thereby reducing the amount of cooling power necessary at 2 K. This shield is similarly enclosed by an 80 K thermal shield, all of which is wrapped with 15 to 20 layers of vacuum multilayer insulation (also called super insulation). This cryogenic onion-layer is demonstrated via the CTF cross-section shown in Fig. 3.3 and pictured in Fig. 3.7. Each multilayer insulation layer consists of a sheet of highly reflective aluminum foil and a thin glass fiber fleece which acts as a spacer between layers. Due to the experimental vacuum chamber bake-out temperatures, the high-purity aluminum thermal shields also achieve high temperatures. For this reason, the 80 K thermal shields require water cooling to ensure their temperature does not exceed 370 K (see Fig. 3.10) which will damage the multilayer insulation.

The actual mean temperature of these two thermal shields during cryogenic operation is lower than the design specifications at 37 K and 70 K. Both of these shields are cooled with the refrigeration system's second autonomous helium line starting at

Table 3.2: CTF temperature sensor ranges

Sensor type	Pt1000	RhFe	Silicon diode
Temperature range (K)	$\approx 30 - 900$	0.65 - 500	1.4 - 500

a temperature of 5 K. The 5 K line is used to thermally anchor portions of the trap suspension as well as cool the cryopump. This line then makes a second pass in the CTF, having warmed up slightly, cooling the 40 K shield components. The helium line makes an additional loop in the CTF, having further increased in temperature and now cools the 80 K shields before exiting the device. A thermal connection between the shields and the helium pipes is established via the use of copper braided wire-band, providing a flexible, easy to install, high thermal conductance line. An example of one of these copper braided wires can be seen in Fig. 3.10.

A large 300 K radiation area is directly exposed to the cryogenic beam-pipe (the pumping chamber) during cryogenic operation via the pumping port (see Fig. 3.4). This is necessary for pumping the experimental vacuum during room-temperature operation, as well as moderate cryogenic temperatures before this pumping region becomes more of a load to the vacuum system than a pump. When the CTF is supplied with 1.8 K superfluid helium, however, this area presents a large heat load onto the cryogenic beam-pipe. As a result, a radiation flap located in the 40 K thermally anchored region between the two bellows below the pumping chamber can be closed to block this radiation. This flap is not vacuum tight, but is constructed to completely stop the radiation from the 300 K region below and is moveable at cryogenic temperatures.

### 3.1.3 Temperature measurement

An array of three different types of temperature sensors are used to monitor the temperatures inside the CTF isolation vacuum: PT1000, RhFe, and Silicon diodes. Table 3.2 displays their respective temperature ranges, while the actual sensors can be seen in Fig. 3.11. These temperature sensors facilitate the monitoring of the experimental chambers, thermal shields, and the temperature distribution of other interesting components (suspension, cryopump to cold head connection, helium pipes, etc) during both the cooling and baking processes for safety and measurement purposes.

In comparison to the commonly used PT100 platinum resistance sensors, the robust PT1000s have a tenfold increase in resistance, facilitating a two-lead measurement. This reduces the number of cables required, and therefore the heat flux into the

### 3.1. The cryogenic electrostatic ion beam trap

---

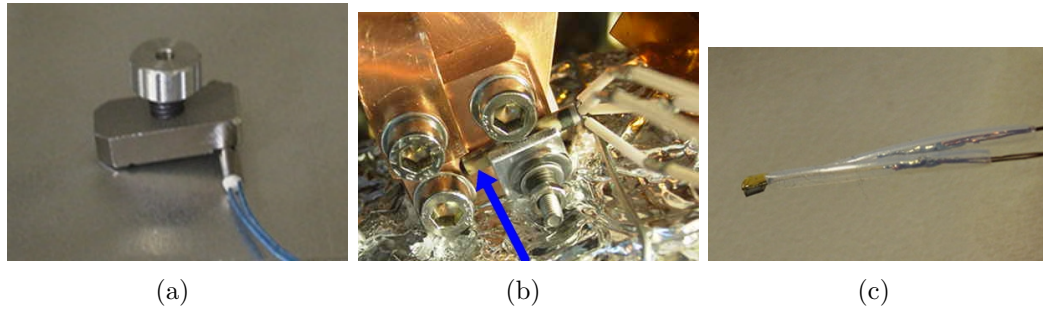


Figure 3.11: Photos of the temperature sensors used in the CTF isolation vacuum. (a) Shield mounted Pt1000 platinum resistance sensor (b) Cooling unit mounted RhFe resistance sensor (c) Silicon diode sensor.

system. As mentioned above, the cables are thermally anchored to the 40 K thermal shields to further reduce the heat load to the cryogenic beam-pipe. Note that the thermal contact between these sensors and the object of interest cannot be improved with standard cryogenic methods as cryogenic grease, varnish and most filled resins cannot withstand the CTF required bake-out procedure. This type of sensor is the most numerous, numbering almost fifty inside the CTF and provide a wide temperature measurement range as shown in Table 3.2. Below the range of 30 K, the electrical resistance of the sensor leads begins to dominate, leading to minimum measured values of at least 15 K, regardless of the sensor temperature.

The six installed silicon diode sensors use a four-point voltage measurement to more accurately measure the lowest temperatures, though they unfortunately cannot withstand the bake-out procedure. This requires dismantling and remounting the sensors before and after baking. Due to these restrictions, the silicon diodes are installed on easier-to-access points on the experimental vacuum chambers, in comparison to those chosen for the RhFe sensors. To minimize the risk of damage to the sensor and wires while moving them, thicker wires are required than would typically be used with these sensors. As a result of the larger wire cross sections, it is likely that this contributes to the disagreement between the lowest temperature measurement (3.1 K) with this sensor and the expected temperature of 1.8 K, given by the liquid helium return line temperature. The silicon diodes are installed using Apiezon N cryogenic high vacuum thermal grease to increase the thermal conductance between the sensor and a given surface.

The two Rhodium iron (RhFe) sensors are also well suited to measuring temperatures around 2 K, in addition to being able to withstand the bake-out procedure with minimal loss of precision. They are, however, more expensive than the silicon diodes. Given these characteristics, three of these sensors are installed in hard-to-



Figure 3.12: Silicon diode sensor and its thermally anchored cables.

access points on the experimental vacuum chambers. As is the case for the PT1000s, the thermal contact to the cryogenic beam-pipe could not be further enhanced with cryogenic grease due to the bake-out requirement.

To accurately measure the temperature of the chamber, as opposed to the sensor itself (due to the heat conductance of the connecting wires), all sensors placed on the experimental chambers have their wires thermally anchored at an intermediate temperature (normally the 40 K shield), in addition to using long wires to decrease the heat-load. For the silicon diode sensors, the wires are also thermally anchored to the object of interest to further reduce the heat load from the cables as shown in Fig. 3.12.

With the use of these sensors, the 80 K thermal shields and the helium pipe temperatures near the refrigeration system are monitored to ensure that the temperature stays below the required 370 K, to avoid damaging the multi-layer insulation. Following standard procedures for baking vacuum chambers, the temperature sensors allow the regulation of the applied heating or cooling power to keep the experimental chamber temperature changes below 10 degrees per hour and minimize the temperature gradients across the vacuum chambers. This is essential in order to prevent uneven cooling or heating of flanges, which would result in vacuum leaks, as well as unnecessary material stress to the chambers.

### 3.1.4 Vacuum system

The CTF employs a complex vacuum system to achieve experimental vacuum pressures of better than  $10^{-13}$  mbar room-temperature equivalent (RTE). This system is

### 3.1. The cryogenic electrostatic ion beam trap

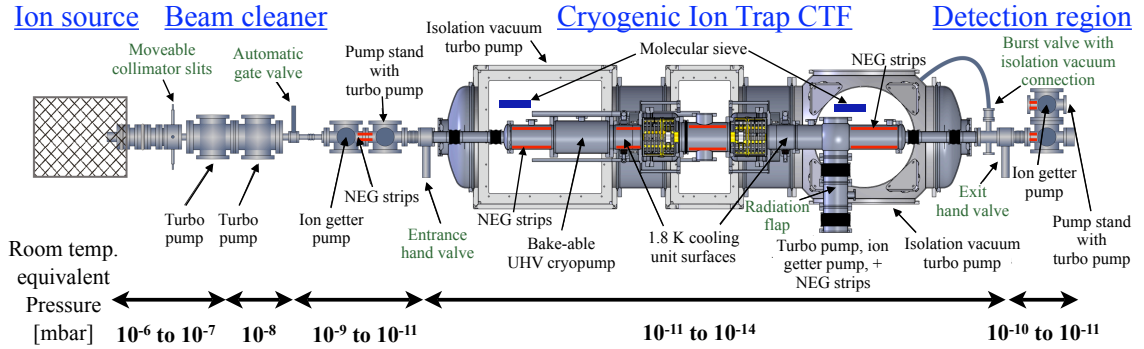


Figure 3.13: CTF and beamline vacuum schematic.

regulated by an equally complex interlock safety system (see Section 3.2.4). As described above in the cryogenic design of the CTF, an isolation vacuum surrounds the cryogenic beam-pipe containing the experimental vacuum. The appropriate pressure ranges for the entire CTF experimental beam line are shown in Fig. 3.13.

The cryogenic beam-pipe is made out of 316L stainless steel, where the individual chambers are connected using DN 150 or 200 mm CF flanges in addition to two DN 300 mm COF flanges. During room-temperature operation, the CTF experimental vacuum is pumped via a bake-able UHV cryopump (see Section 3.1.7 for more details), employing a Leybold CP 140T single stage cold head with a base temperature of 10 K (with a Leybold Coolpak 6000 compressor unit), non-evaporative getter (NEG) strips from SAES Getters (model ST707/CTAM/30D), an ion getter pump (Varian Star Cell), as well as a 500 L/s Pfeiffer turbo molecular pump. The ion getter pumps effectively pump the noble gases present, while the turbo pump, cryopump, and NEG strips pump the remaining species, excluding hydrogen which is pumped at reduced speeds by the cryopump.

During cryogenic operation, the all-metal valves to the turbo pump and ion getter pump below the CTF are closed, since the cryopump and the cryogenic walls of the beam line pump so well, that these are more of a load to the vacuum than a pump. In this operational mode, the cryopump (connected to the 5 K helium line) and the cryogenic walls/cooling units provide all the pumping required, since the pumping speed of the NEG strips decreases with temperature. The cooling units ensure the creation of a 1.8 K surface area, which is essential for the pumping of hydrogen. Hydrogen is the last rest gas species to condense (as significant amounts of helium are not present) as confirmed by the mounted quadrupole mass spectrometer (QMS) located by the burst disc. Rest gas pollution from the baked room-temperature regions of the experimental vacuum is limited through the use of small apertures and differential pumping.

The baked room-temperature regions of the experimental vacuum are pumped via ion getter pumps and NEG strips. These chambers are separated from the trap vacuum via differential pumping tubes to limit the amount of rest gas that would otherwise enter the extra high vacuum (XHV) trapping region. A burst disc is mounted in the room-temperature experimental vacuum region between the cryogenic beam-pipe and the DB2 chamber (in the detection region) which ensures that over-pressure with respect to the isolation vacuum, which could cause bodily harm to the operators and damage to the apparatus, is released at levels exceeding 400 mbar.

The isolation vacuum, as shown in Fig. 3.13, is pumped via two 300 L/s Varian TV301-Navigator turbo molecular pumps at room-temperature to the  $10^{-5}$  to  $10^{-6}$  mbar range. In cryogenic operation, the turbo pumps are greatly assisted by two Zeolite-based molecular sieves (a type of very porous material used to absorb gas), the cryogenic chambers themselves, and the cold head reaching isolation vacuum pressures of  $10^{-6}$  to  $10^{-7}$  mbar. The initial pumping of the large isolation vacuum region is assisted by a high capacity Roots pump. A photograph of one of the molecular sieves contained in a mesh and mounted on a 40 K copper thermal shield cooling line in the isolation vacuum is shown in Fig. 3.14. These sieves also act as cryopumps, offering an extremely large surface area, which when cooled to cryo-



Figure 3.14: Photo of one of the molecular sieves mounted in the isolation vacuum. It is resting on one of the 40 K copper thermal shield cooling lines, suspended above the ion gauge chamber. A mounted silicon diode sensor can be seen in the lower left corner of the picture, in addition to part of the 80 K shield surrounding the 40 K thermal shields.

### 3.1. *The cryogenic electrostatic ion beam trap*

---

genic temperatures, pumps very effectively. In this location, the sieve is also baked along with the vacuum chambers for periodic cleaning. Over-pressure of this large vessel can be released by a 100 mm O-ring flange which is only sealed by atmospheric air pressure.

#### 3.1.5 Trap electrodes

The electrostatic ion beam trap employed in the CTF consists of two electrostatic mirrors. Each of the two stacks consist of eight electrodes, three of which act as an Einzel lens. All of the electrodes create a potential that ensures the ion beam remains focused and in a stable trap orbit. An ion pulse is allowed into the trap since the potentials of the first mirror stack are initially zero. The ions are slowed and reflected by the second electrode stack, then accelerated back towards the ion source. Before the ions reach the first stack again, the potentials are switched on (reaching 95% of their full value within 420 ns), matching the potentials of the second stack, thereby trapping the ions.

The electrodes are made of an aluminum alloy, as opposed to stainless steel or copper, for economic, weight, and ease of machining reasons. They are also plated with  $2\ \mu\text{m}$  of copper, followed by  $5\ \mu\text{m}$  of gold to avoid any surface potential imperfections from oxidized aluminum areas (see Fig. 3.15). The electrodes are suspended via three ceramic rods and isolated from each other using sapphire spacers. The sapphire spacers not only provide electrical isolation, but good thermal conduction as well. This property is exploited at cryogenic temperatures as the aluminum cage supporting the electrode stack and the sapphire spacers have different thermal expansion properties, resulting in the compression of the stack for optimal heat transfer. The

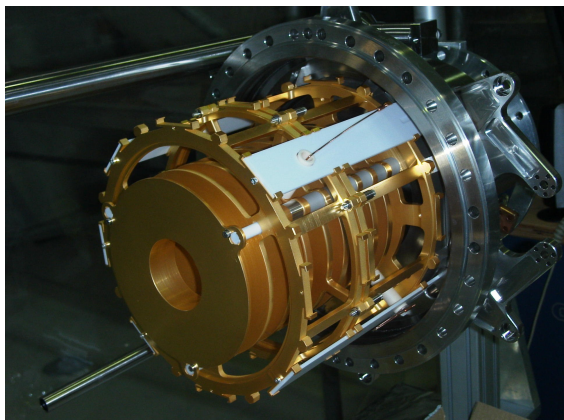


Figure 3.15: Photo of the CTF trap electrodes.

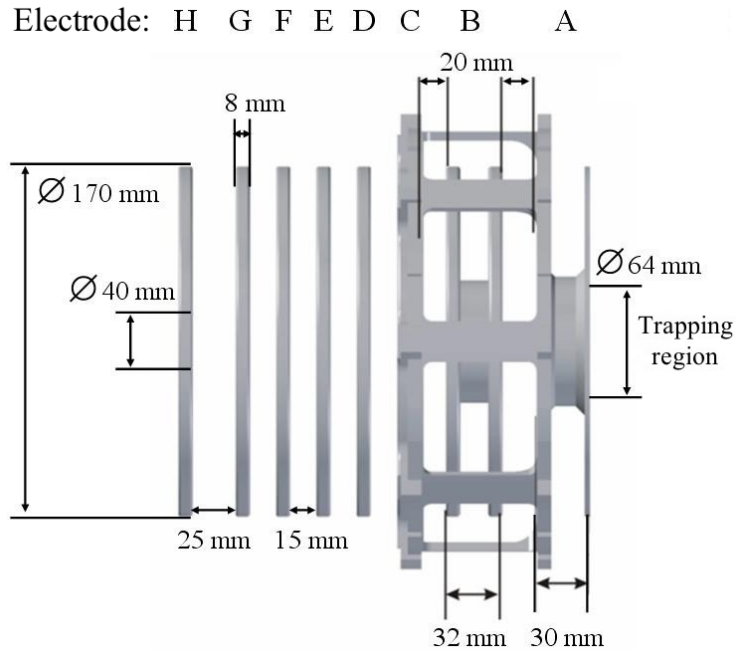


Figure 3.16: Schematic of one of the two mirrored CTF trap electrode stacks.

Table 3.3: Typically employed trap voltages

Electrode	A	B	C	D	E	F	G	H
Fraction of beam energy	0	0.923	0	0.357	0.666	1.067	1.303	0

entire electrode stack assembly is fastened to the cryogenic stainless steel chamber, which is directly cooled with liquid helium in the cooling units, ensuring effective cooling of the trap electrodes.

It was experimentally found that the potentials in Table 3.3 for the trap electrodes as schematically shown in Fig. 3.16 produce the best lifetime results. Note that as this trap is electrostatic, these fractions must simply be multiplied by the beam energy to produce the same scaled potential curve.

The capacitance between the trap electrodes varies between 20 to 70 pF, where the largest value corresponds to the nearest neighbouring electrodes. The capacitance to ground varies between 60 to 80 pF for all trap electrodes. RF cross-talk measurements were also performed on the electrodes using a 15 V square wave at various frequencies. No resonances were seen (i.e. measurements appeared roughly frequency independent), with typical cross-talk on neighbouring electrodes of 1 V at 1 MHz. Electrodes which are partially hidden behind another non-grounded elec-

trode displayed a smaller signal (0.4 V) and those behind a grounded electrode saw effectively nothing (0.03 V), as expected. These tests were done to confirm that both sides were electrically connected in the same fashion, given that they were installed in an identical manner. This was the case for all electrodes on both sides, with the exception of electrode D on the switched side. The cross-talk amplitudes measured on D (or produced by applying a signal on D) with respect to all other electrodes were a factor of three smaller than expected, though no justification for this difference could be determined.

The RF bunching experiments described in Section 4.2.3 require an RF pulse of a few volts to be applied to the static B electrode. This is accomplished through the use of an Agilent 33220A Function Generator/Arbitrary Waveform Generator, as well as a custom-built inverted high-pass RC filter, which uses a capacitor to couple the signal to the applied high voltage.

#### **3.1.6 Pickup electrodes**

The CTF is equipped with three pickup electrodes, all located within the test chamber between the trap electrodes in the field-free region as shown in Fig. 3.17. This non-destructive detection technique measures the image charge induced on the pickup electrodes as the ion bunch passes through them. It should be noted that this technique measures the change in the current passing through the electrodes. Short pulses, or beams with a slight gap in them (caused by the non-instantaneous closing of the trap) of sufficient charge can be easily seen on the oscilloscope. Ion beams that have filled the trap's phase space acceptance over time result in the same number of charges going in both directions through the pickup electrodes. As there is then no net change in the charge passing through the electrodes, no obvious signal is visible.

The middle pickup, called the SUM pickup, is a cylindrical electrode with an inner diameter of 4 cm and a length of 2 cm, while the slightly longer 4 cm pickups on either side are radially segmented into four pieces. The segmented pickups are used for mass-selection in addition to allowing the possibility of measuring the stored ion beam center of charge via the voltage differences between the four electrodes. The SUM pickup is typically read out using a high ohmic low noise FET amplifier from NF (model SA-220F5), which provides a signal amplification of 200 times. The amplified signal is then viewed with a 500 MHz oscilloscope (LeCroy LC374A), as well as a spectrum analyzer (Advantest R3131A). For ion frequency identification, fast fourier transforms of the amplified pickup signal are acquired using the oscilloscope as well as an Acquis computer system with DC282 cards capable of recording in

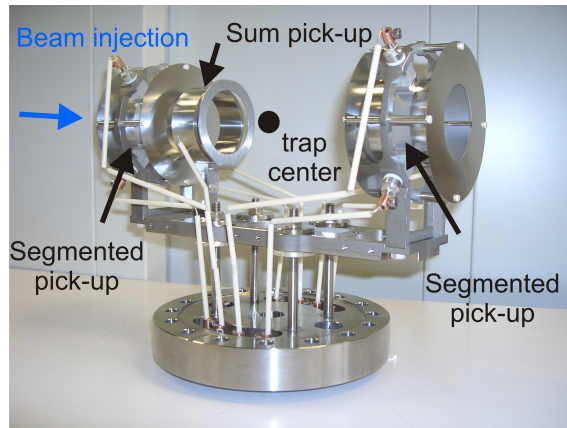


Figure 3.17: Photo of the pickup electrodes installed in the field free region of the trap allowing the non-destructive observation of the ion bunch.

excess of 2 Gigasamples per second for mass resolution tests. By contrast, the spectrum analyzer mixes the input signal with RF at a known frequency to measure the frequency amplitude. A frequency scan can be performed over a set RF frequency range, where each frequency is measured separately, or a scan at one particular frequency as a function of time can be analyzed.

The RF knockout mass selection and tune measurements use one of the segmented pickups (see Section 4.3.2 for more details). RF noise is applied to one half of the pickup (the two bottom electrodes) using an HP 3561A dynamic signal analyzer to supply the base noise, which is then mixed in a custom built module with the desired frequency and amplitude provided by an Agilent 33220A Function generator/Arbitrary Waveform Generator.

The knockout mass selection technique also employs two of four injection-side segmented pickup electrodes. In this technique, high voltage is applied at a given frequency to kick the unwanted ions out of the trap (see Section 4.3.1 for more details). The frequency of the high voltage is provided by an Agilent 33220A Function generator/Arbitrary Waveform Generator, while two FUG high voltage supplies (model MCN 350-1250) are used to apply the voltage. The high voltage cables are connected to a custom built module, which contains the high voltage switches driven by the frequency generator to provide the necessary knockout signal.

### 3.1.7 First bake-able charcoal-based UHV cryopump

With the help of Ch. Day from the Forschungszentrum in Karlsruhe, D. Orlov designed the first bake-able charcoal-based ultra-high-vacuum (UHV) cryopump for

### 3.1. The cryogenic electrostatic ion beam trap

---

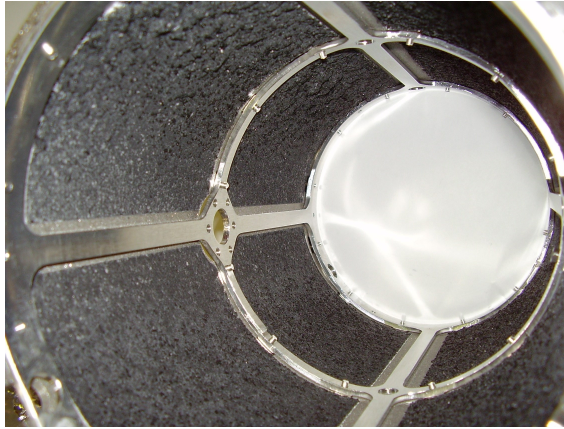


Figure 3.18: Activated charcoal layer of the cryopump.

the CTF and the CSR (see Fig. 3.19) [77]. The main feature of this pump consists of an activated charcoal glued to both sides of a cylindrical carrier by an inorganic, bake-able glue (see Fig. 3.18). This cylinder is directly connected to a solid copper rod, which exits the inner vacuum and is connected to a cryogenic cooling source using a high purity copper cable. Originally a single-stage cold head (Leybold CP 140T with a Leybold Coolpak 6000 compressor) was used to cool the cryopump. To maximize its pumping abilities, the device was later attached via a relatively high purity (99.9%) copper braided wire to the 5 K liquid helium line. Inside the activated charcoal layer are two thermal shields to ensure that the 300 K radiation from the beam line is suppressed during room-temperature operation. There are two additional thermal shields surrounding the charcoal layer to minimize the thermal radiation from the experimental vacuum chamber during room-temperature operation. This pump makes use of the cryo-sorption process as opposed to cryo-condensation. In the cryo-condensation process, the vapour pressure of the adsorbed gas at the temperature of the pumping surface defines the limiting pressure. UHV in the range of  $1.3 \times 10^{-13}$  mbar can be achieved by cooling down the pumping surface to temperatures below 2.67 K for hydrogen [78]. At these temperatures, only helium has a higher vapour pressure (i.e. requires a lower temperature to produce the same pressure). Helium is, however, not produced in amounts comparable to hydrogen in metal vacuum chambers. This type of pump allows multiple monolayers (where a monolayer is a layer one molecule thick) of gas to be pumped on a smooth surface with a relatively small area [78]. Cryo-sorption pumps do not have to be cooled down to such low temperatures to pump hydrogen since they rely on a porous surface which has a very large effective area. The less stringent temperature requirements provide a distinct economic advantage. This type of cryopump cannot



Figure 3.19: Photo of the bake-able, charcoal-based, UHV cryopump.

capture as many monolayers of gas as cryo-condensation pumps due to having higher surface temperatures. The equilibrium pressure created by these pumps is defined by the relative amount of surface area coverage. Such a cryo-sorption pump at 4.2 K covered with less than a monolayer of gas, for example, will still pump all gases to extremely low pressures [78].

## 3.2 Surrounding instrumentation

### 3.2.1 Ion injection beam line

#### Ion sources

During the first year of CTF operation, both a Penning ion source, as well as a multi-purpose ion sputter source (MISS) were used to create cations (eg:  $N_2^+$ ,  $N^+$ ,  $CO^+$ ) and anions (eg:  $Al_n^-$  where  $n = 1$  to  $7$ ), respectively. Refer to Fig. 3.13 for ion source placement with respect to the complete CTF setup.

The first source used with the CTF was the cold-cathode Penning ion source. A hollow metal cylinder is used as the anode, while two end caps on either side are the cathodes. A gas is continuously injected into the anode through a small inlet and a high voltage of 800 to 1500 V is applied between the anode and cathode. A higher initial voltage creates an arc, which ionizes the gas, and the continuously incoming gas when combined with the voltage difference creates a self-preserving

### 3.2. Surrounding instrumentation

---

Table 3.4: Typical Penning ion source operational parameters.

Extraction voltage	2 - 9 kV
Anode voltage	800 - 1400 V
Penning magnet	5 V
Ion energy	Extraction + Anode keV

Table 3.5: Typical operational parameters for the sputter source.

Extraction voltage	6 kV
Cathode	1600 V
Deceleration voltage	14 kV
Cesium oven temperature	80 to 100°C
Filament temperature	270 to 300°C

plasma. The liberated electrons are contained via a magnetic field to ensure that the plasma continues to burn as the electrons oscillate between the two cathodes, ionizing the gas inside the anode. The ions are then pulled out through a small hole by applying a high voltage (1 to 7 kV) to the extraction electrode. This voltage is defined by an external power supply, which is used to float the anode and cathode power supplies to high voltage. The ion energy from this source is given by the extraction voltage plus the anode voltage.

The second source used with the CTF was the sputter ion source, which can be used to produce aluminum cluster anions. A filament is used to heat the source, in combination with an additional heater for the Cesium oven promoting the vaporization of Cesium in the source. The Cesium vapour condenses on the cooled target material. An aluminum target was used in the reported experiments contained in this work. Cesium vapour is also ionized and accelerated towards the target, sputtering off a small cluster on impact. The condensed Cesium on the target provides a donor electron causing the clusters to be negatively charged immediately upon production on the target surface. This process ensures a sharply defined beam energy when compared to the Penning source. The negative aluminum clusters of various sizes are then extracted via an acceleration electrode towards the ion trap. The ion beam energy is defined by the extraction voltage placed on the ion source power supplies. The aluminum cluster focused on for the photon-induced delayed emission experiment used  $\text{Al}_4^-$ , which consists of only 3.4% of the entire beam. The sputter source using an aluminum target produces mainly  $\text{Al}_2^-$  and  $\text{Al}_3^-$ .

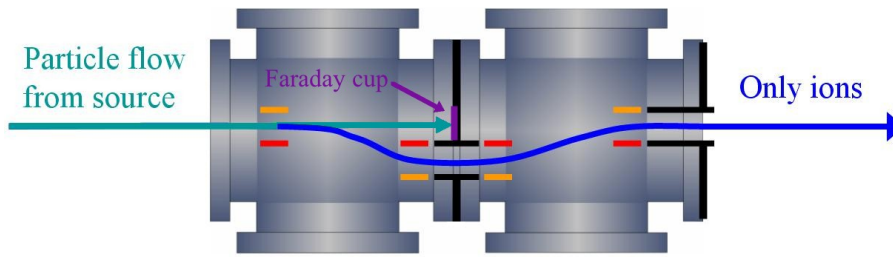


Figure 3.20: Beam cleaner schematic.

### Ion beam optics

As shown in Fig. 3.1, the first Einzel lens is found directly after the ion source to focus the ion beam before it is collimated by a set of moveable slits and enters the beam cleaner. The beam cleaner consists of four electrostatic plates designed to steer the charged beam through a small differential pumping tube, then steer it back along its initial beam axis, as shown in Fig. 3.20. This small opening ensures that the neutral gas effusing from the ion source, as well as the  $10^{-6}$  mbar pressure in the first section of the beam cleaner due to the required operational parameters of the Penning ion source, are effectively prevented from continuing towards the ion trap. The beam cleaner was built by our collaborators at the Weizmann Institute in Rehovot, Israel. A turbo molecular pump under each of the two vacuum chambers, combined with the small connecting tube in the beam cleaner, provide a differential pumping factor of around ten. The beam cleaner is also equipped with two sets of steerers at the entry and exit of the device. After exiting the beam cleaner, the ions pass through a second Einzel lens to focus the beam before it enters the cryogenic vacuum chamber region and the trap contained within.

### Ion beam detectors

The CTF relies on several diagnostic detectors as described in [74]. When the beam cleaner is not deflecting ions through to the trap, the ion beam strikes a Faraday cup, which measures the total current produced by the source. In the first diagnostic chamber located in the last bake-able chamber just before the beam enters the cryogenic chamber region, an aluminum plate can be moved into the beam. The secondary electrons produced by the beam striking the aluminum plate at a  $45^\circ$  angle are then accelerated by a voltage applied to a copper mesh in front of the MCP and phosphorus screen stack (also mounted at  $45^\circ$  with respect to the beam), which are observed using a CCD camera by looking through a window into the vacuum chamber. The electric field between the mesh and MCP is designed such that an image of the beam profile can be seen on the phosphor, which allows the

CCD camera mounted perpendicular to the ion beam axis to see an image which is upright and almost undistorted. A similar setup is also employed in the second diagnostic chamber (called DB2) located on the exit side of the CTF.

Neutral fragments from the trap are detected using two impedance-matched 40 mm multichannel plates (MCP) in chevron geometry, which are mounted directly along the beam axis, located in the DB2 chamber after the second diagnostic assembly. This detector is also called the beam observation system (BOS) MCP. Pulses are detected on the MCP HV supply line, through the use of an RC filter, which are fed to the acquisition system as schematically illustrated in Fig. 3.21. This single-particle counting mode is used to detect the neutral fragments caused by electron capture, collisional detachment, or delayed emission. A phosphor screen and a CCD camera outside the vacuum system allow the visualization of the detector hits.

### 3.2.2 Experimental control and data acquisition

#### CTF control system

The CTF control system is based on the MPI-K EUNET system, which is used to control the power supplies for the entire injection beam line, trap electrodes, and the BOS MCP used to perform the lifetime experiments. Using a desktop computer, settings can be modified, saved, and loaded, allowing the relatively fast switching between different established beam energies.

#### Data acquisition and experimental control

Two separate data acquisition systems are used in the CTF setup; one to carry out MCP lifetime measurements, and a second to record the temperature sensor readings.

A computer with a National Instruments PCI-6602 timing card and various custom LabView programs are used to control the beam injection timing, MCP counting, and a laser system. A schematic outlining the data acquisition is shown in Fig. 3.21, where the models used, in order of appearance in this figure are: Ortec Timing filter Amplifier (model 474), LeCroy Linear Fan-In/Fan-Out (model 428F), LeCroy Discriminator (model 623), LeCroy Level adapter (model 688AL), LeCroy 4-fold logic unit (model 365AL), and a Phillips scientific Quad gate/delay generator (model 794). As outlined in this figure, the impinging neutrals on the MCP result in a signal, which is read out through a capacitor, amplified, discriminated, and then recorded by the data acquisition system. The linear fan is installed to directly observe the signal with an oscilloscope when necessary, and the DAQ timing card signal sets a

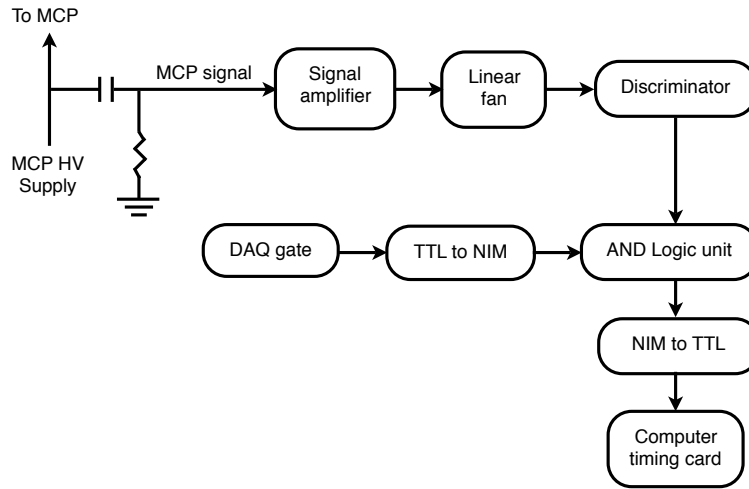


Figure 3.21: MCP data acquisition schematic.

gate to ensure events only arrive when the system is expecting events. If this gate is not used, the system will not consistently record all injections.

The timing scheme used for the multitude of measurements with the chevron MCP in the DB2 vacuum chamber is displayed in Fig. 3.22. By necessity, the trapping duration varies by almost 4 orders of magnitude, due to the observation of both very short decays as discussed in Section 5.2, as well as the long lifetimes required to demonstrate the  $10^{-14}$  mbar RTE vacuum as presented in Section 4.4. For longer lifetime measurements, the automatic valve between the beam cleaner and the DB1 vacuum chamber is opened to allow the ions to pass through, before being closed again to ensure better vacuum conditions in the trap itself. Sending the signal to close the valve as the beam cleaner is triggered offers more than adequate time to allow the ion pulse to pass through due to the relatively slow opening and closing times. The beam cleaner trigger defines the length of time the non-mass selected ions from the source are permitted to pass through, while the trap electrode trigger defines the time the trap is closed, providing a basic time-of-flight mass-selection of the stored ions. As discussed above, the DAQ signal is used to gate the MCP signal and the extra time after the background measurement ensures that the system has enough time to write the recorded events, allowing the data acquisition system to perform optimally. The pickup signal is also displayed in Fig. 3.22, where noise from the switching of the beam cleaner and the trap electrodes is also included.

Yet another standalone computer is coupled with a Lakeshore temperature monitor unit (model 218) and an Adwin system, in addition to individual custom-built signal amplifier units to read out two RhFe sensors, six silicon diode sensors, as

### 3.2. Surrounding instrumentation

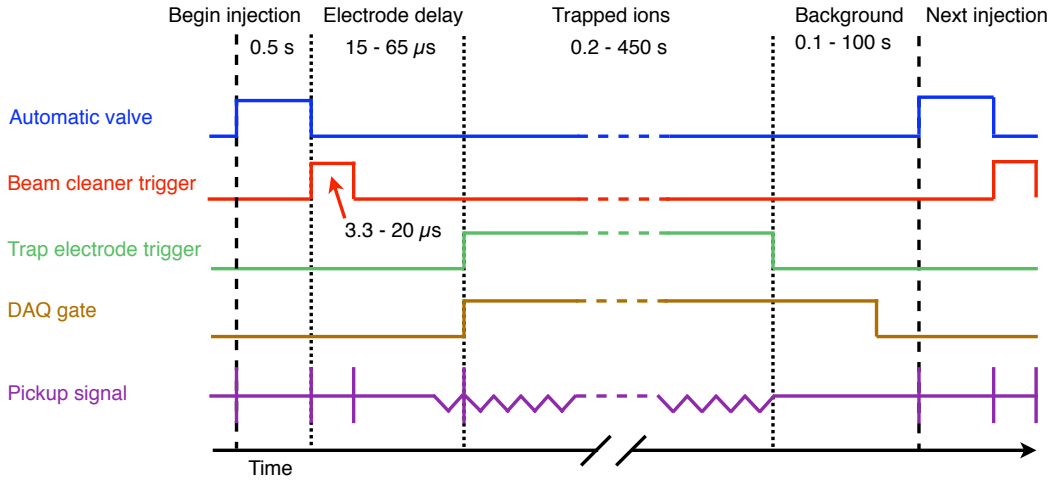


Figure 3.22: MCP timing schematic employed in lifetime measurements.

well as almost fifty PT1000 sensors. These sensors are typically read out once a minute, where the rate of change is automatically calculated and closely monitored during both bake-out and cryogenic cooling to ensure that the temperature in each region does not change faster than 10 K per hour. The temperature of neighbouring experimental vacuum chambers is also closely monitored to avoid large temperature gradients, which could also pose problems for the system. These steps ensure that all flanges remain vacuum tight during the temperature stresses of the 600 K bake-out and the 2 K cryogenic cooling.

Online analysis is performed with LabView and offline final analysis is primarily done using Matlab 7.4.0.287 (R2007a), in addition to Origin 8.0.

#### 3.2.3 Bake-out system

Since the CTF is designed to operate at room-temperature as well, all of the experimental beam line vacuum chambers, particularly the cryogenic beam-pipe need to be baked-out to ensure high vacuum is achieved. In order to facilitate this bake-out process, two separate systems are employed; one for the external, non-cryogenic experimental vacuum chambers on either side of the cryogenic trap as well as below it, and a second for the cryogenic chambers.

Standard technology is used to bake the experimental vacuum beam line chambers, baking up to 570 K where possible. Lower temperatures are required for more sensitive regions, such as the all-metal gate valves and windows. An array of thermocouples and two MPI-K custom-built heating computers, with a total of 30 separate

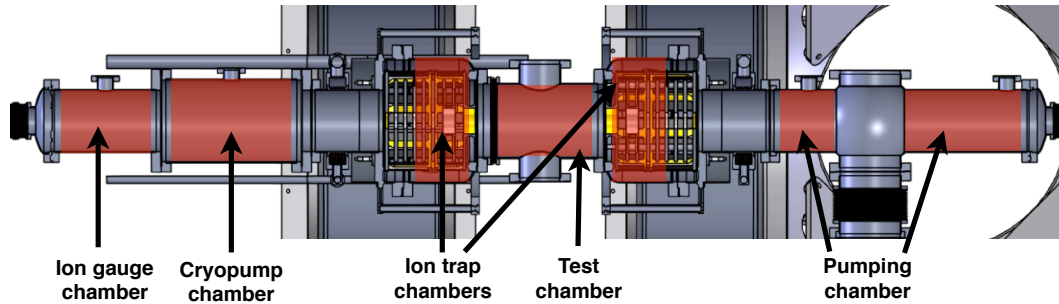


Figure 3.23: Experimental vacuum chamber heating coil schematic. The red regions overlaid on top of the vacuum chambers show the regions where heating coils are installed. Labels with two arrows indicate two separate heating coils connected in series. The properties of these coils are summarized in Table 3.6.

channels are used to monitor and heat the chambers. Regions containing NEG strips are further heated to 600 K to ensure better activation of these pumping units.

The bake-out of the cryogenic beam-pipe, necessarily located inside the isolation vacuum chambers, is understandably more complicated. Care was taken upon initial installation of the heating coils to ensure optimal coverage of the chamber surface area to reduce temperature gradients along both individual chambers, as well as the entire cryogenic beam-pipe (see Fig. 3.23). The heating coils are tightly compressed against the chambers using a thin stainless steel shell in order to help with the temperature distribution. The wires supplying current to the heating coils are guided from the chambers to thermal anchors on the 40 K shields to minimize the heat load on the cryogenic system, before being guided along a long path towards the electrical feedthroughs exiting the isolation vacuum system. Each experimental vacuum chamber has a separate heating channel, with the exception of the ion trap chambers as shown in Fig. 3.23. These two heating coils have the same length/resistance and are therefore connected in series, as both should be heated to the same temperature. The pumping chamber also has its own channel, though two separate heating coils are connected in series to cover the two different areas of this particularly long chamber.

A heating system consisting of a phase control device (Behringer Eurolight LD6230) equipped with a custom computer interface is used to monitor and control the current flowing through the five channels. The specifications of each channel are listed in Table 3.6. The computer used to control the current is also used to monitor the temperatures of the chambers and thermal shields as described above. PT1000s are almost exclusively used here since the silicon diodes have to be removed as they cannot survive the bake-out temperatures. RhFe sensors are used, though the

Table 3.6: Experimental vacuum chamber heating channel characteristics

<b>Vacuum chamber</b>	<b>Max. Temp. (K)</b>	<b>Cable resistance (<math>\Omega</math>)</b>	<b>Max. Power (W)</b>
Ion gauge chamber	600	20	200
Cryopump chamber	600	24	200
Ion trap chambers	560	29	300
Test chamber	600	22	450
Pump chamber	600	25	350

accuracy of these sensors after the first bake-out has become slightly worse according to the company specifications. This minimal degradation is acceptable, particularly given the fact that they are installed in locations that are not easily accessible, which would have involved extensive removal of thermal shields, if at all possible, in order to remove these sensors. Normal procedures for baking vacuum chambers also apply to the inner chambers in the isolation vacuum, therefore fast temperature changes are avoided with a maximum temperature change of typically 10 K per hour. The temperature of the 80 K shields also has to be closely monitored to ensure that the local temperature does not exceed 370 K, at which point the multi-layer insulation would be damaged. For this reason, a water cooling system is also installed on the 80 K shields, since the temperature otherwise would have exceeded the allowable range. The bake-out procedure consists of baking all of the chambers to around 530 K, followed by increasing the temperature of the cryopump to 600 K to clean it out. The cryopump is then allowed to cool down to around 550 K before all of the other chambers are further heated to 600 K, thereby activating the NEG strips contained within. This procedure ensures the cryopump is cleaned without having the NEG strips fill some of their limited pumping capacity by absorbing the emitted gas from the cryopump.

### 3.2.4 Interlock and safety system

Due to the complexity of the CTF vacuum system, coupled with the cryogenic and heating systems, a complex interlock system is used for the safety of the experimenters, as well as the equipment. The system was generally divided into two main sections, one covering trap operation from cryogenic to room-temperature, and a second scenario for the bake-out of the cryogenic beam-pipe. Fig. 3.24 shows a schematic demonstrating the interlock system logic.

The inputs on the left side of the schematic refer to the signals from various devices or sensors which indicate if the device or system in question is operating normally.

## CTF Interlock system

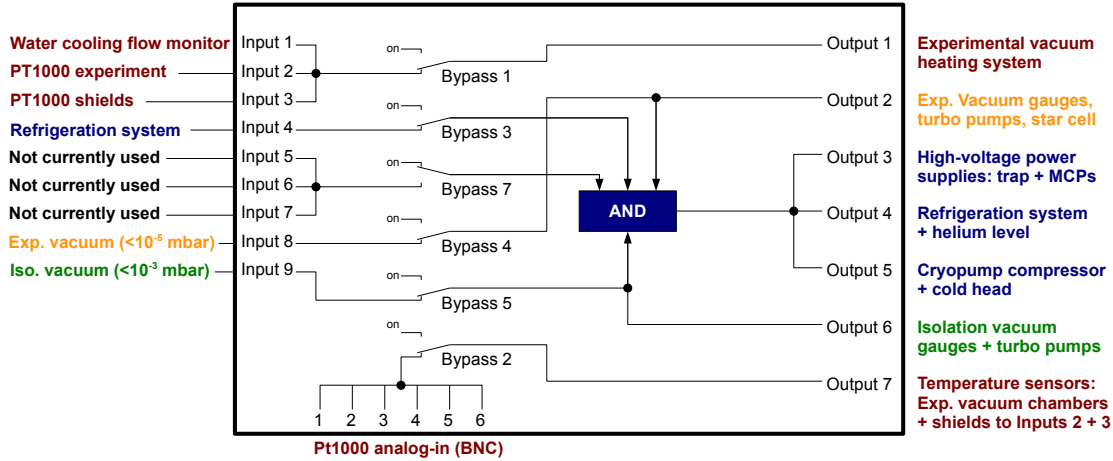


Figure 3.24: CTF interlock schematic.

This corresponds to a pressure better than  $10^{-3}$  mbar and  $10^{-5}$  mbar for the isolation and experimental vacuum, respectively. These limits are in excess of two orders of magnitude worse than normal operation, even at room-temperature. As shown in Fig. 3.24, trap operation at cryogenic temperatures requires that all systems with the exception of those for the bake-out are active. The high voltage trap electrodes and MCP require these conditions since poor vacuum in either the experimental vacuum or the isolation vacuum could result in sparking, and damage the system. Similarly, a failure of the isolation vacuum would necessitate the shutting down of both the cryopump, as well as the refrigeration system to protect both systems, though care must be taken that the isolation roughing pump is still active to ensure that desorbing gas from the warming surfaces is pumped away to avoid over-pressurizing the isolation vacuum.

A failure of the experimental vacuum while the isolation vacuum exists would also put enormous mechanical stress on the bellows, as well as the chambers and their suspension. Such a failure could potentially result from a helium leak into the experimental vacuum, the accidental venting of the experimental vacuum region, or a failure of the experimental forevacuum (this would have to occur before the valve to this region is closed once cryogenic temperatures are reached). While the interlock system would ensure the isolation vacuum would be shut off in such a scenario, the experimental vacuum region could potentially become over-pressurized. If such an event were to occur, a catastrophic failure would be avoided via the installed burst valve, which would vent the over-pressure in the experimental vacuum into

### 3.3. Laser experiments with the CTF

---

the isolation vacuum when a pressure difference between these two regions of over 400 mbar is reached.

The part of the interlock concerned with the bake-out of the experimental vacuum chambers requires that the cooling water for the 80 K shields be flowing to avoid damaging the multilayer insulation, as well as that the monitoring PT1000 temperature sensors are within acceptable range. These sensors monitor the experimental chamber temperatures to ensure they are not heated beyond specifications in addition to sensors on the 80 K shields and helium lines leading to the refrigeration system to avoid damaging the multilayer insulation in these areas.

## 3.3 Laser experiments with the CTF

After the initial tests with the CTF, the setup was modified to facilitate the delayed emission experiment, which required the removal of the Penning source and the installation of a sputter source as well as a laser system as shown in Fig. 3.25. A photo of this setup is also included in Fig. 3.26. The anions produced in the sputter source, in combination with the laser setup described below, allow the photo-detachment of the trapped ions, allowing different properties of the trap as well as the stored clusters to be explored.

A Nd:YAG pump laser (Powerlite Precision II 9019 Plus) is coupled with a Narrow scan pulsed Dye laser from Radiant Dyes to produce 8-10 ns photon bunches with an initial energy of 6 mJ per pulse at 600 nm with a frequency of 10 Hz. As shown in Fig. 3.27, the laser beam is first guided through a telescope, expanding the beam, then guided via a series of mirrors from the laser tent to a position directly above the

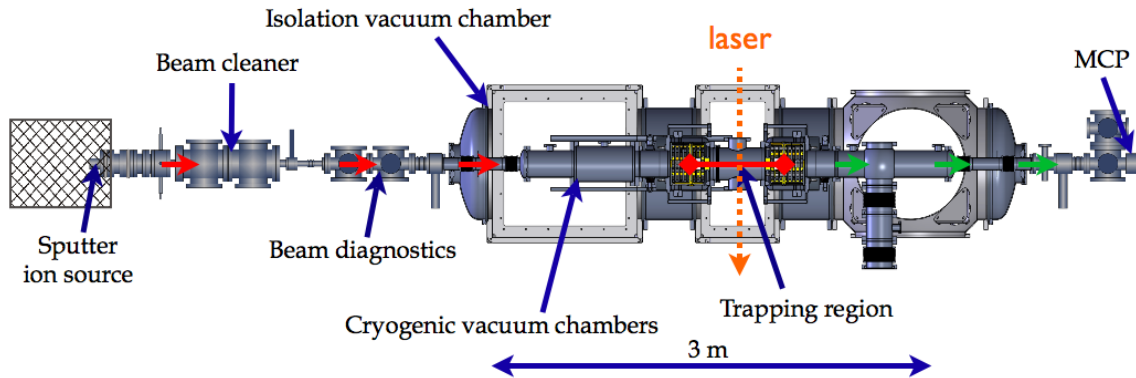


Figure 3.25: CTF setup employing a laser to photo-detach stored anions.

CTF test chamber and deflected perpendicularly to cross the ion beam axis, heading towards the ground. The measured beam diameter at the top outer vacuum window before the laser entered the vacuum system is 12.3 mm, with a typical measured beam power of around 35 mW at this position, ensuring a good overlap between the laser beam and the ion beam, in addition to allowing a larger laser power to be used while still avoiding two-photon absorption processes. The estimated peak power intensity during a pulse typically used in this setup is around  $100 \text{ kW/cm}^2$ . It should be noted that significant laser power is lost due to the two vacuum windows before the laser overlaps with the ion beam as only 3 mW of beam power exits the bottom of the CTF after passing through an additional 2 vacuum windows.

The laser is externally triggered using the data acquisition computer timing card. The measured jitter between the injection timing and the firing of the laser was less than 10 ns. It should be noted, however, that this does not guarantee that the laser timing and the bunch location from injection to injection doesn't vary. A certain

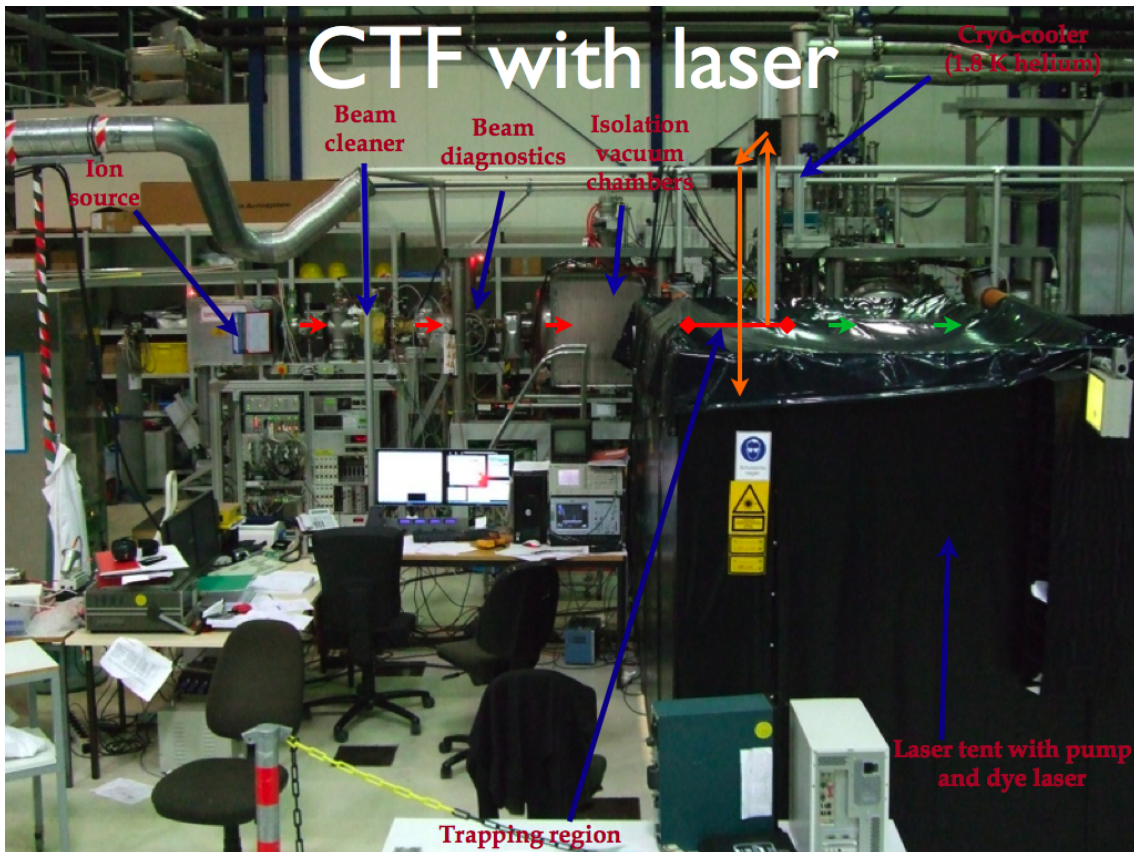


Figure 3.26: A photo of the CTF setup used to perform photo-detachment experiments.

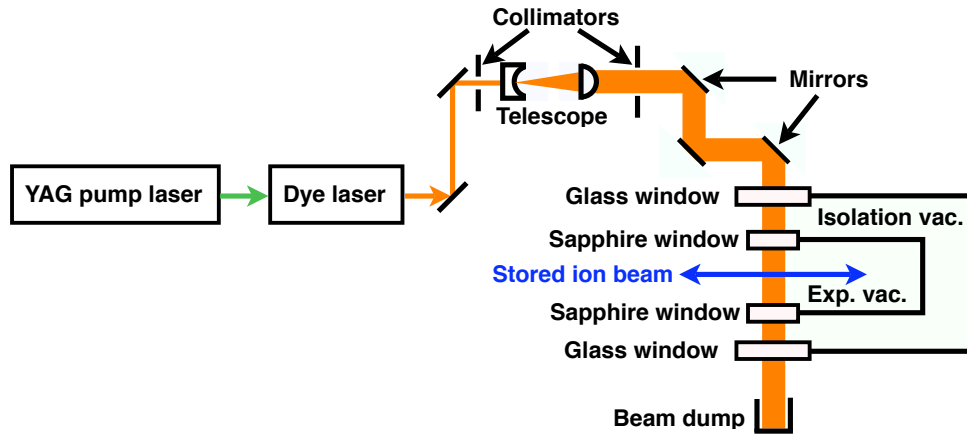


Figure 3.27: CTF laser setup schematic showing the various components used to guide the 600 nm laser beam to the stored ions.

amount of drift could conceivably occur, though the results presented here are not sensitive to such small time variations.

### 3.4 CTF driven CSR design modifications

Due to the assembly experience and initial tests performed using the CTF, the CSR design was modified to optimize the ease of assembly and alignment, maximize the effectiveness of the cooling power available for the experimental vacuum chambers, and minimize the rest-gas-density by increasing the 2 K surface area. This section will provide the justification for these modifications.

The onion-layer thermal shield design employed in the CTF was slightly modified to account for the changes detailed below as shown schematically in Fig. 3.28. The precision-aligned deflector electrodes are mechanically decoupled from the cryogenic beam-pipe and are fastened via thermal isolators to the concrete support below. The outer vacuum chamber containing the required thermal shields and cryogenic beam-pipe also rests on the concrete support. Note that the heating coils on the experimental vacuum chambers and the associated water cooling for the 80 K shields are not shown in this figure.

#### 3.4.1 Experimental chamber suspension

As described in the previous section, the two vacuum chambers containing the two halves of the trap electrodes are each supported using twelve inconel stainless steel

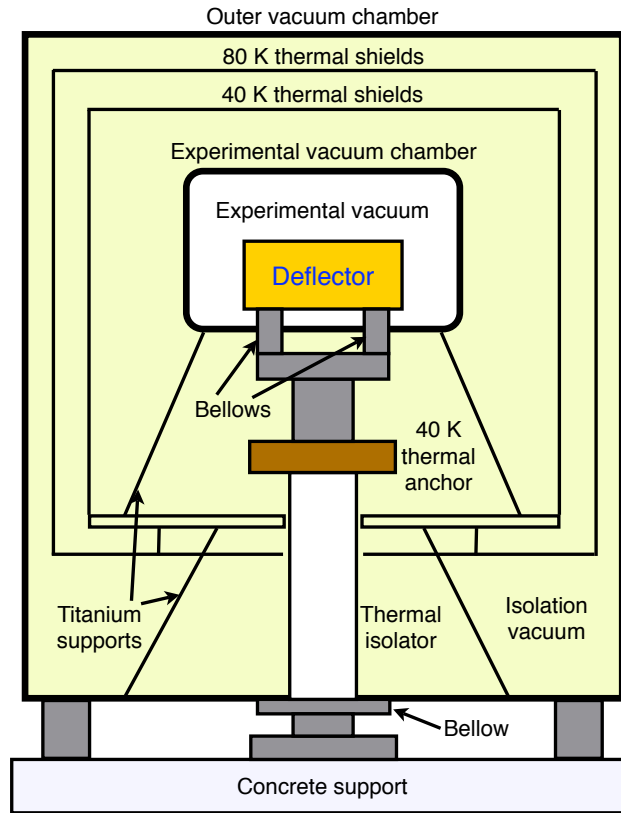


Figure 3.28: CSR cryogenic cross-section schematic, highlighting the mechanical decoupling of the electrodes from the vacuum chambers.

wires to reduce the thermal flux from the 300 K outer vacuum chambers to the 2 K region. The two halves were aligned separately before the test chamber was installed between them. This alignment process required extensive time due to the complexity of the suspension, given the number of degrees of freedom and the 24 wires. The installation of the test chamber after the alignment process was not trivial given the small tolerances and the space in which to work. Multiple installation attempts were required due to leaks in the vacuum system, making this suspension scheme unscalable and inadvisable for the larger CSR design.

The wire suspension scheme was abandoned as a result of these CTF tests, and a thermal-insulated precision suspension stand was developed to support the electrostatic elements as shown in Fig. 3.29. Using this new scheme, the position of these elements is effectively decoupled from that of the experimental vacuum chambers, allowing precision alignment while sufficiently thermally insulating all components

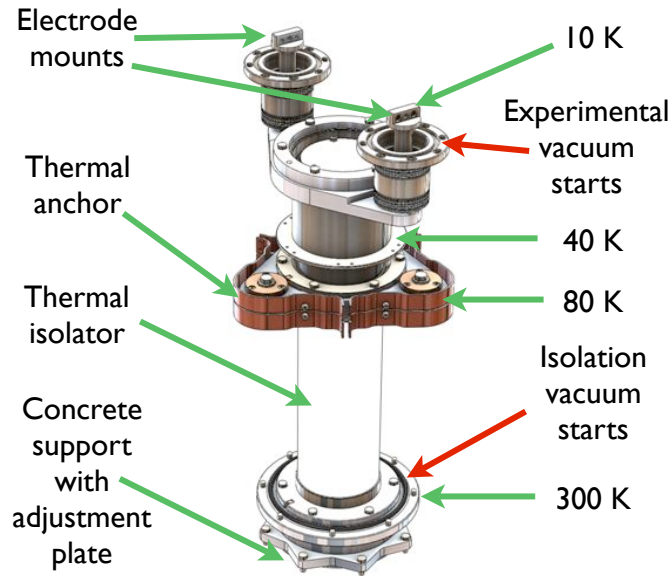


Figure 3.29: CSR precision ion optic support stand schematic.

from room-temperature.

### 3.4.2 Pumping requirements

The primary goal of the CTF was to experimentally prove that pressure on the order of  $10^{-13}$  mbar in a large volume was possible, using the developed cooling methods and techniques described above for use in the CSR. This goal was exceeded as demonstrated in Section 4.4. Due to the number of CTF apparatus changes (see Section 4.1) performed before these pressure results were produced, it cannot be conclusively proven which were essential to meet this goal. It can only be concluded that maximizing the amount of 2 K surface area and the pumping power available from the cryopumps and NEG strips to the similar proportions as employed in the CTF are necessary for the CSR. Careful construction of the injection beam line for the CSR will provide a natural advantage to limiting the amount of 300 K radiation in comparison to the CTF with two open beam lines and a much smaller surface area. Given that room-temperature operation of the CSR is also envisaged, the ring will also be bake-able. Concerning the last remaining change, namely the electrode voltage stability, most of the electrodes in the CSR will have static potentials provided by more stable power supplies. Together, this should ensure that the CSR achieves comparable rest gas densities and possibly longer storage lifetimes than the CTF.

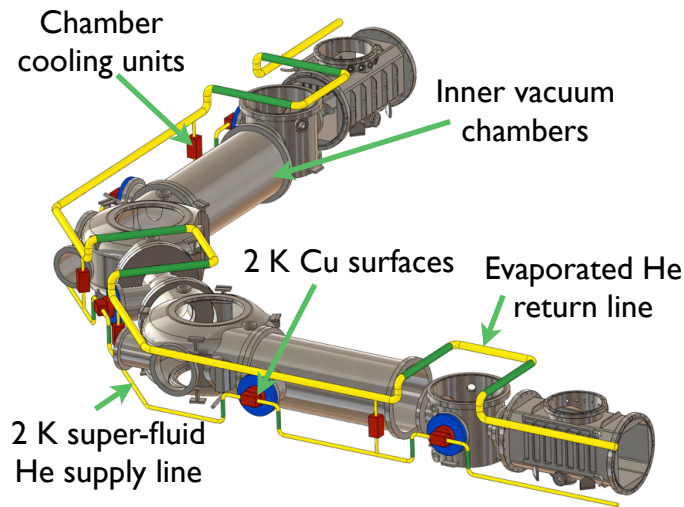


Figure 3.30: CSR pumping schematic for one corner of the ring.

A new, more flexible solution to creating the necessary 2 K surface required for pumping hydrogen was found, eliminating the need for the cooling units employed in the CTF and the adoption of the more modular and easier to construct and install 2 K copper surfaces as shown in Fig. 3.30. The adoption of this technology allows the decoupling of the cryogenic pumping requirements, where maximizing the 2 K surface area is essential for pumping hydrogen, with that of the chamber cooling. Chamber temperatures should also approach values of roughly 10 K, but separating these two requirements should facilitate hydrogen pumping optimization as well as achieving the 10 K blackbody radiation environment needed for rotational cooling of the stored ions in the CSR.

### 3.4.3 Thermal shield design

While the CTF thermal shields exceeded design specifications in terms of the achieved cryogenic temperatures (see section above), the complex design deterred the easy assembly of the shield system and made post-assembly modifications to the CTF extremely difficult and time consuming. The emphasis on making the shields as light-tight as possible to reduce the thermal influx from warmer to colder regions by making overlapping shield components is not worth the complexity and time-consuming fabrication of these components. This is particularly true given the various required holes in the shields due to the array of suspension wires.

The improvised solution of using braided copper grounding wires to transfer the

heat from the shields to the helium lines in the CTF exceeded performance expectations. Given that the shield temperatures are generally above 40 K and have rather little mass, high purity copper is not necessary for this application. The array of PT1000 temperature sensors as well as their custom mounts were quite successful and reliable in monitoring the shield temperatures both during cryogenic cooling and baking the inner chambers.

The thermal shields for the CSR, therefore, are designed to be more modular with a simpler structure to facilitate the easy fabrication, assembly, and access to the components contained within, but still based on the onion-structure used in the CTF as shown schematically in Fig. 3.28.

#### 3.4.4 Thermal conductivity and temperature sensors

The high 99.997% purity copper bands used to bring the cooling power to the experimental chambers from the two cooling units and the cooling finger are quite successful as reported in [47, 79] and described above in Section 3.1.2.

From the experience gained with the CTF, it was determined that ensuring a temperature change when cooling of less than 10 degrees per hour was not a problem; on the contrary, it was hard to achieve cooling rates of higher than 2 degrees per hour in regions not directly cooled by the cooling units or the cool finger. While the cooling speeds accelerated to between 5 to 12 degrees per hour when temperatures dropped below  $\approx 80$  K, since the thermal conductivity of the high purity copper connections dramatically increased, the cross sections of the thin stainless steel vacuum chambers posed a significant barrier. For this reason, the CSR experimental vacuum chambers employ a larger cross-section and higher overall thermal conductivity of the material by using a thin copper layer or foil along the outside of the chamber to help optimize the conduction of heat and facilitate faster cooling rates.

In regards to the temperature sensors used to monitor the experimental chamber temperatures (PT1000s, silicon diodes, and RhFe sensors), the PT1000s are generally sufficient to monitor the temperatures of the experimental chambers during both baking and cryogenic cooling. Their range and accuracy below 40 K falls dramatically, but they are still useful in determining the rate of both chamber cooling and heating throughout the majority of the required range. For absolute temperature determination, the diodes or RhFe sensors are required, but both of these are much more expensive. The silicon diodes, while slightly cheaper than the RhFe, were also extremely unreliable in the CTF setup and often experienced read-out problems. They have the disadvantage of being much more difficult to mount, where slight

movements (due to the contraction of material at cryogenic temperatures for example) can result in disrupting the signal line due to the construction of the sensors.

The CSR should be able to use PT1000 sensors as the main temperature sensors to monitor both the experimental vacuum chambers as well as the thermal shields, while a few select locations could be chosen to be monitored with RhFe sensors. This would also have the benefit of greatly reducing the pre- and post-bakeout work of dismantling thermal shields for the removal and re-installation of silicon diode sensors.

# Chapter 4

## Beam storage in a cryogenic ion trap

### 4.1 First operation of the new ion trap

After 1.5 years of assembly work, an initial investigation of the new cryogenic ion trap was performed by verifying that the trap-electrode precision alignment was maintained throughout the operational temperatures of 10 to 300 K, despite the significant contraction (e.g. stainless steel contracts by 0.3% between room-temperature and around 4 K) of the CTF components [79]. By inserting targets into both electrode stacks, the position of the electrodes was monitored over the entire temperature range. Both electrode stacks were found to have shifted laterally by 0.2 mm in the same direction, in addition to individually tilting by 0.8 mrad and 1.5 mrad, respectively. Again, given the temperature range considered here, these small changes represent a very important achievement. While numerical simulations demonstrated that the trap acceptance may have been slightly effected, subsequent cryogenic ion trapping after this commissioning test proved that this was not a problem. The cryogenic temperature distribution of the various cryogenic beam-pipe vacuum chambers was also monitored during this first cool-down, in addition to those of the thermal shields [79]. The middle chamber of the beam-pipe was not yet installed so that the beam-pipe was open to the insulation vacuum since the electrode position had to be measured. After this first test, the middle chamber between the ion mirror stacks was installed, preventing further observation of the trap electrodes. Improvements to the cryogenic thermal conduction along the beam-pipe were also installed. The first successful trapping using  $\text{N}_2^+$  ions at a typical trap energy of 4.2 keV was achieved at room-temperature (see Fig. 4.1), demonstrating rest-gas-density limited lifetimes on the order of 30 ms, which is typical for pressures in the  $10^{-8}$  mbar range. A clear

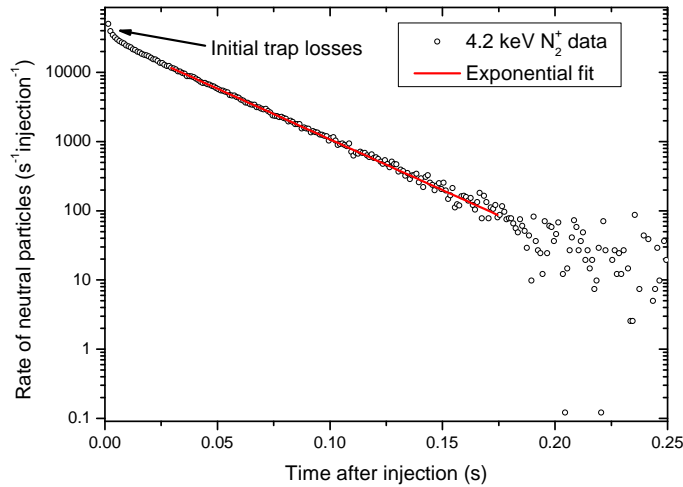


Figure 4.1: Count rate of neutral products escaping the CTF showing the decrease in the number of stored ions for a 4.2 keV  $\text{N}_2^+$  beam at room-temperature. This yields an exponential lifetime around 30 ms at a trap pressure of  $4 \cdot 10^{-8}$  mbar. A detector background rate of  $150 (\text{s} \cdot \text{injection})^{-1}$  has been subtracted.

exponential decay can be seen in addition to initial losses which cannot be clearly studied in room-temperature electrostatic ion beam traps (EIBTs). After this was demonstrated, a one-week cool-down process with two separated vacuum regions was performed. Vacuum leaks between the experimental and isolation vacuum regions became apparent at cryogenic temperatures and after warming up the system (which also takes a week), the middle chamber was dismantled and reinstalled.

A third cool-down process confirmed that no detectable leaks were present and the first trapping characterization measurements at cold temperatures were done. Most notably, the beam energy was varied to determine the relative contribution of trap losses from the two main processes: electron capture and multiple scattering. The first observations that the measured 17 s exponential decay lifetimes at cryogenic temperatures were being limited by a non-rest gas dependent component were noted. Later analysis of this data taken with pre-baked vacuum chambers at cryogenic temperatures yielded vacuum pressures roughly on the order of  $10^{-12}$  mbar. These results are summarized in [47].

Multiple changes to the CTF then occurred simultaneously in an attempt to extend the relatively short 17 s lifetimes to lifetimes on the order of 1000 s, as expected at the rest gas densities required for CSR operation. The HV switch voltage stability was improved since small voltage fluctuations caused by the HV switches were noticed. These were transmitted to one side of the electrostatic mirror, which could result in reduced ion storage time. A jitter was artificially applied to various electrodes to

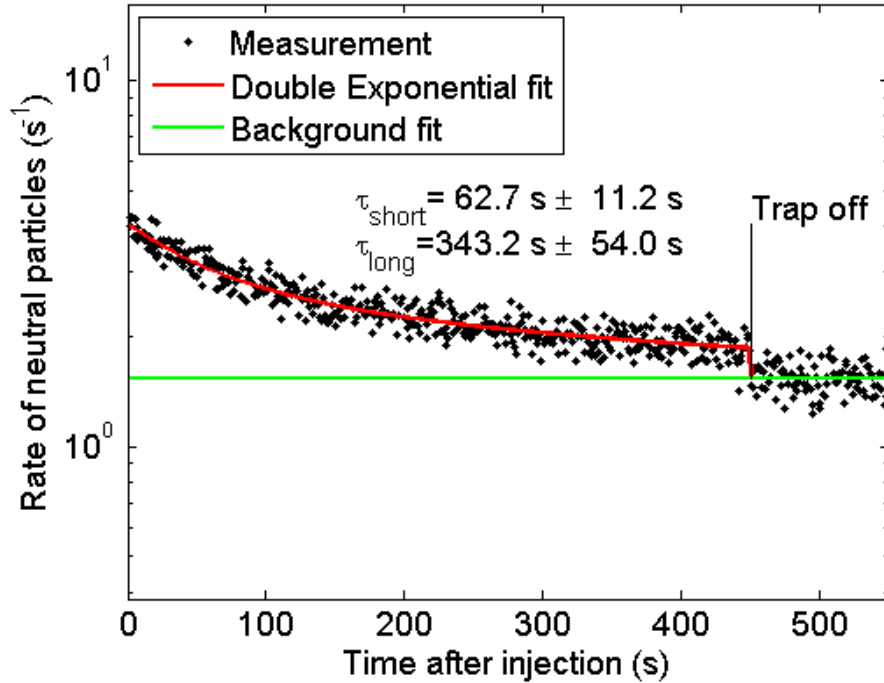


Figure 4.2: A lifetime measurement of the neutral particles produced by electron capture from trapped 7.1 keV  $\text{N}_2^+$  ions at liquid helium temperatures in the CTF.

try and re-simulate the electrode voltage variations after these modifications were completed to determine if the lifetime would be effected, but no change was observed. The amount of open 2 K surface area was increased inside the trap by removing some of the NEG strips which were covering the experimental vacuum sides of the cooling unit between the trap and pumping chamber, and hence may have been reducing the amount of  $\text{H}_2$  pumped by these surfaces. The amount of 300 K radiation entering along the beam axis was reduced by installing long copper pipes with a smaller inner diameter than the beam-pipe on both the entry and exit sides of the CTF. Both were thermally anchored to the cryogenic beam-pipe and the inner surface was oxidized to efficiently absorb entering radiation. Additionally, the cryopump was disconnected from the cold head and connected to the 5 K helium line. This prevents room-temperature operation of the cryopump, but facilitates a lower pump temperature and therefore increased pumping speed and improved base pressure. Finally, the bakeout of the cryogenic beam-pipe to 600 K was completed. This unfortunately led to leaks in multiple feedthroughs and a window, which was confirmed after cooling back down to room-temperature. These pieces were replaced and the bakeout procedure was repeated. After confirming that no detectable leaks were present, the

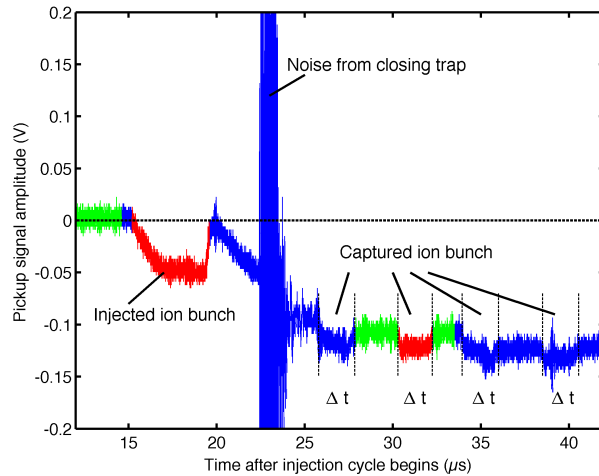


Figure 4.3: Sample 7.1 keV  $N_2^+$  pre-amplified pulse as seen on the pickup electrodes with an oscilloscope plotted vs time after the beam cleaner was pulsed, whereby an ion bunch was injected. The ion pulse, followed by noise from the HV electrodes switching, and the subsequent trapping of the bunch can be seen.

CTF was once again cooled to cryogenic temperatures. Only at this point, were exponential decay lifetimes on the order of hundreds of seconds achieved, as shown in Fig. 4.2.

In the first set of experiments, both at room-temperature and at cryogenic temperatures, 7.1 keV  $N_2^+$  ions were stored in the CTF and the ion bunch was observed using the ring (SUM) pickup electrode located in the test chamber between the electrostatic mirrors (see Section 3.1.6). The beam current measured on the Faraday cup in the beam cleaner was  $1.75 \mu\text{A}$ . In Fig. 4.3, the initial injected  $4.7 \mu\text{s}$  ion pulse (created using a  $7 \mu\text{s}$  beam cleaner pulse) can clearly be seen at times between 15-20  $\mu\text{s}$ , followed shortly after by the noise caused by the electrodes switching (at 22.5  $\mu\text{s}$ ), when the trap was closed after the bunch was reflected and was again passing through the pickup. The ion bunch with a length of  $\Delta t = 2.05 \mu\text{s}$  was visible over many oscillations as shown in Fig. 4.3. The background length is not always the same length as the pickup is not located in the middle of the trap, but slightly to one side, resulting in the two different background periods between the bunch. The pickup signal after the closing of the trap can also be used to determine the trapping efficiency at these particular settings. The integral of the two signal regions (illustrated in red) before and after closing the trap with respect to background was calculated. These integrals are proportional to the amount of charge passing through the pickup, the ratio of which yields a trapping efficiency of 12%.

#### 4.1. First operation of the new ion trap

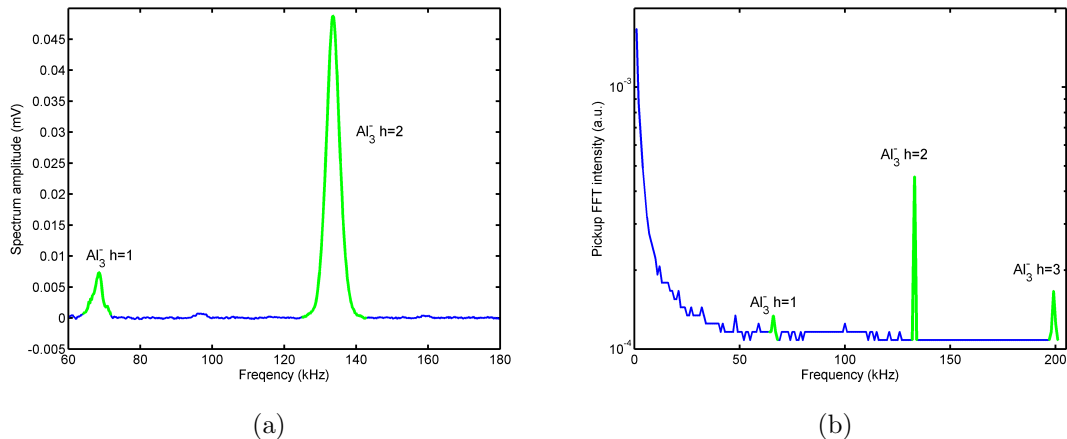


Figure 4.4: (a) Spectrum analyzer sweep (70 ms sweep time, 3 kHz resolution bandwidth) and (b) FFT spectrum (10 to 100 ms integration time) showing the ground and higher harmonic ( $h = 2,3$ ) frequency peaks due to 6.0 keV  $\text{Al}_3^-$  ions at a trap temperature of 92 K. The peaks referred to in both plots are illustrated in thick green lines for clarity.

By feeding this pickup signal to a spectrum analyzer, a frequency spectrum was scanned, typically using a 70 ms sweep time and a resolution bandwidth of 3 kHz. The relative amplitudes of the different ion bunch frequencies, corresponding to different ion bunches oscillating within the trap was investigated, as shown in Fig. 4.4 for a beam of  $\text{Al}_3^-$ . An FFT of the pickup signal using the oscilloscope with an integration time of 10 to 100 ms was also saved, though at a lower resolution than was visible on the scope, showing equivalent results. The spectrum analyzer sweep, therefore, was primarily used to determine the relative abundances of the ions in the trap.

Using only a Penning source with nitrogen gas, and having closed the trap well after  $\text{N}^+$  had left, only the expected oscillation frequency from 7.1 keV  $\text{N}_2^+$  was observed via the spectrum analyzer. By setting the observed frequency to the second harmonic frequency of the ions (246 kHz), the signal amplitude of this frequency could be observed as a function of time. As the acquired resolution bandwidth was 3000 Hz, the peaks were rather broad. Any possible small frequency shifts due to, for example slight energy loss of ions via the induced current produced on the pickup electrode, can be neglected. This procedure was used to study the bunching of the stored ions as described in the following sections. The CTF oscillation frequencies for the various ion species at 6.0 keV presented within this work are listed in Table 4.1.

After all of the changes listed above were completed, the CTF was again cooled with 1.8 K superfluid helium and using a 7.1 keV  $\text{N}_2^+$  ion beam, achieved beam

Table 4.1: Table of employed CTF ion oscillation frequencies and harmonics at 6.0 keV. All ions except  $N_2^+$  were produced by the sputter source.

Ion species	Mass (amu)	Frequency (kHz)		
		Oscillation Freq.	2 <sup>nd</sup> harmonic	3 <sup>rd</sup> harmonic
O <sup>-</sup>	16.00	149.33	298.7	448.0
Al <sup>-</sup>	26.98	114.99	230.0	243.9
Al <sub>2</sub> <sup>-</sup>	53.96	81.31	162.6	199.2
Al <sub>3</sub> <sup>-</sup>	80.94	66.39	132.8	172.4
Al <sub>4</sub> <sup>-</sup>	107.93	57.48	115.0	154.3
Al <sub>5</sub> <sup>-</sup>	134.91	51.43	102.9	140.8
Al <sub>6</sub> <sup>-</sup>	161.89	46.94	93.9	130.4
Al <sub>7</sub> <sup>-</sup>	188.87	43.46	86.9	122.0
Al <sub>8</sub> <sup>-</sup>	215.85	40.66	81.3	122.0
AlO <sup>-</sup>	42.98	91.11	182.2	273.3
Al <sub>2</sub> O <sup>-</sup>	69.96	71.41	142.8	214.2
Al <sub>3</sub> O <sup>-</sup>	96.94	60.66	121.3	182.0
Al <sub>4</sub> O <sup>-</sup>	123.93	53.66	107.3	161.0
Al <sub>5</sub> O <sup>-</sup>	150.91	48.62	97.2	145.9
Al <sub>6</sub> O <sup>-</sup>	177.89	44.78	89.6	134.4
Al <sub>7</sub> O <sup>-</sup>	204.87	41.73	83.5	125.2
N <sub>2</sub> <sup>+</sup>	28.0	112.88	225.8	338.6

lifetimes of over 300 s, as shown in Fig. 4.2. In comparison to the room-temperature results shown in Fig. 4.1, the lifetimes were extended from 30 ms by four orders of magnitude.

## 4.2 Self-bunched ions and ions oscillating in a cryogenic trap

### 4.2.1 Extended self-bunching observation

The self-bunching trapping mode that has been observed before in EIBTs refers to trapping potentials where an injected bunch stays together, or a bunch is formed after injection and remains coherently together over a long time, as described previously in Section 2.4. A similar effect has also been observed very recently in storage rings (see [57] and the references contained within). Previous EIBTs at room-temperature have observed this effect for durations of around 90 ms [80] with Ar<sup>+</sup>

#### 4.2. Self-bunched ions and ions oscillating in a cryogenic trap

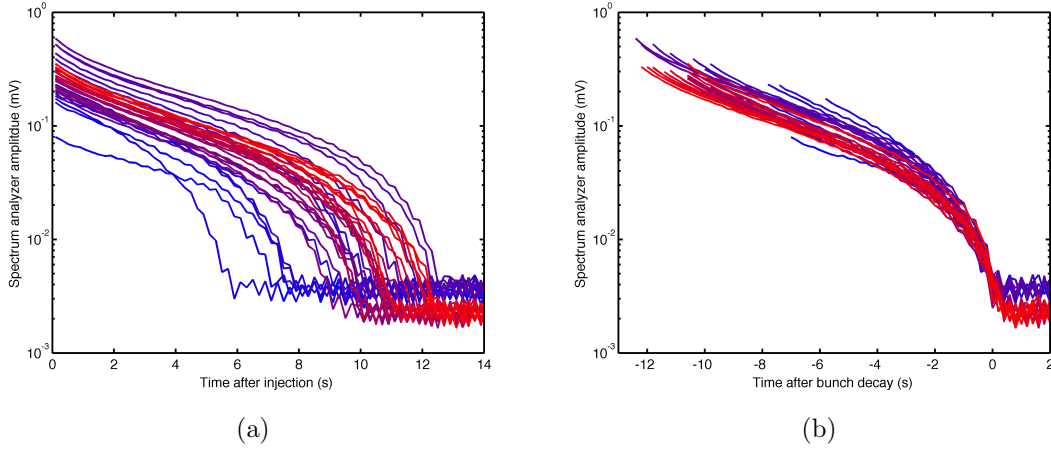


Figure 4.5: Spectrum analyzer frequency amplitude (246 kHz) of trapped  $N_2^+$  ion bunches vs (a) injection time and (b) time after bunch decay. Multiple injections are superimposed.

at 4.2 keV, being most likely limited by the short beam lifetime, which makes it extremely difficult to distinguish between beam loss and bunch decay. Due to the vacuum levels in these previous experiments, extended studies of the bunch were not possible since the ion loss rates were too high. In addition, any initial variation that could have been studied would have required a clear understanding of trap losses, particularly at short time periods right after injection where previous non-linear trap losses were typically observed. The properties of the bunch, therefore, could not be as clearly understood or measured over significant times at room-temperature.

The CTF, however, when operated at cryogenic temperatures, drastically reduces rest gas collisions by reducing pressures to the  $10^{-14}$  mbar range (see Section 4.4), thereby disentangling beam and ion bunch losses for the first time. Given these new self-bunching measurement possibilities, new effects and aspects are expected to be found. Plotting the oscillation frequency amplitude of 7.1 keV  $N_2^+$  in the CTF (at 246 kHz with a resolution bandwidth of 3 kHz) as a function of time after injection yields Fig. 4.5(a). Here the spectrum analyzer's digitized output has been converted into dB, then taking note of the reference level, further converted into a voltage.

Multiple injections have been plotted together demonstrating the comparatively long persistence of the bunch signal (longer than 10 s) with respect to the previously published results of 90 to 100 ms [49, 80]. This is a bunch duration extension by two orders of magnitude, which corresponds to extending the number of revolutions in the trap from tens of thousands to around 1.5 million oscillations. With these increased number of oscillations, the CTF self-bunching measurements were far more

sensitive to any effects that adversely affected the ion bunch. It should be noted that while the ion bunch signal vanished after approximately 10 s, the measured lifetime of the ions in the trap at these pressures ( $10^{-14}$  mbar) was several hundred seconds. The bunch, therefore, eventually dispersed, filling up the longitudinal phase space of the trap so that it was no longer visible using the pickup electrode. Fig. 4.5(a) demonstrates that the number of initially trapped ions significantly varied between injections, and that this also corresponded to a variation in bunch duration. Plotting the same data, but now with respect to the time when the bunch decayed as defined by when the signal amplitude decreases to a value of 5 mV (a factor of 1.6 higher than the background), yields Fig. 4.5(b). It should be recalled that the ions are still trapped, but not in a coherent bunch.

A calibration of the observed spectrum analyzer voltage was possible by comparing it to the absolute pickup voltage of the initially trapped bunch. For each injection, the corresponding trace of an oscilloscope connected to the pickup was also saved (see sample above in Fig. 4.3). The induced voltage drop,  $U$ , caused by the ions passing through the CTF pickup can be transformed into the ion current,  $I$ , via

$$I = \frac{C v U}{A L}, \quad (4.1)$$

where  $C$  is the combined capacity of the electrodes, cables, and amplifier,  $A$  is the amplification factor provided by the amplifier,  $L$  is the length of the pickup electrode, and  $v$  is the velocity of the ions [57]. Despite the spread of the data points, it was assumed that the ion current in the trap scales linearly with the spectrum analyzer amplitude and that the data is far enough away from the origin to avoid any deviations. The linear fit yields a calibration with the slope =  $2.8 \pm 0.5 \cdot 10^{-3}$  A/V.

Given that only singly charged  $N_2^+$  was trapped, the number of ions  $N_{ions}$  can be calculated via

$$N_{ions} = \frac{I t_{pl}}{e}, \quad (4.2)$$

where  $I$  is the ion current,  $t_{pl}$  is the pulse length, and  $e$  is the elementary charge. Plotting the spectrum analyzer voltage as a function of the captured ion current determined from the oscilloscope trace yields Fig. 4.6. Using the effective ion bunch pulse length of  $2.05 \mu\text{s}$  in conjunction with the calibration above permits the plotting of the number of ions in the bunch as a function of storage time (see Fig. 4.7(a)). The bunch was defined to begin decaying when the curve deviated from the exhibited bunch exponential decay by 20% (see Fig. 4.8(a) in the following bunch lifetime section). The number of ions at this point was averaged for all  $N_2^+$  data sets, where the error from the calibration and the statistical spread were added in quadrature, yielding a value of  $N_{cr} = 1.1 \pm 0.3$  million ions. At this critical number of ions  $N_{cr}$ ,

#### 4.2. Self-bunched ions and ions oscillating in a cryogenic trap

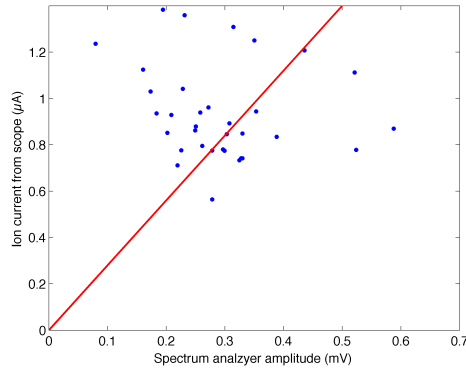


Figure 4.6: Injected ion current vs spectrum analyzer signal calibration.

the self-bunching effect was disrupted and the bunch quickly decayed.

Using the spectrum analyzer calibration from  $N_2^+$ , the same procedure was applied to self-bunching data from  $6.0\text{ keV Al}_2^-$  as shown in Fig. 4.7(b). A beam cleaner pulse length of  $9\ \mu\text{s}$  was used, while switching the electrodes  $30\ \mu\text{s}$  after the beam cleaner pulse started. An effective ion pulse length of  $4.0\ \mu\text{s}$  was used given the longer injected pulse length in comparison to that used for  $N_2^+$ . As the background was slightly lower for these measurements, the bunch was defined as decayed at voltages less than  $1\ \text{mV}$ . The number of  $\text{Al}_2^-$  ions required to sustain the bunch as defined by a 20% deviation from the exponential bunch decay (see Fig. 4.8(b) in the following bunch lifetime section) was given by  $N_{cr} = 3.0 \pm 0.7$  million ions.

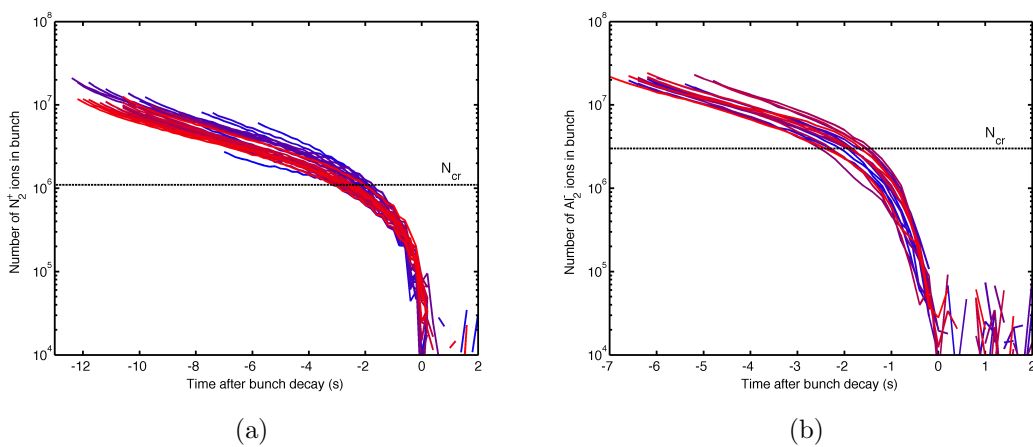


Figure 4.7: Number of bunched (a)  $N_2^+$  and (b)  $\text{Al}_2^-$  ions in self-bunching mode plotted with respect to bunch decay time as derived from the calibration of Fig. 4.5(b).

Both the ion bunch data from  $N_2^+$  and  $Al_2^-$  demonstrate that at a certain point, the ion bunch no longer had a high enough charge density to maintain itself, which was followed by its quick decay. A study of the duration and lifetime of the bunch follows in Section 4.2.2. These observations provide the first experimental confirmation of the idea that self-bunching requires a minimum number of ions to be maintained, as proposed in previous theory papers [55, 81].

The first theoretical paper considers a particle located inside a homogeneously charged sphere (the bunch) oscillating in a simple one dimensional potential, yielding Eq. 2.25 (Section 2.4) as the minimum charge density required for a stable bunch [53]. A ratio of the minimum charge density required for 7.1 keV  $N_2^+$  ions to that from 6.0 keV  $Al_2^-$  anions was derived. Assuming that the differential  $dT/d|P_0|$  is the same for both experiments, the ratio reduces to a number less than one (0.7) multiplied by the squares of the  $N_2^+$  charge sphere radius over that from  $Al_2^-$ . There is no reason to expect that the charge radius from  $N_2^+$  would be larger than that from  $Al_2^-$ , resulting in a value less than one.

The second theoretical model is still a one dimensional model, but does not assume that the bunch remains spherical [55]. When the same ratio is calculated using this model (equation 2.27), assuming the spatial dispersion of the bunch, beam diameter, and bunch length are comparable (i.e.  $\mathcal{I}$  and  $\Delta T_i$  both cancel), the ratio reduces to a slightly smaller value of 0.6. While both models are one dimensional, the second one attempts to account for more realistic ion paths, which do not oscillate along the trap axis, but along paths with slight offsets from the axis and a small velocity component perpendicular to the trap axis, by inserting an additional parameter to try and account for these path differences.

Both of these theoretical models directly contradict the experimental observations above, where  $Al_2^-$  bunches appeared to require *more* charges than  $N_2^+$ , yielding a ratio of  $2.7 \pm 1.0$  (where the errors have been added in quadrature). This particular EIBT trapping phenomenon needs to be more thoroughly explored using the same ion species at various different energies in addition to different masses at the same energy to elucidate the relationship between these factors and assist in the development of a model to describe bunch dynamics inside an EIBT. The crossed laser and ion beam geometry coupled with the CTF's extreme vacuum could also be employed to directly measure the width and length of the bunch in the field-free region, to determine whether the second model's finding (that the bunch is not spherical in the middle of the trap) is correct or if the first, simpler model was correct.

## 4.2. Self-bunched ions and ions oscillating in a cryogenic trap

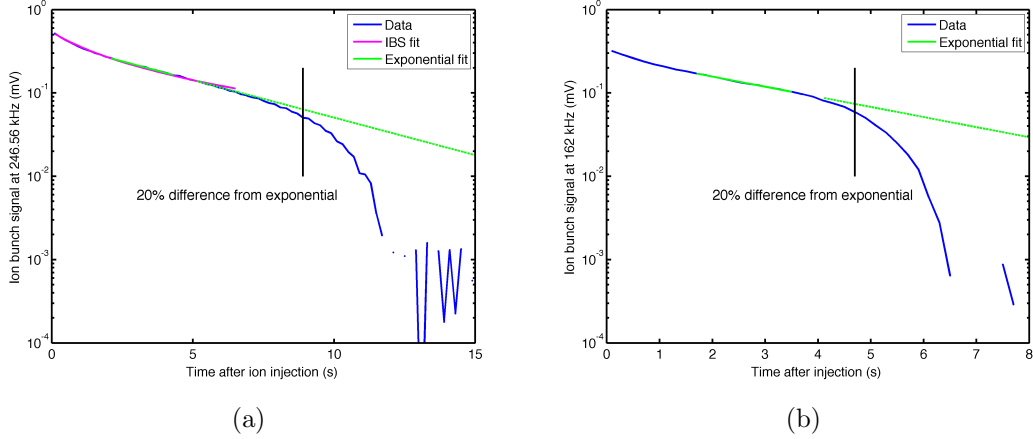


Figure 4.8: Sample 7.1 keV  $N_2^+$  (a) and 6.0 keV  $Al_2^-$  (b) ion bunch decay curves fitted by an exponential decay. Intrabeam scattering was taken into account to model the initial faster decays of  $N_2^+$ .

### 4.2.2 Self-bunching decay lifetimes

Since the main ion loss mechanism, namely collisions with rest gas, has been vastly reduced in the CTFs unprecedented trap vacuum, processes such as the de-coherence of the ion bunch in the trap can be studied in much more detail. In particular, details of self-bunching and RF bunching can be studied over very long time scales.

While previous similar traps have observed self-bunching for 90 ms [80] or 100 ms [49], the CTF has observed this behaviour for over 10 s, as shown above in Section 4.2.1 and in Fig. 4.8(a). This observation alone demonstrates that self-bunching is stable in time scales two orders of magnitude longer than previously observed. At CTF pressures, however, it was possible to measure differences between individual bunches from injection to injection. A 7.1 keV  $N_2^+$  bunch will be considered first. As shown in Fig. 4.9(a), a background-subtracted signal was fitted with a single exponential after the initial faster decay of the bunch at the beginning, but many seconds before the bunch quickly decayed.

The faster initial decay also seemed to vary as a function of ion bunch intensity. Given that the number of charges was determined via the calibration above, the initial decay (first 2 s) was modeled including the effects of intrabeam scattering (see Eq. 2.15 in Section 2.2.4). The rate  $R$  was taken as proportional to the number of ions and fit to the data, assuming that the ions were scattered out of the bunch. While the curves appeared to be accurately reproduced (see the magenta IBS curve in Fig. 4.8(a)), the constant  $c_1$  should equal the number of ions in the trap  $N$  multiplied by a constant  $\alpha$  that includes various other factors described earlier in Section 2.2.4.

As shown in Fig. 4.10, however, it was not possible to correlate the initial number of ions  $N_0$  with the intrabeam scattering constant  $c_1$ .

The procedure above was repeated for 6.0 keV  $\text{Al}_2^-$  bunches, as shown in Fig. 4.8(b). The early region of the bunch decay was again fitted with an exponential lifetime. Plotting the fitted lifetimes vs the number of initial stored ions again yields a spread of lifetimes as plotted in Fig. 4.9(b).

While the range of both the number of ions and the decay duration is small, a large number of ions is not exclusively associated with a short decay time. Further studies covering a larger range of stored ions should be able to more easily determine any present trends. The ion bunch lifetimes are on the order of a few seconds, which is two orders of magnitude less than the decay lifetime of ions in the trap observed with the MCP ( $> 300$  s). This indicates that the bunch stability is not be limited by the rest gas pressure, or the unidentified loss mechanism preventing storage lifetimes above roughly 300 s in the trap. It is particularly noteworthy that the fitted  $\text{Al}_2^-$  bunch lifetimes are almost a factor of two smaller than those produced by  $\text{N}_2^+$ . The aluminum cluster experiments, while carried out at a later time period, had comparable trap temperatures and pressure. The trap was not warmed-up between these measurement periods, so trap alignment and position were also constant. The only differences between these two studies were the number of trapped ions, their mass/velocity, their kinetic energy, and the ion source dependent energy spread of the produced ion beam.

A dependency on the kinetic energy seems unlikely, since rest gas losses are so

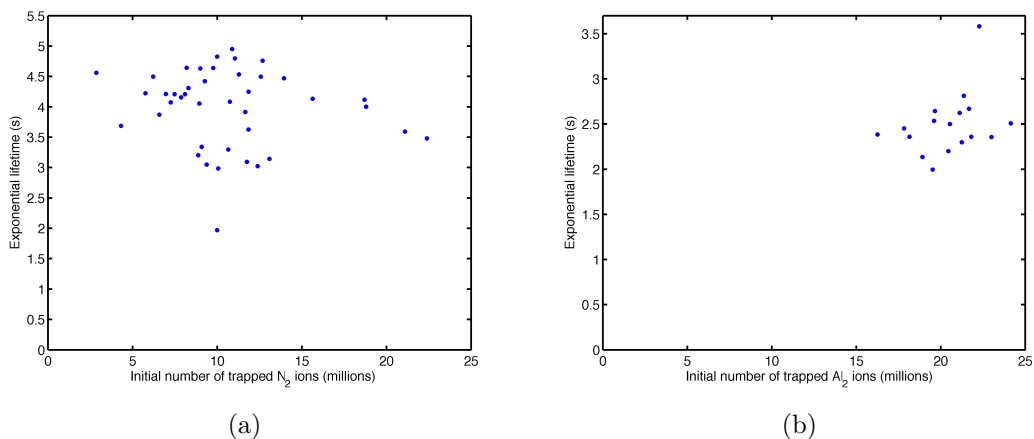


Figure 4.9: Exponential bunch lifetime vs number of initially stored for (a)  $\text{N}_2^+$  and (b)  $\text{Al}_2^-$  ions. A larger range of initially stored ions is required to understand the dependence of the bunch lifetime.

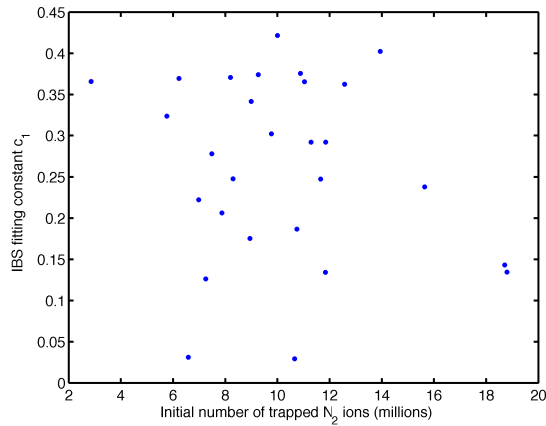


Figure 4.10: Intrabeam scattering fitting results using equation 2.15 for measurements on  $N_2^+$ . No clear linear dependence of the fitting constant was observed, which would be expected if intrabeam scattering was present.

greatly reduced that small differences in collisional cross-sections caused by energy and the ionic species should be negligible. Similarly, differences in mass and velocity are also typically associated with ion loss from the trap, which has been very successfully suppressed. Given that a sputter source produces ions with a narrower energy distribution than a penning source, it is strange that  $Al_2^-$  ion bunches would dissipate faster since they should remain coherent for longer time periods, even without self-bunching, due to smaller energy differences. A dependency on the number of ions, and the resulting ion bunch size and shape is most likely cause for the differences observed in the exponential lifetimes of  $N_2^+$  and  $Al_2^-$ . While self-bunching ensures the ions are localized in the bunch longitudinally (along the trap axis), the space charge of the bunch will also cause the beam to grow transversally over time. The focussing potential of the trap partly counteracts this, but the bunch lifetime observed here could be the result of this particular change of bunch shape as a function of trapping time. Future studies should attempt to determine the loss mechanism leading to the depopulation of the bunch, and ultimately, the breakup of the bunch at a minimum number of charges by covering a larger range of initially captured ions. Quickly dropping the exit-side electrostatic mirror voltages would allow the imaging of the beam on the MCP behind the CTF. This could also be useful in determining the bunch shape as a function of time.

### 4.2.3 RF Bunching

Just as the trap potentials can be tuned to induce self-bunching, an externally supplied radio frequency can also be used to force the ions to remain together in a bunch.

In the CTF,  $10 V_{pp}$  radio frequency at 113.05 kHz was applied to the exit-side einzel lens trap electrode B. This ensured that ions traveling faster than the bunch would be decelerated and conversely, ions traveling slower than the bunch would be accelerated, thereby actively supporting the creation and duration of a single stored ion bunch. The voltage amplitude was chosen by roughly trying a range of values to determine when the ions were affected. A systematic study of these voltages and any possible bunch lifetime dependency has not yet been completed with the CTF.

As shown in Fig.4.11, RF bunching does not require the presence of an initial bunch in order to function properly. The intensity of the ion bunch signal at 246.3 kHz (the second harmonic of the trap oscillation frequency for  $N_2^+$ ) versus time shows that the initial 7.1 keV  $N_2^+$  ion bunch decays after around 10 s, even in the self-bunching trapping mode. The bunch, however, is readily revived a few seconds later when the RF-bunching is turned on. The effect is dramatic since the bunch is immediately formed again, albeit at a lower intensity, but with a longer lifetime than that from self-bunching alone.

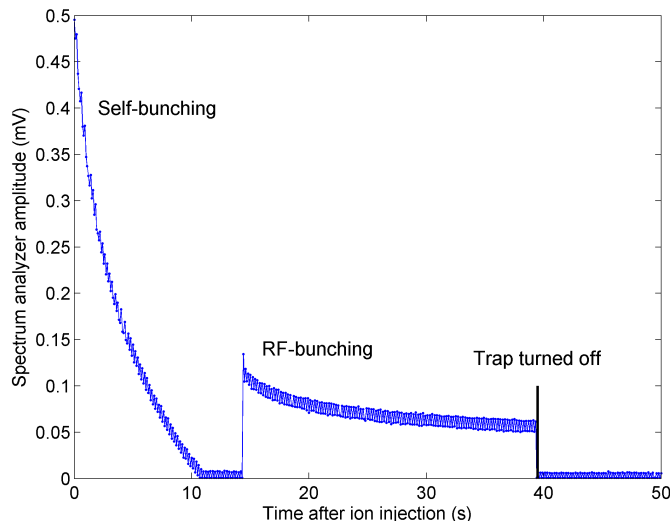


Figure 4.11: Spectrum analyzer frequency amplitude (at 246.3 kHz) is potted as a function of time after injection. Demonstration of  $N_2^+$  re-bunching using RF after bunch has dispersed.

## 4.2. Self-bunched ions and ions oscillating in a cryogenic trap

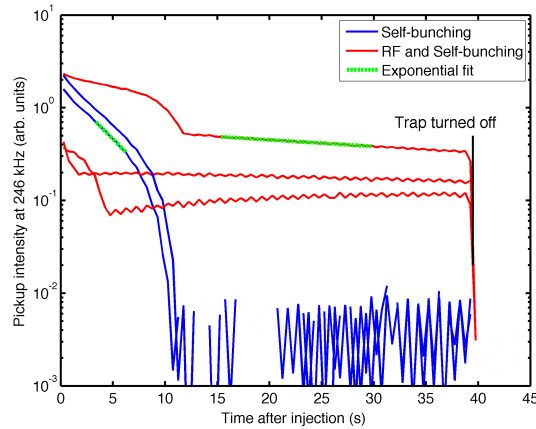


Figure 4.12: Ion bunch signal intensity plotted for ions stored in self-bunching mode with (red) and without (blue) RF bunching. Three arbitrary injections chosen with RF bunching without phase control. The dotted green lines show the two regions fitted by an exponential decay to compare lifetimes.

When the RF was applied continuously, the bunch remained together for much longer times than a bunch supported by self-bunching alone (see Fig. 4.12). In this figure, self-bunching yields exponential bunch lifetimes of 4 s (dotted green portion of the lower blue curve), whereas the addition of RF increased this by over an order of magnitude to 64 s (dotted green portion of the upper red curve).

It can be seen in Fig. 4.12 that for continuously applied RF, the initial seconds of the signal after injection are not reproducible. As no attempt was made to synchronize the RF with the injected ion pulse in this measurement, the relative phase between them was random. The influence of the relative phase was investigated by triggering the RF function generator before the ions entered the trap, thus defining the relative phase between the ion bunch and the RF phase. The initial 5 s of these curves were investigated in detail. As examples, Fig. 4.13 shows three reproducible curves with relative RF phases of  $40^\circ$ ,  $80^\circ$ , and  $180^\circ$  with respect to the injected bunch. By repeating this for various phases, each time taking multiple injections and averaging the results for each phase, a pattern becomes apparent both in the amplitude of the exponential bunch decay (Fig. 4.14(a)), as well as in the mean lifetime (Fig. 4.14(b)).

While beam decay measurements demonstrated exponential lifetimes of over 300 s (see Section 4.1), lifetime measurements performed on the ion bunch itself while applying RF bunching only approached such high values. While bunch lifetimes of 300 s were not observed, they could be extended from self-bunching lifetimes of a few seconds to 100 s by using an additional RF to maintain the bunch. The pickup

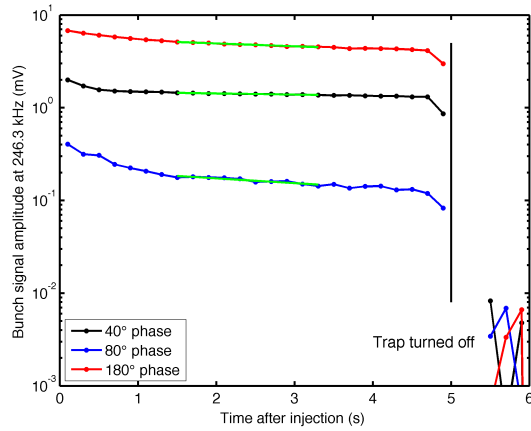


Figure 4.13: Initial pickup signals as a function of storage time for three well-defined relative phases between RF and the injected ion pulse. The trap was switched off after 5 s.

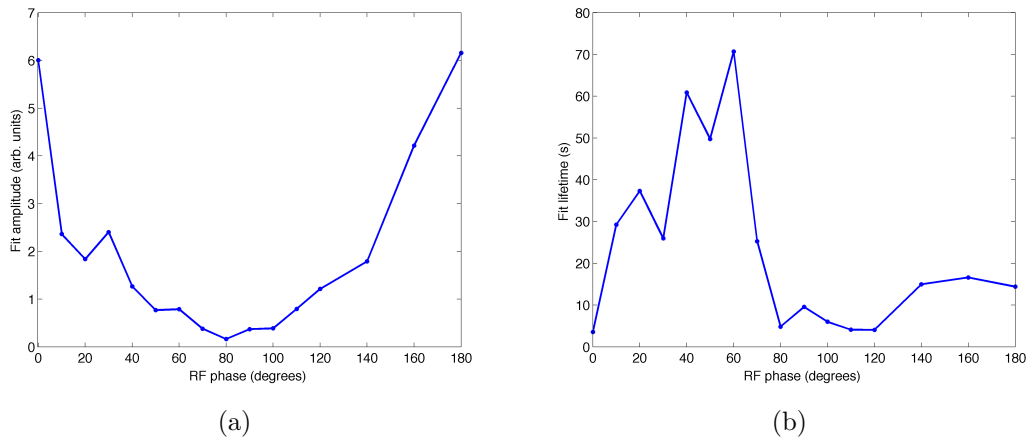


Figure 4.14: Amplitude (a) and lifetime (b) of the pickup signal for an RF-bunched beam vs RF bunching phase.

signals displayed in Fig. 4.15 were recorded with 6.0 keV  $2 \mu\text{A}$ ,  $\text{N}_2^+$  ions using a beam cleaner pulse of  $7 \mu\text{s}$  with RF bunching (113.05 kHz at  $10 \text{ V}_{pp}$ ) and storage times of 600 s. Two sample injections have been plotted, which display different numbers of initially trapped ions. Note that the frequency beating structure superimposed on the bunch decay is an instrumental effect, since they occur both when the trap is filled and empty. As the bunch is observed non-destructively and the pickup signal is proportional to the stored ion current, the measured lifetime is sensitive to all particle loss processes. It is curious to note the difference in shape between the two

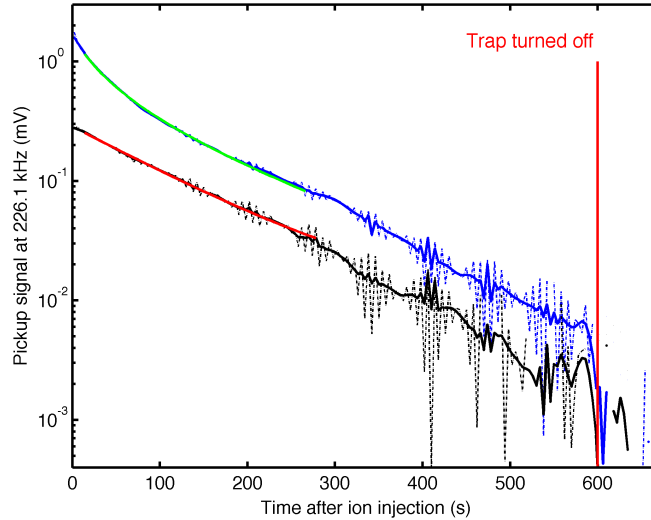


Figure 4.15: 6.0 keV  $N_2^+$  ion bunch signal amplitude stored in self-bunching mode with applied RF. The trap was turned off after 600 s and an exponential fit (displayed in red) has been plotted for the lower curve. The observed oscillatory behaviour was an instrumental artifact.

curves in Fig. 4.15 at short times. The accelerated loss visible only in the injection with the higher number of trapped ions could be the result of intrabeam scattering. Indeed, using equation 2.15, which accounts for this loss process, can reproduce the observed ion bunch decay curve extremely well, as shown by the green curve in Fig. 4.15 with an exponential bunch lifetime of  $170 \pm 10$  s. This value, however, doesn't agree with a single exponential fit of the same region (excluding the initial fast decay), which yields a lifetime of  $120 \pm 10$  s. The black-coloured lower intensity curve also exhibits a similar bunch lifetime. Additional curves are required for absolute proof that intrabeam scattering is responsible for the observed trend, but other known loss mechanisms cannot explain the observed accelerated loss within the first 100 s, particularly its apparent dependence on the number of stored ions. The slight bend in both decay curves at time periods just before 300 s has not yet been explained.

The exponential lifetimes of  $120 \pm 10$  s fitted to both of the ion bunches in Fig. 4.15 in comparison to the lifetime from Fig. 4.2 suggest that an additional loss process affects the bunch. Ion loss from the trap due to collisions with rest gas collisions alone would result in ion lifetimes orders of magnitude longer. The undefined loss process leading to lifetimes of over 300 s (as measured on the neutral detector) are slightly longer than those seen by observing the bunch, but they are in the same

order of magnitude. This is not proof that this loss process is responsible for both the decay of the bunches and that of the beam itself, but it is a possibility which needs to be explored further. As longer bunch lifetimes were demonstrated using RF bunching, this provides clear confirmation that the normal self-bunching lifetime is not pressure dependent. The proposed explanation to account for the differences in bunch lifetimes for two different ion species could also explain the bunch loss mechanism observed in the decay of RF enhanced bunches: not just the number of ions in the bunch, but its shape as well. A combination of future laser measurements mapping out the position and shape of the bunch as a function of the number of stored ions appears feasible for more closely investigating this possibility. Quickly dropping the potentials on the exit-side electrostatic mirror would also provide a method to investigate the bunch shape with the MCP, provided that the count rates are not too high.

#### 4.2.4 Bunch length measurements via photo-detachment

Not only was it possible to use the CTF's extremely high vacuum to measure new ion bunch properties, but the particular crossed-beam geometry of the CTF's 600 nm pulsed laser with pulses of around 10 ns duration permitted an additional and entirely different approach to investigating bunch properties via the photo-detachment of anions. As the CTF employs a laser which is perpendicular to the stored ion beam, as opposed to one along the beam axis as in other EIBT setups, the laser can be used to precisely measure the ion bunch length.

Using a  $3.3 \mu\text{s}$  beam cleaner pulse and switching the electrodes  $26.5 \mu\text{s}$  later (with respect to the start of the beam cleaner pulse), a very short  $2.1 \mu\text{A}$   $6.0 \text{ keV}$   $\text{Al}_2^-$  ion pulse from the sputter source setup described in Section 3.3 was injected into the CTF and trapped at ambient temperatures below 15 K. While almost any anion species could have been chosen for use in this photo-detachment study,  $\text{Al}_2^-$  was the dominant species produced by the ion source. It was, therefore, easy to produce a TOF mass-selected pulse of this species in sufficient quantities. As stated previously, the trap potentials used correspond to a weak self-bunching mode. The expected ion pulse width was around  $1 \mu\text{s}$ , which was slightly more narrow than the beam cleaner pulse width of  $3.3 \mu\text{s}$ . This is due to the beam pulsing properties of the beam cleaner, which mainly arise from electric fields that severely distort the ion path and block their passage while changing potentials. This was the shortest beam cleaner pulse possible which still resulted in producing trapped ions. The 600 nm laser as described previously in section 3.3 was then fired 1.4 ms after the initial injection, and again 100 ms later. The laser trigger time could be slightly varied over a span of

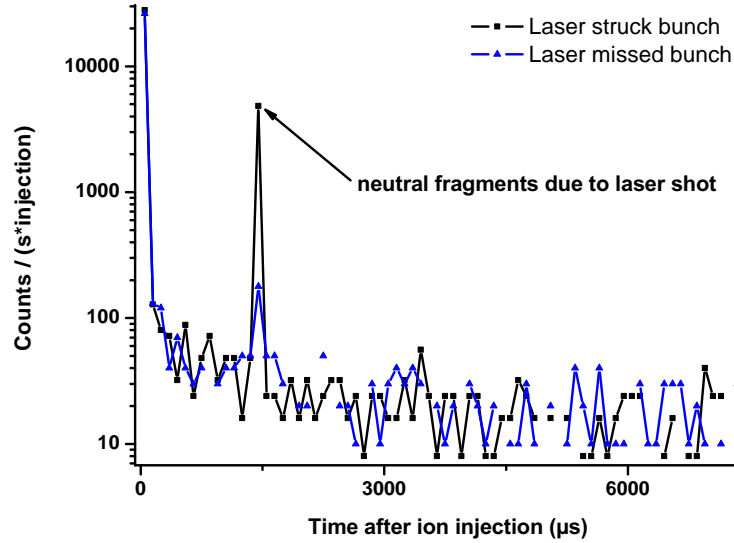


Figure 4.16: Two sample  $\text{Al}_2^-$  ion bunch length measurements with different laser delays, causing the laser to strike or miss the ion bunch during different injections. Even when missing the bunch, an increased count rate is still observed.

$14 \mu\text{s}$  with respect to the beam-cleaner trigger to probe the longitudinal ion density of a very short ion pulse in the trap as a function of ion position in the trap.

While the ion pulse was not visible using the pickup electrode (since the bunch lacked enough charge), the neutral particles created when the laser struck the bunch were detectable with a very high sensitivity on the MCP behind the CTF. A calibration of the number of charges was not possible. An FFT of the neutral particle rate detected by the MCP and averaged over many injections produced a clear signal around  $80 \text{ kHz}$ , which matched the expected trap oscillation period of around  $12 \mu\text{s}$  at this energy (see Table 4.1). The ions had completed just over 100 revolutions before the laser was fired for the first measurement (black curve in Fig. 4.17). The time of flight information after the laser struck the stored ions also allowed the confirmation that only  $\text{Al}_2^-$  was in the trap. As the injected ion current was constant (within 5%) throughout the duration of the experiment at  $2.1 \mu\text{A}$ , only normalization with respect to the number of injections was necessary.

Fig. 4.16 shows two sample plots of the counts detected on the MCP per second per injection; once for the case when the laser struck the bunch (black curve), and a second case with different timing settings (a delay of  $7 \mu\text{s}$ ) so that the laser missed the stored ion bunch (blue curve). As discussed in other lifetime plots presented in this work, the first data point exhibits a very high count rate, which is not due to the laser-bunch interaction, but arises from the many neutral fragments created

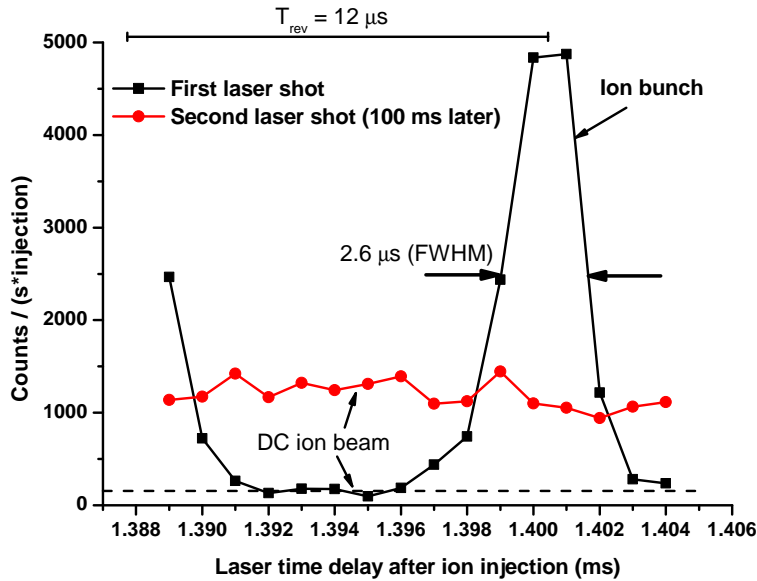


Figure 4.17: Bunch length measurement of 6.0 keV  $\text{Al}_2^-$  ions performed by varying the laser time delay. Note that by the second laser shot, the bunch has dispersed resulting in a higher signal rate regardless of the laser timing. Symbols denote data points and lines were drawn to guide the eye.

between the beam cleaner and the trap which are not blocked, but pass through the trap and are detected on the MCP. The number of neutral fragments detected when the laser struck the ion bunch increased by a factor of 25, as opposed to when it missed. It should also be noted that even when the laser was not expected to hit the bunch, a small elevated signal approximately an order of magnitude larger than the background was observed. This is the first experimental evidence that only a portion of the initially injected ion bunch remained coherently together in self-bunching trapping mode, while a small percentage (from the relative intensity of the signals, approximately 4%) of the captured ions separated from the initial bunch to fill the remaining longitudinal phase space of the trap. Future investigations will be necessary to determine how quickly this apparent partial dispersion of the bunch occurs, which results in a trapped DC beam and ion bunch.

To sample the longitudinal bunch density, the time when the laser fired was varied in  $1 \mu\text{s}$  steps (see Fig. 4.17). Since the signal strength increased dramatically from approximately 200 counts per second near  $1.394 \mu\text{s}$  to almost 5000 counts per second at  $14 \mu\text{s}$  (all normalized with respect to the number of injections), the location and shape of the ion bunch became clear. Since the revolution time of the bunch was  $12 \mu\text{s}$ , a second peak appeared on the left side of the time spectrum as the bunch was back in the middle of the trap, moving towards the MCP. While the bunch

passed through the middle of the trap twice per revolution, a signal on the MCP was only visible once per revolution, as every second time the neutral particles were produced while moving away from the MCP. This measurement clearly demonstrates that the bunch length was  $2.3 \mu\text{s}$  at FWHM with sharply defined flanks. The red circles in Fig. 4.17 show the second laser shot that arrived 100 ms later than the one demonstrating the well-defined bunch. The ion bunch is no longer visible, and from the relative rate amplitude, it is clear that the bunch has dispersed across the entire trap to create a DC ion beam. The complete disappearance of the bunch after 100 ms demonstrates that despite the significantly reduced rest gas collisional losses, the short bunch still decays quite quickly. While the bunch was stored in self-bunching mode, the measurement used a small ion density and apparently lacked sufficient charge to keep the bunch coherent for a longer time, as observed above in Section 4.2.1.

#### 4.2.5 Mass resolution

One of the possible applications of an EIBT is for use as a mass spectrometer. While time-of-flight mass spectrometers (TOFMS) typically have a resolution limited by the length of the free flight region and the TOF dispersion caused by the velocity spread of the ions, it has been proposed that an EIBT can be viewed as an extremely long TOFMS [49]. This, however, was assuming that ions could be stored indefinitely in such a trap using self-bunching mode, and that the pressure could simply be reduced, thus extending beam lifetimes and hence the mass resolution. As shown previously (see Section 4.2.2), bunch dispersion does occur in self-bunching mode at times which are not dependent on the trap pressure. While time was not available to adequately explore this possibility, a simple estimate of the mass resolution which could be attained can be made. Assuming a time resolution of 10 ns as reported in [49] could be achieved, with the maximum ion bunch durations (as opposed to the fitted bunch lifetimes) of  $t=12$  s observed in the CTF without RF bunching, leads to a mass resolution given by  $\Delta m/m = 2\Delta t/t$  of  $2 \cdot 10^{-9}$ . The FFT limit for lower signal harmonics, however, prevents such accuracy, since a signal observed over 12 s can yield a frequency resolution of up to 0.08 Hz. Better resolution, however, can be achieved by measuring the higher harmonic frequencies. Through the use of higher harmonics (e.g.  $10^{\text{th}}$  harmonic) the mass resolution of 7.1 keV  $\text{N}_2^+$ , for example, could be on the order of  $0.08 \text{ Hz}/(10 \times 123 \text{ kHz}) = 7 \cdot 10^{-8}$ . Even higher harmonics may be possible, depending on the sensitivity of the employed electronics. Alternatively, the bunch measurement technique described in the previous section could be performed on stable bunches tens of seconds after injection yielding a mass resolution given by the ratio of the bunch length over the laser delay (e.g.  $\Delta m/m = 2 \mu\text{s}/12 \text{ s} = 2 \cdot 10^{-7}$ ).

Such high mass resolution ( $7 \cdot 10^{-8}$ ) would be competitive with the accuracy achieved with storage rings for stable species [82]. Mass measurements, however, using stable species in a Penning trap still provide the highest mass resolution on the level of  $10^{-11}$  [82].

Using an Acquiris computer system with DC282 cards, a sample rate of 2 GS/s was used to record the pickup signal of injected  $N_2^+$  and  $CO^+$  ions. An FFT of a given time window revealed the amplitude of the ion bunch signal at the expected oscillation frequency determined by the ion energy. Previous scans done with a real-time FFT of the pickup signal using an oscilloscope had measured the frequency of ions at 7.1 keV with a frequency of 246.36 kHz. The longer data acquisition times combined with the higher sampling rate of the Acquiris system allowed a more accurate determination of the frequency, as well as the observation of an apparent shift of the frequency as a function of time. Due to a lack of time, however, this phenomenon could not be investigated beyond a preliminary analysis of the data taken with the Acquiris system.

#### 4.2.6 Ion bunching conclusions

Due to the CTF vacuum in the  $10^{-14}$  mbar range (see Section 4.4), the disentanglement of beam and ion bunch losses was possible, allowing ion bunching in an EIBT to be investigated over long durations for the first time. A multitude of new self-bunching measurement techniques were investigated, yielding new insight into ion bunch behaviour in addition to revealing new, unexplained effects.

The first experimental evidence of a minimum required particle number to sustain a bunch stored in self-bunching mode was observed for both  $Al_2^-$  and  $N_2^+$  ion bunches. The ratio of the required number of charged particles in both cases was compared to two theoretical models. Both one-dimensional models, however, were unable to reproduce the present observation that more charges are required for a stable 6.0 keV  $Al_2^-$  bunch than for a 7.1 keV  $N_2^+$  bunch.

The decay of ion bunches stored in self-bunching mode was investigated and found to exhibit a lifetime of around 5 s. The 10 s duration of these bunches is about a factor of 100 longer than reported so far, but also at least 100 times shorter than the residual gas related lifetime of the present stored beam. Such bunch decays were studied for two different species, namely  $Al_2^-$  and  $N_2^+$ . Bunch lifetimes differed by a factor of 10 between these two species of molecular ions, which is most likely due to differences in the number of trapped ions and the resulting ion bunch size and shape. While the intrabeam scattering model can reproduce the observed initial

accelerated decays of the ion bunch, the scaling of intrabeam scattering with the number of initially trapped ions could not thus far be demonstrated.

Applied RF was successfully used to extend the observed exponential ion bunch lifetimes from several seconds to over 100s. A clear dependence of the number of stored ions captured in a bunch was observed as a function of the relative RF phase. The lifetime of the bunch also varied as a function of the relative RF phase. Intrabeam scattering appears to account for the initial decay of the bunches, but additional scans are necessary to conclude that this loss mechanism is responsible for the observed unexplained initial bunch decay.

The photo-detachment of anions by the crossed pulsed laser beam conclusively demonstrated that at 1.4ms after injection (100 ion oscillations), a stored DC ion beam component was present, in addition to an ion bunch characterized by sharp ion density flanks while stored in self-bunching mode. This is the first experimental evidence for the simultaneous storage of these two components, indicating that not all of the ions are coherently kept together in a bunch during self-bunching mode. Future measurements are required to study how quickly the release of ions from the self-sustained bunch occurs and how it possibly depends on the number of charges in the bunch.

The proposed use of EIBTs as long time-of-flight mass spectrometers (TOFMS) can probably be greatly extended by the bunch lifetimes possible in the CTF. Preliminary estimates suggest that mass resolution of  $\Delta m/m$  of  $7 \cdot 10^{-8}$  appears possible and should be explored in the future.

## 4.3 Mass selection inside the electrostatic ion trap

Given the lengths to which atomic and nuclear physics experiments go in order to select a specific ion to trap, it is of great importance to be able to select a given mass species quickly and accurately, with the highest possible resolution, and with the lowest losses. The CTF employed low-level mass separation during the reported measurements in this work, exploiting the time of flight differences of the injected species with respect to when the trap was closed. As longer injected bunch lengths result in the trapping of multiple masses simultaneously, mass selection inside the trap was also investigated. In this context, the CTF has successfully demonstrated mass selection inside the electrostatic trap using two different procedures which will be explained below.

The RF-kick method has been employed in another EIBT before [83] and is useful in separating one species from many others by simply exploiting time of flight differ-

ences between ions of different masses which are simultaneously trapped. The RF knock-out method, while regularly used in storage rings (for example in [84]), has never been successfully demonstrated in an ion trap before. This method employs an inherent property of the trap, namely the tune (see Section 2.3), to very accurately excite the betatron frequency of a given trapped species, thereby deflecting it out of the acceptance of the trap, using a comparatively small voltage that exerts little influence on all other trapped species.

### 4.3.1 RF-kick

The RF-kick method employs an electrostatic deflector placed in the middle of the trap. Ions are injected into the trap and high voltage is applied to the deflector at all times except during the intervals when the wanted species is passing through, thereby deflecting all unwanted species out of the trap as shown schematically in Fig. 4.18. This process can be repeated over many oscillations, improving the mass selectivity.

In the CTF, the bottom two electrodes of the injection side segmented pickup were used as the deflector. An Agilent 3260A function generator was used to supply a roughly square-shaped pulse, which was used to drive a high voltage switch at around 300 V. The switch had a rise and fall time of approximately  $0.5 \mu\text{s}$  each. Given that

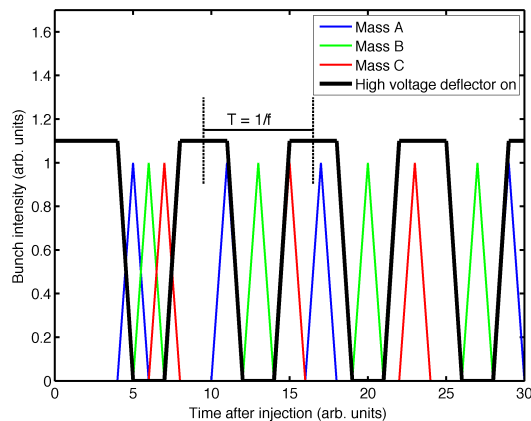


Figure 4.18: Schematic demonstrating three different ion bunches with different masses oscillating at their respective frequencies. A high voltage is applied to a deflector at times when the wanted mass is not near the deflector. The frequency  $f$  of the high voltage is given by the frequency of the desired mass (mass B in this case).

### 4.3. Mass selection inside the electrostatic ion trap

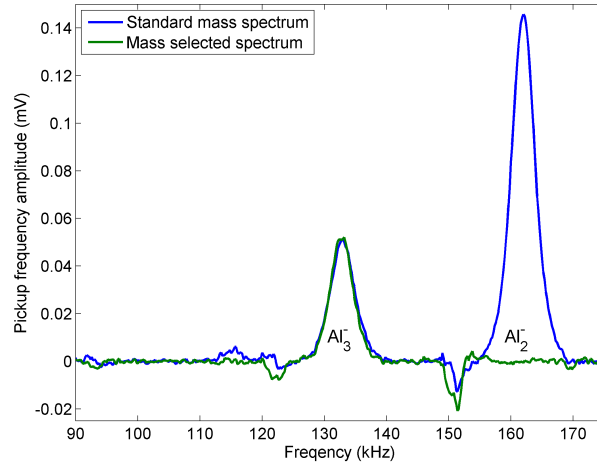


Figure 4.19: Background-corrected spectrum analyzer signal demonstrating kick-out mass selection with a scan of a normal injection and one using the described mass selection technique.

the oscillation time of most species is on the order of tens of microseconds, the plateau of the 300 V deflection was set to about a  $2 \mu\text{s}$  duration (excluding the rise and fall times). The applied frequency varied according to the desired-species' oscillation frequency inside the trap. For this test, an electrode switching delay of  $30 \mu\text{s}$  was used, resulting in the injection of a beam containing both  $\text{Al}_2^-$  and  $\text{Al}_3^-$  into the trap. Fig. 4.19 shows two ion bunch frequency spectra recorded with the spectrum analyzer (after background subtraction), which were measured with the SUM pickup electrode in the middle of the trap using the y-scale calibration described in Section 4.2.1. The blue trace was taken without applying the RF-kick voltage, resulting in both ion species being clearly identified by their respective oscillation frequencies. Their relative intensities roughly correspond to previous sputter source calibration measurements demonstrating that  $\text{Al}_2^-$  (162 kHz) and  $\text{Al}_3^-$  (132 kHz) each contribute roughly 74% and 15% to the beam, respectively. Turning the kicker deflector electrode on with a potential of 300 V and using a frequency of 66.39 kHz for 50 oscillations produced the green curve, where the strongest component ( $\text{Al}_2^-$ ) has now been entirely removed, leaving only  $\text{Al}_3^-$  in the trap. The loss of the desired species after applying this mass selection technique over 50 oscillations is extremely small, as the signal intensity is approximately identical to the blue trace and the injected ion beam current was also relatively constant. Table 4.1 shows the oscillation frequencies used for mass selecting various aluminum cluster species with a beam energy of 6.0 keV in the CTF and their corresponding higher harmonics, where

the second harmonic was typically the strongest signal seen using the CTF pickup electrode.

### 4.3.2 RF Knock-out and trap tune measurement

As previously mentioned, the RF knock-out mass selection method depends on the trap's tune. This parameter is determined by the trap geometry and the applied potentials (see Section 2.1). In this method, RF noise of only a few volts and a narrow bandwidth is applied to a deflector or trap electrode. Energy is thereby imparted only to those ions with the corresponding transverse oscillation or betatron frequency, knocking them out a little further during each oscillation, so that they are resonantly deflected out of the radial acceptance of the trap. This mass selection technique is particularly useful for purging the trap of a specific mass, as opposed to kicking everything else out except a desired mass. Provided that the noise bandwidth is narrow enough, very similar masses (e.g. isotopes or even isobaric molecules) could also be separated relatively quickly, instead of depending on many oscillations to increase the TOF differences in two species, thereby allowing the application of the RF-kick procedure described above.

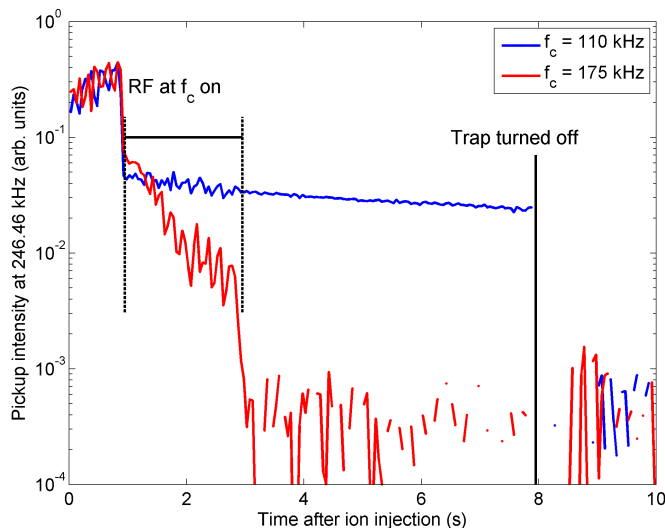


Figure 4.20: Pickup intensity from a self-bunched 7.1 keV  $N_2^+$  beam with 4 V RF noise of 8-10 kHz bandwidth applied during the time interval shown with center frequencies  $f_c = 110$  kHz (blue) and 175 kHz (red). The latter frequency corresponds to the betatron frequency of the  $N_2^+$  ions (see equation 2.24, where  $f_B = 175$  kHz,  $n=1$ ,  $q=0.4$ ), ejecting them from the trap.

### 4.3. Mass selection inside the electrostatic ion trap

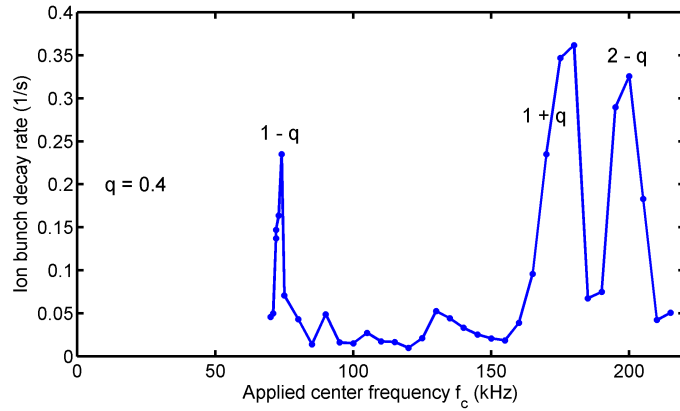


Figure 4.21: Trap tune measurement using RF Knock-out mass selection.

To ensure that any remaining ions in the trap can be efficiently detected after the knock-out mass selection technique has been applied, active RF bunching was employed. This entailed applying a constant RF voltage at 246.36 kHz with an amplitude of 5 V on the exit-side einzel lens electrode. The forced bunching method would ensure that despite the effects of the knockout technique, any remaining ions would be bunched and form a detectable pickup signal.

Using the lifetime-optimized trapping potentials for the CTF where there is weak self-bunching, 7.1 keV  $N_2^+$  ions were trapped and after 1 s, RF noise of 4 V amplitude and 8-10 kHz bandwidth was applied for 2 s (see Fig. 4.20). The trap was on for a duration of 8 s, followed by a 2 s background measurement. The strong noise during the first second is most likely due to slight phase differences between the initial ion bunch and the applied RF bunching as demonstrated in Section 4.2.3, which was on during the entire scan. The effects of the knock-out can be seen between 1 and 3 s, where the loss rate depends on the applied RF noise frequency  $f_c$ . After 3 s the RF noise was turned off. When  $f_c = 175 \text{ kHz} = f_B$  was selected (red trace) corresponding to the transversal oscillation frequency of the stored ions, the signal intensity registered on the pickup from the ions dropped by over an order of magnitude, where the signal level is consistent with the background level. In contrast to this observation, when  $f_c = 110 \text{ kHz}$  was applied (blue trace), the beam loss was much less dramatic.

As shown in Fig. 4.21, the applied RF noise frequency  $f_c$  was then roughly scanned from 70 to 215 kHz. An exponential fit yielded a mean lifetime in the time interval when  $f_c$  was applied, where the loss rate is the inverse of this fitted lifetime. The average loss rate was then calculated from multiple injections at each frequency and plotted, facilitating the measurement of the trap's tune with these particular

trap potentials. The scanned frequency,  $f_c$ , can be related to the trap's tune using equation 2.24. Here the trap oscillation frequency  $f_0$  is 123.18 kHz for 7.1 keV  $N_2^+$ . Again,  $n$  and  $q$  are the integer and non-integer parts of the tune respectively. The peaks in Fig. 4.21 correspond to frequencies which were successful in ejecting the ions from the trap, producing a higher ion loss rate. These results have already been published [85]. The non-integer tune  $q$  of 0.4 agrees with simulations, assuming a maximum transversal ion position spread of  $\pm 5$  mm [47] from the trap axis.

## 4.4 Demonstrating $10^{-14}$ mbar RTE

Using the experimental setup as described previously (see section 3.1), various measurements were made during the first experiments using  $N_2$  gas in a Penning ion source to produce  $N_2^+$  and  $N^+$ . The first lifetime measurements as a function of energy at both room-temperature and at liquid helium temperatures have already been reported and discussed [47]. These initial results allowed the determination of the strength of the electron capture process and also yielded some information about the contribution of multiple scattering as a second loss process in the trap. This, however, also presented the first evidence of an additional possible loss mechanism, which is not dependent on residual gas collisions.

As discussed previously in Section 4.1, various CTF changes were implemented to extend the previous 20 s mean lifetimes to the expected 1000 s range in order to demonstrate vacuum on the order of  $10^{-13}$  mbar (density equivalent at room temperature). Via these major upgrades,  $N_2^+$  lifetimes at 7.1 keV were increased from the 20 s range to over 300 s as demonstrated in Fig. 4.2. The observed lifetime of 340 s corresponds to a pressure (taken at room-temperature) in the low  $10^{-12}$  mbar range.

While the beam lifetime is influenced by all beam loss mechanisms present in the trap, the count rate on the detector is exclusively determined by collisions with the residual gas and therefore its composition and density, since the ions have to be neutralized in order to reach it. This was investigated by warming up the CTF while constantly measuring the neutral particle count rate on the detector, as a function of time after each injection into the trap. Intuitively, the count rate increases linearly with the pressure and hence, the number of target residual gas molecules in the trap increases. The pressure in the trap can, therefore, be determined using two separate methods: the lifetime of the ions in the trap and the rate amplitude of the fitted exponential. The first pressure measurement in the CTF was already published [85]. From this experience, a second, more controlled measurement was performed. In this second experiment, 7.1 keV  $N_2^+$  ions were injected and stored for

150 s, which was followed by a 30 s background measurement. This procedure was repeated as the supply of He II to the inner circuit of the CTF was cut off (while the shield circuit was continuously supplied with cold He). The beam-pipe warmed up by roughly 15 K over the course of 6 hours, as shown in Fig. 4.22 (a). As mentioned before in Section 3.1.3, the PT1000 temperatures represented by the band in this figure provide an upper limit to the temperatures of the cryogenic beam-pipe. Given the large heat capacity of the cryogenic vacuum chambers, the temperature of the system did not significantly warm over these 6 hours. Instead, the slight warming-up of the system caused the desorption of almost exclusively hydrogen from the chamber surfaces, as indicated by the partial pressures in Fig. 4.22, acquired using the quadrupole mass spectrometer behind the CTF. All other gas components had considerably lower partial pressures than the ones shown in Fig. 4.22. The two large hydrogen peaks located at 3 and 4.5 hours after the start of the warm-up period are clearly related to hydrogen desorbing from the cold chamber walls of the cooling units, as they also closely correlate to the temperature recorded in this location. This is reasonable since both units would have pumped significant amounts of hydrogen, being in direct contact with 1.8 K liquid helium. As shown in Fig. 4.22 (c), the injected ion current was relatively stable throughout the entire measurement period. The rest-gas-densities presented here conservatively ignored the fluctuations of the pick-up signal and used the current intensity at 5 hours after warming began. Including the observed fluctuations in the analysis would have resulted in further decreasing the achieved rest-gas-density by a factor of at least 3.

Fitting the ion decay lifetime and combining the literature electron capture cross-section  $\sigma_c = 23 \cdot 10^{-16} \text{ cm}^2$  for electron capture by  $\text{N}_2^+$  on  $\text{H}_2$  [86, 87] and the known beam energy, permits the direct determination of the rest-gas-density. While the kinetic energy of the beam changes in the trap,  $\sigma_c$  is almost constant over this energy range and any small variation here does not significantly affect the rest-gas-density. This calculation was done at the highest pressure achieved during this warmup, since the corresponding beam lifetime is electron capture dominated. This also agrees with an ionization gauge with an average pressure of  $4.2 \cdot 10^{-9}$  mbar (hydrogen atmosphere corrected), which was not located in the cryogenic trap, but rather at room-temperature in the pumping stand with a closed radiation flap between them (see section 3.1 for details). The pressure determination using the rate of detected particles was dependent on the number of ions in the trap. While this value was not measured separately, this curve can be multiplied by a constant to match the observed peak pressure (the average of a few points during a steady pressure period) just before 5 hours (see the averaged line in Fig. 4.22 (d)). Tracing back from the peak pressure, the two pressure measurements agree very well with each other until roughly 3 hours after the cooling system was turned off. At this point, the

pressure from the rate amplitude continues to drop, while the pressure determined from the exponential lifetime stays relatively constant. If the lifetime was indeed a reliable method to measure the pressure, the inverse lifetime would have continued to decrease and match the decreasing count rate on the MCP. Instead, the measured CTF lifetime was limited by a pressure independent effect. The pressure determined by the rate amplitude, however, starting when the cooling was turned off, exhibits a slow rise in count rate and therefore pressure. At around 2.5 hours, the pressure starts to increase more rapidly and shortly after, the lifetime finally begins to show a change. The dip at 4 hours was caused by temperature fluctuations, while after 5 hours the pressure began to drop despite the continual beam-pipe warming. This is most likely due to the re-pumping of the released gas by the cryopump. In these time scales, the temperatures of the chambers did not change sufficiently to release any gas except hydrogen.

The rest-gas-density achieved in the CTF during 1.8 K cryogenic operation was thus measured via the rate amplitude on the MCP to be  $2000 \pm 1000$  particles/cm<sup>3</sup>, which corresponds to a room-temperature equivalent pressure (RTE) of  $8 \pm 4 \cdot 10^{-14}$  mbar. Assuming a conservative trap temperature of 10 K, this corresponds to a pressure of  $3 \pm 1.5 \cdot 10^{-15}$  mbar. This value was determined from the first data point shown in Fig. 4.22, as via the rest gas quadrupole mass spectrometer, the presence of hydrogen begins to increase immediately after the refrigeration system was turned off. While a trapping limitation does elucidate the apparent inconsistency between the rate amplitude and the lifetime measurement, its cause has not yet been definitively identified. This experiment will be published shortly [45].

For comparison, the reported CTF rest-gas-density is 200 times smaller than that estimated for the moon's atmosphere at  $3\text{-}5 \cdot 10^5$  particles/cm<sup>3</sup> [88]. Such higher densities are also of the same range as observed in the Horsehead nebula ( $10^4$  to  $10^5$  particles/cm<sup>3</sup>) [89], where various physical and chemical processes occur in this molecular cloud. The densities achieved in the CTF are also comparable to those observed in planetary nebulae ( $10^2$  to  $10^4$  particles/cm<sup>3</sup>) [90]. The CTF low rest-gas-density is most likely the best vacuum ever achieved in a system of this size. While an estimated rest-gas-density of 100 particles/cm<sup>3</sup> was reported by Gabrielse *et al.* in [91] through a mass measurement of the antiproton, this was created in a Penning trap in a comparatively small enclosed 4.2 K volume (no larger than several cubic centimeters). The size of the vacuum achieved in the CTF, particularly given the required 300 K beam line entry and exit pipes is several orders of magnitude larger. A cryogenic vacuum chamber of almost the same proportions of the CTF was created for the calibration of ultrahigh vacuum gauges and reported a pressure of  $4 \cdot 10^{-13}$  mbar (assuming the pressure published is the room-temperature equivalent

#### 4.4. Demonstrating $10^{-14}$ mbar RTE

---

value. If this is not the case, the RTE value would be roughly a factor of 10 worse) [92]. The measured CTF pressure, however, is still almost an order of magnitude lower than this other extremely high vacuum chamber.

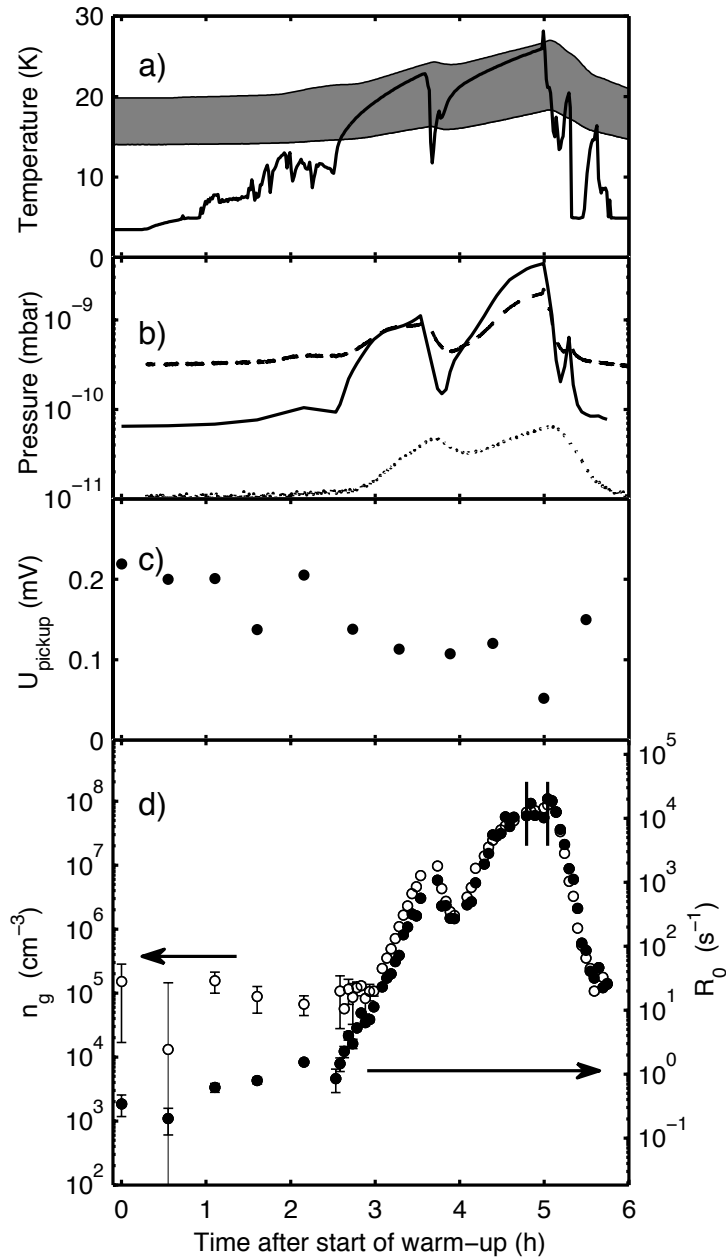


Figure 4.22: Warm-up of the CTF as a function of the time after cutting off the 1.8 K fluid helium supply. (a) The solid black line is the temperature of a RhFe sensor on a cooling unit, while the band represents the cryogenic beam line temperature range given by various PT1000 sensors. (b) The solid black line is the ion gauge pressure measured outside the trap below the CTF at room-temperature, while the dashed line is the partial pressure of  $\text{H}_2$  and the dotted line is the partial pressure of  $\text{N}_2$  and  $\text{CO}$ . (c) Amplitude of the pickup voltage at the second harmonic of the trap oscillation frequency, which is proportional to the injected ion current. (d) Residual gas density deduced from the beam decay constant (open symbols, left axis); MCP count rate amplitude (solid symbols, right axis).

# Chapter 5

## Decay and fragmentation of excited aluminum cluster anions

### 5.1 Long-time decay of negative atomic ions and $\text{Al}_n^-$ clusters

#### 5.1.1 Neutral fragment decay

Using the CTF setup as described in section 3.3 but without the laser, a number of long decay measurements were performed using negative atomic ions ( $\text{O}^-$  and  $\text{Al}^-$ ), in addition to  $\text{Al}_n^-$  clusters. The lifetime measurement of  $\text{O}^-$  was performed using time of flight mass selection between the source and the trap. The kick-out mass selection technique, as described previously in section 4.3.1, was used to select the stored aluminum species. Due to the excellent CTF vacuum, the signal rate for all of these measurements was extremely small, limiting the reasonable amount of statistics that could be taken.

When the sputter source was initially installed, it produced  $\text{O}^-$  until the aluminum oxides on the surface of the target were depleted. This opportunity was utilized with a  $9\ \mu\text{s}$  beam cleaner pulse and an electrode delay of  $20\ \mu\text{s}$  to trap  $\text{O}^-$  without the use of the kick or knock-out mass selection technique. With a mass of only 16 amu, time of flight differences were more than adequate to ensure that the next heavier species ( $\text{Al}^-$ ) did not enter the trap. This was confirmed via the pickup electrode and the spectrum analyzer. The ions were stored for 100 s, followed by a 20 s background measurement. The resulting background-subtracted lifetime is shown in Fig. 5.1(a).

A double exponential decay fits best to the lifetime curve generated by the neutral fragments detected by the MCP behind the CTF in Fig. 5.1(a). Any short decay

components ( $< 1$  s) were not visible due to the available statistics at short times. Such short decays will be discussed later in Section 5.2. The two exponential lifetimes ( $36 \pm 3$  s, and  $12 \pm 1$  s) are most easily explained by considering that the CF40 valve between the beam cleaner and DB1 (see Section 3.1) was pulsed, opening it to allow the ion bunch to pass through before closing it for 2 minutes. This most likely produced a small burst of gas that entered the trap, temporarily making the pressure worse. The heavier ions were blocked from entering the trap impinged on the vacuum walls. In combination with the neutrals produced during the flight time between the beam cleaner and the trap, both of these effects could temporarily worsen the vacuum right after injection, resulting in a slightly shorter lifetime until the vacuum recovered. Both decays, are therefore, most likely due to collisional detachment with the extremely reduced rest gas in the CTF.

A mass-selected  $\text{Al}^-$  beam was stored by applying an effective  $2 \mu\text{s}$  “kick” for twenty oscillations at a frequency of 115 kHz, in combination with a beam cleaner pulse length of  $10 \mu\text{s}$  and an electrode delay of  $20 \mu\text{s}$ . The resulting background-subtracted count rate of the mass-selected beam on the MCP behind the CTF is shown in Fig. 5.1(b). The first point has been ignored, as it includes the neutrals formed by the injected beam before entering the trap from all source produced species. Trapping, however, for 1 s then opening the trap for a background measurement clearly demonstrates an exponential decay with a mean lifetime of  $3.0 \pm 0.7$  s for  $\text{Al}^-$ . The observed lifetime is longer than the measurement time, so it cannot be accurately

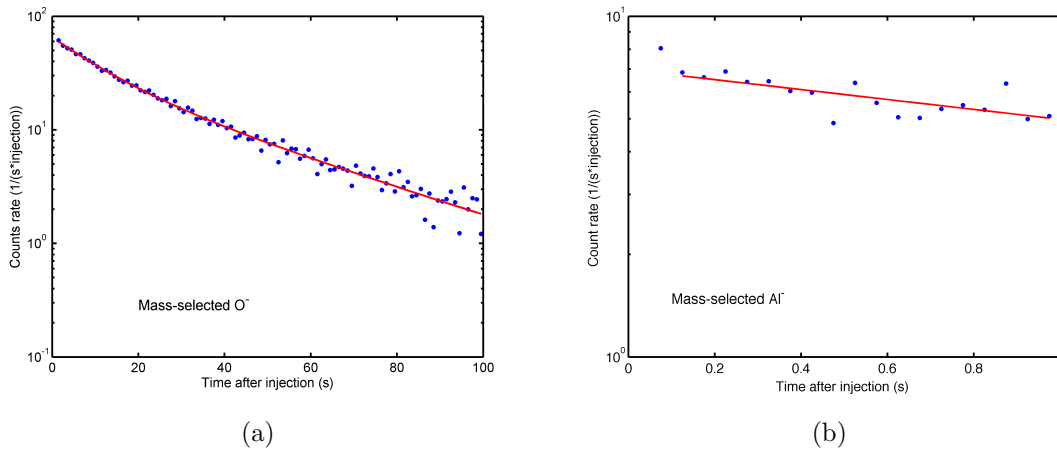


Figure 5.1: Lifetime measurements of mass-selected (a)  $\text{O}^-$  and (b)  $\text{Al}^-$ . The  $\text{O}^-$  decay was fit with a double exponential lifetime curve after a detector background rate of 1500 counts/(s\*injection) was subtracted. The  $\text{Al}^-$  decay was fit with a single exponential decay after a detector background rate of 26.6 counts/(s\*injection) was subtracted. See text for details.

### 5.1. Long-time decay of negative atomic ions and $Al_n^-$ clusters

determined. In case of a multi-component exponential decay, a much longer decay component may exist. The observed decay is most likely due to collisional detachment with the rest gas in the trap. The very short initial decay of the signal cannot be investigated with this data set, but is examined further in Section 5.2.

Following a similar procedure for  $Al_2^-$  ( $9\ \mu s$  beam cleaner pulse with an electrode delay of  $30\ \mu s$ ), however, yields a vastly different spectrum, as shown in Fig. 5.2(a). As the revolution frequency of  $Al_2^-$  is  $81.31\ kHz$  and 30 cycles were used for mass selection, the mass selection process was over after roughly  $0.4\ ms$ . It is, therefore, reasonable to use all the data-points after this period, which can be roughly described by a super-position of three exponential functions with the lifetimes:  $10.1 \pm 0.2\ ms$ ,  $59 \pm 3\ ms$ , and  $1.03 \pm 0.10\ s$ , respectively. As the long lifetime component is of the same magnitude as the measurement time, and the fit clearly appears to be too low at long times, a second measurement using a trapping time of  $100\ s$  was performed (see Fig. 5.2(b)). A single exponential fit of this longer measurement yields a lifetime of  $42 \pm 3\ s$  which is most likely due to rest gas collisions. This multi-component decay is further discussed in Section 5.2.3 in comparison to other metal anion dimers, as well as in the temperature dependence of the initial decay rate in Section 5.2.4. The obvious qualitative differences between the negative atomic anion species and that of the aluminum dimer anion decays are not unexpected given the influence of the available vibrational excitations in the latter. The excellent CTF vacuum during cryogenic operation combined with the low ion production rates hampered similar

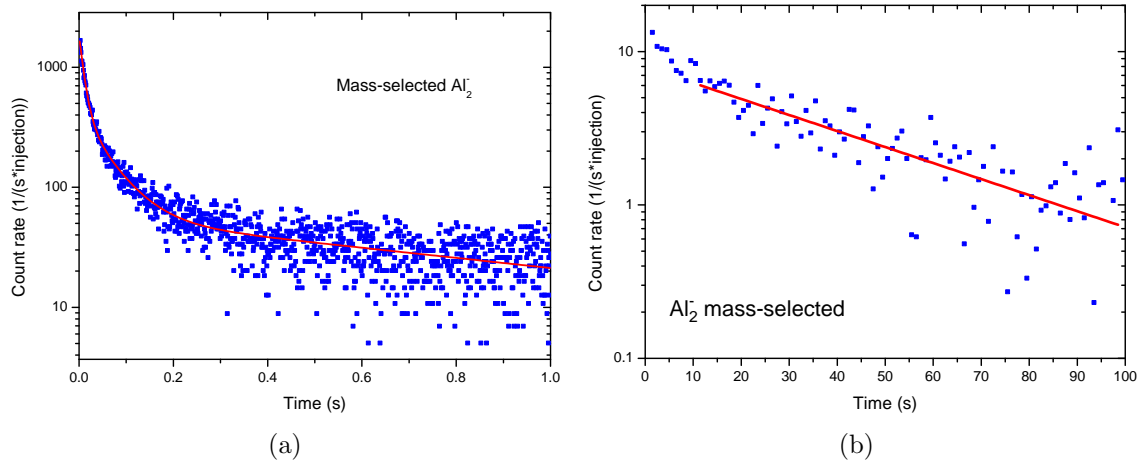


Figure 5.2: Decay measurements of  $Al_2^-$  over (a) 1 s and (b) 100 s. The kick-out mass-selection technique was used. The first figure has been fit with a three-component exponential function after a detector background rate of  $42.4\ \text{counts}/(s \cdot \text{injection})$  was subtracted. A single exponential function was fit to the second figure after a detector background rate of  $28.3\ \text{counts}/(s \cdot \text{injection})$  was subtracted.

long lifetime measurements using this method for larger aluminum anion clusters.

### 5.1.2 Decay measurements via photo-detachment

A novel approach of performing decay measurements, particularly suited for the extreme vacuum conditions in the CTF, was successfully demonstrated. The stored ions produce an extremely weak neutral fragmentation signal on the exit-side MCP due to the CTF's low rest-gas-density, but via laser-induced electron detachment, the signal can be greatly enhanced.

Using aluminum cluster anions and the 600 nm laser setup described previously (see Section 3.3), the laser was used to photo-fragment the anions that were passing through the center of the trap. The estimated peak power intensity during a pulse typically used in this setup was around  $100 \text{ kW/cm}^2$ . The MCP located behind the CTF was then used to measure the neutral fragments, but with enough time resolution, depending on the employed trapping time and the corresponding computer memory limitations) to identify the various cluster sizes via time of flight (TOF). Fig. 5.3 demonstrates the arrival signals of the various clusters on the MCP at the two different employed injection timing settings, where the colour assignments correspond to the arrival of the stated masses in the figure. The TOF values correspond to the neutral fragments of the laser-excited ions immediately produced after laser absorption and detected behind the CTF. To distinguish these signals

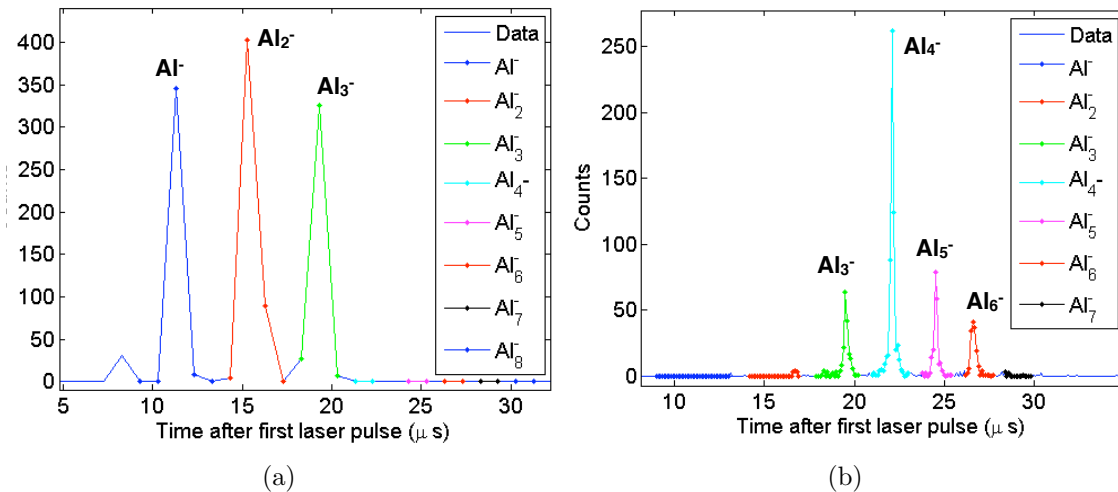


Figure 5.3: TOF spectra of neutrals counted immediately after a laser pulse for two different injection timing settings yielding (a) smaller and (b) larger aluminum cluster masses. The employed time resolution was (a)  $1 \mu\text{s}$  and (b)  $0.1 \mu\text{s}$ , respectively. The colour assignments identify the peaks according to their time of flight.

### 5.1. Long-time decay of negative atomic ions and $Al_n^-$ clusters

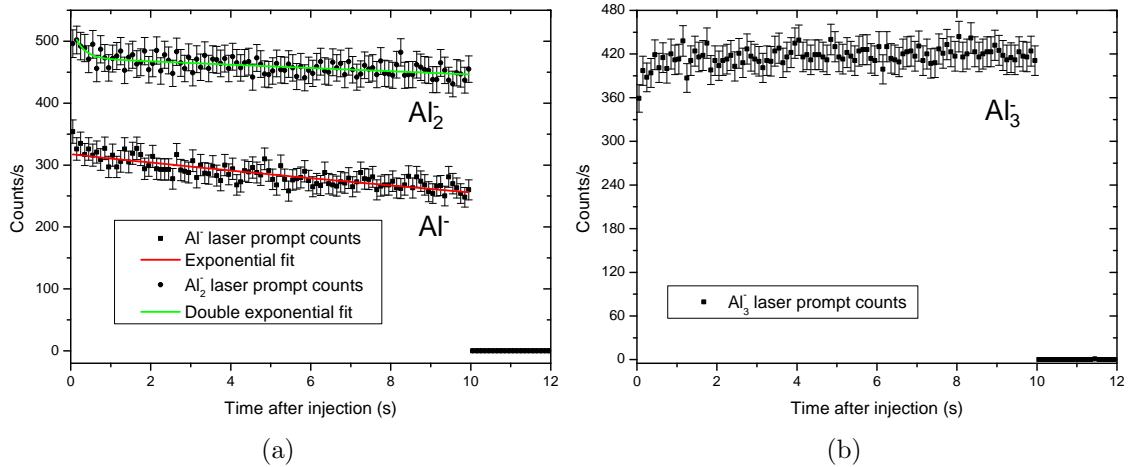


Figure 5.4:  $Al^-$ ,  $Al_2^-$ , and  $Al_3^-$  photo-detachment decay curves. An exponential function has been used to fit the data where possible. Detector background has not been subtracted, but is illustrated to demonstrate that it can be neglected.

from those which occur after multiple ion oscillations in the trap (delayed emission), these TOF spectra will be referred to as the laser prompt throughout this work.

For the decay measurements presented here, the integral of the number of counts over a given cluster peak in the TOF spectrum was used to determine the signal. This was then repeated for each laser shot, occurring every 100 ms throughout the ion storage time. Background has not been subtracted from any of the decay measurements as the selective time windows combined with the CTF's extreme vacuum have reduced the background to almost zero, demonstrating the impressive signal to noise ratio possible with this method. It should be noted that the decays presented here are free from detector saturation, due to the low count rates.

Based on the results from the measurement of a short bunch in the trap (see Section 4.2.4), the first laser shot at 50 ms was ignored to ensure that the density of the ions throughout the entire measurement was comparable. The previous results demonstrated that in the first 100 ms, a short bunch would disperse and fill the entire trap. Inhomogeneity in the stored ion beam density due to slight differences in the bunch decay between laser shots would change the observed signal amplitude of a given laser shot. Assuming that a homogenous ion density existed for every laser shot, and that the number of ions lost due to previous laser shots is negligible, a decay curve can be generated for every mass simultaneously stored in the trap.

Using a  $25 \mu s$  beam cleaner pulse and a  $29.5 \mu s$  electrode delay, a  $0.75 \mu A$  beam was stored containing  $Al^-$ ,  $Al_2^-$ , and  $Al_3^-$  as seen in Fig. 5.3. The ions were stored for 10 s, then the trap was opened and a two second background measurement was

taken. The number of counts due to photo-detached  $\text{Al}^-$  as a function of time after injection are plotted in Fig. 5.4(a). The first point, as described above, is ignored, and fitting an exponential function yields a  $46 \pm 3$  s lifetime. This is far longer than the 10 s measurement time, so this value cannot be considered accurate, though it demonstrates that a long lifetime component exists as seen using the neutral collisional measurement method above. In comparison to the previous decay measurement method, which monitors fragment rate production from the trap, this lifetime is significantly higher. Though, as seen in Fig. 5.1(b), the limited statistics permit beam lifetimes well above the 3 s, particularly given that the measurement time was only 1 s. This exhibited lifetime component is most likely due to collisional decay of the atomic ions with rest gas in the trap and qualitatively agrees with the employed lifetime measurement presented above. The statistics in Fig. 5.4(a) can also not rule out a faster initial decay at early times, though this will be further discussed in Section 5.2.

Using the same set of data, but shifting the TOF window to study  $\text{Al}_2^-$ , generates the second data set in Fig. 5.4(a). As seen previously for  $\text{Al}_2^-$  using the residual gas-based decay measurement method in Fig. 5.2(a), a shorter decay component is also visible using this laser-induced fragmentation method as well. The available time resolution is not high enough to accurately fit this short component, although it qualitatively agrees with the two shorter lifetime components (around 10 ms and 60 ms) in Fig. 5.2(a). The fitted exponential decay of  $170 \pm 60$  s for the long component is not within range of the previously fitted value of  $42 \pm 3$  s in Fig. 5.2(b). This difference may be caused by an enhancement of photo-excitation at later storage times when the molecule has radiatively cooled.

No CTF collisional decay measurements currently exist to compare to those taken with this new method for the larger clusters. The photo-detached decay data for  $\text{Al}_3^-$  is shown in Fig. 5.4(b). What is curious is an apparent increase in the count rate within the first second, indicating that the photo-excitation yield increases within these time scales. Given the low count rates, detection saturation can be excluded. An exponential fit excluding the first second yields extremely long lifetimes, orders of magnitude larger than the measurement duration. This particular cluster size should be further investigated to clarify the shape of this decay.

A second measurement was used for the larger aluminum cluster anions shown in Fig. 5.3(b). While neutral collisional decays are not available for comparison, exponential decay components longer than the measurement window of 3 s used here are achieved for all species (see Figures 5.5(a) and 5.5(b)). Single exponential fits with lifetimes of  $5.7 \pm 0.4$  s and  $118 \pm 100$  s were obtained for  $\text{Al}_4^-$  and  $\text{Al}_5^-$ , respectively. The two larger clusters, however, displayed a faster, second component

### 5.1. Long-time decay of negative atomic ions and $Al_n^-$ clusters

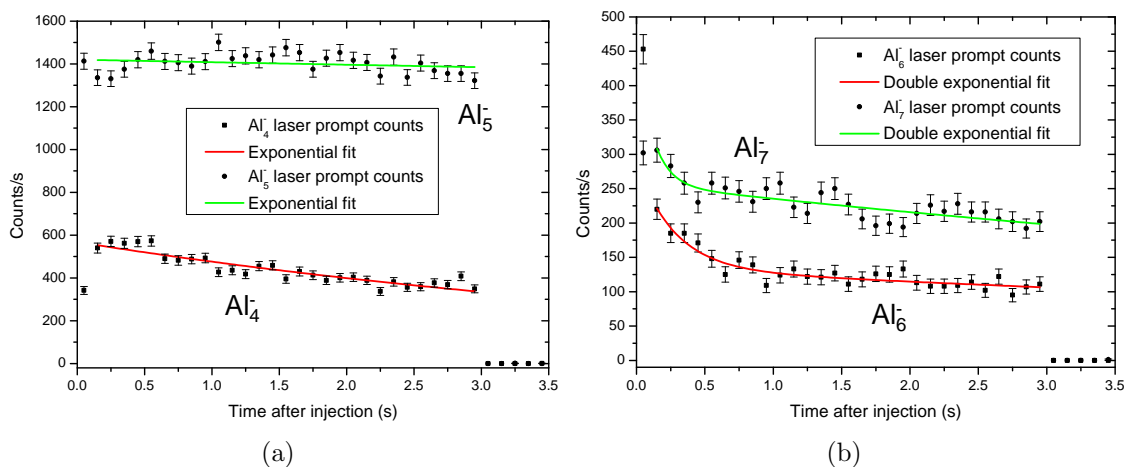


Figure 5.5:  $Al_4^-$ ,  $Al_5^-$ ,  $Al_6^-$ , and  $Al_7^-$  photo-detachment decay curves. An exponential function has been used to fit the data where possible. Detector background has not been subtracted, but is illustrated to show it can be neglected.

as well. For  $Al_6^-$ , it was found that a double exponential with the following lifetimes reproduced the data:  $0.27 \pm 0.09$  s and  $13 \pm 6$  s. These values also agree with those from  $Al_7^-$ :  $0.12 \pm 0.09$  s and  $12 \pm 3$  s. It is curious to note that a double exponential fit was best used to describe both the two largest clusters and  $Al_2^-$ . Given that the photoelectron spectra of  $Al_6^-$  and  $Al_7^-$  appear to represent the transition sizes between molecules with planar and 3D geometry [23], these decay differences to the smaller clusters appear reasonable.

It is also important to note that the employed photon energy ( $600$  nm  $\approx 2.07$  eV) is larger than the electron vertical detachment energies of the investigated aluminum anions smaller than  $Al_4^-$  [93]. In principle, this could allow the assumption that an electron is simply promoted into the continuum. The decay curve for  $Al_3^-$  demonstrates, however, that the process is more complex. Qualitative differences exist between the small and large aluminum cluster anion species investigated.  $Al_4^-$  and  $Al_5^-$  both exhibit binding energies around  $2.0$  eV, while the two heaviest cluster species investigated ( $Al_6^-$  and  $Al_7^-$ ), have experimentally determined vertical detachment energies larger than that of the photons used in this investigation [93]. Qualitatively, the observed decays of  $Al_4^-$  and  $Al_5^-$  look similar since both appear to only consist of a single exponential decay curve, which could result from rest gas collisions. The decay curves for  $Al_6^-$  and  $Al_7^-$ , however, show an entirely different structure. A double exponential fit appears to describe their decays, which does not lend itself to be easily understood. The observed decays, do suggest that the cluster size (and the resulting variation in vibrational modes and binding energy) plays an important role in the resulting decays, as they qualitatively group according to the binding energy

values. It should also be noted that over such long storage times, these hot clusters also radiatively cool (see Section 5.14(d)), which most likely further complicates the observed decays. The largest cluster studied here, for example, could be initially formed in an excited state which is readily photo-detached. After seconds of storage at ambient temperatures below 15 K, these clusters could have already radiatively decayed to the ground state at which point two photon processes would be required to photo-detach an electron from this anion cluster. Since the employed peak laser power intensity was around  $100 \text{ kW/cm}^2$  (see Section 3.3), two photon processes were generally avoided.

## 5.2 Fast decays of highly excited $\text{Al}_n^-$

The observation of fast decays from various highly excited (hot) negative metal clusters and other anions, as they are typically produced in most ion sources, has been extensively studied previously, as described in Section 2.5. Measurements with the CTF offer, however, an environment where the blackbody radiation may be significantly reduced and varied, facilitating a temperature dependent investigation of this decay and explore the influence of radiative cooling in this emission process. The CTF's vacuum of  $10^{-14}$  mbar (RTE) in cryogenic operation also greatly suppresses background events, allowing the decay events to be studied in detail and understood for longer times where count rates are weak. Even for smaller masses with large loss rates the beam lifetime is still greatly extended, so that the time-dependent particle count rates show almost no influence due to beam decay.

The fast initial decay of stored aluminum molecular and cluster anions is expected because these systems are produced with considerable internal excitation energy in the ion source. In a series of experiments, different aluminum cluster anions ( $\text{Al}_n^-$ , where  $n=1$  to 8) were stored and investigated. A description of the experimental setup can be found in Section 3.1, while the details of the sputter ion source and the laser used during these particular experiments are documented in Section 3.3. Time of flight mass separation was applied, where the switching time of the trapping electrodes was used to select the cluster of interest. The pickup electrode signal was used to observe and confirm the oscillation frequency of the ion bunch in the trap, as each species have distinct frequencies as previously shown in Table 4.1. An FFT of the pickup signal, in addition to the observation via the spectrum analyzer, confirmed the presence of the trapped species. Due to the low level mass selection employed, unwanted masses were also present in most cases. Mass selection was only employed in one case as the time window of interest, namely the first ten to twenty milliseconds, overlaps with the required time to perform this procedure. In this case,

the RF-kick procedure was used (see Section 4.3.1 for details) and data points from this time window have been ignored during the data analysis. This was not repeated for species other than  $Al_2^-$ , as the ion production rates were so small that longer ion bunches were necessary to improve the filling of the trap, defeating the mechanism of this mass selection method. The knockout mass selection technique would have taken even longer time periods, possibly disturbing the signal throughout the entire region of interest.

After the fast initial decay of the clusters, the trapped anions were further scrutinized 50 ms after ion injection by using a pulsed 600 nm laser in the setup described above to photo-detach a portion of the stored ions. The trapped masses were identified via time of flight at a higher sensitivity level than what is possible with the pickup detector, as some species were trapped in such small quantities that no pickup signal was produced. The resulting laser prompt plots could not be used to determine the concentration of the stored ions as this would require the consideration of the ion/laser beam overlap, position of each mass bunch in the trap, and laser absorption cross sections for each cluster size at a photon wavelength of 600 nm. While the employed timing settings minimized contaminants, a compromise had to be made to facilitate reasonable signal rates and measurement periods.

As the ions decayed within the trap after each injection, the MCP behind the CTF detected the neutral fragments for a time on the order of 200 ms, plus 100 ms for a background measurement without ions. While injected ion beam currents on the order of 1 to 2  $\mu A$  (integrated over all mass species) were required for the larger clusters, smaller currents between 0.2 and 0.6  $\mu A$  were injected for the more abundant  $Al_2^-$  and  $Al_3^-$  clusters to avoid detector saturation.

$Al^-$  and  $Al_2^-$  present two special cases, as these few body systems have significantly fewer degrees of freedom when compared to the larger aluminum clusters studied here; thus, differences between these two regimes are expected.

### 5.2.1 $Al^-/O^-$ results

The  $Al^-$  ion, being composed of a single atom, cannot possess vibrational energy. Experiments trapping a mixed beam of  $Al^-$  and  $O^-$  with a trap temperature of 90 K were accomplished using a 0.1  $\mu A$  beam, with a 6  $\mu s$  beam cleaner pulse and an electrode switching delay of 21  $\mu s$ . Due to the low ion source production rates, no FFT or frequency spectra are available to determine the relative abundances of the two ions.  $O^-$  is typically produced by this type of ion source after installation of the partially oxidized aluminum target, but a far higher abundance of  $Al^-$  is expected, as it had been over a week since the target was installed. Taking this into account,

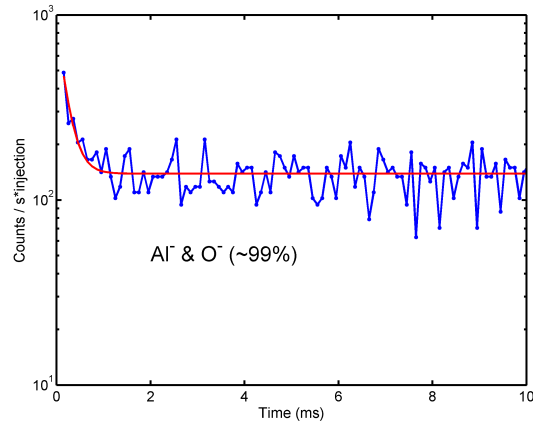


Figure 5.6: The normalized count rate of spontaneous delayed emission as a function of the time since injection for a hot  $\text{Al}^-/\text{O}^-$  mixed beam stored at a trap temperature of 90 K. An exponential decay was used to fit the data. See the text for details and discussion.

it seems reasonable to assume that a  $\text{Al}^-$  dominated beam was stored, though the relative concentrations cannot be confirmed. While only these two species are known to be produced from the sputter source in this mass range, the lack of a more precise mass selection method has led to an estimate that these two species account for at least 99% of the stored beam. Contaminants from  $\text{Al}_2^-$  and heavier clusters could not have entered the trap before it was closed. A laser prompt (see Section 5.1.2 for details) 50 ms after ion injection also confirmed that only these two species were in the trap.

In the observed decay curve of this atomic mixture in Fig. 5.6, an initial decay with an exponential time dependence or a  $1/t$  dependence is seen over a short time interval (the number of points in the decay does not permit the time dependence to be determined). For its possible explanation it is useful to consider the electronic states of the two trapped species.  $\text{Al}^-$  has a  $3s^23p^2(^3P_0)$  electronic ground state with an electron affinity (EA) of around 433 meV [94] and a bound excited state with an EA of around 0.1 eV [95].  $\text{O}^-$  by comparison, has a  $1s^22s^22p^5(^2P_{3/2})$  electronic ground state, and is known to have two fine-structure levels, in addition to a doubly excited state. No initial fast decays at room-temperature have been observed by the CTF for  $\text{O}^-$ . It is, therefore, possible that the observed  $190 \pm 25 \mu\text{s}$  exponential decay is due to the decay of  $\text{Al}^-$ , though subsequent measurements at room-temperature produced a longer initial lifetime.

Another possibility is that in the first millisecond, during which the ions perform

over 100 oscillations in the trap, a previously unstudied form of trap loss is occurring, which is perhaps due to semi-stable ion orbits. Intrabeam scattering is highly unlikely, given the very low number of trapped ions and the fast decay of the feature. The magnitude of the observed effect is rather small in comparison to similar decays observed in the aluminum clusters (see Fig. 5.14). Subsequent room-temperature measurements on a mass-selected  $O^-$  beam appear to rule out some form of trap loss to explain this observed decay curve.

A third possibility which can unfortunately not be excluded, is mass contamination. While another low-mass ion in this range (16 to 54 amu) was not seen with the diagnostic tools available,  $AlO^-$  can be produced from this source in low concentrations. If this molecular ion was present, it could also be responsible for the observed decay, which due to the limited number of points, could be fit with either an exponential or power law fit. Such delayed emission has also been observed for transition metal oxides [96].

Additional decay measurements with mass-selected  $Al^-$  at different trap temperatures are required to determine if the observed decay is temperature dependent or if this measurement also contained aluminum oxides.

### 5.2.2 Aluminum molecular and cluster anion measurement conditions

The complexity of the stored ion species was increased from  $Al^-$  to the diatomic aluminum anion, thereby introducing one vibrational degree of freedom in addition to the larger clusters which possess many vibrational degrees of freedom. The following section documents the experimental timing settings as well as the measured laser prompts and spectrum analyzer frequency sweeps of the stored ion beams. These measurements were performed at trap temperatures below 15 K and again later while warming up at trap temperatures around 90 K. As described in Section 2.5, the fast decay of highly excited cluster systems in a statistical description of the many participating levels yields a  $1/t$  decay law which is best illustrated by showing the observed decay signal in a doubly logarithmic representation.

The aluminum cluster anions stored in each measurement were controlled by choosing the appropriate beam cleaner pulse, thereby defining the pulse length of the ion beam, in addition to the time delay used to close the trap (see Table 5.1). This low-level mass selection via TOF was sufficient to store various beams and optimize the relative abundance of the target species. The spectrum analyzer frequency sweeps were used to determine the relative abundance of the ions in the trap, while the laser prompts were used to determine if small amounts of mass contamination were also

Table 5.1: Table of experimental parameters used to select the aluminum cluster anions in the fast decay experiments. The dominating ion cluster(s) is/are marked in bold with the relative abundance determined from the spectrum analyzer sweep in brackets. Ion abundances have been estimated in the last four cases where the injected beam current was too small to produce a pickup signal.

Setting	Trapped ion species (Abundance)	Beam cleaner ( $\mu\text{s}$ )	Trap electrode ( $\mu\text{s}$ )	Total ion current ( $\mu\text{A}$ )	Trap temp. (K)
A	<b><math>\text{Al}_2^-</math> (100%)</b>	9	30	1.7	<15
B	$\text{Al}_2^-, \text{Al}_2\text{O}^-$ <b><math>\text{Al}_3^-</math> (99%), <math>\text{Al}_3\text{O}^-</math></b>	6	35.5	0.6	92
C	$\text{Al}_3^-, \text{Al}_4^-$ (88%), $\text{Al}_5^-, \text{Al}_6^-$	16	49	0.75	<15
D	<b><math>\text{Al}_4^-</math> (78%), <math>\text{Al}_5^-, \text{W}^-</math></b>			1.7	83.5
E	<b><math>\text{Al}_4^-</math> (77%), <math>\text{Al}_5^-, \text{W}^-</math></b>			1	95
F	$\text{Al}_4^-, \text{Al}_5^-$ (99%), $\text{Al}_6^-, \text{Al}_7^-$	20	57	0.75	<15
G	$\text{Al}_4^-, \text{Al}_4\text{O}^-, \text{Al}_5^-$ (21%), $\text{Al}_5\text{O}^-, \text{Al}_6^-, \text{Al}_6\text{O}^-, \text{W}^-$ $\text{Al}_7^-, \text{Al}_7\text{O}^-$			1.65	83.5
H	<b><math>\text{Al}_6^-, \text{Al}_7^-</math> (<math>\approx 60\%</math>)</b>	20	63	0.75	<15
I	<b><math>\text{Al}_6^-, \text{Al}_7^-</math> (<math>\approx 60\%</math>)</b>			1.5	84

stored. The frequency sweeps for beams stored at trap temperatures below 15 K are shown in Fig. 5.7, while those at trap temperatures around 90 K are displayed in Fig. 5.8. Similarly, the laser prompts for the clusters stored at trap temperatures below 15 K are shown in Fig. 5.9 and those around 90 K are in Fig. 5.10.

A few details must be clarified for specific data sets presented here, particularly concerning  $\text{Al}_2^-$ . The kick-out mass selection technique as described previously in Section 4.3.1 was used to select  $\text{Al}_2^-$  for a measurement at trap temperatures below 15 K (Setting A). As the revolution frequency of  $\text{Al}_2^-$  is 81.31 kHz and 30 kick cycles were used for mass selection, the mass selection process was over after 0.4 ms. Data analysis, therefore, was only carried out on data points after this time period. This species was very abundantly produced by the ion source, so mass selection was employed here. Given that we were particularly interested in the first few milliseconds of the decay signal, however, this mass-selection procedure was not employed for the other masses.

All of the measurements with trap temperatures around 90 K were done within a

## 5.2. Fast decays of highly excited $Al_n^-$

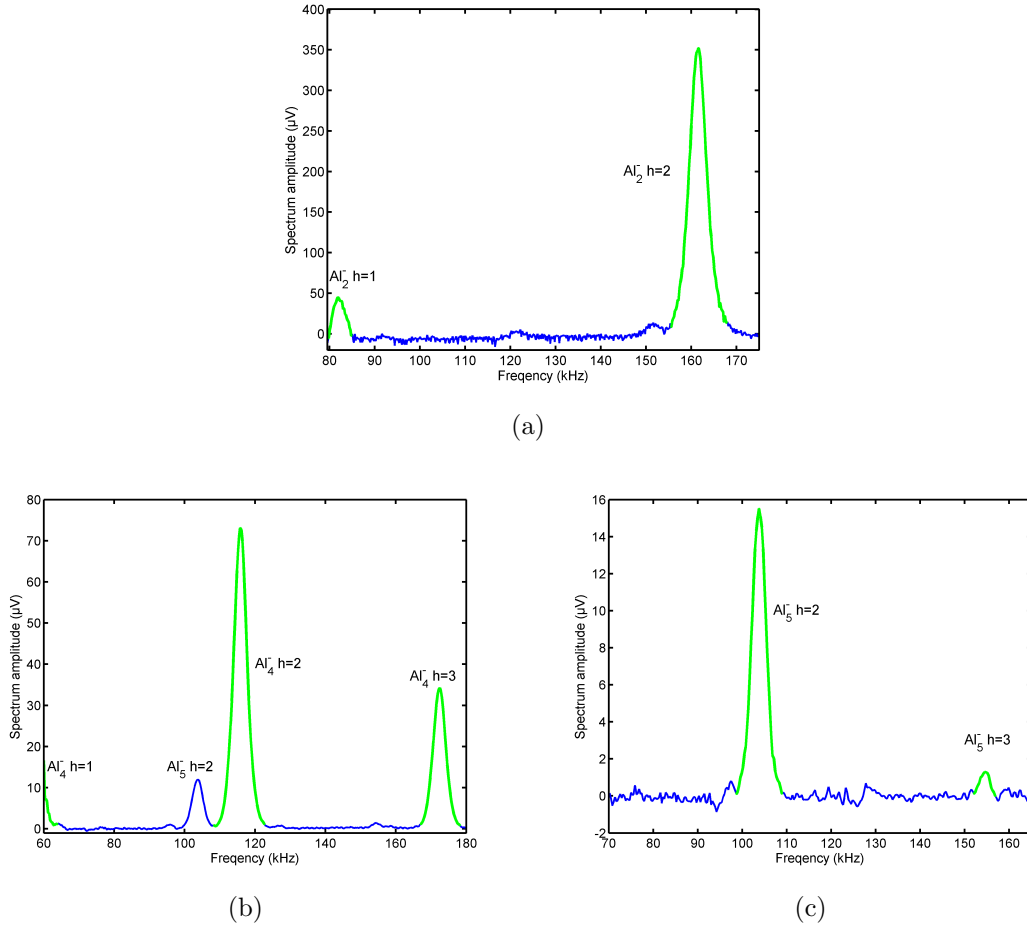


Figure 5.7: Spectrum analyzer sweeps of different stored ion beams at trap temperatures below 15 K. (a) Settings A: Mass-selected  $Al_2^-$  was the only ion species stored. See text for details. (b) Settings C: Peaks from  $Al_4^-$  clearly dominate over those from  $Al_5^-$  (d) Settings F: Only frequency peaks from  $Al_5^-$  are visible. The target ions are illustrated in thick green lines for clarity.

few hours. The ion source was operating differently in comparison to the previous  $<15$  K measurement. The different composition of produced ions, as demonstrated by the spectrum analyzer sweeps using the same timing settings but at different temperatures (see Figures 5.7 and 5.8), might be explained by the sputtering of a material other than the target, since the ion source experienced a water cooling failure shortly after this measurement. The previously unseen heavy mass with a trap oscillation frequency around 90 kHz is most likely  $W^-$ . A laser prompt identification of the trapped masses also yields a much different time of flight spectrum in comparison to the previous  $<15$  K measurements. Various intermediate peaks are also visible, spaced between the expected clusters masses with an offset of 16 amu.

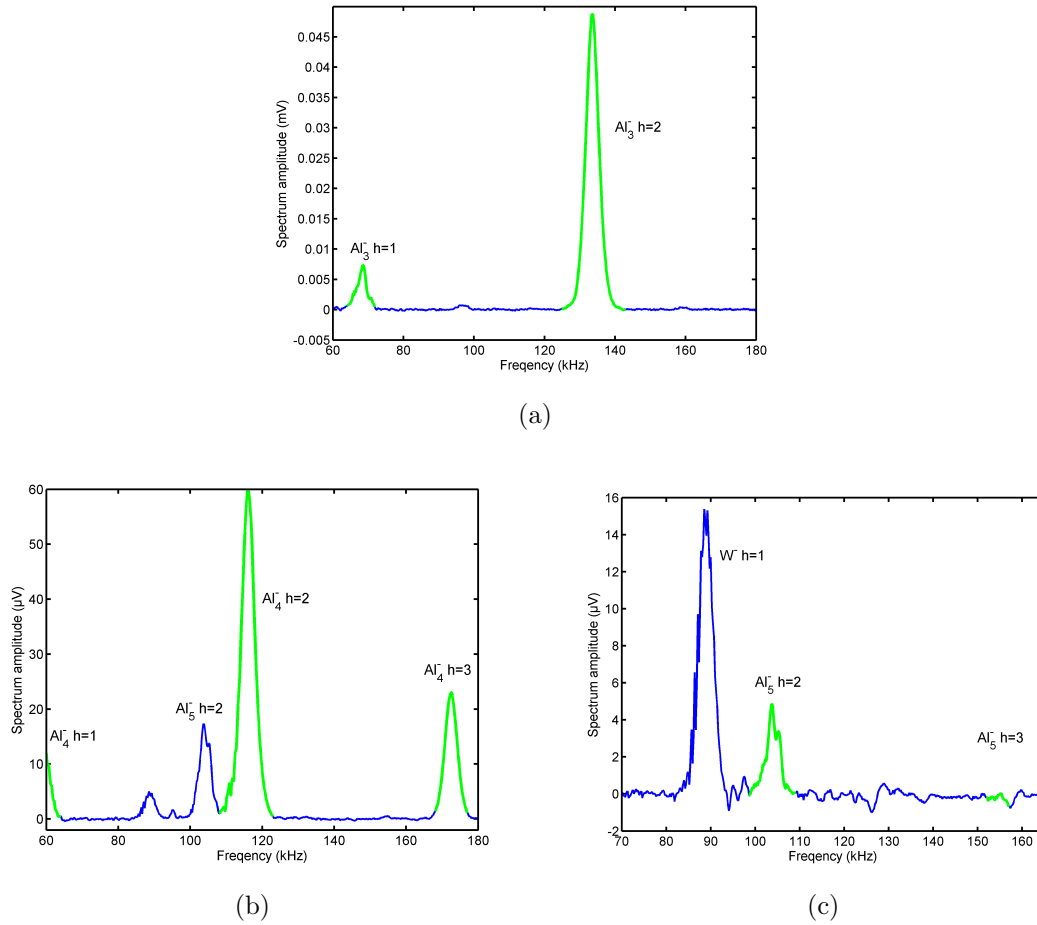


Figure 5.8: Spectrum analyzer sweeps of different stored ion beams at trap temperatures around 90 K. (a) Setting B: Only frequency peaks from  $\text{Al}_3^-$  are visible. (b) Setting D:  $\text{Al}_4^-$  frequency peaks dominate the spectrum, though contamination of  $\text{Al}_5^-$  and  $\text{W}^-$  is also present. (c) Setting G: The target species  $\text{Al}_5^-$  is present, though strong contamination from  $\text{W}^-$  is as well. The target ions are illustrated in thick green lines for clarity.

These aluminum oxides are normally produced from the sputter source directly after changing the aluminum target due to the aluminum oxides still initially present on its surface. The relative concentrations of these aluminum oxide contaminants should, however, be rather small since the target had already been used quite heavily for a week after installation. The large aluminum oxide photo-detachment signals, despite their low abundance in the trap, can most likely be attributed to lower electron binding energies [97] and possibly larger photon absorption cross-sections.

Due to the very low production rates of  $\text{Al}_6^-$ , it was only realistically possible to trap a mixed beam of  $\text{Al}_6^-$  and  $\text{Al}_7^-$ . At such minimal production rates, there

## 5.2. Fast decays of highly excited $Al_n^-$

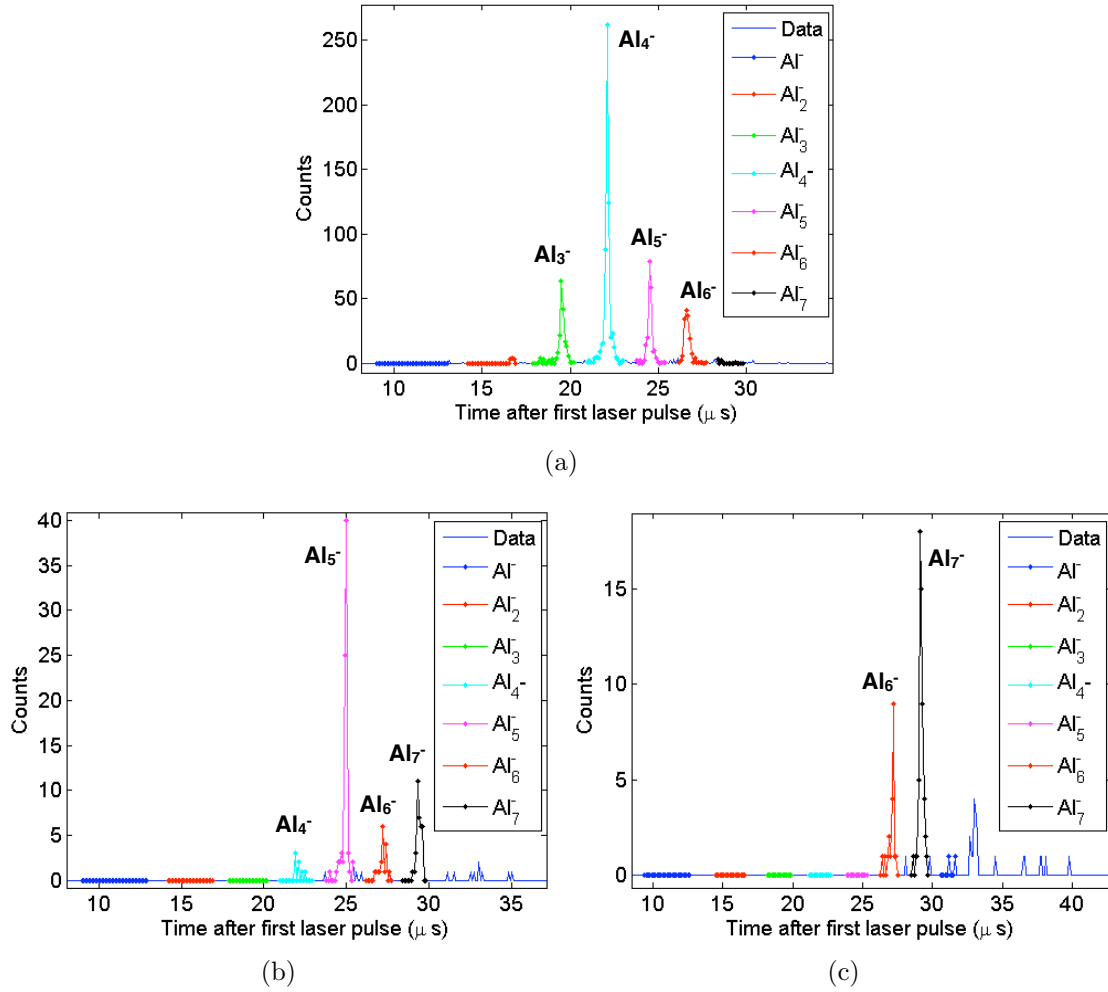


Figure 5.9: Laser prompts of different stored beams at trap temperatures below 15 K. (a) Setting C:  $Al_4^-$  dominated beam (c) Setting F:  $Al_5^-$  dominated beam (d) Setting H: Mixed  $Al_6^-$  and  $Al_7^-$  beam with trace amounts of heavier clusters. Mass identification via TOF is shown for clarity via the peak colour in all plots.

were not enough ions to observe a bunch of the target species passing through the pickup, nor was any peak seen using the spectrum analyzer or an FFT of the pickup signal. The known time of flight times and the trap timing settings were used to select the target species. The laser prompt signal at cryogenic temperatures shown in Fig. 5.9(c) was comparable to that seen at higher trap temperatures. At these electrode delay times, all other light masses would have entered and left the trap tens of microseconds before.

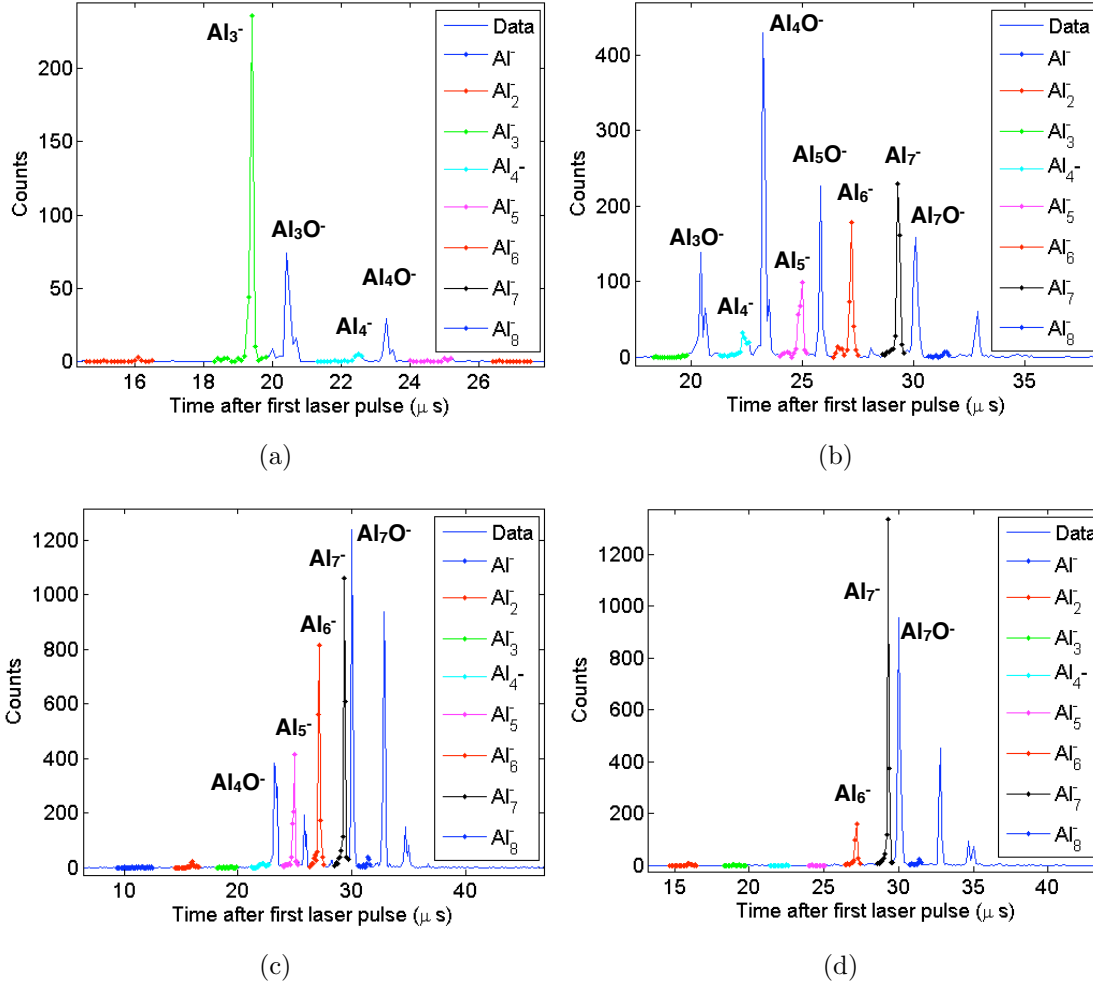


Figure 5.10: Laser prompts of different stored beams at trap temperatures around 90 K with various aluminum oxide contamination masses. (a) Setting B:  $\text{Al}_3^-$  dominated beam (b) Setting E:  $\text{Al}_4^-$  dominated beam (c) Setting G: Mixed  $\text{Al}_5^-$  and  $\text{W}^-$  dominated beam. (e) Setting I: Mixed  $\text{Al}_6^-$  and  $\text{Al}_7^-$  beam. Mass identification via TOF is shown for clarity via the peak colour in all plots. Peaks between identified masses consist of aluminum oxides more easily produced due to smaller electron affinities. See text for details.

### 5.2.3 Fast decay of initially, highly excited $\text{Al}_2^-$

As described in Section 2.5, it was found that the decay of other dimer anions ( $\text{Cu}_2^-$  and  $\text{Ag}_2^-$ ) as a function of time was well described by a power law with an exponent of -1, signaling the presence of a continuum of decay states and constants in the ensemble. Fedor *et al.* [65] argue that this continuum could be provided by the quantum mechanical tunneling decay of high angular momentum rotational states

## 5.2. Fast decays of highly excited $Al_n^-$

populated in the high temperature source. The analysis procedure of these previous metal dimer anions was performed for mass-selected 6.0 keV  $Al_2^-$  at trap temperatures below 15 K. The previously fit background-subtracted MCP count rate using a three-component exponential function in Fig. 5.2(a) is displayed this time using a double logarithmic plot. While equation 2.44 was used to describe the other two dimer anions in [65], it was found adding a small time offset  $t_0$ , as well as a constant term  $B$  to account for residual gas losses yields a better fit, particularly at times directly after injection. The detector rate  $R$  is then given by

$$R = A/(t + t_0) + B, \quad (5.1)$$

where  $A$  is an arbitrary scaling constant. The data points at times after 10 ms were re-binned for clarity; 100  $\mu$ s bins were used at the beginning, while 1 ms bins were used after the initial 10 ms. Already in this figure, a clear  $1/t$  law becomes obvious at times after 10 ms. Note that a short times, this modified  $1/t$  fit more accurately describes the data than the three-component exponential fit.

Due to the excellent vacuum in the CTF, the background from rest gas collisions

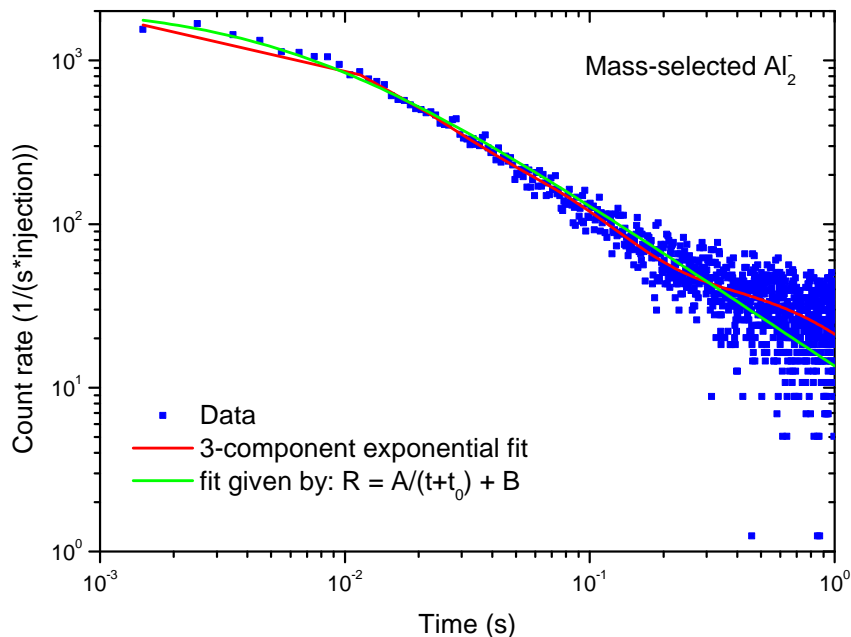


Figure 5.11: The normalized count rate is plotted as a function of the time after injection for a hot, mass-selected  $Al_2^-$  beam stored at a trap temperature of  $<15$  K. The same three exponentials from Fig. 5.2(a) are plotted in this double logarithmic plot for comparison. A second curve (shown in green) based on equation 5.1 is also plotted. See text for details.

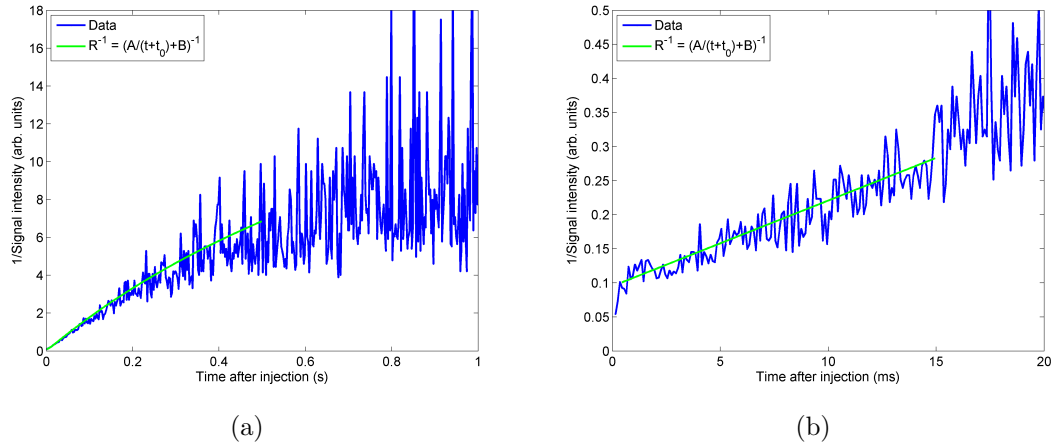


Figure 5.12: (a) Inverted decay rate of a hot, mass-selected  $\text{Al}_2^-$  beam at a trap temperature  $<15$  K. A modified  $1/t$  curve (shown in green) based on equation 5.1 is also plotted. (b) Same data and curve as (a), but over the first 20 ms. See text for details.

is significantly reduced, allowing longer observation times in comparison to the Cu and Ag spectra [65], which deviate from the curve due to background after only 0.007 to 0.02 s, respectively. Plotting the inverse of the detector rate, as similarly done in [65], yields Fig. 5.12(a). The inverse linear decay behaviour is quite clearly visible for  $\text{Al}_2^-$  until at least 0.15 s after the initial ion injection, roughly an order of magnitude longer than previous dimer observations.

While a  $1/t$  relationship is also observed for  $\text{Al}_2^-$  (see Fig. 5.12(a)), an offset is apparent near the origin, as shown in Fig. 5.12(b). Fitting equation 5.1 to the data reproduces the data very well with an offset  $t_0 = 8(3)$  ms. An offset ( $\approx 1$  ms) was observed for one of the species ( $\text{Cu}_2^-$ ) in [65] and was described as being due to the finite extraction time from the source. While deviations near the origin are expected for  $1/t$  fits, an offset in the millisecond range is far too long to simply account for the time of flight between the source and the trap as this is around  $25 \mu\text{s}$  for the CTF. It is also highly unlikely that the ions would require any significant amount of time to leave the source, much less several microseconds. The origin of this offset is, therefore, not yet determined. A strong similarity, however, between the decay of the aluminum dimer anion stored at trap temperatures of  $<15$  K in the CTF and the previously observed decays of Cu and Ag dimer anions at room temperature [65] has been observed.

### 5.2.4 Fast decay of initially, highly excited $\text{Al}_n^-$ clusters

Here the count rate of neutral fragments on the MCP behind the CTF is plotted on a log-log scale, where the first point, due to the initial neutrals produced by the ions inflight along the beam path towards the trap, has been removed. The cluster decays were fit with a  $1/t$  power law model, which includes radiative cooling corrections (see Equation 2.42) as proposed by Andersen *et al.* in [62]. Statistical weighting has been used and the corresponding one sigma (68% confidence level) errors for each fit are shown in Table 5.2. This equation can no longer be used for storage times much longer than 10 ms, since an exponential decay accounting for beam losses due to rest gas collisions must now be included. While the model function reproduces the data for all clusters very well, the previously reported values and proposed limits for the parameter  $\delta$  (the power law exponent correction factor) are much too small to explain observations made with the CTF at trap temperatures below 15 K. Note, that at early times ( $t < \tau$ ) the fitted power law is proportional to  $t^n$ , where  $n = -1 + \delta$ .

Comparing the data taken for all clusters at trap temperatures below 15 K and around 90 K yields Figures 5.13 and 5.14. These spectra are dramatically different in three aspects: the time scale of the fitted characteristic time  $\tau$ , as well as the curve shape and slope correction factor  $\delta$  between the  $<15$  K data sets and those taken around 90 K. In comparison to previous room-temperature measurements, the observed power law slope and  $\tau$  values are extremely different under cryogenic conditions.

The characteristic time  $\tau$  of 0.5 ms observed for both  $\text{Al}_3^-$  and  $\text{Al}_4^-$  is a factor of 20 smaller than the previously published data between 9 and 17 ms for small clusters

Table 5.2: Table of fitted values using equation 2.42 to describe the delayed emission from various aluminum anion clusters by including the effects of radiative cooling. The value in brackets indicates the abundance of the desired species stored in trap.

Ion species (Abundance)	Trap temperature			
	<15 K		$\approx 90$ K	
	$\delta$	$\tau$ (ms)	$\delta$	$\tau$ (ms)
$\text{Al}_3^-$ (99%)			-0.14(11)	0.4(2)
$\text{Al}_4^-$ (88%/78%) (77%)	-0.44(1)	2.03(4)	0.11(5)	0.5(1)
$\text{Al}_5^-$ (99%/21%)	-0.35(1)	2.4(5)	-0.13(2)	1.6(4)
$\text{Al}_6^-/\text{Al}_7^-$ ( $\approx 60\%$ )	-0.26(1)	4(1)	-0.16(4)	2.0(7)

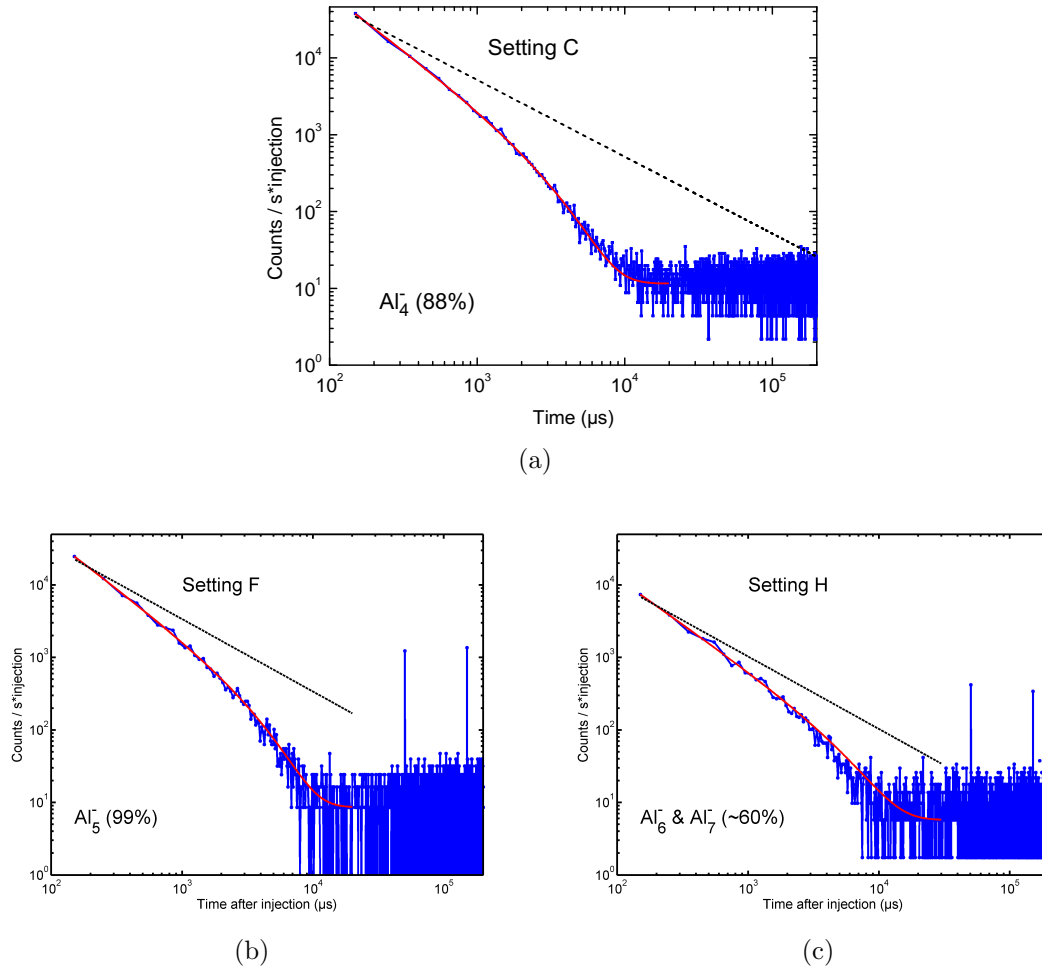


Figure 5.13: The normalized count rate is plotted as a function of the time after injection for a hot  $\text{Al}_n^-$  dominated beam stored at a trap temperature of  $<15$  K. The measured or estimated relative abundance of the target species in the stored beam is indicated in each figure. A modified  $1/t$  power law (equation 2.42) was used to fit the data. A  $1/t$  line has been drawn for comparison (dotted line). The two peaks at later times are the result of laser-dissociated neutral fragments. See the text for details and discussion, and Table 5.2 for the fitted values.

of other species and amino acids stored at room-temperature [62]. This parameter describes the point at which radiative cooling competes with the  $1/t$  decay. It makes intuitive sense that in a colder blackbody environment, the cooling rates should be faster, allowing the stored clusters to cool more quickly than at room-temperature, which would decrease the time at which radiative cooling becomes dominant. What is noteworthy, is that the cooling rates for the larger clusters appear slightly faster at 90 K than below 15 K. Additional research, however, is required to investigate if this is a real effect.

## 5.2. Fast decays of highly excited $Al_n^-$

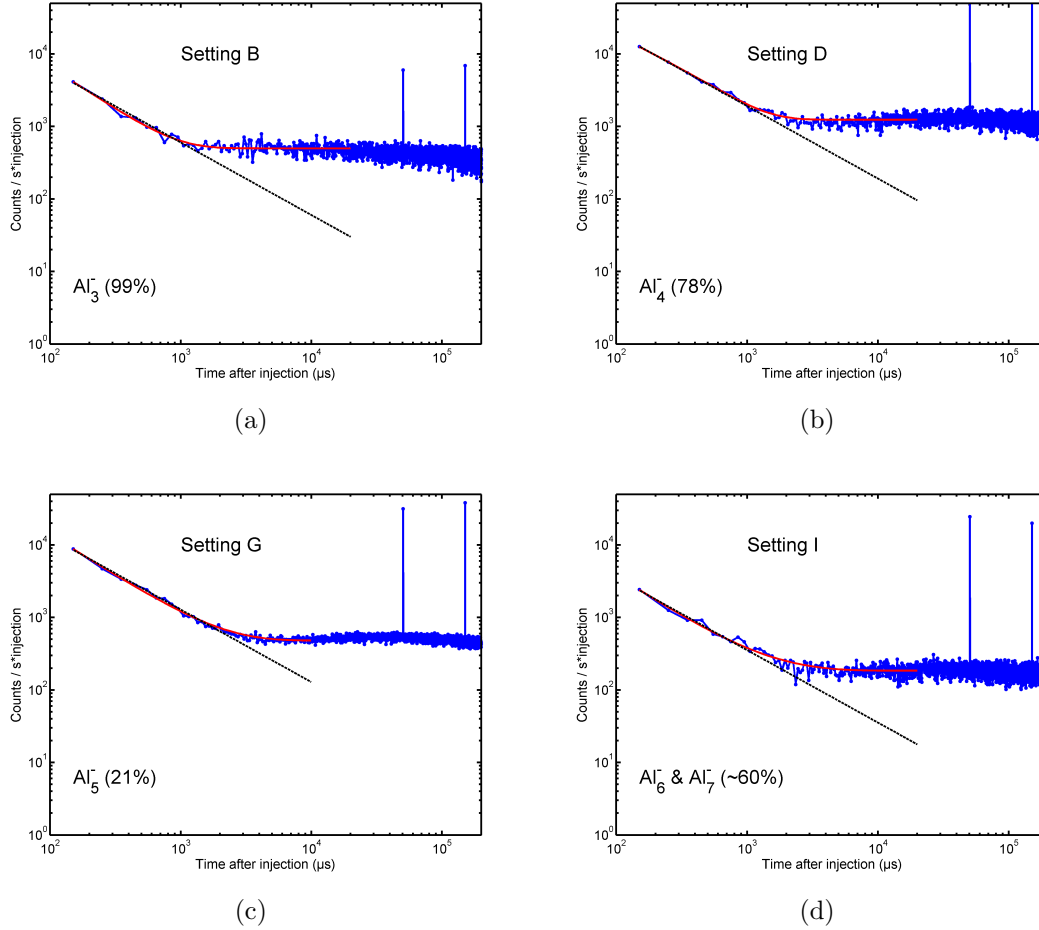
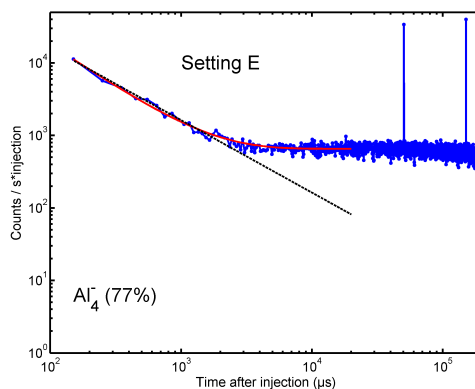


Figure 5.14: The normalized count rate is plotted as a function of the time after injection for a hot  $Al_n^-$  dominated beam stored at a trap temperature of around 90 K. The measured or estimated relative abundance of the target species in the stored beam is indicated in each figure. A modified  $1/t$  power law (equation 2.42) was used to fit the data. A  $1/t$  line has been drawn for comparison (dotted line). The two peaks at later times are the result of laser-dissociated neutral fragments. Higher count rates, in comparison to the  $<15$  K measurements, are a result of a higher trap pressure ( $P = \approx 8 \cdot 10^{-10}$  mbar). See the text for details and discussion, and Table 5.2 for the fitted values and exact trap temperatures.

The change in the decay shape can be partially explained, since the warmer 90 K data was taken when the trap pressure had significantly increased to  $\approx 8 \cdot 10^{-10}$  mbar. The resulting increased background ensured that the previously observable decay shape at trap temperatures of  $<15$  K was obstructed. This, however, cannot account for the change in the curve slope at short times after injection. In all experimental runs, detector saturation was checked for and ruled out, so the change in shape is

Figure 5.15: Fast decay of a highly excited  $\text{Al}_4^-$  dominated beam at a trap temperature of 95 K. A modified  $1/t$  power law (equation 2.42) was used to fit the data. A  $1/t$  line has been drawn for comparison (dotted line). The two peaks at later times are the result of laser-dissociated neutral fragments. See the text for details and discussion, and Table 5.2 for the fitted values.



due to the temperature variation.

A line proportional to  $1/t$  is plotted in Figures 5.13 and 5.14 to show that while the 90 K data seems to have a similar shape as data taken around room-temperature for many other molecules and clusters, the  $<15$  K data is remarkably different. The expected range of the power law exponent correction  $\delta$  of  $\pm 0.1$  [62] clearly does not fit with the presented data. These deviations were previously attributed to possible competition between fragmentation channels (where each one has a different Arrhenius parameter), though this should cause smaller correction values, as explained by Andersen *et al.* in [62]. For all of the larger clusters, the decay results in a far steeper slope. While data is not available for  $\text{Al}_3^-$  at trap temperatures below 15 K, Fig. 5.14(a) suggests this cluster would behave similarly to larger clusters. The observed steeper slopes indicate four possibilities: i) an accelerated cluster decay emptying the  $<15$  K trap, ii) the suppression of the decay via the stabilization (e.g. radiative cooling) of the clusters from their initial highly excited states when stored at temperatures below 15 K, iii) an unknown trap loss mechanism, iv) or alternatively a radiation-induced delayed emission at higher storage temperatures.

Cluster energy stabilization through radiative cooling within the first hundreds of microseconds would be necessary to explain the initial slope of the observed decay described by  $\delta$ . Given that radiative cooling typically requires much longer times scales of tens to hundreds of milliseconds for hot, aluminum cluster anions (as shown in Section 5.3), this doesn't appear very likely. The fitted  $\tau = 0.4$  to 3 ms values, however, qualitatively agree with those seen for amino acids at room-temperature ( $\tau = 9$  to 17 ms). The smaller values obtained here can very likely be attributed to faster cooling rates given the  $<15$  K ambient trap temperatures.

An accelerated decay at temperatures below  $<15$  K is not possible since the ion bunches observed with the pickup do not exhibit any remarkably strong decay, much less one in which almost 99% of the stored ions leave the trap, which would be

## 5.2. Fast decays of highly excited $Al_n^-$

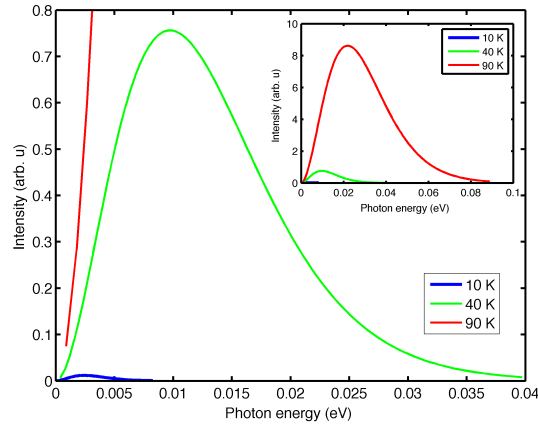


Figure 5.16: Blackbody spectrum as a function of photon energy at 10, 40, and 90 K.

required to produce the observed emission spectra.

A possibility that has not been thoroughly discussed previously in the observation of such  $1/t$  decays is the possibility of beam loss through other mechanisms. A beam loss mechanism dependent on cluster size such as enhanced collisional cross-sections for highly excited clusters could be possible, but this would be expected to scale with the pressure, which would produce the same decay slopes with different background offsets. This can, therefore, be ruled out. Delayed fragmentation of the clusters [73], a process which is most likely temperature dependent (see Section 5.3), does occur. This process, however, should be detected with reasonable efficiency at the employed beam energies, and moreover, would also produce the same decay curve slope under the assumption that radiative cooling cannot happen on such short (within the first milliseconds) time periods. Followup room-temperature measurements on mass-selected  $O^-$  also ruled out some initial trap loss mechanism as an explanation for the observed decay spectra. Such a loss mechanism would also have to be cluster-size dependent, which appears rather unlikely. Intrabeam scattering can be safely ruled out, since far more  $Al_2^-$  ions were available in similar experiments presented in the previous section and the magnitude of trap loss was far smaller than that observed for the larger clusters (see Fig. 5.11). Since both scattering and collisional detachment loss mechanisms scale with the rest-gas-density, which is highly suppressed in the CTF for all 15 K measurements yielding beam lifetimes on the order of hundreds of seconds, this too can be neglected. The possibility of charged cluster fragments being stored in a semi-stable orbit can also be excluded, since any fragment created would not have enough energy to be trapped in an orbit consisting of multiple oscillations, much less thousands of orbits yielding the observed delayed emission

curves. Displacement causing a change in the alignment of the trap electrodes can also be ruled out, since the thermal expansion of metal between 4 and 90 K is also negligible. It is, therefore, very unlikely that trap losses could account for the observed decays.

The fourth possible option is that the  $1/t$  power law decay typically observed at room-temperature is actually radiation-induced. If the absorption of IR radiation is required to dissociate the clusters yielding the typically observed  $1/t$  slope at times directly after ion injection, the removal of this blackbody field would lead to a suppression of the decay rate. As opposed to radiative cooling which requires a relatively much longer time to occur, IR radiation induced decays could occur in the time scales observed here (within the first 20 ms after ion injection) to explain the observed large  $\delta$  deviations from the initial  $1/t$  decay. This suggests that photon energies of over 0.01 eV are required to induce decays in excited aluminum clusters given the blackbody field resulting from an ambient temperature of 15 K (see Fig. 5.16). When the trap temperature was increased to 90 K, the initial decay deviation  $\delta$  approached (within a factor of 3) values typically seen at room temperature for amino acids [62]. It, therefore, seems likely that the initial power law slope of these decays, is radiation-induced.

In summary, the delayed emission results for aluminum cluster anions stored in the CTF at temperatures below 15 K and around 90 K provide the first experimental evidence that the typically observed  $1/t$  power law decay is temperature dependent. Significant differences appear even between the two temperature ranges observed here. The two sets of presented spectra were dramatically different in three aspects: the time scale of the fitted characteristic time  $\tau$ , as well as the curve shape and slope between the  $<15$  K data sets and those taken around 90 K. The CTF's significantly reduced blackbody environment allowed the clusters to cool faster, shortening the time  $\tau$  when radiative cooling dominates the decay to times on the order of 1 ms, as summarized in Table 5.2. What is curious about the  $\tau$  values is that they appear slightly shorter (i.e. radiative cooling dominates earlier after injection) for ions stored at 90 K, which was the *warmer* temperature of the two studied. The initial power law slopes of the decay curves between 15 K and 90 K are clearly temperature dependent. The results presented here suggest that this initial decay is radiation-induced, since radiative cooling on such short time scales appears very unlikely. Clearly, the physics behind the relationship between delayed electron emission and the blackbody temperature of the storage device needs to be investigated further. The CTF will continue with such measurements in its new location, where it is equipped with a magnet mass separator installed in the injection line, permitting single as opposed to mixed masses to be studied.

### 5.3 Photon-induced delayed electron emission and fragmentation of $Al_n^-$

The process of photon-induced delayed emission and the theory required to extract the internal temperature of the cluster was described earlier in Section 2.5.2. The experiment is schematically presented in Fig. 5.17.  $Al_n^-$  ( $n = 4$  to 8) cluster anions are produced in a sputter ion source, injected into the CTF, and stored for a certain time to allow their initially highly excited rovibrational degrees of freedom to relax. This can be accomplished via emission of infrared photons. The clusters are then illuminated by a short laser pulse with a photon energy that is, in principle, sufficient to detach the excess electron. For a portion of the ions, the absorbed energy leads to the immediate emission of an electron (the laser prompt introduced in Section 5.1.2). The absorbed photon can also promote an electron to an excited electronic state, which then couples to the vibrations of the cluster, ensuring that the subsequent emission of the electron can be described by a statistical process similar to thermionic emission from a bulk material. The energy is eventually transferred to the excess electron, which is then detached from the cluster with a delay (typically on the order of several hundred microseconds). The delay depends on the total internal energy of the cluster, where colder clusters emit electrons at later times in comparison to hot clusters. It is important to note that the observed time dependence of the delayed electron detachment rate after the laser shot is related to the energy stored in the cluster *before* the absorption of the photon.

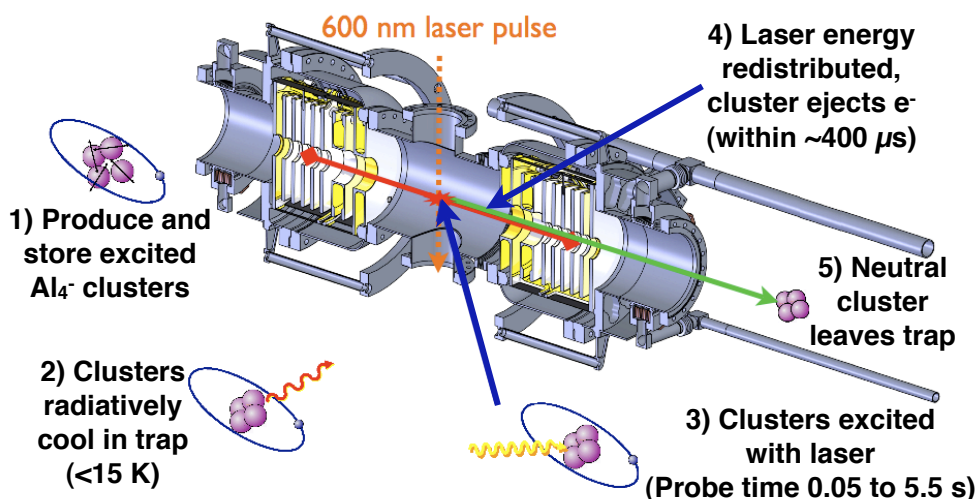


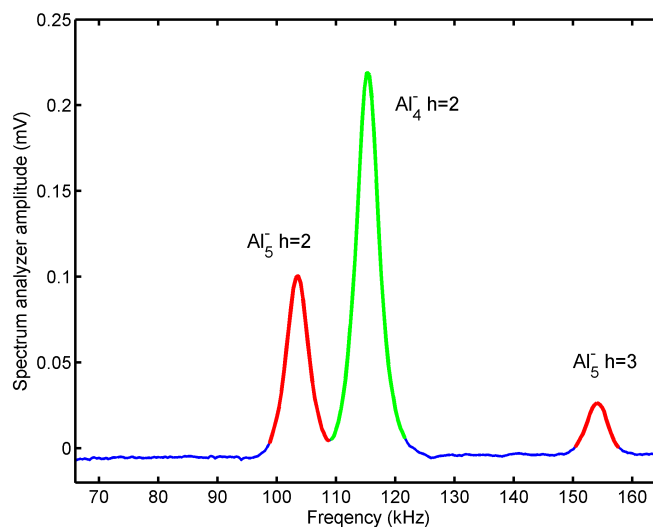
Figure 5.17: An illustration of the photon absorption induced delayed emission used to measure aluminum anion cluster temperatures.

This laser probing was repeated at different times after ion injection, allowing the temperature to be measured as a function of time as the clusters radiatively cool in a blackbody environment below 15 K. This process has already been studied for  $\text{Al}_4^-$  using a trap at room-temperature [67], and our goal was to further investigate the cooling of this species down to cryogenic temperatures and test the model used thus far to explain photon-induced delayed emission in aluminum anion clusters and to extract information about the internal cooling of ions stored in the very low-thermal radiation environment of the CTF.

### 5.3.1 Basic observations

As described in detail in Section 3.3, the CTF was equipped with a sputter source and a 600 nm laser, which produced pulses of 8-10 ns duration with an energy of 3-4 mJ per pulse at a repetition frequency of 10 Hz. This laser was guided perpendicularly through the stored ion beam, entering the trap from the top of the test chamber through a sapphire window. Before entering the CTF, the laser was expanded to a beam diameter of 12.3 mm, as measured at the upper CF40 window of the isolation vacuum, to increase beam overlap and hence the reaction rate, while keeping the power density low to minimize two-photon absorption events. It was ensured that the employed laser intensity only resulted in single-photon absorption by varying the laser intensity and ensuring that the number of delayed events observed linearly scaled with the laser power. The laser was only used at reduced power due to significant losses between the laser and the overlap region with the ions (multiple

Figure 5.18: Sample oscillation frequency scan of the ion beam used in the delayed emission experiment. Despite the presence of various cluster species as shown in the laser prompt peak (see Fig. 5.19), a frequency scan of the pickup signal shows that only significant populations of  $\text{Al}_4^-$  ( $2^{\text{nd}}$  harmonic frequency, green line) and  $\text{Al}_5^-$  ( $2^{\text{nd}}$  and  $3^{\text{rd}}$  harmonic frequencies, red lines) are present.



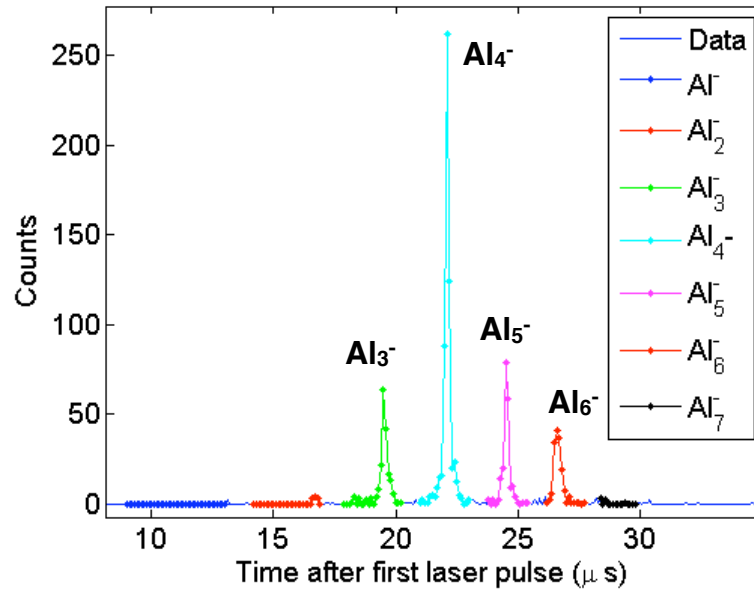


Figure 5.19: Fragment arrival TOF spectrum for a sample laser prompt demonstrating the various masses inside the  $Al_4^-$  dominated (see Fig. 5.18) trap during a delayed emission experiment.

mirrors, a glass window, and a sapphire window). Two-photon processes were, therefore, avoided.

Exploiting the differences in flight times between the different species, the timing of the trap injection process was adjusted to maximize the amount of  $Al_4^-$  in the trap, while avoiding the large contamination of  $Al_2^-$  and  $Al_3^-$  produced by the source. The pickup electrode in combination with the spectrum analyzer was used to observe the stored ion bunch for each mass, shown in Fig. 5.18. Integrating the area under the peaks corresponding to the second harmonic for both  $Al_4^-$  and  $Al_5^-$ , the only significant ion populations, demonstrates that the  $Al_4^-$  abundance is 2.2 times larger than that of  $Al_5^-$ . As illustrated in Fig. 5.19, which shows the intensity of the prompt detachment, created by the immediate dissociation of some of the ions by the laser, other masses in small quantities are also present. As discussed in the previous section, the laser prompt signal is not proportional to the abundance of the various species in the trap, due to cluster-size dependencies of the ion bunch position, laser absorption cross-sections, and the ion cloud/laser beam overlap. The abundances of the respective masses in the trap were therefore measured by the relative integrals of the corresponding second harmonic peaks from the spectrum analyzer, where  $Al_4^-$  accounted for 70 to 80% of the stored ions.

A typical plot of the delayed emission counts versus time after injection can be seen

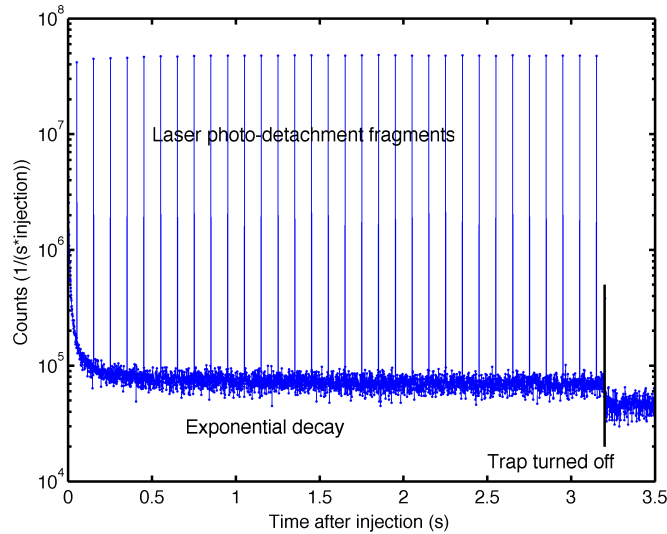


Figure 5.20: A sample 3.5 s aluminum cluster instantaneous decay rate measurement showing a rapid initial decay, the expected long exponential decay, as well as fragments due to laser pulses every 100 ms.

in Fig. 5.20. No mass selection, other than the time of flight selection by injection timing was employed. In the lifetime spectrum, the first data point from the neutrals produced along the beam axis can be seen, followed by a strong, short decay, then a slow exponential decay occupying the majority of the figure, ending with dark counts from the MCP when the trap was turned off. Superimposed on the slow exponential decay, are counts from laser dissociated clusters every 100 ms. A delayed emission signal was acquired in every laser shot, so as time evolved and the clusters had the opportunity to radiatively cool, the laser probed the cluster temperature every 100 ms.

Zooming in on the first laser pulse, the presence of a variety of ions in the trap becomes evident. Due to the different cluster sizes inherently having a different mass, but the same energy (6.0 keV), they arrive at the detector at different times. Simple time of flight between the laser shot and fragment arrival was, therefore, used to identify the various masses in the trap (see Fig. 5.19). This figure is called the prompt signal, as this is the signal that results from clusters which are instantaneously dissociated by the laser, producing neutral counts on the MCP detector behind the trap. While having the laser perpendicularly crossing the ion beam yields far lower photon absorption rates than the merged-beam geometry used in the room-temperature experiment [67], it does allow the simultaneous measurement of delayed emission for multiple aluminum cluster masses.

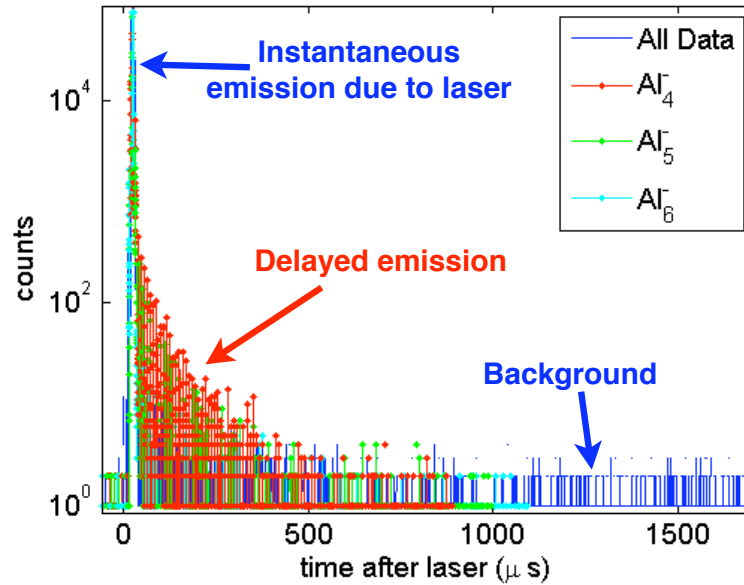


Figure 5.21: A sample delayed emission spectrum including the initial laser prompt, the delayed emission events from mainly  $Al_4^-$  and  $Al_5^-$ , as well as background counts. Plotted are the summed counts from all 30 laser shots as a function of the time after the laser shot for a sample set of data.

Zooming out, and summing up all of the laser pulses, the number of counts on the MCP can be plotted with respect to the time when the laser pulse occurred, as shown in Fig. 5.21. Again, the first strong peaks are those already shown in the laser prompt (Fig. 5.19), followed by periodic counts recurring for several hundred microseconds afterwards at much higher rates than the observed rest gas collisional background.

The periodic structure of these delayed emission events can be seen more clearly and identified by considering a shorter time-scale as displayed in Fig. 5.22. The prompt at the beginning was clearly visible, followed by periodic peaks from the various aluminum clusters, distinguished by their respective trap oscillation periods. The packet of laser-excited ions (a subset of the stored ion beam) traveled up to tens of trap oscillations before it decayed by emitting an electron and thereby yielding a count on the MCP. The injected ions, however, had sufficiently dispersed over the trap during the first 100 ms of storage so that when the laser fired, packets of excited ions were traveling both towards the MCP and away from it. The expected signal, therefore, from each packet of ions arrived every half oscillation period.

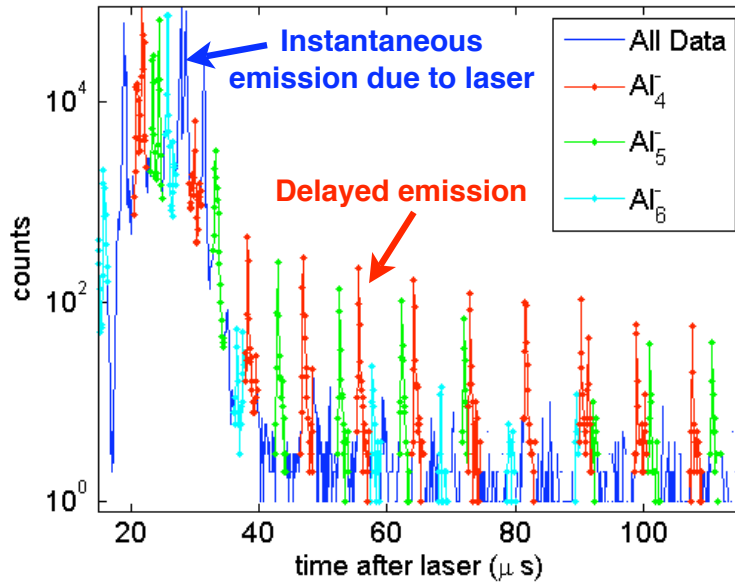


Figure 5.22: A sample delayed emission spectrum showing the initial laser prompt and the signal from the first few trap oscillations. The expected mass peak overlap around  $80 \mu\text{s}$  is also clearly shown. Three colours have been used to label events within the time window for a given cluster size.

### 5.3.2 Analysis and Discussion

While this perpendicularly crossed laser-ion beam method allowed multiple masses to be studied simultaneously, there were points where the signals coincided due to the different ion oscillation frequencies. One such region can be seen for  $\text{Al}_4^-$  and  $\text{Al}_5^-$  at around  $82 \mu\text{s}$  in Fig. 5.22. These events have been ignored in the data analysis.

A second possible effect due to the CTF laser geometry that was considered is a difference in ion density. While it was already stated that the laser shot excited ions traveling both towards and away from the MCP, it cannot be assumed a priori that the ion density of those going in each direction are the same. This is due to the finite length of the stored ion bunch, where during the first laser shot at  $50 \text{ ms}$  after injection, the bunch might not yet have fully dispersed over the entire trap (see section 4.2.4), thus allowing the possibility of the laser striking a denser ion region or part of a gap in the ion beam cloud for a given species. Two cooling curves will be considered for every laser shot to ensure that any differences in ion density are visible. Both sets of data, despite a possible offset in the number of counts, should yield the same cooling behaviour. All data runs were taken using the same trap potentials and were summed over all ion currents and laser powers as justified

### 5.3. Photon-induced delayed electron emission and fragmentation of $Al_n^-$

---

Table 5.3: Table of values (barrier energy, Arrhenius factor, and heat capacity) used in the temperature analysis of the observed  $Al_4^-$  and  $Al_5^-$  photon-induced delayed emission. The heat capacity  $C(T)$  is temperature dependent, so a typical value is shown to indicate the approximate size of the values used.

Anion	$E_b$ (eV)	$A$ ( $s^{-1}$ )	$C(T)$ ( $k_b/N_{atoms}$ )
$Al_4^-$	1.74 [98]	$3.3 \cdot 10^{10}$ [67]	$\approx 2.3$ [99]
$Al_5^-$	1.82 [98]	$1.3 \cdot 10^{12}$ [100]	$\approx 2.6$ [99]

later in this section. Note that while the statistics sometimes appear limited, a solid month of data acquisition was required to produce the results for this particular experiment.

The counts due to the delayed emission of  $Al_4^-$  in a given time window, again identified by the time of flight, are summed and plotted with respect to time after the laser shot. Equation 2.48 can now be used to fit the temperature of the cluster at any given time. The fit employs the cluster specific values, namely, the number of atoms in the cluster, the heat capacity, and the barrier energy in addition to the wavelength used to probe the temperature. This formula is then integrated over a Gaussian energy distribution of states, which is given by a canonical ensemble as shown in equation 2.47, each with the same temperature,  $T_i$ .

The model parameter values used in the analysis presented here were the same values used in the analysis of the  $Al_4^-$  experiment at room temperature reported by Toker *et al.* [67] (see Table 5.3). It should be noted that the published value of  $1.4 \cdot 10^{10} s^{-1}$  differs from the value most likely used in this study. This will be discussed in detail later. The employed value of  $A = 3.3 \cdot 10^{10} s^{-1}$  essentially assumes that the temperature assignments in the previous study were correct, namely that the  $Al_4^-$  ions were almost cooled to room-temperature after 0.5 s of storage in a trap at room-temperature. The temperature dependent heat capacities were taken from calculations of neutral aluminum clusters [99], where a typical value has been stated in Table 5.3 to give a rough idea of the order of magnitude. To fit a curve, a normalization constant was varied to find the lowest Chi-squared value, thus minimizing the difference between the data and the fit. The only other parameter remaining in the fit was the temperature of the ion ensemble,  $T$ .

Overlaying the delayed emission curves of three fitted sample laser shots taken at times 0.05, 0.75, and 2.75 s after ion injection produces Fig. 5.23. It can be clearly seen that at times shortly after ion injection, the ions are still relatively hot, resulting in a very steep delayed emission curve. At later trap times  $t_i$ , the ions have had a chance to radiatively cool, reducing their internal temperature and

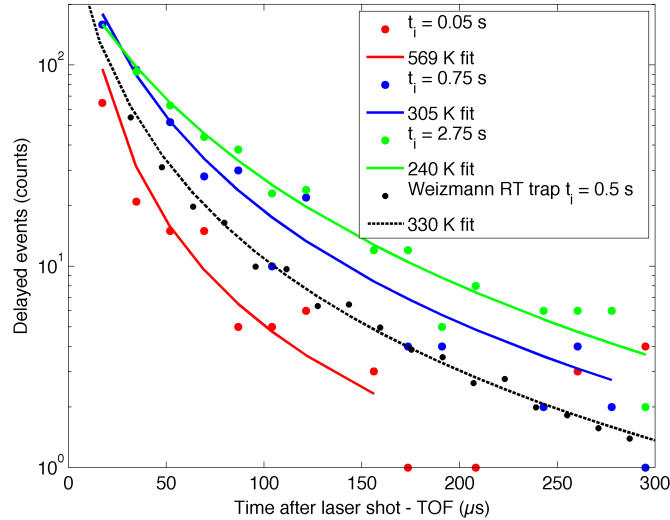


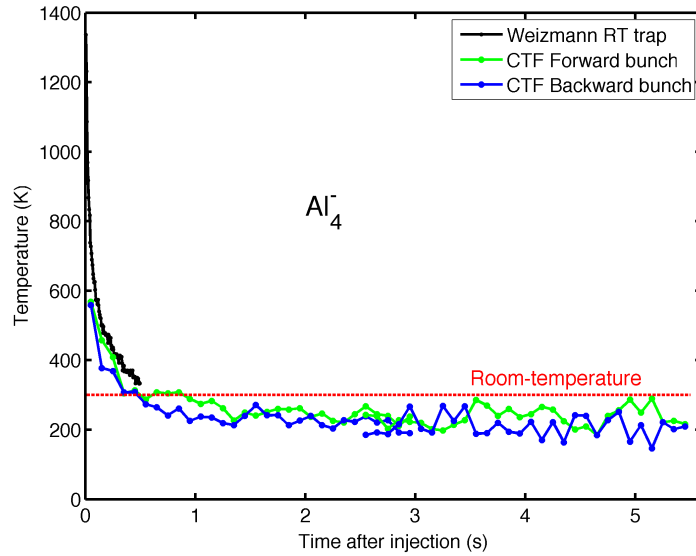
Figure 5.23:  $\text{Al}_4^-$  delayed emission as a function of time after laser excitation (minus the time of flight from the middle chamber to the detector) for 3 CTF sample probe times after ion injection (0.05 s, 0.75 s, and 2.75 s) with a trap temperature  $< 15$  K. The last published probe time ( $t_o = 0.5$  s) at room temperature by Toker *et al.* [67] is also plotted for comparison, where these values have been scaled to match the unscaled CTF values.

producing a delayed emission curve, which is flatter and contains more delayed events at later times. Fig. 5.23 also contains the last delayed emission curve taken 0.5 s after trap injection in the room-temperature experiment performed by Toker *et al.* [67]. The time dependency of the delayed emission is consistent with what was observed at the CTF (i.e. both have similar curve shapes). Further measurements at times longer than 0.5 s were not possible due to pressure-dependent ion losses. The curves demonstrate that regardless of the absolute temperature scale calibration, the delayed emission of the cluster ensemble in the CTF continued to cool resulting in flatter curves at later storage times.

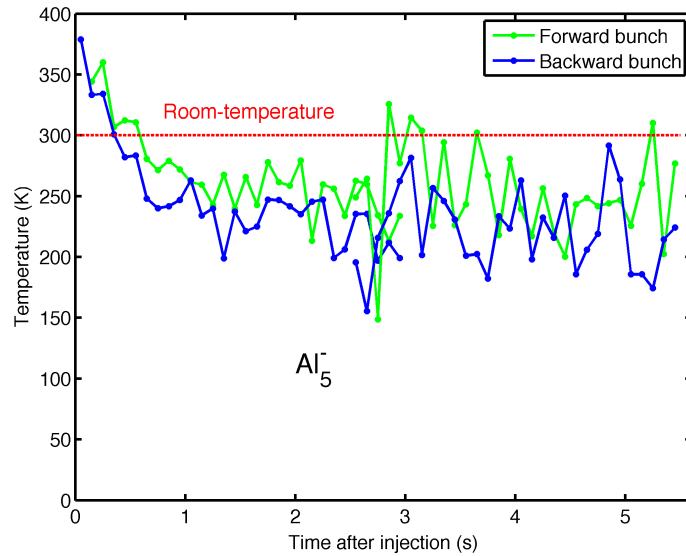
Repeating this fitting procedure for all laser shots for both the ions moving towards and away from the MCP and plotting the fitted cluster internal temperature  $T$  as a function of ion injection time yields Fig. 5.24(a). The derived  $\text{Al}_4^-$  cluster temperatures from the room temperature experiment by Toker *et al.* [67] are also plotted with the data taken with the CTF. The calculated temperatures are consistent at times shortly after injection, where the obtained cluster temperatures in the CTF appear slightly cooler at comparative times than in the room-temperature case. The accuracy of the obtained temperature is statistics limited, as can be seen

### 5.3. Photon-induced delayed electron emission and fragmentation of $Al_n^-$

in the spread of the two bunches illustrated in Fig. 5.24(a). The fitted temperature appears to stabilize after around 1.5 s after ion injection and an average of the data points after this point yields a temperature of  $230 \pm 30$  K. The data spread cannot



(a)



(b)

Figure 5.24: Fitted (a)  $Al_4^-$  and (b)  $Al_5^-$  internal cluster temperature as a function of time after ion injection at trap temperatures  $<15$  K. The data taken by Toker *et al.* [67] for  $Al_4^-$  in a room-temperature EIBT is also plotted for comparison.

rule out a slow decrease in temperature at later times, but the fitted temperature value does appear to be stable at these times.

While delayed emission was seen in additional clusters, only enough statistics for  $\text{Al}_5^-$  exist to perform the same temperature analysis. For consistency, all of the employed model parameter values originate from the same sources as those used for  $\text{Al}_4^-$  (see Table 5.3), where  $A$  was taken from previous unpublished measurements [100]. Performing the same fitting procedure as outlined above, but now for  $\text{Al}_5^-$  yields Fig. 5.24(b). As was similarly observed for  $\text{Al}_4^-$ ,  $\text{Al}_5^-$  also starts at a hot source temperature and radiatively cools to a mean temperature of  $240 \pm 40$  K (summing all points after 1 s). One point at the beginning of the backward labeled curve is not displayed, since there were too few events to fit the temperature. It is worth noting that  $\text{Al}_5^-$  appears to cool faster, suggesting that the additional vibrational degrees of freedom allow more efficient radiative cooling. The fitted temperature values for both cluster sizes, should however be considered cautiously due to the problems with the theoretical model discussed below. While the model can accurately reproduce the observed delayed emission and it appears that the changes in the delayed emission spectra are a direct result of the radiative cooling of the clusters, it will be shown that the temperature calibration is not reliable.

#### **Delayed emission in $\text{Al}_n^-$ ( $n = 4$ to $8$ )**

As multiple masses were trapped simultaneously in the trap, the data also conclusively demonstrates that delayed emission occurs in  $\text{Al}_4^-$ ,  $\text{Al}_5^-$ ,  $\text{Al}_6^-$ ,  $\text{Al}_7^-$ , and  $\text{Al}_8^-$  (see Fig. 5.25). The background counts are displayed in the first  $100 \mu\text{s}$  before the laser pulse, followed by the prompt peak (the counts produced from the instantaneous dissociation of a given species), and the delayed events over the next  $600 \mu\text{s}$ . Note that data points corresponding to times when multiple species arrived simultaneously have been deleted where easily identifiable (i.e. there were enough counts to visibly check the overlap region). The delayed emission temperature fits for  $\text{Al}_4^-$  and  $\text{Al}_5^-$  only considered data up to  $500 \mu\text{s}$ , where overlapping peaks could be clearly identified. The delayed event peaks for  $\text{Al}_6^-$ ,  $\text{Al}_7^-$ , and  $\text{Al}_8^-$  had far fewer statistics, so data at times beyond  $150 \mu\text{s}$  after a laser shot was ignored, since it could not be conclusively determined if the peaks overlapped or not.

As the cluster temperature decreases, the produced delayed emission curve changes shape, as shown previously in Fig. 5.23. Taking an integral of the number of  $\text{Al}_4^-$  delayed emission counts from all such a curves (from 0.05 to 3 s after ion injection) at times between 8 and  $400 \mu\text{s}$  after a laser shot is plotted in Fig. 5.26. Due to data acquisition computer memory limitations, it was only possible to acquire a maximum of 3 s of data with enough time resolution to perform mass identification. Additional data runs starting 2.5 s after injection extended the aluminum cluster

### 5.3. Photon-induced delayed electron emission and fragmentation of $Al_n^-$

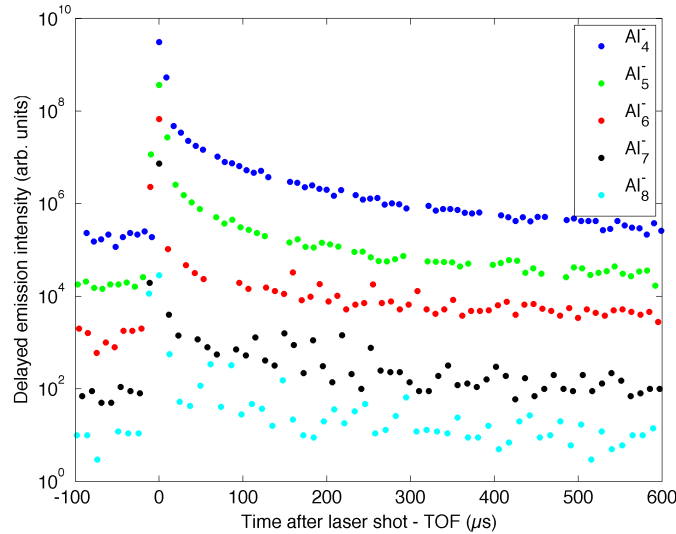


Figure 5.25: Summed delayed emission counts over all laser shots (from 0 to 3 s after ion injection) as a function of time after laser excitation (minus each cluster’s respective time of flight from the middle chamber to the detector) for  $Al_4^-$ ,  $Al_5^-$ ,  $Al_6^-$ ,  $Al_7^-$ , and  $Al_8^-$ . See text for details.

temperature probing experiments to 5.5 s. This data set has been normalized to the first by taking the average of the overlapping entries and scaling the second data set (including errors). While the statistical errors have been plotted, the scatter of the data demonstrates that the errors associated with each point may be slightly larger. It is interesting to note that there is a downward trend over longer periods of time, which would normally be associated with the temperature of the ions increasing. The temperature fits indicate, however, that no significant  $Al_4^-$  temperature change has occurred (see Fig. 5.24(a)).

The integral of the number of delayed events observed performed for the other larger clusters (see Fig. 5.26) demonstrates very different behaviour for the five aluminum clusters investigated. In particular,  $Al_6^-$  shows a time development that’s remarkably different from that of the other clusters (increasing, plateauing, then slowly returning to the initial level). This could result from the photon energy employed in this experiment, which may correspond to a prominent feature in the absorption cross-section. It could also indicate differences in cooling rates, or branching ratios between electron emission and fragmentation. Aluminum clusters with up to 5 atoms are expected to be planar and their corresponding photoelectron spectra seem to support this [23]. It is, however, noteworthy that  $Al_6^-$  and  $Al_7^-$ , while showing some characteristics of the smaller clusters, represent a transition to larger clusters

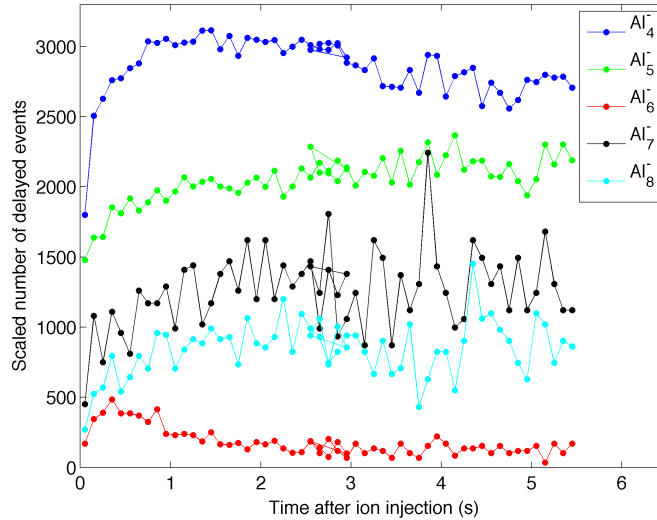


Figure 5.26: Total delayed emission events for  $\text{Al}_4^-$  to  $\text{Al}_8^-$  as a function of time after injection. Note that the amplitudes have been scaled for easy visual comparison.

with 3D structure. It has been suggested that these clusters may have a nearly planar or slightly buckled geometry [23]. Future investigations of these clusters should address the observed cluster-size differences, particularly the anomalous  $\text{Al}_6^-$  delayed event events as a function of storage time.

### Choice of $\text{Al}_4^-$ $A$ factor

While an Arrhenius factor of  $1.4 \cdot 10^{10} \text{ s}^{-1}$  was published in [67], the actual employed value was most likely  $3.3 \cdot 10^{10} \text{ s}^{-1}$ , which can be deduced from the ratio between two given points on a delayed emission curve from the fit model (see Fig. 5.30(a)). Had the first value actually been employed, the final fitted temperatures achieved in their room-temperature trap would have been significantly higher. Using the published value of  $A = 1.4 \cdot 10^{10} \text{ 1/s}$  [67] and performing the same data analysis procedure outlined above, an offset in the temperature scale presented in Fig. 5.24(a) is introduced. In this case, an internal temperature of  $350 \pm 40 \text{ K}$  after 1.5 s (averaging all data points after this time) would be obtained. This erroneous value of  $A$  also explains why the CTF data at trap temperatures of  $<15 \text{ K}$  yields hotter  $\text{Al}_4^-$  cluster temperatures than a trap at room-temperature using shorter storage times. Moreover, the delayed emission spectrum presented in Fig. 5.23 from Toker *et al.* [67] is consistent with a model temperature of 330 K which employed an  $A$  value of  $3.3 \cdot 10^{10} \text{ s}^{-1}$ . This temperature is also consistent with the extracted temperature presented in [67]. This confirms the choice of the Arrhenius factor employed in this

### 5.3. Photon-induced delayed electron emission and fragmentation of $Al_n^-$

study. Various problems with this statistical model, as discussed below, show that a reliable temperature calibration is not possible, at least at cryogenic temperatures.

#### Investigating ion current dependency

A change in the injected ion beam current does not result in a different final cooled temperature, as shown by three data sets taken at total injected ion currents (all masses) of 0.65, 2.4, and 2.9  $\mu A$ . As all three sets of  $Al_4^-$  data showed no change in the shape or number of delayed events in storage times larger than 1.5 s, the last 15 laser shots were added together to provide better statistics. This combined plot of delayed events vs time after the laser shot was then fitted for each ion beam current, as shown in Fig. 5.27(a). The resulting final  $Al_4^-$  temperatures of between 237 and 265 K are relatively consistent with each other, which is also evident from the identical curve shapes. A different curve shape would be indicative of a different cluster temperature, as shown in Fig. 5.23. While there were indications that the cooling rate of the ions within the first second after ion injection varied with the beam current as shown in Fig. 5.27(b), the final temperature was invariant and not enough statistics were available to fit the temperature of each data set separately. It can only be concluded that if some current dependent property such as intrabeam scattering is present, and the model used for this fit is correct, it doesn't result in a different final temperature for the three currents studied here.

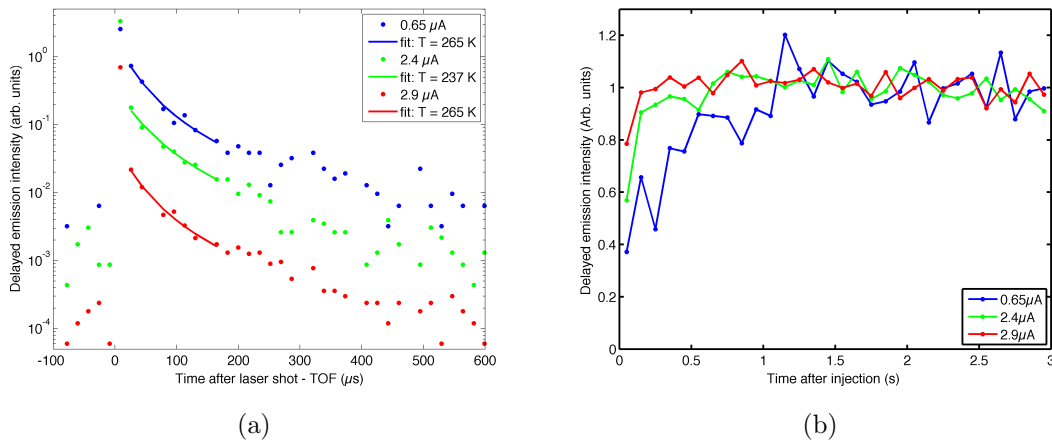


Figure 5.27: (a)  $Al_4^-$  delayed emission intensity as a function of time after laser excitation (minus the time of flight from the middle chamber to the detector) for 3 different injected ion currents resulting in the same fitted temperature. (b)  $Al_4^-$  delayed emission intensity as a function of time after injection for 3 different injected ion currents, normalized to the average value after 1.5 s.

### Early signal not reproducible using theoretical model (Evidence of delayed fragmentation as opposed to delayed electron emission)

The prompt peak from the excited ion packet moving away from the MCP at the time of the laser pulse cannot be detected as there is no detector on the ion injection side. This excited beam packet, however, turns around and produces a clear delayed event signal just  $8\ \mu\text{s}$  after laser excitation (where the TOF between the middle chamber and detector has already been subtracted). These counts are clearly identified as delayed events coming from the trapped  $\text{Al}_4^-$  clusters, since the background events (visible in Fig. 5.30(c) before the laser shot) due to rest gas collisions are negligible. The magnitude of this  $8.7\ \mu\text{s}$  signal relative to the expected number of counts from the statistical model is a factor of 10 larger, as shown in Fig. 5.30(c). Conceivably  $\text{Al}_8^-$  could also arrive at the same time, but the trap electrode timing combined with the very low production rate of this species ensured delayed emission rates were almost 30 times smaller than for  $\text{Al}_4^-$ , excluding this possibility. This new, unexpectedly large number of delayed events at early times already demonstrates a problem with the employed model.

As a result of this large incongruity, the inclusion of this point in the fitting range would have yielded grossly inaccurate fitted curves. Only by allowing the Arrhenius factor, barrier energy, and temperature to all simultaneously take on extremely unrealistic values, could the data be somewhat reproduced. This point was, therefore, ignored in the temperature analysis, but still represents valid delayed events. The

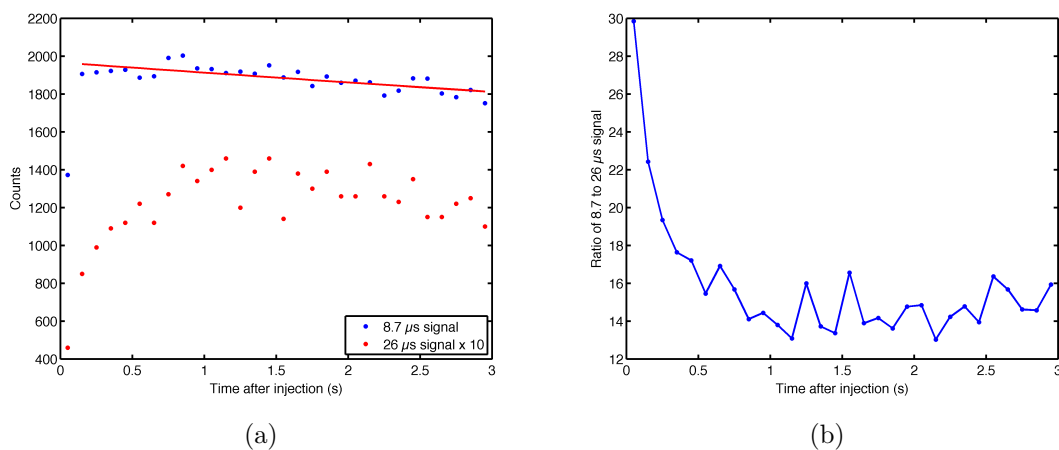


Figure 5.28: (a) Counts of the first and second  $\text{Al}_4^-$  delayed emission signal plotted vs time after injection. An exponential fit shows the loss of the beam with time. (b) Ratio of the first to second delayed emission signal showing a temperature dependence of this ratio.

### 5.3. Photon-induced delayed electron emission and fragmentation of $\text{Al}_n^-$

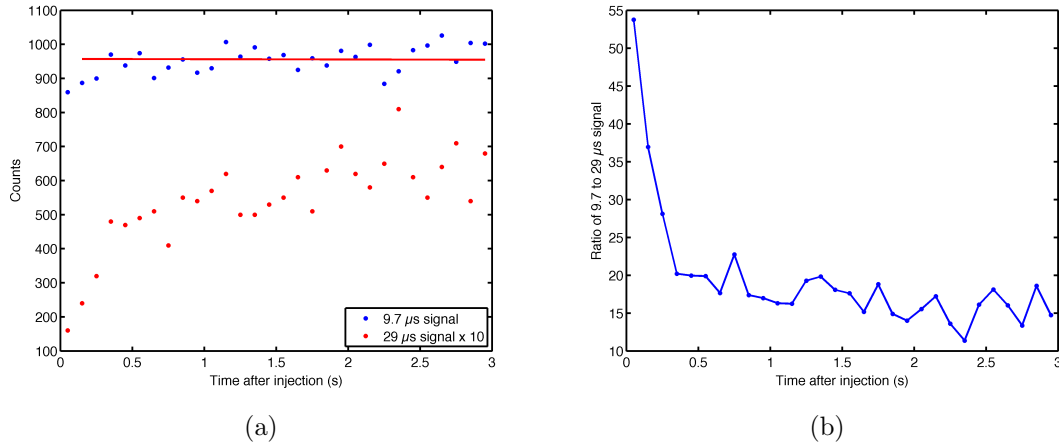


Figure 5.29: (a) Counts of the first and second  $\text{Al}_5^-$  delayed emission signal plotted vs time after injection. An exponential fit shows the loss of the beam with time. (b) Ratio of the first to second delayed emission signal showing a temperature dependence of this ratio.

previous room-temperature study [67], due to the geometry of their experimental setup, was not able to identify delayed events this early after each laser shot, but instead around  $20 \mu\text{s}$  (again, TOF is already subtracted for easier comparison). Our results are, therefore, still consistent. This large number of delayed emission events was also observed and ignored in the fitted treatment of  $\text{Al}_5^-$ , when it occurred  $9.7 \mu\text{s}$  after laser absorption.

A possible explanation for the  $8.7 \mu\text{s}$  signal could rest with the newly reported delayed *fragmentation* of  $\text{Al}_4^-$  [73], which the employed theoretical model does not consider. As opposed to emitting an electron, the anion can also fragment into an aluminum atom and an  $\text{Al}_3^-$  anion after a certain delay. This channel occurs with a branching ratio (at laser photon wavelengths of 600 nm) of at least 8% [73]. At CTF beam energies, the neutral aluminum atom should be detected. The charged fragment will be ejected from the trap, since it doesn't have enough energy to be stored, while the trap potentials prevent them from hitting the on-axis detector. As the branching ratio between these two processes may also be temperature dependent, this may have a huge impact on the shape of the combined delayed emission curve. As shown in Fig. 5.28(a), the absolute number of counts from the  $8.7 \mu\text{s}$  signal, excluding the first point, varies slowly as a function of time. As the first point is measured 50 ms after the initial injection, the stored bunch is still coherent and does not yet homogeneously fill the entire trap. This has already been observed for low ion density  $\text{Al}_2^-$  bunches as reported in Section 4.2.4. After around 150 ms, the ions are assumed to have spread uniformly throughout the trap, leading to a

beam decay due to rest gas collisions. The plotted exponential fit of the  $8.7 \mu\text{s}$  signal yields a decay lifetime of 36 s, though given the relatively short measurement time, it can only be concluded that a long lifetime component exists. The next trap oscillation of this ion packet after the large signal at  $26 \mu\text{s}$  displays a slow increase of the delayed emission as a function of storage time. This should correspond to the cooling of the clusters. This signal slightly decreases with the number of ions in the trap at later trapping times. Plotting the ratio of the counts at  $8.7 \mu\text{s}$  and at  $26 \mu\text{s}$ , Fig. 5.28(b) clearly shows a time dependence, and therefore a change in the cluster temperature, which could be explained via delayed fragmentation. Similar trends were found for  $\text{Al}_5^-$  as shown in Fig. 5.29, where the ratio is even larger at early times. Assuming delayed fragmentation is responsible for this large signal (as opposed to a fast decaying isomer for example), this would suggest that the branching ratio between delayed fragmentation and electron emission is temperature dependent, and is more enhanced in  $\text{Al}_5^-$ , in comparison to  $\text{Al}_4^-$ .

While changes in the photon absorption efficiency for these two cluster sizes as they cool could explain changes in the delayed emission amplitude as a function of time (see Fig. 5.26), this cannot explain the observed ratio of the first two consecutive trap oscillation signals for  $\text{Al}_4^-$  (Fig. 5.28(b)) and  $\text{Al}_5^-$  (Fig. 5.29(b)). Delayed fragmentation and its temperature dependence, is therefore, the most likely explanation for this signal at short times after laser absorption.

### **Possible reasons preventing cluster temperatures below 230 K**

Before investigating problems with the theoretical model, the effective trap temperature seen by the ions must be considered. A small amount of 300 K radiation does penetrate the trapping region directly along the beam axis from both ends of the trap by necessity of the openings for ion injection and fragment detection. The solid angle of this radiation influx is, however, less than  $1/20,000$  of the  $4\pi$  radiation that is emitted at temperatures below 15 K. From the total radiation input power, even very conservative estimates would yield an effective radiation trap temperature of 25 K, which cannot explain the fitted cluster temperatures of around 230 K for  $\text{Al}_4^-$  and  $\text{Al}_5^-$ . Since the chambers storing the ions were below 15 K and contribute the majority of the radiation field seen by the ions, this temperature has been typically cited as the trap temperature.

Heating of the ions due to trap potential stability was also considered, as the HV on those electrodes which are switched exhibit slight ripples of less than 10 V in amplitude due to the switches themselves. Even unrealistically estimating that the radiation power emitted is given by the product of the ripple current and voltage amplitude (60 mVA), and that this over-estimated radiation is absorbed by the clusters with the same cross-section as infrared photons, the clusters could still cool to

50 K.

While the final fitted temperature of  $Al_4^-$  at times after 1.5 s appears to be independent of the employed total ion beam current (as displayed in Fig. 5.27(a)), a difference does exist in the number of delayed emission counts at short time scales as shown in Fig. 5.27(b). The available statistics of these individual runs were, however, not enough to make any claim about this effect. It would be worthwhile to study this in the future to determine if internal beam interactions played a role in the observed cooling and therefore the cluster temperature.

As discussed below, various problems with the statistical model strongly indicate that accurate temperature calibration was not achieved. In light of this conclusion, the derived aluminum cluster temperatures ( $\approx 230$  K) after 5 s of storage in a trap with an ambient temperature below 15 K are not considered accurate. It seems very unlikely, however, that other factors could have prevented the stored aluminum anions from radiatively cooling down in the CTF.

#### **Problems of the statistical emission model**

The physics of delayed emission is far more complicated than that which is included in the applied statistical model. The discrepancies between the CTF delayed emission measurements and the employed model are discussed below.

Firstly, due to a lack of theoretical heat capacities of the aluminum cluster anions, the values for the corresponding neutral clusters were used. According to [99], these values are almost constant (they vary by less than a factor of two) between 0 and 1000 K and in the case of  $Al_4^-$  have a low-temperature limit of around  $8.8 k_b$ . It may not be valid to assume that the anion clusters have the same characteristics, even if the theoretical calculations themselves are correct. Assuming, instead, that the initial magnitude of the heat capacity at high temperatures is correct, but approaches zero as the temperature decreases to absolute zero, these modified heat capacity values return a temperature difference of less than 4 K between the achieved cooled temperature after 1.5 s of storage. The employed statistical model is, therefore, not sensitive to such changes and the employed neutral cluster heat capacity values are also questionable.

Secondly, the time dependence of the observed delayed emission curve for laser pulses after 1.5 s was not well reproduced by the single exponential component returned by the applied model if the clusters cooled down to cryogenic temperatures, as shown in Fig. 5.30(c). This indicates that either the ions have not cooled down to these temperatures, or the theoretical model used does not accurately reproduce the observed data. Using a different  $A$  value would also not produce fitted temperatures of either cluster species significantly below 200 K, since the model-delayed

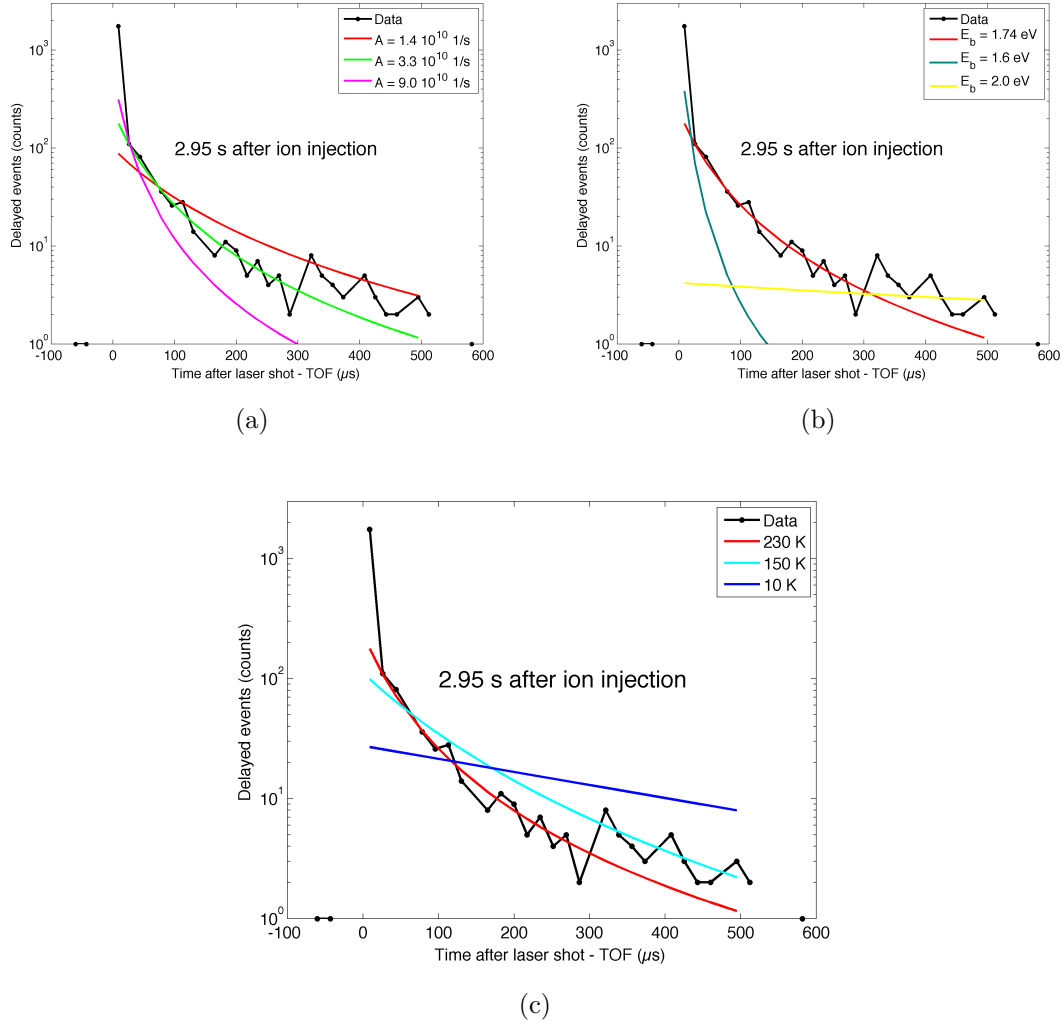


Figure 5.30: Sample  $\text{Al}_4^-$  delayed events vs time after a laser shot (minus the time of flight from the middle chamber to the detector) demonstrating the unexpected large number of delayed events at short times and the model effect of varying the (a) Arrhenius factor, (b) barrier energy, and (c) temperature. The time after injection  $t_i = 2.95 \text{ s}$  for the plotted data. If not varied, the default values stated in Table 5.3 were used in the presented model curves, in addition to a temperature of 230 K.

emission curve shape quickly approaches a single exponential that will not reproduce measured data at later times after injection (see Fig. 5.30(c)). Since the measured delayed emission curves consist of multiple exponential components, lower temperatures, will not be returned from the model, regardless of the employed parameter values. The observed delayed emission curve can be reproduced by extending the employed model to include multiple isomers of  $\text{Al}_4^-$ . The photoelectron spectra of

$Al_4^-$  also contain features which could be explained by the presence of isomers for this species [23]. New theoretical calculations for  $Al_4^-$  were not able to rule out the existence of isomers, but did indicate that this particular species was far more complicated than initially treated. Even the ground state of this anion appears rather uncertain [101]. The cooling cluster could thus get trapped in these different geometries, each of which would demand the existence of an individual exponential component in the emission curve. The resulting total delayed emission curve would then produce the shape observed in the CTF after long trapping times.

Thirdly, while the barrier energy  $E_b$  is treated as an experimentally known value for these aluminum clusters, experiments can only yield an upper limit, as opposed to an exact value. While the same  $E_b$  values from [98] were assumed here as in the previous study [67], higher resolution experiments [23, 93, 102] put into question how well this value is actually known, by stating that while the vertical (Franck-Condon) detachment energies can be clearly measured, only an upper limit on the adiabatic electron energy (the barrier energy  $E_b$ ) of 2.0 eV can be established for  $Al_4^-$  [102]. Given the sensitivity of the theoretical model applied in the temperature fits as shown in Fig. 5.30(b), even small changes in  $E_b$  result in completely different temperatures and require different Arrhenius factors to produce meaningful results.

The fourth problem is the hugely enhanced delayed emission that occurs at times shortly after laser absorption (8-10  $\mu$ s) as observed for  $Al_4^-$  and  $Al_5^-$  that cannot at all be explained with the current model. Increasing the  $A$  factor to account for the vast difference in magnitude between the first two data points cannot reproduce the remaining portion of the curve. A fast decaying isomer may also be able to explain this feature, but additional cluster information is needed to confirm or reject this idea. Future measurements at different beam energies, and therefore different times shortly after laser absorption, should be able to further elucidate this process.

### 5.3.3 Conclusions on cluster cooling

The delayed emission of  $Al_4^-$  and  $Al_5^-$  were analyzed using a statistical model to fit the cluster temperature as they radiatively cooled after formation in a hot sputter source and were stored in an electrostatic trap at ambient temperatures below 15 K. The derived temperatures obtained of both  $Al_4^-$  and  $Al_5^-$  after 5.5 s of storage in this cryogenic trap were significantly higher ( $\approx$  230 K) than the blackbody environment they were stored in.  $Al_5^-$  was also observed to radiatively cool faster than  $Al_4^-$ , which can most easily be explained by considering that the larger cluster has more vibrational degrees of freedom. The theoretical model applied is, however, too simple to fully explain the delayed emission curves seen here. The confirmed

presence of delayed fragmentation in  $\text{Al}_4^-$  [73] and its possible temperature dependence seen in this work, in addition to the significant possibility of different isomeric states of  $\text{Al}_4^-$ , both of which significantly affect the observed delayed emission spectra, are not included in this model. Furthermore, the cluster properties which this model depends upon, are not known well enough to accurately determine a reliable calibration temperature, preventing the calculation of the cooled aluminum cluster temperature after storage in a reduced blackbody environment below 15 K.

Delayed emission from multiple aluminum anion clusters ( $\text{Al}_4^-$ ,  $\text{Al}_5^-$ ,  $\text{Al}_6^-$ ,  $\text{Al}_7^-$ , and  $\text{Al}_8^-$ ) has been observed. The number of delayed events as a function of storage time varies as a function of cluster size, showing dramatic differences, particularly for  $\text{Al}_6^-$ . Cluster dependent absorption cross-sections, cooling rates, or branching ratios between delayed electron emission and fragmentation could explain such differences. The significant differences observed for  $\text{Al}_6^-$  also correspond to a cluster size that exhibits a photoelectron spectra thought to represent a geometry transition between 2D planar structures and 3D geometrical shapes [23].

$\text{Al}_4^-$  beams employing three different ion currents were compared and produced the same fitted temperature after summing the delayed emission events from 1.5 to 3.0 s after ion injection. Significant differences in the relative amount of delayed emission within the first second after ion injection was, however, observed as a function of ion current. It is not clear if this corresponds to an ion current dependent cooling rate during the first second after injection, but this should be investigated in the future.

The large delayed emission signal observed for both  $\text{Al}_4^-$  and  $\text{Al}_5^-$  shortly after laser absorption could not be reproduced with the employed statistical model. The ratio of this signal to that from the same laser excited ion packet one trap revolution later demonstrates a storage time dependence, and therefore, a cluster temperature dependence. Since delayed fragmentation for  $\text{Al}_4^-$  has already been observed, with branching ratios that change as a function of time after laser absorption [73], the most likely explanation for the observed signal is the delayed fragmentation of both of these anion species. The findings here show that this process is temperature dependent and more enhanced for  $\text{Al}_5^-$  in comparison to  $\text{Al}_4^-$ .

Future investigations of the delayed emission of multiple aluminum anion cluster-sizes, both at room temperature and at cryogenic temperatures in the CTF, are planned and should lead to a better understanding of this process.

# Chapter 6

## Summary and Prospects

The Cryogenic Trap for Fast Ion Beams (CTF) was successfully commissioned and fulfilled both of its primary goals, which were to test and develop the technologies required for the design of the Cryogenic Storage Ring (CSR see Section 3.4) and to demonstrate vacuum on the order of  $10^{-13}$  mbar. This latter goal was surpassed, with a measured pressure of  $8 \pm 4 \cdot 10^{-14}$  mbar (density equivalent at room-temperature), or a density of  $2000 \pm 1000$  particles/cm<sup>3</sup> (see Section 4.4).

In addition to meeting and exceeding these expectations, this extremely high vacuum suppressed ion loss to such an extent that unprecedented measurements expanding the understanding of ion bunching in an electrostatic ion beam trap (EIBT) were possible. These findings included the confirmation of a minimum number of charges required to maintain stable bunches in self-bunching mode, a new unexplained relationship that most likely exists between the size and shape of an ion bunch and its resulting lifetime in self-bunching mode, the demonstration that supporting the bunch via RF can dramatically extend the bunch lifetime from several seconds to over 100 s, possible observation of intrabeam scattering, an unknown rest-gas-density independent bunch loss mechanism, and a demonstration of the importance of phase matching the ion beam and the applied RF bunching pulses. A measurement of the ion bunch spatial distribution was also made possible via a novel method employing photo-detachment, simultaneously demonstrating that in self-bunching mode, a DC component of ions remains apart from the bunch. The observed ion bunch durations also suggest that mass resolution on the order of  $\Delta m/m = 7 \cdot 10^{-8}$  may be possible at these pressures, which is competitive to the performance of storage rings.

In addition to these ion bunching results, two mass-selection techniques were successfully demonstrated, where the knock-out procedure commonly used in storage rings was implemented inside an EIBT for the first time, also allowing the first measurement of an EIBT's tune. Storage lifetimes were extended from 30 ms at

room temperature to over 5 minutes with the dramatic pressure reduction at cryogenic temperatures using 7.1 keV  $\text{N}_2^+$  ions. This lifetime is not limited by the CTF's vacuum, but rather by a newly discovered rest-gas-density independent trap loss mechanism. A novel approach of performing decay measurements employing the photo-detachment of anions was also demonstrated.

Two experiments using aluminum cluster anions studied the fast decays of hot clusters and photon-induced delayed emission as a function of storage time. To our knowledge, this is the first time that the typically observed  $1/t^n$  decay exponent ( $n$ ) of hot clusters is shown to be temperature dependent and is most likely due to a radiation-induced decay. The photon-induced delayed electron emission studies were able to demonstrate the cooling of  $\text{Al}_4^-$  and  $\text{Al}_5^-$  as a function of storage time in the cryogenic trap. They also clearly show that the previously employed statistical model cannot accurately reproduce all of the observed emission spectra features nor produce a reliable temperature calibration of the clusters. Delayed emission was identified for a range of aluminum clusters, including  $\text{Al}_n^-$  ( $n = 4$  to  $8$ ). Dramatic emission variations as a function of storage time were found between the smaller clusters ( $n = 4$  and  $5$ ) and a transitional clusters ( $n = 6$ ), where cluster geometries are expected to evolve from planar structures to the 3D structures formed by larger clusters. Possible evidence for at least one isomeric state of  $\text{Al}_4^-$  was observed, in addition to what is most likely the temperature dependence of delayed fragmentation.

While this work primarily covered measurements performed with the CTF, it should be stated that the CSR is currently being assembled. During the fall and early winter of 2009, the isolation vacuum chambers will be delivered, the first of which have already been installed on precision aligned supports. The inner cryogenic chambers will be delivered and assembled with the electrodes in the new year.

To make space for the CSR, the CTF was disconnected from the helium refrigeration system and moved to a nearby laboratory. Installation and room-temperature trapping have already commenced with construction plans underway to supply the trap with 4 K helium. The injection beam line has been significantly changed with the introduction of a  $90^\circ$  bending magnet, allowing higher level mass selection of the injected beam before injection into the trap.

Before the trap is cooled to cryogenic temperatures again, room-temperature investigation of mass-selected aluminum cluster decays occurring within the first 20 ms will be studied to further elucidate the observed temperature dependence of this  $1/t$  decay. Lifetime measurements of molecular metastable states such as  $\text{SF}_6^-$  are also planned. The reinstallation of the laser, perpendicularly crossing the trap is also underway. Further study of the delayed emission of various mass-selected cluster anion species at room-temperatures will help to elucidate this process, in addition

---

to allowing an easy comparison of data taken at different trap temperatures.

After the trap has been cooled again in its new location in early 2010, a variety of exciting experimental investigations have been proposed.

The opportunity to disentangle the various ion loss processes in an EIBT due to the extreme CTF vacuum levels needs to be thoroughly studied. This will contribute to a better understanding of how EIBTs in general function, and how to limit the various losses. Given the long lifetimes which are also expected in the CSR, determining which other previously unimportant and possibly unseen loss mechanisms exist in the CTF could significantly help in maximizing the beam lifetimes. Confirming the presence of intrabeam scattering, which appears to fit initial beam losses in at least two cases, for example, or understanding losses that lead to what room-temperature EIBTs simply call ‘non-linear’ losses just after injection, would promote a better understanding of beam dynamics inside these traps.

CTF cryogenic temperatures and their associated extremely low rest gas densities could also be used to perform a precise, mass-selected  $\text{Al}_4^-$  lifetime measurement to check for isomeric states. room-temperature lifetimes have already been investigated, but due to the insufficiently understood initial trapping losses, possible states cannot be distinguished. The presence of multiple exponential components could further strengthen the case for the presence of various isomers, which need to be theoretically studied more closely. Working with theorists to more thoroughly understand the ground state of  $\text{Al}_4^-$  and explore the presence of isomeric states is also important since this could help explain some of the observations in this work. Such studies involving other aluminum anion cluster sizes would also be worthwhile. Performing lifetime measurements on other cations and anions, which are thought to have metastable states, would also be of interest to study at cryogenic temperatures, as their decays can be more clearly observed than at room-temperature.

An additional possibility is performing temperature dependent blackbody induced radiative dissociation (BIRD) measurements of species such as  $\text{SF}_6^-$ . Such species are produced in cold ion sources and begin to decay when warmed, as they are not stable at higher temperatures. The decay rate of such clusters is temperature dependent, so that measurements at different temperatures should be able to yield their binding energy.

The delayed emission of a multitude of mass-selected cluster anions will be revisited at cryogenic temperatures. Investigating the cluster-size dependence of the delayed emission is of particular interest, along with the possibility of further measurements on what appears to be the temperature dependence of delayed fragmentation.

More in-depth measurements of the trap’s tune using a finer frequency scan are

also planned. Investigating this trap property as a function of the trap potentials to better understand the associated knock-out mass selection technique, and to possibly achieve better mass selection than is currently possible with the bending magnet will also be explored. Performing this measurement as a function of trap temperature should also allow the determination of the small trap length change as the electrodes move along the beam axis while they cool down.

The CTF is uniquely set up to investigate a large variety of ion bunching experiments. Significantly extending the mass measurement resolution of EIBT type devices is envisaged due to CTF vacuum levels and the ion bunch duration times of over ten seconds already observed. Similarly, further investigating the minimum number of charges required for a stable bunch is warranted, particularly since both existing theoretical models do not reproduce the differences observed between  $N_2^+$  and  $Al_2^-$ . The crossed laser and ion beam geometry coupled with the CTF's extreme vacuum could also be employed to directly measure the width and length of the bunch in the field-free region, to further test the two models and their differing bunch shapes. Additional studies on RF bunching would assist in elucidating the loss mechanism preventing the artificially bunched beam from achieving lifetime decay rates longer than 100 s. Investigating self-bunching itself offers a variety of possible experiments; clarifying the relationship between the bunch size and shape with the bunch decay lifetime, and determine how the minimum number of charges required for a stable bunch varies as a function of properties such as mass and beam energy. Additional studies measuring the bunch length as a function of time after injection to 'watch' the bunch expand are envisaged (as opposed to just the two times after injection studied here), in addition to measuring the beam width by narrowing the laser beam size and scanning across the trap width.

# Bibliography

- [1] Delsemme, A. (1984) The cometary connection with prebiotic chemistry. *Origins of Life*, **14**, 51. 1.1
- [2] Oro, J. (1961) Comets and the formation of biochemical compounds on the primitive earth. *Nature*, **190**, 389. 1.1
- [3] Chyba, C. and Sagan, C. (1992) Endogenous production, exogenous delivery and impact-shock synthesis of organic molecules: an inventory for the origins of life. *Nature*, **355**, 125. 1.1
- [4] Anders, E. (1989) Pre-biotic organic matter from comets and asteroids. *Nature*, **342**, 255. 1.1
- [5] Anders, E., Hayatsu, R., and Studier, M. (1973) Organic compounds in meteorites. *Science*, **182**, 781. 1.1
- [6] Carr, J. and Najita, J. (2008) Organic molecules and water in the planet formation region of young circumstellar disks. *Science*, **319**, 1504. 1.1
- [7] Cernicharo, J., Guélin, M., Agúndez, M., McCarthy, M., and Thaddeus, P. (2008) Detection of C<sub>5</sub>N and vibrationally excited C<sub>6</sub>H in IRC+ 102161. *Astrophysical Journal Letters*, **688**, L83. 1.1
- [8] Herbst, E. and Klemperer, W. (1973) The formation and depletion of molecules in dense interstellar clouds. *The Astrophysical Journal*, **185**, 505. 1.1
- [9] Roueff, E. and Herbst, E. (2009) Molecular ions in astrophysics. *J. Phys.: Conf. Ser.*, **192**, 012008. 1.1
- [10] Wootten, A., Boulanger, F., Bogey, M., Combes, F., Encrenaz, P., Gerin, M., and Ziurys, L. (1986) A search for interstellar H<sub>3</sub>O<sup>+</sup>. *Astronomy and Astrophysics*, **166**, L15. 1.1

- 
- [11] Hollis, J., Churchwell, E., Herbst, E., and Lucia, F. D. (1986) An interstellar line coincident with the P(2, 1) transition of hydronium( $\text{H}_3\text{O}^+$ ). *Nature*, **322**, 524. 1.1
- [12] McCarthy, M., Gottlieb, C., Gupta, H., and Thaddeus, P. (2006) Laboratory and astronomical identification of the negative molecular ion  $\text{C}_6\text{H}^-$ . *The Astrophysical Journal Letters*, **652**, L141. 1.1
- [13] Remijan, A., Hollis, J., Lovas, F., Cordiner, M., Millar, T., Markwick-Kemper, A., and Jewell, P. (2007) Detection of  $\text{C}_8\text{H}$  and comparison with  $\text{C}_8\text{H}$  toward IRC+ 10 216. *Astrophysical Journal Letters*, **664**. 1.1
- [14] Brunken, S., Gupta, H., Gottlieb, C., McCarthy, M., and Thaddeus, P. (2007) Detection of the carbon chain negative ion  $\text{C}_8\text{H}$  in TMC-1. *Astrophysical Journal Letters*, **664**, L43. 1.1
- [15] Cernicharo, J., Guélin, M., Agúndez, M., Kawaguchi, K., McCarthy, M., and Thaddeus, P. (2007) Astronomical detection of  $\text{C}_4\text{H}^-$ , the second interstellar anion. *Astronomy and Astrophysics*, **467**, L37. 1.1
- [16] Thaddeus, P., Gottlieb, C., Gupta, H., Brunken, S., McCarthy, M., Agundez, M., Guelin, M., and Cernicharo, J. (2008) Laboratory and astronomical detection of the negative molecular ion  $\text{C}_3\text{N}$ . *The Astrophysical Journal*, **677**, 1132. 1.1
- [17] Wolf, A., Buhr, H., Grieser, M., von Hahn, R., Lestinsky, M., Lindroth, E., Orlov, D., Schippers, S., and Schneider, I. (2006) Progress in stored ion beam experiments on atomic and molecular processes. *Hyperfine Interactions*, **172**, 111. 1.1
- [18] Kreckel, H., et al. (2007) Electron collisions and rovibrational action spectroscopy of cold  $\text{H}_3^+$  molecules. *J. Phys.: Conf. Ser.*, **88**, 012064. 1.1
- [19] Novotny, O., et al. (2010) Fragmentation channels in dissociative electron recombination with hydronium and other astrophysically important species. *Journal of Physical Chemistry A: To be published*. 1.1
- [20] Novotny, S., et al. (2008) Anisotropy and molecular rotation in resonant low-energy dissociative recombination. *Physical Review Letters*, **100**, 193201. 1.1
- [21] Orlov, D., Krantz, C., Bernhardt, D., Brandau, C., Hoffmann, J., Müller, A., Ricsóka, T., Schippers, S., Shornikov, A., and Wolf, A. (2009) High resolution low-energy dielectronic recombination rate coefficients of beryllium-like

- germanium: Qed test bench for two-valence-electron systems. *J. Phys.: Conf. Ser.*, **163**, 012058. 1.1
- [22] Litvinov, Y., et al. (2005) Mass measurement of cooled neutron-deficient bismuth projectile fragments with time-resolved Schottky mass spectrometry at the FRS-ESR facility. *Nuclear Physics A*, **756**, 3. 1.1
- [23] Cha, C., Ganteför, G., and Eberhardt, W. (1994) The development of the 3p and 4p valence band of small aluminum and gallium clusters. *The Journal of Chemical Physics*, **100**, 995. 1.1, 5.1.2, 5.3.2, 5.3.2, 5.3.3
- [24] Møller, S. (1997) ELISA, an electrostatic storage ring for atomic physics. *NIM A*, **394**, 281. 1.2
- [25] Tanabe, T., Chida, K., Noda, K., and Watanabe, I. (2002) An electrostatic storage ring for atomic and molecular science. *Nuclear Inst. and Methods in Physics Research A*, **482**, 595. 1.2
- [26] Jinno, S., Takao, T., Omata, Y., Satou, A., Tanuma, H., Azuma, T., Shiromaru, H., Okuno, K., Kobayashi, N., and Watanabe, I. (2004) TMU electrostatic ion storage ring designed for operation at liquid nitrogen temperature. *Nuclear Inst. and Methods in Physics Research, A*, **532**, 477. 1.2
- [27] Schlachter, A., Stearns, J., Graham, W., Berkner, K., Pyle, R., and Tanis, J. (1983) Electron capture for fast highly charged ions in gas targets: An empirical scaling rule. *Physical Review A*, **27**, 3372. 1.2
- [28] von Hahn, R., et al. (2008) The cryogenic storage ring project at Heidelberg. *Proceedings of EPAC08, Genoa, Italy*, p. 394. 1.2, 3.1.2
- [29] Fadil, H., Grieser, M., von Hahn, R., Orlov, D., Schwalm, D., Wolf, A., and Zajfman, D. (2006) Low energy electron cooling and accelerator physics for the Heidelberg CSR. *AIP Conference Proceedings*. 1.2
- [30] Orlov, D., Fadil, H., Grieser, M., and Wolf, A. (2006) Cold photocathode electron sources and perspectives for low energy magnetically guided electron beams. *AIP Conference Proceedings*. 1.2
- [31] Shornikov, A., Orlov, D., Grieser, M., Blaum, K., and Wolf, A. (2009) Ultra-low energy electron cooler for the Heidelberg CSR. *Proceedings of COOL Lanzhou, China*. 1.2

- [32] Sieber, T., Fadil, H., Grieser, M., von Hahn, R., and Wolf, A. (2006) A beam diagnostics system for the Heidelberg Cryogenic Storage Ring CSR. *Proceedings of EPAC 2006, Edinburgh, Scotland*, p. 1067. 1.2
- [33] Laux, F., Grieser, M., von Hahn, R., Sieber, T., Wolf, A., and Blaum, K. (2009) Position pickups for the Cryogenic Storage Ring. *Proceedings of DIPAC09, Basel, Switzerland*. 1.2
- [34] Sieber, T., Blaum, K., Grieser, M., Laux, F., Lange, M., Orlov, D., Hahn, R. V., and Wolf, A. (2009) Intensity and profile measurement for low intensity ion beams in an electrostatic cryogenic storage ring. *Proceedings of DIPAC09, Basel, Switzerland*. 1.2
- [35] Kühnel, K., Putignano, M., Welsch, C., Schröter, C., and Ullrich, J. (2008) A novel beam profile monitor based on a supersonic gas jet. *Proceedings of EPAC08, Genoa, Italy*. 1.2
- [36] Moshhammer, R., Unverzagt, M., Schmitt, W., Ullrich, J., and Schmidt-Böcking, H. (1996) A 4pi recoil-ion electron momentum analyzer: A high-resolution 'microscope' for the investigation of the dynamics of atomic, molecular and nuclear reactions. *NIM B*, **108**, 425. 1.2
- [37] Zajfman, D., Heber, O., Vejby-Christensen, L., Ben-Itzhak, I., Rappaport, M., Fishman, R., and Dahan, M. (1997) Electrostatic bottle for long-time storage of fast ion beams. *Physical Review A*, **55**, 1577. 1.3, 2.1, 3, 3.1
- [38] Dahan, M., Fishman, R., Heber, O., Rappaport, M., Altstein, N., Zajfman, D., and van der Zande, W. (1998) A new type of electrostatic ion trap for storage of fast ion beams. *Review of Scientific Instruments*, **69**, 76. 1.3, 3.1
- [39] Plaß, W. R., Dickel, T., Czok, U., Geissel, H., Petrick, M., Reinheimer, K., Scheidenberger, C., and I.Yavor, M. (2008) Isobar separation by time-of-flight mass spectrometry for low-energy radioactive ion beam facilities. *Nuclear Inst. and Methods in Physics Research, B*, **266**, 4560. 1.3, 3.1
- [40] Aviv, O., Toker, Y., Errit, M., Bhushan, K. G., Pedersen, H. B., Rappaport, M. L., Heber, O., Schwalm, D., and Zajfman, D. (2008) A bent electrostatic ion beam trap for simultaneous measurements of fragmentation and ionization of cluster ions. *Review of Scientific Instruments*, **79**, 083110. 1.3, 3.1
- [41] Pedersen, H., et al. (2009) Neutral and charged photofragment coincidence imaging with soft x rays on molecular ion beams: Breakup of  $\text{H}_3\text{O}^+$  at 13.5 nm. *Physical Review A*, **80**, 012707. 1.3

- [42] Zajfman, D., Rudich, Y., Sagi, I., Strasser, D., Savin, D., Goldberg, S., Rappaport, M., and Heber, O. (2003) High resolution mass spectrometry using a linear electrostatic ion beam trap. *International Journal of Mass Spectrometry*, **229**, 55. 1.3
- [43] Wolf, A., Bhushan, K., Ben-Itzhak, I., Altstein, N., Zajfman, D., Heber, O., and Rappaport, M. (1999) Lifetime measurement of  $\text{He}^-$  using an electrostatic ion trap. *Physical Review A*, **59**, 267. 1.3
- [44] Turco, R., Zhao, J., and Yu, F. (1998) A new source of tropospheric aerosols: Ion-ion recombination. *Geophysical research letters*, **25**, 635. 1.3
- [45] Lange, M., et al. (2010) A cryogenic electrostatic trap for storing keV ion beams. *To be published*. 2.2.3, 4.4
- [46] Pedersen, H., Strasser, D., Heber, O., Rappaport, M., and Zajfman, D. (2002) Stability and loss in an ion-trap resonator. *Physical Review A*, **65**, 042703. 2.2.4
- [47] Menk, S. (2009) A cryogenic trap for fast ion beams. *Diploma Thesis: University of Heidelberg*. 2.2.4, 3.1.2, 3.4.4, 4.1, 4.3.2, 4.4
- [48] Serio, M. (1989) *Transverse betatron tune measurements*, vol. 343. 2.3
- [49] Pedersen, H., Strasser, D., Ring, S., Heber, O., Rappaport, M., Rudich, Y., Sagi, I., and Zajfman, D. (2001) Ion motion synchronization in an ion-trap resonator. *Physical Review Letters*, **87**, 055011. 2.4, 4.2.1, 4.2.2, 4.2.5
- [50] Pedersen, H., Strasser, D., Amarant, B., Heber, O., Rappaport, M., and Zajfman, D. (1997) Diffusion and synchronization in an ion-trap resonator. *Anal. Chem Phys Rev A*, **65**, 042704. 2.4
- [51] Bhushan, K., Gadkari, S., Yakhmi, J., and Sahni, V. (2007) Electrostatic ion trap and fourier transform measurements for high-resolution mass spectrometry. *Review of Scientific Instruments*, **78**, 083302. 2.4
- [52] Zajfman, D., Strasser, D., Heber, O., Goldberg, S., Diner, A., and Rappaport, M. (2004) Dynamics of stored ions in an electrostatic ion beam trap. *Nuclear Inst. and Methods in Physics Research A*, **532**, 196. 2.4
- [53] Strasser, D., et al. (2002) Negative mass instability for interacting particles in a 1D box: Theory and application. *Physical Review Letters*, **89**, 283204. 2.4, 2.4, 4.2.1

- 
- [54] Geyer, T. and Tannor, D. (2004) A mapping approach to synchronization in the 'Zajfman trap': stability conditions and the synchronization mechanism. *Journal of Physics B*, **37**, 73. 2.4
- [55] Geyer, T. and Tannor, D. (2005) A mapping approach to synchronization in the 'Zajfman trap': II. the observed bunch. *Journal of Physics B*, **38**, 3423. 2.4, 2.4, 2.4, 4.2.1
- [56] Nielsen, C. E., Sessler, A. M., and Symon, K. R. (1959) *High energy accelerators and instrumentation*. 2.4
- [57] Bastert, R. (2009) Erzeugung kurzer ionenpulse in einem speicherring. *Dipoma thesis: University of Heidelberg*. 2.4, 4.2.1, 4.2.1
- [58] Lawson, J. (1988) *The Physics of Charged Particle Beams 2nd. ed.*, vol. 75. 2.4
- [59] Dushman, S. (1930) Thermionic emission. *Reviews of Modern Physics*, **2**, 381. 2.5
- [60] Andersen, J., Bonderup, E., and Hansen, K. (2002) Thermionic emission from clusters. *Journa of Physics B*, **35**, R1. 2.5, 2.5.1, 2.5.1, 2.5.1, 2.5.1
- [61] Andersen, J., Brink, C., Hvelplund, P., Larsson, M., Nielsen, B. B., and Shen, H. (1996) Radiative cooling of C<sub>60</sub>. *Physical Review Letters*, **77**, 3991. 2.5, 2.5.1, 2.5.1
- [62] Andersen, J., et al. (2003) Power-law decay of collisionally excited amino acids and quenching by radiative cooling. *European Physical Journal D*, **25**, 139. 2.5, 2.5.1, 2.5.1, 2.5.1, 2.5.2, 5.2.4, 5.2.4, 5.2.4
- [63] Andersen, J., Andersen, L., Hvelplund, P., Lapierre, A., Møller, S., Nielsen, S., Pedersen, U., and Tomita, S. (2003) Studies of clusters and biomolecules in ELISA. *Hyperfine Interactions*, **146/147**, 283. 2.5, 2.5.1, 2.5.1
- [64] Andersen, L., Heber, O., and Zajfman, D. (2004) Physics with electrostatic rings and traps. *Journal of Physics B*, **37**, R57. 2.5, 2.5.1
- [65] Fedor, J., Hansen, K., Andersen, J. U., and Hvelplund, P. (2005) Nonthermal power law decay of metal dimer anions. *Physical Review Letters*, **94**, 1. 2.5, 2.5.1, 2.5.1, 2.5.1, 2.5.1, 5.2.3, 5.2.3, 5.2.3

- [66] Nielsen, S., Andersen, J., Forster, J., Hvelplund, P., Hvelplund, P., Liu, B., Pedersen, U., and Tomita, S. (2003) Photodestruction of adenosine 5'-monophosphate (AMP) nucleotide ions in vacuo: Statistical versus nonstatistical processes. *Physical Review Letters*, **91**, 048302. 2.5, 2.5.2
- [67] Toker, Y., Aviv, O., Eritt, M., Rappaport, M., Heber, O., Schwalm, D., and Zajfman, D. (2007) Radiative cooling of  $Al_4^-$  clusters. *Physical Review A*, **76**, 053201. 2.5, 2.5.2, 5.3, 5.3.1, 5.3, 5.3.2, 5.23, 5.3.2, 5.24, 5.3.2, 5.3.2, 5.3.2
- [68] Hansen, K., Andersen, J., Hvelplund, P., Moller, S., Pedersen, U., and Petrunin, V. (2001) Observation of a  $1/t$  decay law for hot clusters and molecules in a storage ring. *Physical Review Letters*, **87**, 123401. 2.5, 2.5.1, 2.5.1, 2.5.2
- [69] Andersen, J. U., Gottrup, C., Hansen, K., Hvelplund, P., and Larsson, M. O. (2001) Radiative cooling of fullerene anions in a storage ring. *The European Physical Journal D*, **17**, 189. 2.5.1, 2.5.1
- [70] Campbell, E. and Levine, R. (2000) Delayed ionization and fragmentation en route to thermionic emission: Statistics and dynamics. *Annual Review of Physical Chemistry*, **51**, 65. 2.5.2
- [71] Ganteför, G., Eberhardt, W., Weidele, H., Kreisle, D., and Rechnagel, E. (1996) Energy dissipation in small clusters: Direct photoemission, dissociation, and thermionic emission. *Physical Review Letters*, **77**, 4524. 2.5.3
- [72] Shi, Y., Spasov, V., and Ervin, K. (1999) Competitive fragmentation and electron loss kinetics of photoactivated silver cluster anions: Dissociation energies of  $Ag_n^-$  ( $n=7-11$ ). *J. Chem. Phys.*, **111**, 938. 2.5.3
- [73] Aviv, O., Toker, Y., Strasser, D., Rappaport, M., Heber, O., Schwalm, D., and Zajfman, D. (2010) Competition between delayed ionization and fragmentation in small hot aluminum cluster anions. *To be published*. 2.5.3, 5.2.4, 5.3.2, 5.3.3
- [74] Sieber, T., Blaum, K., Grieser, M., Lange, M., Laux, F., Sorg, T., von Hahn, R., and Wolf, A. (2008) Beam diagnostics for the prototype of the cryogenic storage ring CSR. *Proceedings of EPAC08, Genoa, Italy*, p. 1287. 3, 3.2.1
- [75] Weisend, J. (1998) *Handbook of cryogenic engineering*. 3.1.1
- [76] Hahn, R. V., et al. (2008) Commissioning of the cryogenic plant for the Cryogenic Storage Ring (CSR) at Heidelberg. *Proceedings ICEC*. 3.1.2

- 
- [77] Orlov, D., Lange, M., Froese, M., von Hahn, R., Grieser, M., Mallinger, V., Rappaport, M., Sieber, T., Weber, T., and Wolf, A. (2008) Cryogenic and vacuum technological aspects of the low-energy electrostatic cryogenic storage ring. *AIP Conference Proceedings*. 3.1.7
- [78] Redhead, P. (1999) Extreme high vacuum. *CERN Accelerator School on Vacuum Technology*, p. 213. 3.1.7, 3.1.7
- [79] Lange, M., et al. (2008) Commissioning of the Heidelberg cryogenic trap for fast ion beams (CTF). *Proceedings of EPAC08, Genoa, Italy*, p. 319. 3.4.4, 4.1
- [80] Zajfman, D., Heber, O., Rappaport, M., Pedersen, H., Strasser, D., and Goldberg, S. (2003) Self-bunching effect in an ion trap resonator. *Journal of the Optical Society of America B*, **20**, 1028. 4.2.1, 4.2.1, 4.2.2
- [81] Strasser, D., Heber, O., Goldberg, S., and Zajfman, D. (2003) Self-bunching induced by negative effective mass instability in an electrostatic ion beam trap. *Journal of Physics B*, **36**, 953. 4.2.1
- [82] Blaum, K. (2006) High-accuracy mass spectrometry with stored ions. *Physics Reports*, **425**, 1. 4.2.5
- [83] Toker, Y., Altstein, N., Aviv, O., Rappaport, M., Heber, O., Schwalm, D., Strasser, D., and Zajfman, D. (2009) The kick-out mass selection technique for ions stored in an electrostatic ion beam trap. *Journal of Instrumentation*, **4**, P09001. 4.3
- [84] Lee, J., Wang, M., Hsu, K., Sheu, R., Lin, G., and Hsue, C. (1996) Suppression of the transverse oscillation in the SRRC storage ring by RF knockout method. *Proceedings of the 1995 IEEE Particle Accelerator Conference*, p. 2968. 4.3
- [85] Froese, M., et al. (2009) Cryogenic ion beam storage. *Proceedings of PAC09, Vancouver, Canada*, p. 1. 4.3.2, 4.4
- [86] Sheridan, J., Merlo, T., and Enzweiler, J. (1979) Cross sections for asymmetric charge transfer and collisional dissociation reactions of atmospheric ions at keV energies. *Journal of Geophysical Research*, **84**, 7302. 4.4
- [87] Haugsjaa, P., Amme, R., and Utterback, N. (1968) Charge-transfer cross sections for  $\text{N}_2^+$  ions incident on  $\text{H}_2$  and  $\text{D}_2$  between 20 and 1000 eV. *J. Chem. Phys.*, **49**, 4641. 4.4

- [88] Oepik, E. (1962) The lunar atmosphere. *Planetary and Space Science*, **9**, 211. 4.4
- [89] Habart, E., Abergel, A., Walmsley, C., Teyssier, D., and Pety, J. (2005) Density structure of the horsehead nebula photo-dissociation region. *Astronomy & Astrophysics*, **437**, 177. 4.4
- [90] Osterbrock, D. (1989) *Astrophysics of Gaseous Nebulae and Active Galactic Nuclei*. 4.4
- [91] Gabrielse, G., Fei, X., Orozco, L., Tjoelker, R., Haas, J., Kalinowsky, H., Trainor, T., and Kells, W. (1990) Thousandfold improvement in the measured antiproton mass. *Physical Review Letters*, **65**, 1317. 4.4
- [92] Ishimaru, H. (1989) Ultimate pressure of the order of  $10^{-13}$  torr in an aluminum alloy vacuum chamber. *Journal of Vacuum Science & Technology A: Vacuum, Surfaces, and Films*, **7**, 2439. 4.4
- [93] Li, X., Wu, H., Wang, X., and Wang, L. (1998) s-p hybridization and electron shell structures in aluminum clusters: A photoelectron spectroscopy study. *Physical Review Letters*, **81**, 1909. 5.1.2, 5.3.2
- [94] Scheer, M., Bilodeau, R., Thøgersen, J., and Haugen, H. (1998) Threshold photodetachment of  $\text{Al}^-$ : Electron affinity and fine structure. *Physical Review A*, **57**, R1493. 5.2.1
- [95] Andersen, T. (2004) Atomic negative ions: structure, dynamics and collisions. *Physics Reports*, **394**, 157. 5.2.1
- [96] Nieman, G., Parks, E., Richtsmeier, S., Liu, K., Pobo, L., and Riley, S. (1986) Multiphoton ionization and fragmentation of transition-metal cluster oxides: high-temperature metal oxide compositions. *High temperature science*, **22**, 115. 5.2.1
- [97] Ganteför, G., Gausa, M., Meiwes-Broer, K., and Lutz, H. (1988) Photoelectron spectroscopy of jet-cooled aluminium cluster anions. *Zeitschrift für Physik D*, **9**, 253. 5.2.2
- [98] Taylor, K., Pettiette, C., Craycraft, M., Chesnovsky, O., and Smalley, R. (1988) UPS of negative aluminum clusters. *Chemical Physics Letters*, **152**, 347. 5.3, 5.3.2

- [99] Werner, R. (2005) Melting and evaporation transitions in small Al clusters: canonical monte-carlo simulations. *The European Physical Journal B*, **43**, 47. 5.3, 5.3.2, 5.3.2
- [100] Toker, Y. Private communication. 5.3, 5.3.2
- [101] Sommerfeld, T. Private communication. 5.3.2
- [102] Ganteför, G., Meiwes-Broer, K., and Lutz, H. (1988) Photodetachment spectroscopy of cold aluminum cluster anions. *Physical Review A*, **37**, 2716. 5.3.2

## **Acknowledgements:**

I wish to thank Andreas Wolf for giving me the opportunity to work on such an exciting, new, and challenging project. Thank you for your guidance, persistence, and encouragement throughout my three years here!

To Klaus Blaum, while you became our group director after I started, I would like to thank you for your consistent encouragement throughout the CTF measurements.

Robert, thank you for always having an open door and being available to listen and talk about whatever was new and exciting about the prototype! My thanks to Manfred for providing some theoretical support, as well as ensuring that everyone ate regularly! Dima, you and your sense of humour are sorely missed. I had a great time working with you and your cryogenic experience was invaluable. Just remember who the real hockey champions are (I'll give you a hint - their flag only contains two colours)! My thanks to Thomas and Felix for all your help with the pickup and its electronics. The data acquisition of the scope and spectrum analyzer, resulting in some of the figures in this work, was made possible by Felix! Thank you! I'd particularly like to thank Thomas for going on two Ebay expeditions with me as well as some great conversations! My thanks to Herr Repnow for answering my many questions about ion sources! I'd also like to thank Hicham for a great first year with this project before he left! It was great getting to know you, even if it was just a short time.

I have to thank Florian, Robin, and Sebastian for a great office atmosphere and sharing the joys and frustrations throughout this project! You three are great, understanding, as well as a little crazy!

To my CTF colleagues Michael, Sebastian, and Jozef - it's been an amazing time together putting this incredibly complex device together. Michael, you have a real gift for explaining concepts and I really value the discussions we've had. You're also really good at sewing, I wonder if that just applies to multilayer insulation! Remember: Don't feed the scientists! Jozef, it might have only been 6 months, but I'm really glad you were there to help out late in the evenings, despite (or maybe because of) the crazy music! Your enthusiasm and really one of a kind jokes can't be beat! As for Sebastian, I'm glad you signed up to spend yet more time on this project. Regardless of how long or late a measurement took, you were always there with me. I couldn't have wished for a better coworker! To all three of you, just remember which tools were the most useful during the assembly work!

To my friends Brandon, Ingrid, Martin, Rainer, Jule, Simon, Annemieke, and Werner who helped by providing a home away from home to try and minimize a little stress and time on the train, thank you! You have no idea how much this meant to me. I'd particularly like to thank Brandon and Ingrid for adopting me as the Canadian brother you didn't know you had!

Dirk und Michael, vielen Dank für eure Geduld, trotz der Vielzahl nötiger Besuche

während des Aufbaus. Ich bin froh, dass ich eure Unterstützung hatte, die CTF Komponenten anzupassen, damit letztlich alles zusammenpasste. Ich bin nicht nur zu euch gekommen, wenn ich etwas gebraucht habe, sondern auch nur um euch zu ärgern!

An unseren Computer Experten Rolf und unsere oft benötigten Elektroniker Oli, Peter und Thomas im Büro nebenan, danke euch. Von speziellen Computer Kontrollsystemen über Ausheizkabel bis hin zu Computer Netzteilen, eure Hilfe habe ich sehr geschätzt.

To the many visitors who not only provided good company, but many rewarding discussions, my thanks to Yoni, Oded, and Xavier! To Dirk, who was at the very least, a regular visitor hopping between Israel and Germany, my thanks for your input and the discussions we had about our results and generally at the coffee table!

To the entire cooking group, I'm really glad we were able to pretty consistently meet and cook for each other. I'm particularly happy that all of you like spicy chili! As for the running group, throughout the last three years people have come and gone, but to everyone who has participated at some point, I really enjoyed, and sometimes needed, the stress-relief of running up and down the mountain side!

I owe a big thank you to my parents. I wouldn't be here without you, and I don't just mean that literally! Thank you for all of your support, despite the long distance. Thank you for proof-reading the English in this thesis! To you and the rest of my family, I wouldn't be the person I am without you!

Schließlich möchte ich meiner liebe Freundin Ruth danken. Ohne deine Liebe, Unterstützung, Verständnis und Geduld wäre diese Arbeit nicht möglich gewesen. Danke insbesondere, dass du die unvorhersehbaren Arbeitszeiten akzeptiert hast!